MANIPULATION OF MOLECULES ON SURFACES WITH THE SCANNING TUNNELLING MICROSCOPE

by

DOGAN KAYA

A thesis submitted to the University of Birmingham

for the degree of

DOCTOR of PHILOSOPHY

June 2016

Nanoscale Physics Research Laboratory
School of Physics & Astronomy
University of Birmingham

ABSTRACT

An experimental study of buckminsterfullerene on the Au(111) surface and of chlorobenzene and oxygen molecules on the Si(111)-7x7 surface has been conducted with variable and room temperature (RT) scanning tunneling microscopes, respectively. First, the formation of hybrid clusters, $(C_{60})_n$-$(Au)_m$, from 110 K to RT has been studied at different C_{60} molecule coverages. The properties of the hybrid clusters, such as rotation, transformation and diffusion, were observed at RT. Mechanical manipulation of C_{60} molecules in the hybrid cluster was performed in order to explore the production of a single type of hybrid cluster. Cascade manipulation was achieved by downsizing $(C_{60})_{14}$-$(Au)_{63}$ clusters to $(C_{60})_7$-$(Au)_{19}$ clusters at RT. The manipulation of the hybrid clusters was performed at 110 K in addition to RT. A comparative study of the non-local manipulation of chlorobenzene molecules and oxygen on the Si(111)-7x7 surface was performed with the RT STM via electron induced from the STM tip. It is found that a suppression region (~40 Å) for both molecules is quite universal in the STM experiments. A local desorption threshold of +1.4 V was found for the chlorobenzene molecule. Local manipulation of bright and dark sites of oxygen were induced six different transformations on the molecular sites.

ACKNOWLEDGEMENTS

I would like to express the deepest appreciation to all those who helped me to complete my Ph.D. First and foremost, I would like to express my sincere thanks to my first supervisor Prof. Richard E. Palmer, and the second supervisor Dr. Quanmin Guo for their valuable guidance and encouragement, and providing me with a good environment and facilities and valuable discussions to complete this project. I learned lots of valuable skills in and out of the laboratory from them and hope to become like them.

I would like to express my appreciation to my colleague Dr. Tianluo Pan who trained me in RT-STM. Moreover, many thanks go to Mahroo Rokni Fard for her great friendship and collaboration on VT-STM working together on the magic number clusters project. Many thanks to my friends, current NPRL group members William, Scott, Dawn, Caroline and many others for their real friendships and help reading my thesis.

In addition, my sincere thanks go to my marvelous Turkish nation and the Republic of Turkey Ministry of National Education for the full scholarship. I am looking forward to serving my country willingly as opportunity provides.

Finally, honourable mention goes to my lovely and beloved family, my mother, father and sisters for their understanding, support, belief and prayer from a thousand miles away for me. The last thanks go to my lovely wife, Saadet Kaya, the person to whom my heart beats for my deepest love, not only for supporting, believing, helping and most importantly loving me since the first day of my Ph.D. journey, but also for being my inspiration, my smiles and the reason behind my happiness.

ABBREVIATIONS

CH	Corner Hole
DAS	Dimer-Adatom-Stacking-Fault
DC	Direct Current
DFT	Density Functional Theory
DR	Dimer Row
FC	Faulted Corner (Adatom)
FCC	Face Cubic Centered
FEMM	Finite Element Method Magnetics
FM	Faulted Middle (Adatom)
FR	Faulted Rest (Atom)
HCP	Hexagonal Close Packed
HOPG	Highly Ordered Pyrolitic Graphene
HREELS	High Resolution Electron Energy Loss Spectroscopy
IET	Inelastic Electron Tunneling
LDOS	Local Density of State
LEED	Low-Energy Electron Diffraction
PDOS	Partial Density of States
PhCl	Chlorobenzene (Phenyl Chloride)
RGA	Residual Gas Analyser
RHEED	Reflection High-Energy Electron Diffraction
SEM	Scanning Electron Microscopy
STM	Scanning Tunneling Microscopy
STS	Scanning Tunneling Spectroscopy
TDS	Thermal Desorption Spectroscopy
TEM	Transmission Electron Microscopy
TP	Turbo Pump
TSP	Titanium Sublimation Pump

UC	Unfaulted Corner (Adatom)
UHV	Ultra High Vacuum
UM	Unfaulted Middle (Adatom)
UPS	Ultraviolet Photoelectron Spectroscopy
UR	Unfaulted Rest (Atom)

TABLE OF CONTENTS

Page

Chapter 2. Experimental Methods

CHAPTER 1

INTRODUCTION

1.1 Overview

In the last century, one of the greatest scientific achievements was to produce an image of an atom with the transmission electron microscope (TEM) [1, 2]. The scanning tunnelling microscope (STM) was later invented by Binnig and Rohrer in 1981 [3], and subsequently Eigler and Schweizer not only imaged Xe atoms but also wrote the IBM initials with Xe atoms on a Ni surface at 4 K with the STM tip [4]. Now, the STM has been extensively used to create images of individual atoms/molecules, and manipulate them for nanoengineering applications via various mechanisms: mechanical (lateral, vertical), electric-field induced, and inelastic tunnelling induced techniques [5]. The physical, chemical, electronic, and bonding properties of adsorbed atoms and molecules have been widely investigated with the STM [6-10].

Miniaturization of electronic devices at the nanometer scale is one of the greatest challenges for researchers. In this context, fullerenes attract considerable interest due to their diverse potential applications in e.g. solar cells, organic electronics and single molecule devices in nanoelectronics [11, 12]. There is a need to produce desired materials and properties derived from C_{60} molecular nanostructures for real-world industrial applications at realistic temperatures. Such applications drive fundamental research on fullerene adsorption and assemblies. In this context, the Au(111) surface offers beneficial properties, such as resistance to oxidation and contamination over extended periods under in ultra-high vacuum (UHV) conditions. This surface also exhibits a unique herringbone structure, which allows molecular trapping due to nucleation at the elbow sites [13] and charge transfer from the surface to the adsorbed molecule (in this case, the fullerene).

By adsorbing C_{60} molecules and exploiting the surface properties of Au(111), Xie *et al.*[14] recently reported the fascinating production of hybrid $(C_{60})_m$–$(Au)_n$ clusters such as $(C_{60})_7$–$(Au)_{19}$, $(C_{60})_{10}$–$(Au)_{35}$, $(C_{60})_{12}$–$(Au)_{49}$, and $(C_{60})_{14}$–$(Au)_{63}$ at the elbow sites of the herringbone of the Au(111) surface. These clusters were generated by sequential deposition of Au atoms and C_{60} molecules on the Au (111) surface at 110 K. The $(C_{60})_m$–$(Au)_n$ clusters show a clear magic number effect where only certain combinations of m and n are found to be stable [14]. Because of the covalent interaction between the close-packed Au island at the heart of the hybrid clusters and the surrounding C_{60} molecules, the clusters are stable up to 400 K even though individual Au atoms and C_{60} molecules are mobile on the Au (111) surface at this temperature.

The STM is a versatile tool for manipulation selected C_{60} molecules on different surfaces using different approaches [15-22]. First, mechanical manipulation of C_{60} at Cu(111) steps was performed by Cuberes et al. [1996] via the repulsive interaction between the molecule and the tip at room temperature [21, 22]. They could build an abacus by pushing of the molecules using a STM tip. Afterward, pushing the molecule was studied to explore the binding site, polar angle and an azimuthal site using STM as well as STS measurements and DFT calculations [23], and also vibrational modes [24]. Both experimental [25, 26] and theoretical [18, 27, 28] studies have shown that rolling of C_{60} molecules on the Si(100)-2x1 reconstructed surface may be induced using the attractive force between the molecule and the STM tip.

More recently, the non-local manipulation of C_{60} molecules has been observed by Nouchi *et al.* [29]. In their work, the manipulation was stimulated by electron injection rather than direct tip-molecule mechanical interaction. Non-local electron (or hole) injection of a C_{60} close-packed layer on the Si(111)-7x7 surface at room temperature resulted in a ring-shaped structural rearrangement of the C_{60} molecule/s (polymerisation and depolymerisation). An example of local manipulation is the rotation of the 5-6 bond of the C_{60} molecules on the Si(111)-7x7 surface via bias voltage pulses at room temperature [15]. This rotation occurs possibly by first weakening the Si-C bond with electron injection into the molecule, followed by rotation as a result of low energy electron bombardment. Based on this mechanism, the manipulation of C_{60} molecules is possible at positions remote from the tip, without direct mechanical interaction with the molecule.

The study of *local* and *non-local* manipulation is based on electronic excitation of the bond between adsorbate and surface atoms remote from the tip [30]. The local manipulation process is an electron injection (or holes) directly into the adsorbent. Similarly the adsorbate on a surface can be manipulated far away from the STM tip by non-local electron (or hole) injection. After manipulation, a desorption [31-35], diffusion [36-38], or transformation event [35] can be observed due to electron injection into the adsorbent. The non-local desorption of chlorobenzene molecules on the Si(111)-7x7 surface was investigated experimentally previously [39-41]. Local manipulation of oxygen molecules on the Si(111)-7x7 surface was performed by Mayne *et al.* [35].

1.2 Structure of Thesis

In this thesis, the STM manipulation of molecules on surfaces at room and low temperature will be discussed. **Chapter 1** establishes the context for these experiments via a literature review covering the principles of STM and details of its previous use in manipulation experiments. **Chapter 2** presents the experimental methods used, including a description of the STM systems employed in these experiments. All experiments described in this work were performed in ultra-high vacuum (UHV) using either a room-temperature (RT) or variable-temperature (VT) STM. The VT-STM was used to produce hybrid magic number clusters at liquid nitrogen (~77 K) temperatures, whilst the RT-STM was used for chlorobenzene (PhCl) and oxygen studies of the Si(111)-7x7 surface. **Chapter 3** is concerned with understanding the hybrid magic number clusters $(C_{60})_m-(Au)_n$ on the Au(111) surface. The manipulation of these clusters has been studied in terms of reproducibility, structure formation, and transformation in terms of increasing C_{60} coverage. To explore the effect of the initial C_{60} deposition on the surface, experiments have been performed where the amount of Au atoms is kept constant whilst the amount of C_{60} molecules on the surface is increased. The idea was to control the growth process by controlling the amount of C_{60} molecules. **Chapter 4** introduces the concept of cascade manipulations of the hybrid magic number clusters at room temperature and 110 K. Producing and manipulating nanostructures at room temperature offers a significant advantage for realistic applications, e.g. bottom-up assembly of novel electronic structures. The manipulation of a selected C_{60} molecule from the top of a cluster and the rotation of a cluster, taking into account the tip effect and temperature effect are also discussed. **Chapter 5** describes a comparative study of the non-local manipulation of chemisorbed chlorobenzene and oxygen molecules on the Si(111)-7x7 surface in order to explore a suppression region in the ~40 Å diameter range. It also covers the details of the *local* manipulation of chlorobenzene and oxygen molecules on the Si(111)-7x7 surface at room temperature. In chapter 5, a detailed investigation of the origins of the suppression region is described, including the effect of increasing tunnelling current (thus decreasing tip-sample separation) and an electric field simulation (FEMM) on the suppression region. Finally, an overall summary and consideration of the prospects for future manipulation experiments will be presented in **chapter 6**.

1.3 The Principle of STM

One of the greatest recent advances in surface science has been the ability to directly image single atoms and detailed surface structures. The Scanning Tunnelling Microscope (STM), which was invented by Binnig and Rohrer in 1981 [3], has become an indispensable tool, not only for atomic resolution imaging but also for three-dimensional imaging on surfaces [3]. Since then, the STM has also been used to manipulate atoms and molecules for nanoengineering applications. For example, mechanical (lateral, vertical), electric field-induced, and inelastic tunnelling-induced manipulation are all major manipulation techniques applied in STM [5]. Before discussing STM-based manipulation experiments it is worthwhile to first briefly recap the principles of operation behind the STM.

In classical mechanics, if an object does not have sufficient energy to pass over a potential barrier, it will never pass through the potential barrier. On the contrary, in quantum mechanics, when a particle with energy E meets a potential barrier, which has height U_0 and width L, there is a finite probability of the particle traversing the classically forbidden region and being found on the other side. This phenomenon is known as *tunnelling* and can be explained by solving the one-dimensional Schrödinger equation.

In Figure 1, the one-dimensional rectangular potential barrier has a height of U = U_0 in the region 0 ≤ x ≤ L [9]. The solution of the wave function for the three regions and the transmission coefficient can be found via Schrödinger equation, as shown below

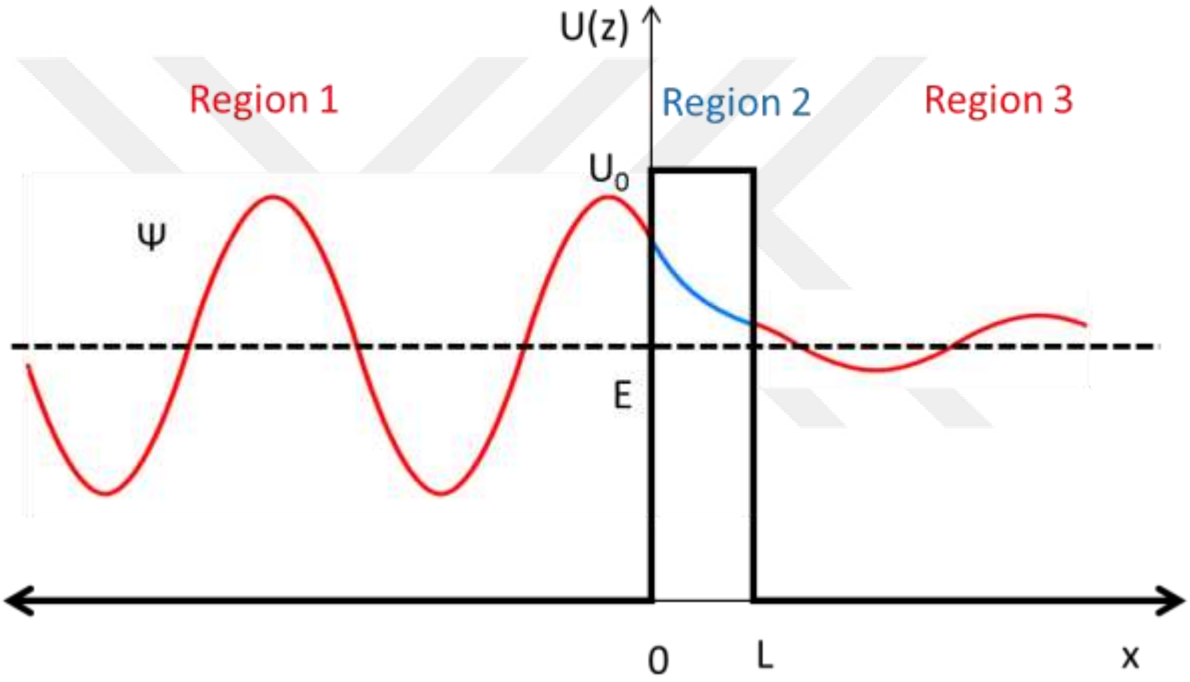

Figure 1: Schematic diagram for a 1-dimensional potential barrier with U=U_0 in the range 0≤x≤L shows quantum tunnelling. The solution of the wave functions in the three regions and the transmission coefficient can be found via the Schrödinger equation.

$$-\frac{\hbar^2}{2m}\frac{d^2}{dx^2}\Psi(x) + U\Psi(x) = E\Psi(x).$$

where *ħ* is Planck's constant, *m* is the mass of the particle, *E* is the energy of the particle. We can consider three regions in Figure 1 and the solution of the wave function will be different in each region. In region 1, x ≤ 0 and U = 0, so the Schrödinger equation is

$$-\frac{\hbar^2}{2m}\frac{d^2}{dx^2}\Psi_1(x) = E\Psi_1(x).$$

The solution of this equation is

$$\Psi_1(x) = Ae^{+ik_1x} + Be^{-ik_1x},$$

where k_1 is given by

$$k_1 = \frac{\sqrt{2mE}}{\hbar}.$$

For region 2, $0 \le x \le L$ and $U = U_0$, so the equation becomes

$$-\frac{\hbar^2}{2m}\frac{d^2}{dx^2}\Psi_2(x) = (E - U_0)\Psi_2(x).$$

The solution of this equation is

$$\Psi_2(x) = Ce^{+k_2x} + De^{-k_2x},$$

where the second term becomes zero and the function exponentially decays in the region 2. Here k_2 is given by,

$$k_2 = \frac{\sqrt{2m(U_0 - E)}}{\hbar}.$$

The solution for region 3, $L \le x$ and $U = 0$, is similar to region 1, so that,

$$\Psi_3(x) = Fe^{+ik_1x} + Ge^{-ik_1x}, \text{ where } k_1 = \frac{\sqrt{2mE}}{\hbar}.$$

The coefficients of these three equations (A, B, C, D, F, and G) can be found in terms of the decay constants k_1, k_2 and k_3 by inserting the boundary conditions into the wave functions, their first derivatives have to be equal at x = 0 and x = L. The probability of a particle being transmitted for G=0 is given by,

$$T = \frac{|\Psi_3(transmitted)|^2}{|\Psi_1(\text{incident})|^2} = \frac{F * F}{A * A}$$

After finding the coefficients and using the fact that $k_2L \gg 1$, the transmission probability becomes

$$T = \frac{16\mathrm{E}}{U_0}\left(1 - \frac{E}{U_0}\right)e^{-2k_2L} \cong e^{-2k_2L}$$

Therefore, the transmission probability of particle decays exponentially across the barrier (region 2) [9].

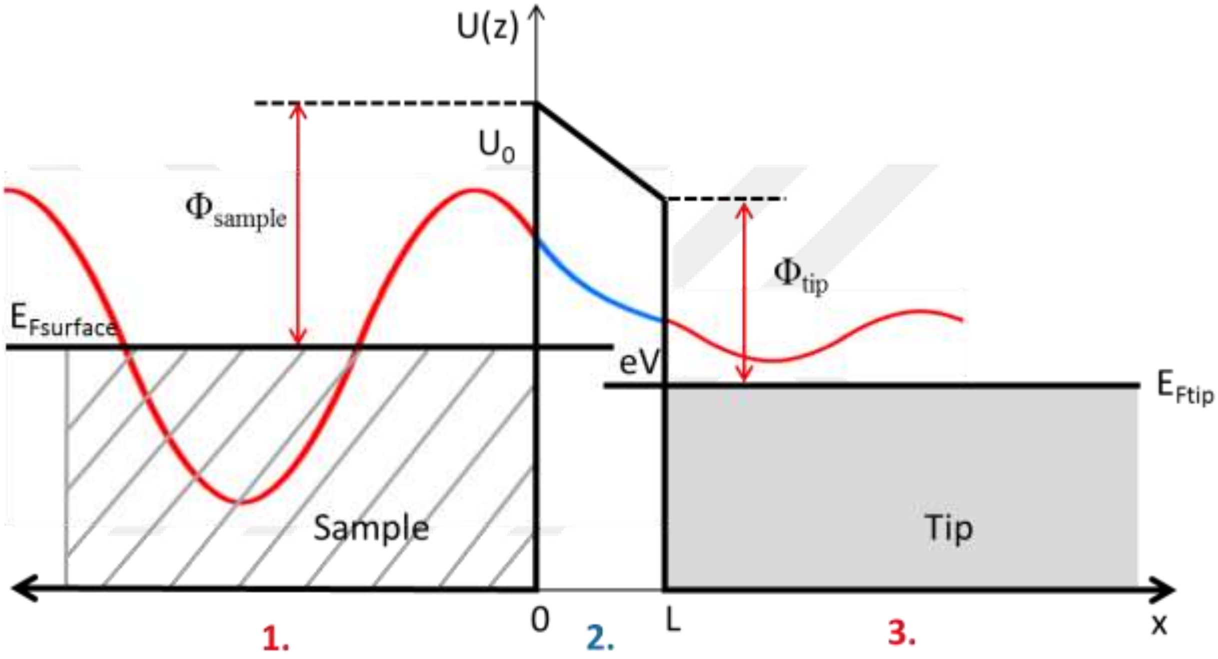

Figure 2. A one-dimensional potential barrier diagram representative of tunnelling in the STM. L is the tip-sample separation distance; the work function of the sample (tip) is Φ_{sample} (Φ_{tip}). Here a positive voltage is applied to the tip which means the electron tunnels from the sample surface to the tip through the vacuum.

When the STM tip is in the tunnelling regime, ~5-15 Å, [42, 43], the number of electrons which tunnel through the vacuum energy barrier depends on the bias voltage. The bias voltage, (a result of tip or sample bias), causes a shift of the Fermi energy level away from equilibrium. A one-dimensional potential barrier diagram representative of the tunnelling in the STM is given in Figure 2: L is the tip-sample separation distance and the work function of the sample (tip) is Φ_{sample} (Φ_{tip}). The shaded areas show the occupied states for the surface, $E_{Fsurface}$, and the tip,

E_{Ftip}-eV. As shown in Figure 2, the filled sample states are shifted by eV from the Fermi energy level of the tip. Therefore, there is a probability that the electrons can tunnel from $E_{Fsurface}$ to unoccupied tip states. The work function of Si and W is 4.60-4.85 eV and 4.32-5.22 eV, respectively [44]. The average work function of the Si(111) surface and the W tip is approximately 4.5 eV [43]. When a positive bias voltage is applied to the tip, the average work function can be written as,

$$\Phi = \frac{1}{2}(\Phi_{\text{samp}} - \Phi_{\text{tip}}).$$

And the decay constant becomes

$$k = \frac{\sqrt{2m(\Phi - E)}}{\hbar}.$$

Applying a bias voltage increases the Fermi energy of the surface, thus, the electrons (0 < E < eV) can tunnel through the tip to fill empty states in the tip. The transmission probability for a small bias voltage, $\Phi \gg \text{eV}$, is:

$$T(x = L) = e^{-2\frac{\sqrt{2m\Phi}}{\hbar}L}.$$

For a large bias voltage the energy, E, is included so the transmission probability is given by:

$$T(x = L) = e^{-2\frac{\sqrt{2m(\Phi - \text{E} + \text{eV}/2)}}{\hbar}L}.$$

There is a probability that electrons tunnel the barrier, thus, the tunnelling current can be written as,

$$I \propto \sum_{E_n = E_F - eV}^{E_F} |\Psi(\text{x})|^2 \, e^{-2kL}.$$

The local density of state (LDOS) [9], which is related to the Fermi energy of the sample, is given by

$$\rho(x,E) \propto \frac{1}{eV} \sum_{E_n=E_F-eV}^{E_F} |\Psi(\mathrm{x})|^2.$$

Finally the tunnelling current can be expressed by

$$I \propto \int_0^{eV} \rho(0,E)T(x,E)dE$$

$$I \propto \mathrm{V}\rho(0,E_{Fsample})e^{-1.025\mathrm{L}\sqrt{\Phi}}.$$

The tunnelling current is proportional to the local density of surface states and the applied bias voltage. The current shows an exponential dependence on the tip-sample separation, L e.g. decreasing the tip-sample separation by 1 Å causes the tunnel current to increasing by a factor of ten [9]. Therefore, the tunnelling current can be extremely sensitive to atomic-scale corrugations on a sample surface.

Finally, an important capability of the STM is Scanning Tunnelling Spectroscopy (STS) by which the occupied and unoccupied local density of states of the surface can be probed. STS can be performed to record an I-V curve by sweeping the voltage (typically from -2.0 V to +2.0 V) while recording the tunnelling current. The differentiation of the I-V curve gives the LDOS [9],

$$\frac{dI}{dV} \propto \rho(L,E_{Fsample}).$$

1.4 STM Atomic Resolution

As mentioned above, the fundamental physics behind the STM is the quantum tunnelling effect, which occurs when a bias voltage is applied between a sharp metallic probe (the STM tip) and a surface that are less than 1.5 nm apart [42]. Once the tunnelling current is detected the surface topography can be measured by rastering the tip in the x and y directions. During a surface scan, a small change in the distance between the tip and the surface can be determined by observing the change of the tunnelling current. Thus, a surface image can be generated by recording tip displacement due to the tunnelling current over the surface. An atomic resolution image is strongly dependent on the tip apex and the local density of the state of the sample [11, 45]. Figure 3 shows a schematic diagram illustrating the essential components of an STM system.

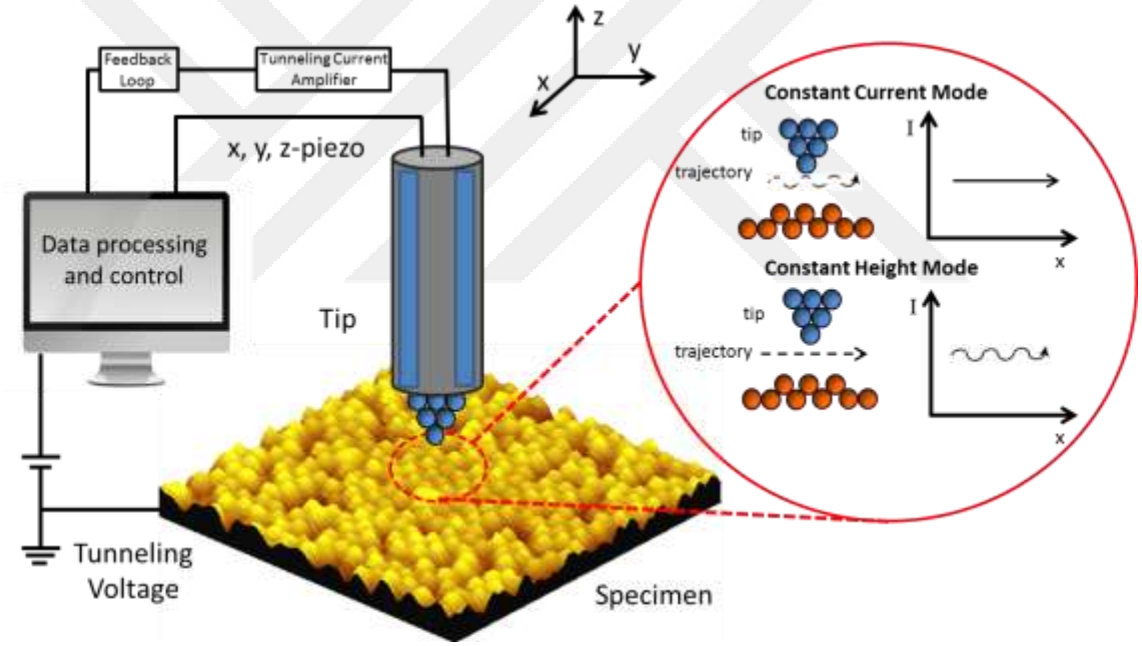

Figure 3. A schematic diagram showing the components of an STM system. Scanning the surface in the constant current mode or constant height mode is possible, the former relies on using a z-piezo with a feedback loop for the control of the tip displacement (The diagram is modified from ref. [46] and the 3-D image of the Si(111)-7x7 surface was produced in this study).

A constant tunnelling current, a feedback system is required for control of the z-height displacement of the tip. The STM can work in different modes: a constant current mode and a constant height mode (as shown in Figure 3). For the constant current mode, during scanning, the tunnelling current and bias voltage are fixed, as the tip scans the surface and the z-height constantly adjusted via a feedback loop in order to maintain a constant current. Therefore, the z trajectory represents the surface topography via a constant charge density of surface. The contrast on the image is due to variations in charge density [47]. On the other hand, in constant height mode, the z-position of the tip is fixed and the tunnelling current change depending on variations in the tip-sample separation due to the surface topography. In this thesis, for all experiments, the constant current mode was used unless otherwise specified.

1.5 Atomic Manipulation

Since 1982, STM has not only been used for atomically-resolved individual atom imaging but also for atomic manipulation, i.e. nanoengineering using the STM tip as a tool. Atomic manipulation with the STM is possible by pulling, pushing, rearranging, and removing atoms and/or molecules on a surface. This is achieved by utilising the tunnelling current, bias voltage, electric field or via mechanical interaction with the STM tip. Lateral, vertical, electric-field induced, and inelastic tunnelling induced manipulation are the major methods for STM manipulation [3, 4, 30, 48].

1.5.1 Lateral Manipulation

The first manipulation technique, the famous “lateral manipulation” was performed in the IBM Almaden Laboratory. As seen in Figure 4A, Eigler *et al*. [4] wrote the IBM initials with 35 Xe atoms on a Ni(110) surface at 4K. This technique relies on the tip-atom mechanical interaction, and has been performed with many different atoms/molecules on various surfaces

[30, 48-54]. Briefly, when the tip approaches the atom, a weak chemical interaction occurs between them. As illustrated in Figure 4B, firstly the tip is lowered over a Xe atom until it experiences an attractive force to the tip (a to b), it is then possible to slide the atoms (b to d) due to the decreased tunnelling resistance, finally the tip is retracted to its initial position (d to e) and leaves the atom on the surface [55].

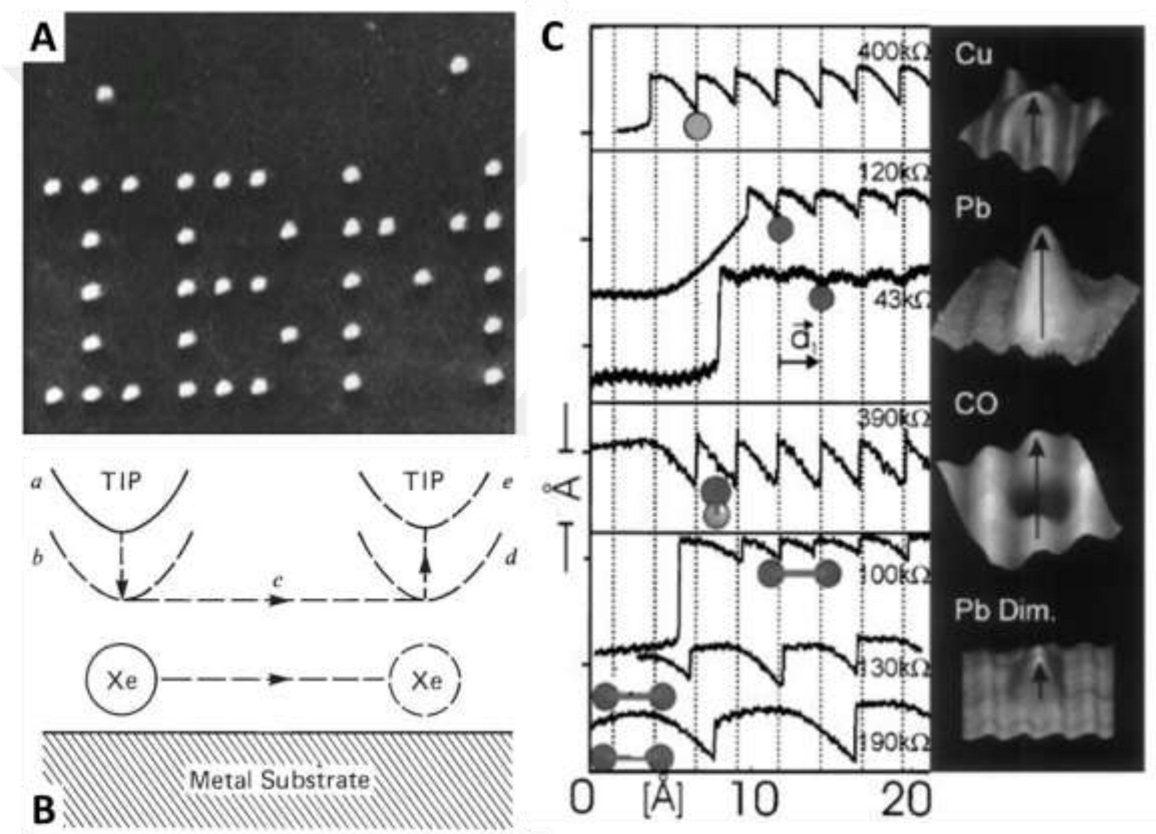

Figure 4. Examples of atomic manipulation with the STM. A. IBM logo formed of Xe atoms on the Ni surface at 4 K [4], generated by the lateral sliding manipulation process in B. C. Lateral manipulation of Cu, Pb, CO, and Pb dimers on the Cu(211) surface with vertical and lateral tip movement profiles, left to right, and STM images [55]. Images are modified from given references.

When the tip approaches an atom, the tunnelling resistance (R) decreases and a strong interaction (van der Waals) occurs between the tip and the atom [48]. For this manipulation, minimum distances are required between the atom and the tip apex. The tip-atom distances (or R) can be determined via the tunnelling current at a fixed bias voltage. At a certain tip height, the tip/atom interaction is strong enough so that the tip is able to move the atom parallel to the surface (preferably via a low-energy pathway e.g. a close-packed row [56]) without desorption.

In Figure 4C, another example is given for lateral manipulation. When the STM tip is close enough to the atom/molecule (Cu, Pb, CO, and Pb dimers), an attractive force occurs between the tip and the atom/molecule. Due to this force, the atom/molecule can actually hop onto the tip and be transferred to elsewhere on the surface. This hopping is recorded as a tip displacement, which is given in Figure 4C. Here, Cu, Pb, and Pb dimers are displaced by an attractive force and the CO molecule is displaced by a repulsive force. Moreover, lateral manipulation is not only used for single atom manipulation but also for the displacement of large molecules [52, 57].

1.5.2 Vertical Manipulation

Once an interaction is established between the STM tip and the atoms/molecules, they may hop between the tip and the surface. This movement between the tip and the sample is called vertical manipulation [52, 58, 59]. Both electric field and inelastic tunnelling electrons can be involved in this manipulation technique [55].

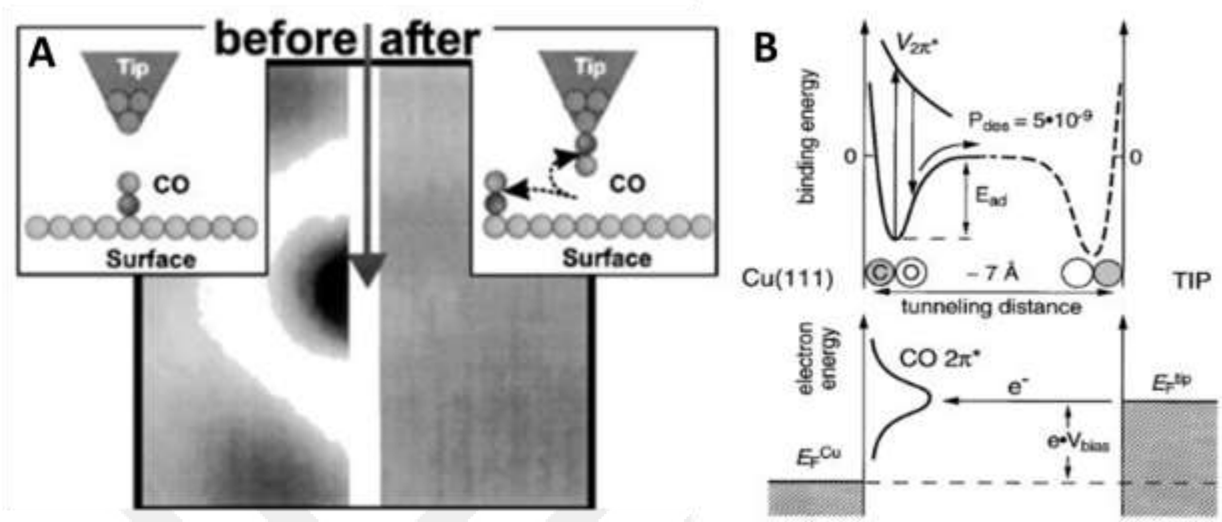

Figure 5. A. Before and after images show CO manipulation performed by locating the tip over the molecule at +2.7 V for 3.2 s and the molecule hops to the tip apex [5]. B. Assuming the tip binding energy is higher than the surface, with the desorption probability of P = 5 x 10^{-9}, the CO molecule desorbs from the surface and moves to the tip apex [5, 60].

Figure 5A shows before and after images of CO manipulation performed by positioning stopping the tip over the molecule at +2.7 V for 3.2 s. Here, the molecule either hops to the tip apex or moves on the surface. Consider the double well for the transfer of atoms/molecules, there are two possible states: at the surface or at the tip apex as shown in Figure 5B. In the initial state in Figure 5A, the tip has the lower energy and the atoms/molecules are adsorbed on the surface state. When the tip has approached the surface and is directly over the atom/molecule and an electric field is applied, the surface energy increases and the atoms/molecules prefer to move to the lower energy state which is adsorbed onto the tip (as seen in Figure 5B). Thus, the atoms/molecules are transferred from the surface to the tip. When a mechanical contact is achieved between an adsorbate and the tip, the potential wells of the sample and tip are overlapped. Applying the opposite bias voltage reverses the potential well between the tip and the surface, and the atoms/molecules transfer back to the surface state. When the tip is close enough to the atoms/molecules so that the tip and the surface potentials overlap, the tip can hold onto the atoms/molecules and transfer them across the surface.

STM provides a unique opportunity to image the bond structure of molecules due to the fact that the tunnelling current is proportional to the LDOS close to the Fermi level. One of the groundbreaking applications of vertical manipulation is the use of a metallic tip that is terminated with an atom or molecule (H_2, Xe, CO, CH_4) to probe molecular bonds [6-8, 61, 62]. This was first demonstrated by Gross *et al.* [8] who observed the molecular bonds of the pentacene molecule on the NaCl(2 ML)/Cu(111) surface by probing short-range forces with a CO terminated tip.

1.5.3 Electric Field Induced Manipulation

The electric field in the tunnelling region is widely used for single atom/molecule manipulation and is performed by changing the bias voltage between the tip and surface [63-66]. Increasing the bias voltage ($>+3$ V), which induces a stronger electrical field between the tip and surface, is a method used for bond-breaking molecular manipulation and dissociation experiments [64, 65]. Figure 6 illustrates one dissociation experiment in which a high field is used to manipulate a $B_{10}H_{14}$ molecule on the Si(111)-7x7 surface. Figure 6A shows the $B_{10}H_{14}$ molecule (bright spot) on the Si(111)-7x7 surface, while Figure 6B shows the dissociated molecule after applying a voltage pulse of +8.0 V. Moreover, desorption and readsorption can be observed between the tip and the surface by changing the bias voltage polarity between negative and positive, in other words producing a repulsive or attractive electric field, respectively [67]. Alternatively, the electric field can result in the diffusion of atoms and molecules beneath the tip (for both positive and negative voltages) rather than dissociation [68]. This is because the electric field bends the surface potential well; therefore, molecules/atoms migrate to the lower surface energy site under the tip (see Figure 6C). The electrical field between the tip and the surface is inversely proportional to the radial distance from the injection site (1/r) [69, 70].

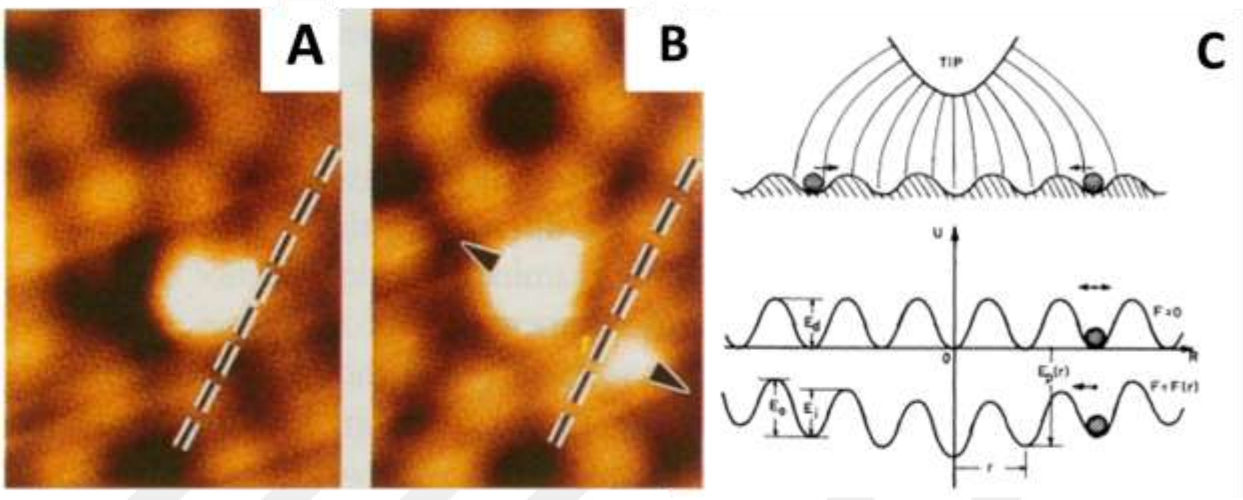

Figure 6. STM images of the $B_{10}H_{14}$ molecule. A. The $B_{10}H_{14}$ (bright spot) molecule on Si(111)-7x7 surface. B. After electron injection which leads to molecular dissociation at +8.0 V bias voltage [64]. C. The electric field effect on atoms/molecule leads to migration under the STM tip for both positive and negative bias voltages [68].

1.5.4 Inelastic Tunnelling

One of the most widely used manipulation techniques is inelastic electron tunnelling (IET) manipulation where energy is transferred from the tunnelling electron to an atom/molecule to cause a transition of the vibration excitation of the atom/molecule [31]. This excitation may be caused by single or multiple electron excitation processes. One electron may lead to the vibration excitation of the atom/molecule [71]. Moreover, multiple electronic excitations with sufficient

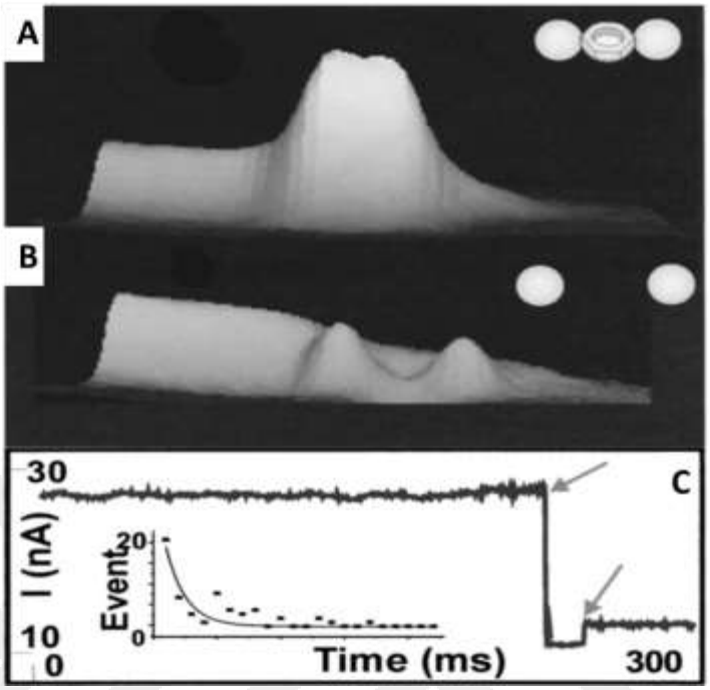

Figure 7. The STM images for the p-diiodobenzene ($C_6H_4I_2$) molecule on the Cu(111) surface. A, before and B, after the inelastic tunnelling process, which breaks the C-I bonds of the molecule. C. Current-time graph indicates bond-breaking events with two arrows during the manipulation. The first corresponds to the breaking of the C-I bonds, while the second corresponds to the diffusion of benzene away from the tip on the surface. The inset shows a plot of the dissociation probability over 70 events (This figure is taken from ref. [48]).

lifetime may contribute to desorption of the atom/molecule [72, 73]. This process can be controlled by applying a bias voltage and varying the tunnelling current to change the number of electrons that interact with the atom/molecule. Moreover, IET manipulation may induce molecular rotation [15], bond breaking [48] or dissociation and diffusion (see Figure 6A and B) [64, 74] of the atom/molecule on the surface. Figure 7 represents a bond breaking process with p-diiodobenzene on the Cu(111) surface due to inelastic tunnelling manipulation. Figure 7A and B present the STM images for the p-diiodobenzene ($C_6H_4I_2$) molecule on the Cu(111) surface: before varying the current (electron injection), and after varying the current, which stimulates the bond-breaking process. The C-I bond is broken by electrons originating from the STM tip. The current-time graph in Figure 7C shows two steps: first, the bond breaking and second, the C_6H_4 diffusion away from the tip on the surface. Furthermore, inelastic electron tunneling can manipulate atoms or molecules on surfaces either locally or non-locally. These techniques will be discussed in section 1.8 in detail.

1.5.5 Other Manipulation Techniques

There are some other special techniques that can be performed using a combination of lateral, vertical, IET, and the electric field manipulations. The first of these is atomic/molecular switching [53, 75] which can be applied the electronic properties of atoms/molecules or for moving from one state to another via a voltage pulse (on and off mode). This switching technique is useful in electronic devices applications. The second is chiral molecule (molecular motor) manipulation via a voltage pulse that is applied to the legs of the molecule using the STM tip. The molecule may rotate (90, 180 etc.) or move on the surface [76-78]. The next is the break-junction technique [79], which is used to fabricate nanowires and is applicable at low or room temperature [80]. Briefly, the STM tip makes contact with a metallic surface, and is subsequently withdrawn slowly to produce an atomic scale nanowire. Applying a bias voltage or tunnelling current breaks the junction. The electronic properties of the metal can be determined with this technique. Finally, there is tunnelling current induced tautomerisation which is interconversion of the positions of the constituent atoms of molecules. This process has been performed both locally [81] and non-locally [82]. The idea is to vibrationally excite a single porphycene molecule by injecting electrons via IET, allowing H atoms to switch positions internally.

In this thesis, mechanical manipulation will be introduced for the manipulation of hybrid $(C_{60})_m$-$(Au)_n$ on the Au(111) surface at RT and 110 K. Also, IET manipulation via electron injection will be performed for the local and non-local manipulation of chlorobenzene and oxygen molecules on the Si(111)-7x7 surface at RT.

1.6 Si(111)-7x7 Surface

Silicon surfaces are widely used in the semiconductor technology due to their excellent electronic properties, the ability to obtain extremely high purity Si, the abundance of the raw material and the maturity of Si wafer processing technology. The complex Si(111)-7x7 surface was first studied with Low Energy Electron Diffraction (LEED) [83, 84], was later directly imaged by [85, 86] and was also comprehensively investigated by other combined studies [87, 88].

Takayanagi *et al.* [89] proposed the dimer-adatom-stacking-fault (DAS) model to describe the bulk structure of the Si(111)-7x7 surface. This stacking fault consists of a unit cell with unfaulted and a faulted halves. The faulted half arises from misalignment with the surface bilayer and can be seen at negative bias voltage (i.e. occupied rest-atom states).

Figure 8 illustrates the Si(111)-7x7 surface which has 4 covalently bonded layers of surface atoms: adatoms, rest-atoms, dimer, and corner hole, which occupy the uppermost, second layer, third layer, and fourth layer, respectively, as shown in Figure 8A and B. The images in Figure 8C and D show the reconstructed clean surface image of Si(111)-7x7 at +1.0 V and -1.5

V allowing the unfaulted and faulted halves to be distinguished. The unit cell is indicated with a white parallelogram.

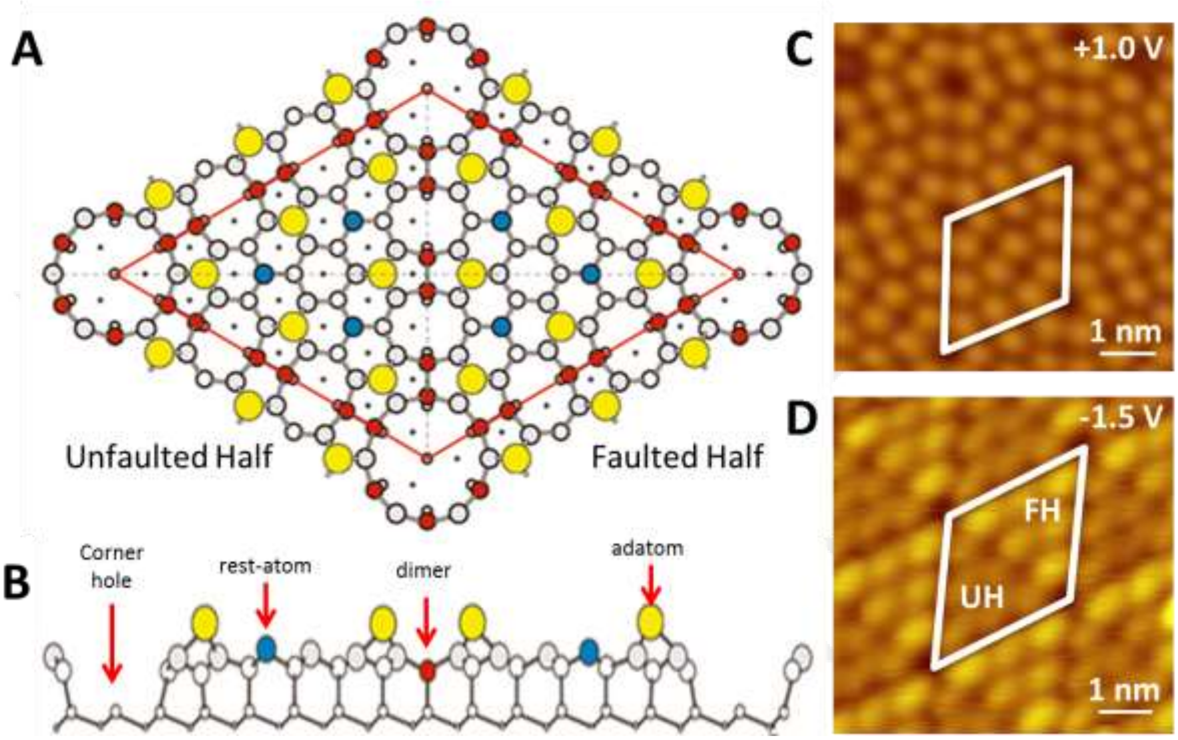

Figure 8. Schematic diagram of the Si(111)-7x7 surface, A and B: top and side view showing the unfaulted and faulted half and the surface atoms: adatom, rest-atom, dimer, and corner hole atom (ball model modified from ref. [89]). C and D: Reconstructed clean surface images of the Si(111)-7x7 surface at +1.0 V and -1.5 V (images produced in this study). The unit cell is indicated by a white parallelogram which outlines the unfaulted and faulted half.

Adatoms form the topmost layer of the surface and there are 12 Si adatoms in a unit cell These adatoms together with the rest-atoms and corner holes contribute 19 dangling bonds (12 adatom, 6 rest-atom, and 4 corner holes shared between four unit cells) [90]. The STM can only image the adatoms because they are in the uppermost layer, have states that are close to the Fermi level and behave like a metallic surface. The experimental preparation method used to obtain the Si(111)-7x7 reconstructed structure will be detailed in section 2.6.1.

1.7 Chlorobenzene and Oxygen Molecules on the Si(111)-7x7 Surface

1.7.1 Chlorobenzene Molecules on the Si(111)-7x7 Surface

Chlorobenzene (C_6H_5Cl) is mostly used as a solvent, a degreasing agent and in the production of other chemicals. Therefore, understanding the adsorption mechanism of chlorobenzene molecules on surfaces provides a useful insight into its properties. The first systematic study of the adsorption of chlorobenzene molecules on the clean Si(111)-7x7 surface was reported by Cao *et al.* using high-resolution electron energy loss spectroscopy (HREELS) and thermal desorption spectroscopy (TDS) [91]. Further experimental studies [66, 91] and density functional theory (DFT) calculations [92] indicated that the di-σ binding geometry is the most stable form for PhCl adsorption. The Si-C interaction for the chemisorbed and physisorbed PhCl molecule is caused by a covalent bond and a weak attractive force, respectively. A recent theoretical study [93] (in terms) of experimental results [37] of activation energies of the chemisorbed and physisorbed PhCl molecule on the Si(111)-7x7 surface yielded values of 1.6 eV and 0.6 eV for the chemisorbed and physisorbed states, respectively. These energies are presented in Figure 9 with a simplified potential energy diagram as a function of the reaction coordinate.

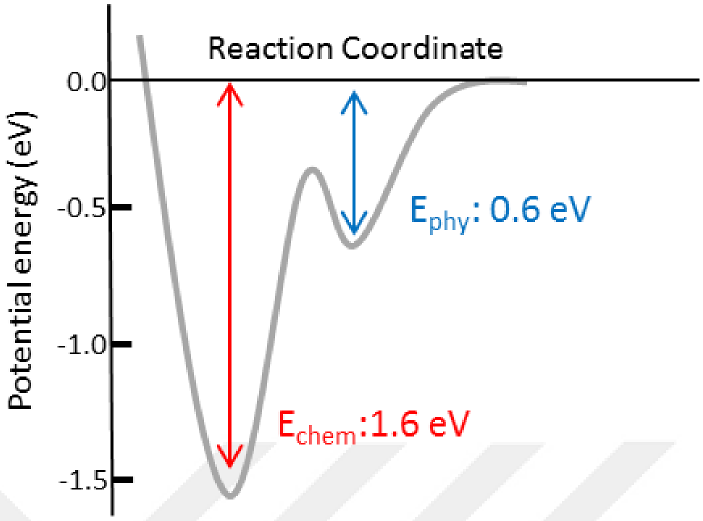

Figure 9: Simplified potential energy diagram as a function of reaction coordinate for chlorobenzene on the Si(111)-7x7 surface showing the chemisorbed and physisorbed states with binding of 1.6 eV and 0.6 eV [93], respectively.

Figure 10 shows schematic diagrams and an STM image of the PhCl adsorption on the Si(111)-7x7 surface. The clean surface schematic, with dangling bonds on adatoms and rest-atoms, is presented in Figure 10A. Once PhCl molecules are exposed to the surface, the carbon atoms of the PhCl molecule are saturated by the dangling bonds of an adatom and a neighboring rest-atom (see Figure 10B). The adsorption of the PhCl molecule by an adatom (yellow) and rest-atom (blue) site is illustrated in Figure 10C with a ball model within one half of the Si(111)7x7 unit cell and indicated in the STM with a white arrow in Figure 10D. The STM image was obtained with a bias voltage of +1.0 V and tunnelling current of 100 pA using a dose of 0.4 L of PhCl.

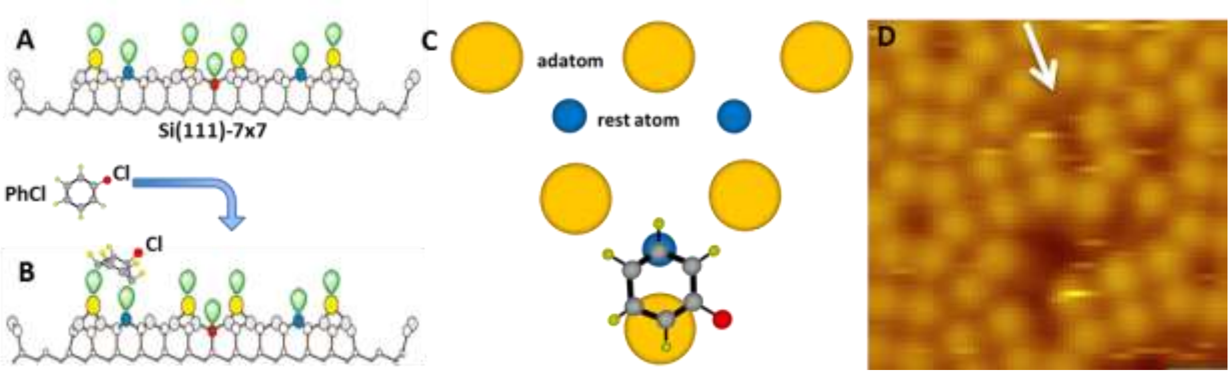

Figure 10. Schematic diagrams of PhCl adsorption on the Si(111)-7x7 surface which is also highlighted with a white arrow in the STM image. A. Clean surface diagram with dangling bonds on adatoms and rest-atoms. B. PhCl molecular bonding on the surface to an adatom and a neighbouring rest-atom [89]. C. Ball model for adsorption states of a chlorobenzene molecule within one half of the Si(111)-7x7 unit cell. D. STM image of PhCl adsorption (indicated with the white arrow) by an adatom (yellow) and rest-atom (blue). The image was taken at +1.0 V, 100 pA with a dose of 0.4 L PhCl on the surface (image produced in this work).

1.7.2 Oxygen Molecules on the Si(111)-7x7 Surface

Ultrathin silicon oxide films are very important in the semiconductor device technology. Due to device miniaturisation requirements there is an impetus to reduce the thickness of gate oxides in transistors. The oxidation process of silicon surfaces (Si(001), Si(100), Si(111)) has therefore been extensively studied [94-96]. It is important to understand and be able to produce a high-quality oxide layer on the Si(111)-7x7 surface, which depends greatly on the initial oxidation process [97-99].

The initial oxidation process has been studied with the high-resolution electron energy loss spectroscopy (HREELS) [100, 101], near edge x-ray absorption fine structure (NEXAFS) [98] and ultraviolet photoelectron spectroscopy (UPS) [99] amongst others. The O-O bond length (1.24 Å) changes when introduced onto the Si surface and the bond length become 1.31 Å, while O atoms establish a bond with silicon adatoms and rest-atoms [97]. The activation energy of 0.8 eV, requires the generation of molecular precursors and the stabilization energy of the Si-O-O-Si is 4.2 eV [97]. The Si-O-O-Si type configuration appears as bright spots (higher electron density), while the Si-O-Si-O appears as dark spots (lower electron density) under STM [97]. The structure has a different nature at different substrate temperatures. Therefore, the appearance under STM can vary with the substrate temperature.

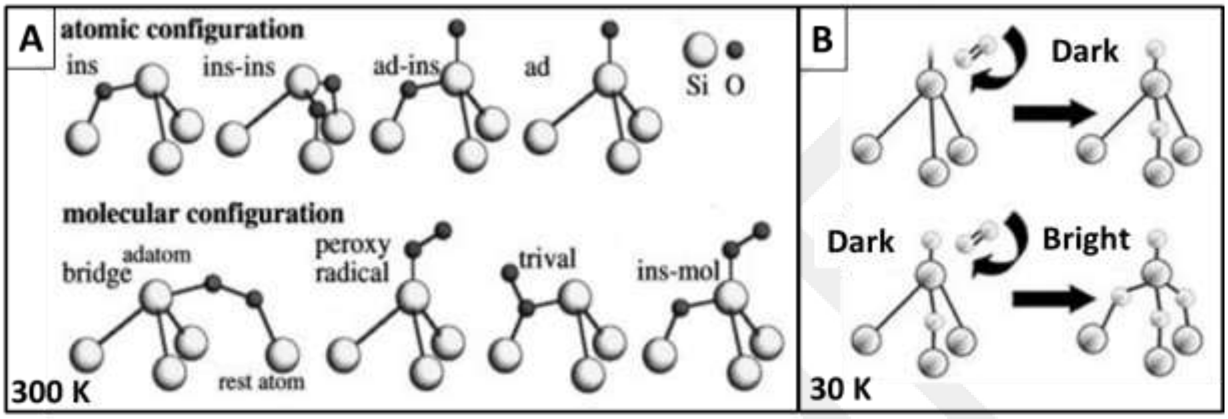

Figure 11: A. Ball model for the initial configurations of atomic and molecular oxygen adsorption on a Si(111)-7x7 surface at 300 K from ref. [99] (ins-oxygen *inserted* into the back bond of a Si adatom, ad-oxygen *adsorbed* on top of a Si adatom). B. Primary and secondary oxidation processes of the Si(111)-7x7 surface at 30 K give rise to dark and bright sites in the STM from ref. [35].

Ball models for the oxidation configuration of the Si(111)-7x7 surface at 300 K and 30 K are presented in Figure 11A and B, respectively. The initial atomic and molecular oxygen bonding configurations are indicated in Figure 11A for 300 K [99]. Here "ins" means oxygen is *inserted* into the back bond of a Si adatom and "ad" means oxygen is *adsorbed* on the top of a Si adatom. These configurations give rise to metastable oxygen via back bonding of silicon adatoms at low coverages such as 0.05 and 0.1 Langmuir. The oxidation process at 30 K [35] is shown in Figure 11B. When the oxygen molecule is introduced onto the surface, one oxygen atom bonds with an adatom and rest-atom, while the other oxygen stays on top of the adatom.

This configuration can appear as a dark spot under STM. Further oxidation causes two more bonds between adatoms and rest-atoms which can appear as bright spots in the STM.

The numbers of bright and dark sites on faulted and unfaulted site of the Si(111)-7x7 surface have been studied at an oxygen exposure of 0.05 and 0.1 L at 300 K and 30 K by Mayne *et al.* [35]. It was found that the number of bright sites was greater than the number of dark sites and that the faulted half of the surface unit cell is more reactive than the unfaulted half. In addition, the sticking coefficient varies with temperature from 0.1 at 30 K to 0.08 at 300 K.

1.8 Electron (or Hole) Induced Manipulation: Local and Non-local

1.8.1 Local Manipulation

The local desorption experiment is a bond breaking or weakening for an atom/molecule located directly beneath the STM tip by electron (or hole) injection. It is induced by vibrational excitation of molecules via inelastic electron tunnelling in the STM at varied temperatures. Basically, there are two mechanisms involved in local desorption: multiple vibrational excitation and electronic excitation [10, 102, 103]. In most cases, the dissociation, diffusion or desorption rate increases with increasing current and increasing bias voltage but becomes constant at a high voltages [65, 102-104]. Positive or negative bias voltages lead to different molecular dynamics. When applying a positive sample bias, electron injection creates negatively charged molecules, while a negative bias voltage causes the opposite effect. In the following dissociation, diffusion and desorption will all be mentioned as examples of local manipulation.

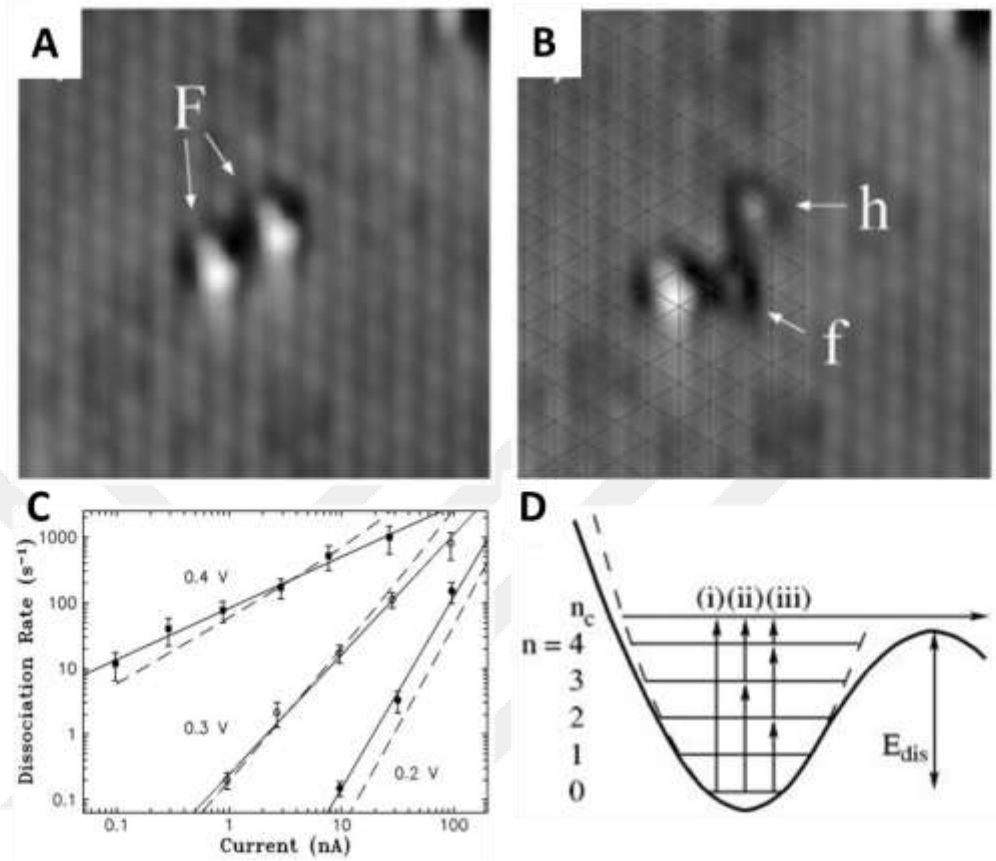

Figure 12: Consecutively acquired STM images, from ref. [104], before and after an electron pulse for 30 sec. at +0.3 V over oxygen molecules adsorbed on the Pt(111) surface. A. Two O_2 molecules on the FCC (F) site before injection. B. After electron injection, the image shows oxygen dissociation on the HCP (h) site via electron injection. C. The dissociation rate, $R_d \sim I^N$, determined as a function of bias voltage. N = 0.8 ± 0.2, 1.8 ± 0.2 and 2.9 ± 0.3 are found for +0.4, +0.3 and +0.2 V, respectively. D. Thus one, two, or three electrons were involved in the bond breaking process at +0.4, +0.3 and +0.2 V sample bias, respectively.

The bond breaking of oxygen molecules on the Pt(111) surface via resonant inelastic electron tunnelling is presented in Figure 12. Electron pulses lasting for 30 s at +0.3 V break O-O bonds by vibrational excitations and cause dissociation on the HCP surface site (see Figure 12B and C). Further pulses cause additional bond breaking and then desorption from the surface (see Figure 12D). The dissociation rate, $R_d \sim I^N$, was determined as a function of bias voltage, where

N = 0.8 ± 0.2, 1.8 ± 0.2 and 2.9 ± 0.3 was found for bias voltages of +0.4, +0.3 and +0.2 V, respectively. It was found that one, two, or three electrons were involved in the bond breaking process with respect to a +0.4, +0.3 and +0.2 V sample bias, respectively.

The manipulation of dark (D) and bright (B) sites of oxygen atoms on the Si(111)-7x7 surface at 300 K were investigated by Mayne *et al.* (2003) [35]. The manipulation was performed at different bias voltages between +4 V to +10 V using a fixed tunnelling current of 6 nA for 50 ms. The manipulation of dark and bright sites are summarised in Table 1. Different types of transformations were observed during manipulation for both sites. The manipulation results for the dark site are: 1) D removed, 2) D transforming into B, and 3) D displacing to a neighbouring adatom. The bright site manipulations are: 1) B transforming into D, 2) B disappearing and a new D appearing next to an adatom and 3) B remaining and a new D appearing next to an adatom.

Table 1: Possible manipulation outcomes for bright and dark sites with the number of events and percentages at room temperature [35].

Transformation on Dark (D) Site	Event	Percentage	Transformation on Bright (B) Site	Event	Percentage
D removed	9	56.2%	B transformed into D	10	43.5%
D transformed into B	5	31.3%	B disapp+new D next adatom	7	30.4%
D moved to next adatom	2	12.5%	B remains+new D next adatom	6	26.1%

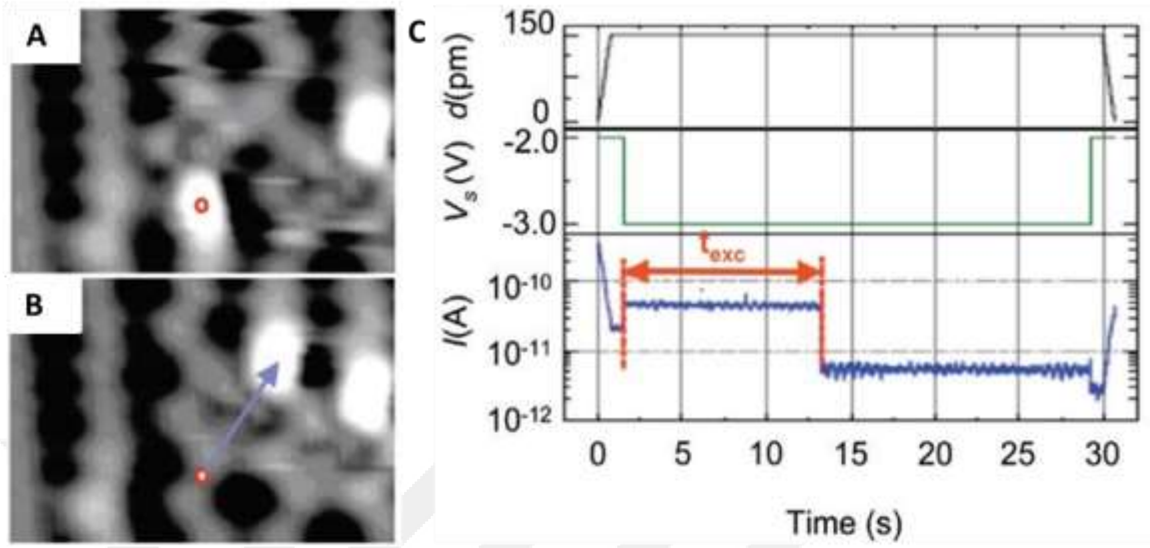

Figure 13. A and B. STM images before and after electron-induced diffusion of a biphenyl molecules on the Si(100) surface. The red circles indicate the initial position of the molecule and the blue arrow shows the diffusive event hopping to the next atomic site, without affecting the neighbour molecules. C. The record of the tip displacement (d), the bias voltage (V_S) and the tunnelling current (I) as a function of electron-injection time (figures modified from ref. [105]).

To determine the properties of PhCl and polychlorinated biphenyl molecules on the Si(111)-7x7 surface, our group performed many experiments at low and room temperature [65, 66, 106, 107]. Riedel *et al.* [105] studied the time-dependent diffusion of the biphenyl molecules on the Si(100) surface at different bias voltages at low temperature (5 K). As shown in Figure 13A, before and B, after STM manipulation, the molecule diffused on the surface. During manipulation, the tip displacement, bias voltage, and tunnelling current recorded as a function of injection time (see Figure 13C). The tunnelling current were changes indicate the excitation time of the molecule and the excitation time decays exponentially. In this experiment, the diffusion threshold is observed at a bias voltage of about -2.7 V.

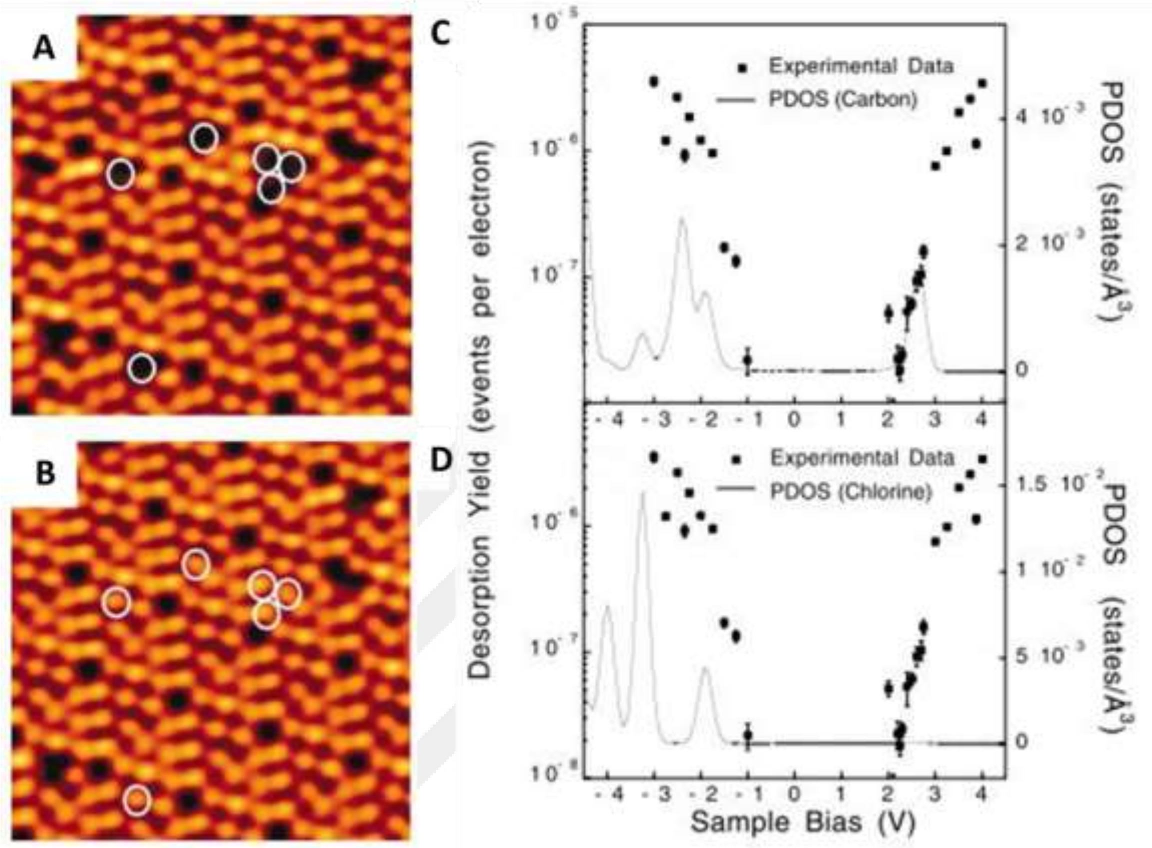

Figure 14: Before and after manipulation STM images for chlorobenzene molecules on Si(111)-7x7 surface and desorption yield over a wide range of bias voltage, with the partial density of p states (PDOS) calculation; from ref. [66]. A. PhCl molecules on the Si(111)-7x7 surface at room temperature show up as dark features at +1.0 V, which are marked with white circles. B. After the scanning surface at +2.2 V and 50 pA. C and D. Desorption yield per electron, and PDOS for carbon and chlorine, plotted as a function of sample bias from +4.0 V to -3.0 V.

Desorption of PhCl molecules from the Si(111)-7x7 surface was performed at room temperature as a function of bias voltage (from +4.0 V to -3.0 V) and tunnelling current by Sloan *et al.* [66]. Figure 14 shows the STM images, before and after manipulation, which are taken at +1.0 V and 50 pA, along with the partial density of p states (PDOS) calculation for carbon and chlorine. Chemisorbed PhCl molecules on the Si(111)-7x7 surface appear on the surface as dark features at +1.0 V which are marked with white circles in Figure 14A. After the scanning the surface at +2.2 V and 50 pA, the molecules are desorbed (see Figure 14B). This desorption is induced by single electron injection (N= 0.88 ± 0.09) with threshold voltages at +2.0 V for electrons and -1.1 V for holes as seen in Figure 14C and D. The desorption yield per electron, and PDOS for carbon and chlorine, increased with increasing sample bias voltage in the range of +4.0 V to -3.0 V. This desorption mechanism is independent of field desorption, thermally induced desorption, and mechanical tip-surface effects.

1.8.2 Non-local Manipulation

Polymerisation and depolymerisation, diffusion, dissociation and desorption events can be performed non-locally. For these events, one or more electrons (or holes) may be involved in manipulating numerous adsorbates on the surfaces which can be located far away from the injection site. The first non-local reaction was observed by Nouchi *et al.*[29], where non-local electron injection caused a ring-shaped surface modification (via polymerisation and depolymerisation) of a C_{60} close-packed layer on Si(111)-7x7 surface at room temperature. Figure 15A and B show STM images after electrons were injected into the close-packed C_{60} layer at +3.3 V. Injected electrons propagated in 3D and dissipated their energy through interacting with phonons along the close-packed layer which caused polymerisation and depolymerisation as seen in Figure 15C. The radius of the ring-shaped formation increased with increasing bias voltage. The author also performed the experiments at grain boundaries of the Si(111)-7x7 surface for both positive and negative bias voltage. Asymmetric rings observed due to the grain boundaries arise from back scattering of injected electrons (or holes).

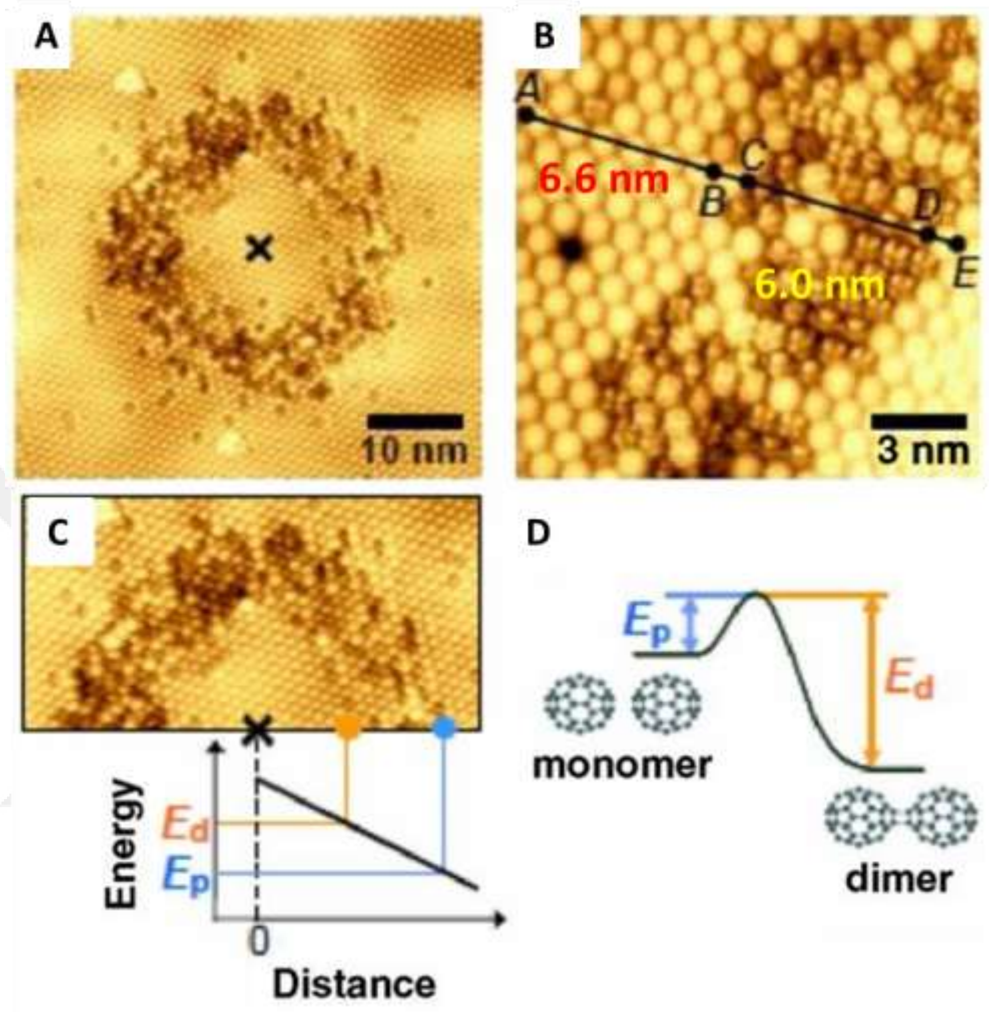

Figure 15: Ring formation in a C_{60} close-packed multilayer on the Si(111)-7x7 surface, modified from ref. [29]. A. STM image taken after electron injection into the marked point at +3.3 V leading to ring formation. B. Selected area from image A on the ring shows six monomers (individual C_{60} molecule) and six dimers (intermolecular bonded two C_{60} molecules) with separations of 6.6 nm (from A to B) and 6.0 nm (from C to D), respectively. C. A schematic energy plot with the STM image showing a energy decrease from depolymerisation, E_d to energy polymerization, E_p for the monomer and dimer molecules after electron injection. D. Potential curve of ionic polymerization and depolymerisation.

A non-local CH_3SSCH_3 dissociation experiment was reported by Maksymovich *et al.* [108] on the Au(111) surface at 5 K with increasing sample bias voltage from +1.2 V to +2.2 V. In Figure 16A, an STM image is shown after electron injection for 200 ms at +2.5 V, 1.0 nA at the position of the blue dot and the dissociation range can be observed. In Figure 16B and C STM images and ball models of the molecule before and after electron injection are presented. Dissociation occurs through breaking the S-S bond when electrons collide with a molecule on the surface (Figure 16C). The experiment was repeated at +1.8 V, 350 nA for 150 ms and remained constant for 18 frames. The threshold was found to be > +1.4 V for the diffusion events, which increase with increasing bias voltage (1.0 nA, 200 ms). The authors proposed two possible mechanisms to explain the non-local effect for dissociation; first, the electric field due to the high bias voltage and second, through localized injections from microtips. The group found that dissociation was induced via a one-electron process.

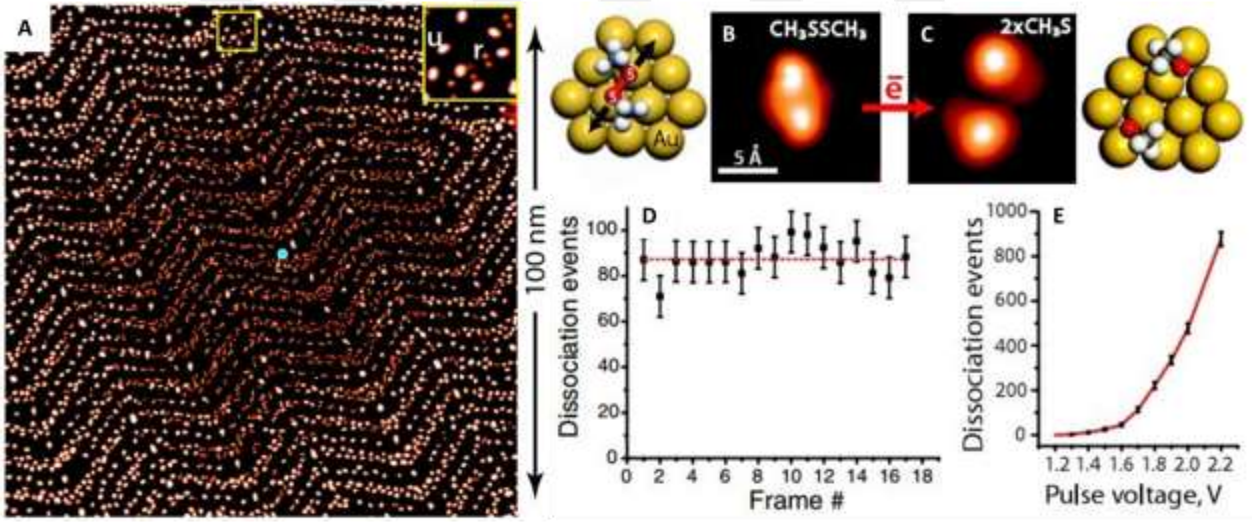

Figure 16:Non-local CH_3SSCH_3 dissociation on the Au(111) surface at 5 K with increasing sample bias voltage (figures are taken from ref. [108]). A. STM image after electron injection for 200 ms at +2.5 V, 1.0 nA at the position marked by the blue dot. The dissociation range can be clearly discerned in the image. Inset: Zooming area in A showing u marks unreacted and r marks reacted CH3SSCH3 molecules. B and C. STM images and ball model of the molecule before and after electron-induced S-S bond breaking or dissociation occur. D. The number of dissociation event for electron injection at +1.8 V, 350 nA for 150 ms remaining unchanged over 18 events. E. Dissociation events increase with increasing bias voltages (1.0 nA, 200 ms).

A combined study of dissociation and desorption events of chlorobenzene molecules on the Si(111)-7x7 surface was performed by Sakulsermsuk *et al.* [106]. Figure 17A and B present STM images at +2.0 V and +1.0 V with the green circles indicating a chlorobenzene molecule and the blue circles an empty adatom site. After scanning the surface at +3.5 V and 100 pA, the molecule dissociated and desorbs from the surface (the green circle) and a new feature is imaged due to chlorine atom adsorption on an adatom site, which is indicated by the blue circle in Figure 17C and D. All images were taken at +1.0 V and +2.0 V, 100 pA. Arrhenius plots for desorption (E_{des}= 0.98 ± 0.08 eV, A= $10^{12.7 \pm 1.4}$ s-1), diffusion (E_{diff}= 0.84 ± 0.08 eV, A= $10^{10.8 \pm 1.3}$ s-1) and one-electron C-Cl dissociation (E_{Act}= 0.8 ± 0.2 eV) events are presented in Figure 17E.

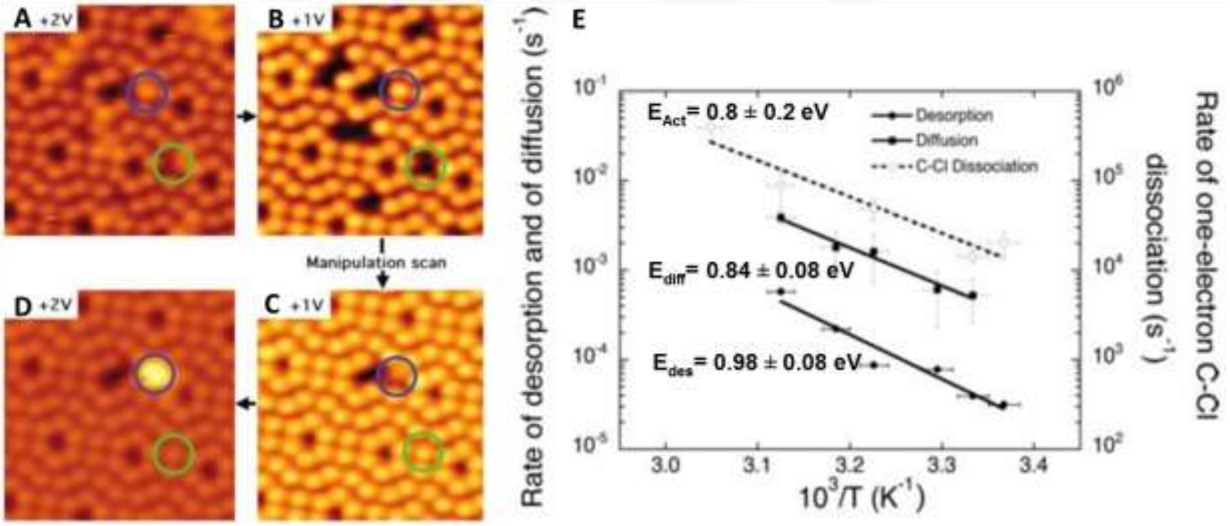

Figure 17: Consecutive STM images for dissociation and desorption events of chlorobenzene molecules on the Si(111)-7x7 surface at room temperature, from ref. [106]. A and B. STM images taken before dissociation and desorption, at +2.0 V and +1.0 V, respectively. Green circles indicating the chlorobenzene molecule which is imaged as semi-bright at +2.0 V and dark at +1.0 V. C and D. After the surface scanned at +3.5 V, 100 pA (not shown), the surface was again scanned at +1.0 V and +2.0 V. The molecule indicated with green circles is desorbed and the blue circle indicates the new absorption site for a chlorine atom. E. Arrhenius plots for desorption (E_{des}= 0.98 ± 0.08 eV), diffusion (E_{diff}= 0.84 ± 0.08 eV), and C-Cl dissociation (E_{Act}= 0.8 ± 0.2 eV) events with activation energies.

Non-local STM manipulation was performed by Sloan *et al.* [39] to desorb chemisorbed chlorobenzene molecules on the Si(111)-7x7 surface by electron injection. The idea was to break the C-Si bonds of chemisorbed PhCl via electron injection by applying a voltage pulse (+2.7 V [106]). The probability of PhCl desorption per electron was calculated as a function of radial distances from the injection site by comparing the number of the molecules on the surface in images taken before and after injection (see Figure 18A and B). The cleaned area is clearly visible in Figure 18B. Non-local desorption was performed by increasing the tunnelling current (while keeping the number of electrons constant) at +2.7 V and is plotted as a function of radial distance from the injection site (Figure 18C). Electrons propagate across the surface and interact with the molecules so that desorption occurs. Non-local desorption was found to be independent of coverage (2-4 molecule per unit cell) and a single electron caused non-local desorption of the chlorobenzene molecule (0.90 ± 0.03 eV). The injected electrons induced desorption over a range of 25 nm. Therefore, the effect of electric field and mechanical interaction between the tip and sample were ruled out. Here, 2D diffusive electron transport is attributed to the desorption event. Electrons decay across the surface and therefore, less desorption occurs further away from the location of the tip.

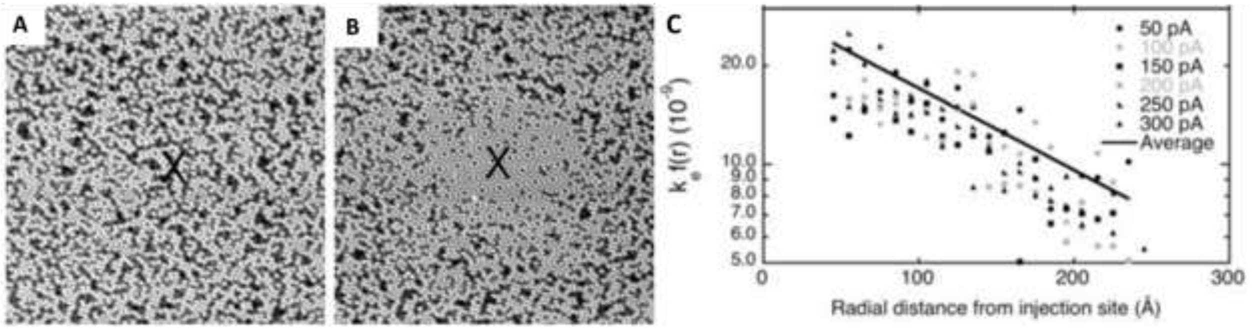

Figure 18: Before and after STM images for non-local desorption of chlorobenzene molecules on the Si(111)-7x7 surface at room temperature, yielding the desorption probability as a function of radial distance from the injection site (figures are taken from ref. [39]). A and B. STM images before and after electron injection at +2.7 V, 250 pA for 7.5 s. C. The desorption probability as a function of radial distances from the injection site for 50 pA/37.8s, 100 pA/18.9s, 150 pA/12.8s, 200 pA/10 s, 250 pA/7.5s, 300 pA/6.3s (i.e. same total electron dose).

As seen in Figure 18C, the probability of non-local desorption as a function of radial distance from the injection site has been reported at different tunnelling currents (50 pA/37.8s, 100 pA/18.9s, 150 pA/12.8s, 200 pA/10 s, 250 pA/7.5s, 300 pA/6.3s, same total electron dose) with an exponentially fitted decay length. However, there is a suppression region observed at about 40 Å. This region between 0-40 Å is omitted in this exponential fitting. This suppression region was not explained in this work. However, in Chapter 5, the region will be explored with chlorobenzene and oxygen molecules on the Si(111)-7x7 surface at RT.

Figure 19A and B present an STS map of the clean Si(111)-7x7 surface and STS spectra and the desorption probability per injected electron at different sites as a function of distance along the unit cell axis (CH: corner hole, FC: faulted corner adatom, FR: faulted rest-atom, FM: faulted middle adatom, DR: dimer row, UM: unfaulted middle adatom, UR: unfaulted rest-atom, UC: unfaulted corner adatom, here, the figures have been modified from ref. [39]).

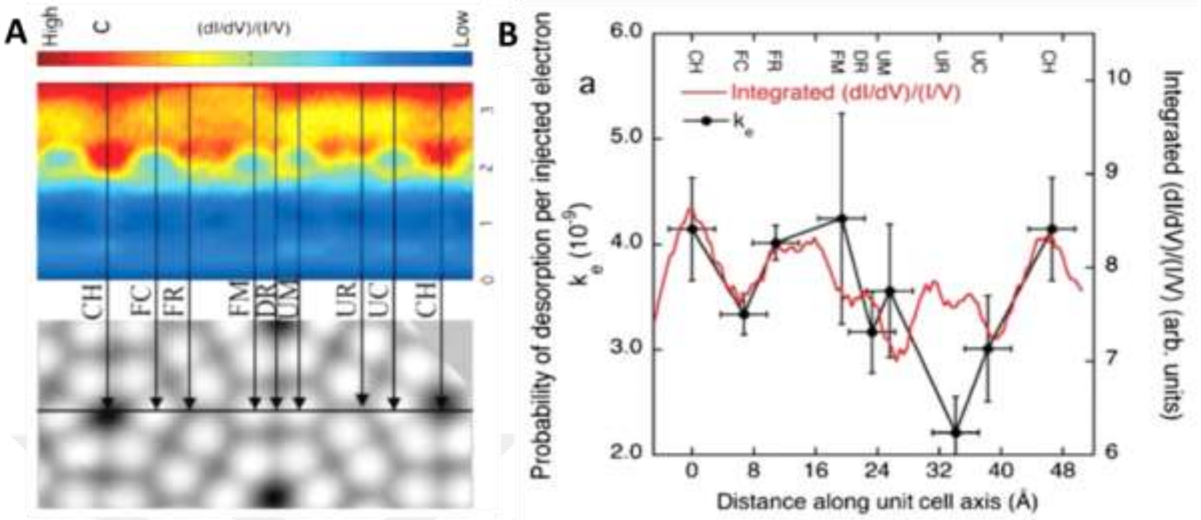

Figure 19. A. STS map of the clean Si(111)-7x7 surface, corresponding to dI/dV spectra taken at different sites (CH: corner hole, FC: faulted corner adatom, FR: faulted rest-atom, FM: faulted middle adatom, DR: dimer row, UM: unfaulted middle adatom, UR: unfaulted rest-atom, UC: unfaulted corner adatom). B. The probability of desorption of chlorobenzene molecule per injected electron compared with STS were taken from 0 V to +3.5 V on the clean Si(111)-7x7 surface plotted as a function of distance along the unit cell axis refer to Figure 19A (figures modified from ref. [39]).

The maximum probability was found at the corner hole site and the probabilities for the faulted side were found to be higher than for the unfaulted side. These results demonstrate that, not only the bias voltage, but also the injection site plays an important role for non-local desorption experiments.

STM is a powerful tool for studying surface transport. Depending on the energy of the electron and the properties of the surface or bulk, the electron can be transported in a certain radius in the specimen via 2D-3D, ballistic or diffusive mechanisms. The electron transport model for aromatic molecules on the Si(111)-7x7 surface at RT has been proposed as 2D diffusive transport by Lock *et al.* [109] for the non-local desorption mechanism. This model proposes more desorption in the suppression region, where we experimentally observe less desorption of the molecules. The non-local desorption decay length decreases with decreasing temperature [110]. As we mentioned earlier in section 5.2.3 the 2D diffusion mechanism suggests that the decay length is $\lambda = \sqrt{D\tau}$ [109]. The diffusion coefficient, D, is temperature dependent [111, 112], so the diffusion of the hot electrons, which are injected via the STM tip into the surface, decreases with decreasing temperature.

1.9 Magic Number C_{60}-Au Complexes on the Au(111) Surface

1.9.1 Au(111) Surface Properties

The crystallographic orientations of Au (111), (110) and (100) surface are widely used as a template to explore atoms, molecules, and self-assembly properties in surface science and nanoscience. The Au substrates offer the possibility to determine adsorbate properties due to its inert metallic nature. The Au (111) template is preferred surface to the Cu and Ni surfaces because of two-dimensional atomic [113-115] and molecular [116-118] growth on its unique surface herringbone reconstruction. This reconstruction is formed of face-centered cubic (FCC) and hexagonal close packed (HCP) stacking regions [119, 120].

Two STM images from a clean Au(111) surface [13] and the corresponding structural model of the surface [121] are presented in Figure 20. The image in Figure 20A shows pinched and bulged elbow sites. In Figure 20B presented a zoomed area from Figure 20A is presented with atomic resolution that clearly shows the FCC and HCP regions and the nucleation site. The 4.55 % uniaxial compression along the $[1\bar{1}0]$ direction of the first layer of the Au(111) surface results in a (22 x $\sqrt{3}$) super-cell with three-fold symmetry. This cell consists of 23 Au atoms in the topmost layer and 22 atoms in the second layer, giving rise to alternating the FCC and HCP stacking regions with a 63 Å periodicity [119, 122-125]. A single-atom vacancy on the elbow site occurs due to atomic distortion plays important role for the molecular adsorption. The bulk lattice constant is found to be 4.078 Å with an atomic diameter of 2.88 Å by using the $[11\bar{2}]$ surface direction [124]. The FCC region is ~3.5 nm wide and the HCP region is ~2.4 nm which are confirmed with by STM [122]. The surface potential well of the FCC region was found to be 25 ± 5 meV deeper than the HCP region [125]. Therefore, when atoms and molecules are deposited onto the surface, there is a tendency for them to accumulate in the FCC region.

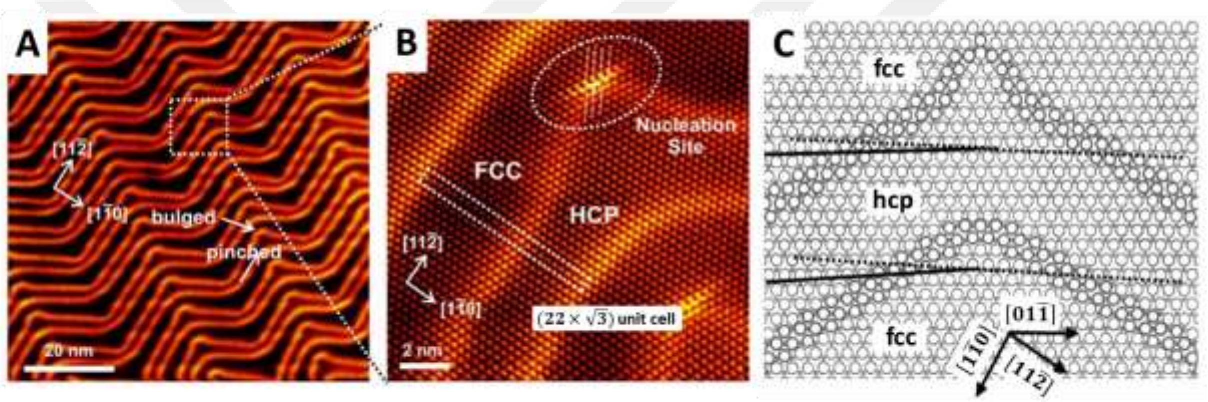

Figure 20: STM images of clean Au(111) surface and atomic model. A. The clean surface showing the FCC and HCP regions with pinched and bulged elbow sites shown plus the surface directions, $[11\bar{2}]$ and $[1\bar{1}0]$. B. Atomic resolution image of Au surface showing the nucleation site of FCC bulged and the atomic alignments through the FCC and HCP stacking regions (images A and B are taken from ref. [13]). C. Atomic structural model for the reconstructed Au(111) surface showing herringbone ridges, from ref. [121].

1.9.2 Au Atoms and Islands on the Au(111) Surface

Although at the macro scale most of the noble metallic surfaces are not reactive with environment, at the nanoscale the two and three dimensional atomic metal clusters (Au_n [126], Ni_n [127], Pt_n [128], Ag_n [129], Cu_n [130], Pd_n [131], $0 < n < 100$) are highly reactive. The productions of metallic clusters have been of great interest as electrocatalysts for fuel cell applications in nanotechnology. The clusters offer the possibility of reduction of NO or oxidation of CO molecules for fuel cell, catalytic, biological, and microelectronic applications [132].

Specifically, nanoscale Au clusters are of major interest due to their chemical, catalytic, and electronic properties [126]. The Au(111) surface is widely used as a template for the production of islands. Most of atomic clusters grow on the pinched and bulged elbow sites of the herringbone surface due to the deeper surface potential energy and atomic defects on the elbow sites. It is observed that two-dimensional Au islands grow on the elbow sites and are influenced by the surface directions of the uppermost layer of the Au(111) surface. The growth of the planar island on the elbow site is possible when the substrate temperature is less than 160 K. At high temperatures, individual Au atoms diffuse to the surface step edges. The step edges of the planar Au islands, as well as Ag and Cu island, are found parallel to the $[1\bar{1}0]$ direction of the surface [133].

The charge state of the Au clusters is a key factor for the growth of atom/molecule complexes due to electron donating/accepting relations. The 2D Au cluster has a different charge state at its edges (negatively charged) and it's middle (positively charged) [134]. A strong (or weak) chemical bonding may occur due to the charge state relations between cluster atoms and adsorbates at the cluster edges or on top of the cluster. Thus, the adsorbate electronic and chemical properties can be altered.

Other metals, such as Ni, Pt, Pd [127, 135] grow on the elbow sites of the Au(111) surface. However, during the annealing process of the surface, these metals submerge and mix with Au surface atoms to create Ni/Au (570 K [127]), Pt/Au [136], or Pd/Au [137] bimetalic surfaces. Therefore, for the magic number cluster production study, Au clusters were used rather than other metals to avoid changing the electronic structure of the surface.

1.9.3 C_{60} Molecule Properties on Surfaces

Fullerenes are made of carbon atoms (60, 70, 76, 84, etc.) with a shape like a sphere, ellipsoid, etc. A unique spherical molecule containing 60 carbon atoms (C_{60}), which is called buckminsterfullerene (or bucky-ball), was discovered in 1985 [138]. This unique symmetry has drawn widespread attention for applications in optoelectronic, superconductor and semiconductor technologies. C_{60} is made of 12 pentagonal and 20 hexagonal rings [138, 139]. This geometry is formed of localized single and double bonds that lead to pentagon-hexagon rings (5:6) and hexagon-hexagon rings (6:6). The length of the C-C bonds of the C_{60} molecule for the two type of rings are found to be 1.45 ± 0.015 Å, and 1.40 ± 0.015 Å for (6:6) and (5:6) rings, respectively [140]. A schematic diagram of a C_{60} molecule is presented in Figure 21A in which the hexagonal and pentagonal rings of the C_{60} molecule are highlighted in red and green, respectively. The diameter of C_{60} is 7.1 Å [141] as determined by electron diffraction. The electronic diameter was found to be 10.34 Å [142].

STS spectra obtained with two different parameters over C_{60} molecules on the Au(111) surface are shown in Figure 21B. The spectra were obtained on a C_{60} molecule site which is indicated with a red cross in the inset STM image: the red spectrum was obtained at +0.45 V bias and 0.16 nA while the blue was obtained at +0.46 V bias, 0.20 nA. Two peaks for filled states and a peak for an empty state are observed for both spectra, which are located at -2.06 eV, 0.60 eV, 1.80 eV for the red curve and -1.83 eV, 0.84 eV, 2.08 eV for the blue curve.

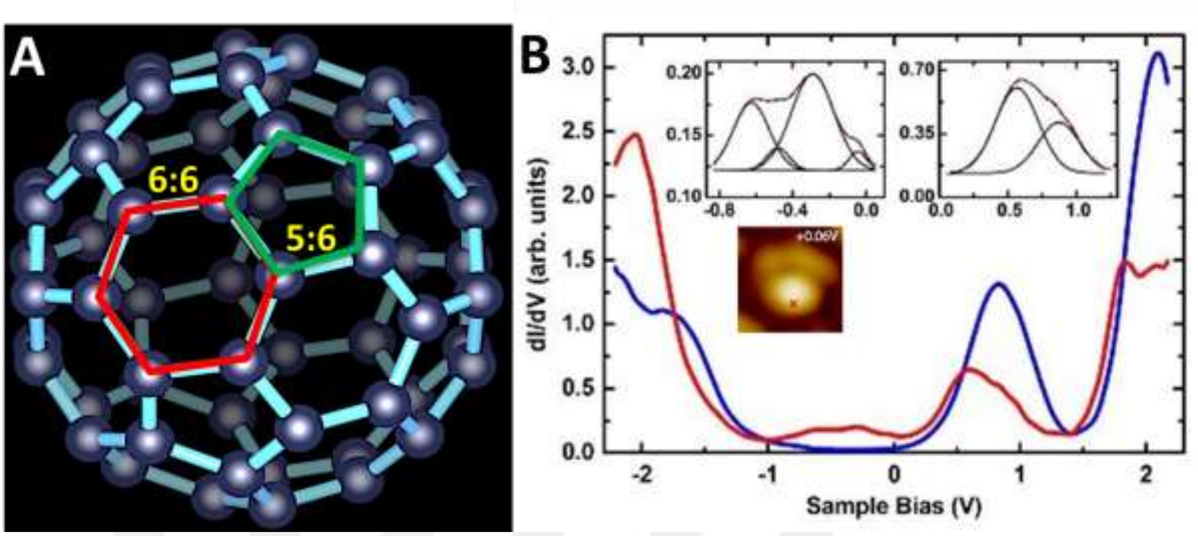

Figure 21: A. Schematic diagram of a C_{60} molecule. Hexagonal and pentagonal rings highlighted in red and green. B. Two different STS spectra performed over C_{60} molecules on the Au(111) surface, the site of the spectra is indicated with a red cross on the STM image: the red is at +0.45 V bias, 0.16 nA tunnelling current and the blue is at +0.46 V bias, 0.20 nA tunnelling current. Two peaks for filled states and a peak for an empty state is observed for both the red and blue parameters. The figure in B is modified from ref. [143].

The adsorption and growth of C_{60} molecules has been widely studied on a variety of surfaces such as Au(111), Ag(100) and Cu(111). A charge transfer of 0.8, 1.7 and 1.6 electrons per C_{60} molecule were found for the Au(111), Ag(100) and Cu(111), respectively [144]. Therefore, the adsorption, diffusion and desorption energies slightly differ from one surface to the next [143]. The substrate temperature has an effect on the growth of C_{60} layers supported on metal substrates. At room temperature, the molecule can diffuse through long distances and will eventually become bound at step edges where two-dimensional island growth starts. At low temperature (less than ~200 K), the growth starts from the elbow sites of the herringbone reconstructed Au(111) surface [145], as surface defects at the elbows sites are able to trap molecules.

Due to the depth of the surface potential energy of the FCC region [122, 125], the growth on the FCC region is faster than on the HCP regions [146, 147]. The close-packed direction of C_{60} islands are found to have rotations of R0, R14, R30 with respect to the $[11\bar{2}]$ surface direction on the Au(111) surface [146-150]. The molecules reach sufficient energy to escape from the elbow site at around 284 K and diffuse on the surface.

1.9.4 Magic Number C_{60}-Au Complexes

Magic number clusters, $(C_{60})_m$-$(Au)_n$, were first observed by Xie *et al.* [14] by adding C_{60} molecules and Au atoms one after another (or vice versa) on to the Au(111) surface at 110 K and then annealing the substrate up to room temperature. The growth was observed only on the elbow sites at 110 K. These clusters are formed with C_{60} molecules around and on top of planar Au islands. The interaction between individual C_{60} molecules is by strong van der Waals force and between the molecules and Au atoms by charge transfer, which plays an important role in keeping the cluster components together. Here, the Au island atoms behave like step edges of the Au(111) surface.

Figure 22 shows STM images (at bias voltage of -1.8 V and tunnelling current of 0.03 nA) of magic number clusters on the Au(111) surface from ref. [14]. C_{60} molecules and Au atoms were deposited on the surface at 110 K. The molecules and Au atoms prefer to sit on the elbow sites (mostly FCC regions) with irregular shapes (see Figure 22A). Figure 22B shows a room temperature scan of a surface area with $(C_{60})_7$-$(Au)_{19}$ clusters. The magic number clusters were formed by bringing the substrate temperature gradually to room temperature. As seen in Figure 22C the height variations of two clusters as a function of lateral distance are indicated with the red and the blue line over $(C_{60})_7$-$(Au)_{19}$, $(C_{60})_{12}$-$(Au)_n$ clusters, respectively. Here, the C_{60} molecules surround the Au island (the orange balls) with an average height of 0.75 ± 0.05 nm. One atomic layer of Au island atoms (0.22 ± 0.02 nm) raises the C_{60} molecule/s (bright feature) to a total height of 0.98 ± 0.05. The most frequently observed magic number clusters, $(C_{60})_7$-$(Au)_{19}$, $(C_{60})_{10}$-$(Au)_{35}$, $(C_{60})_{12}$-$(Au)_{49}$, and $(C_{60})_{14}$-$(Au)_{63}$ and some other types of irregular clusters are presented in Figure 22D.

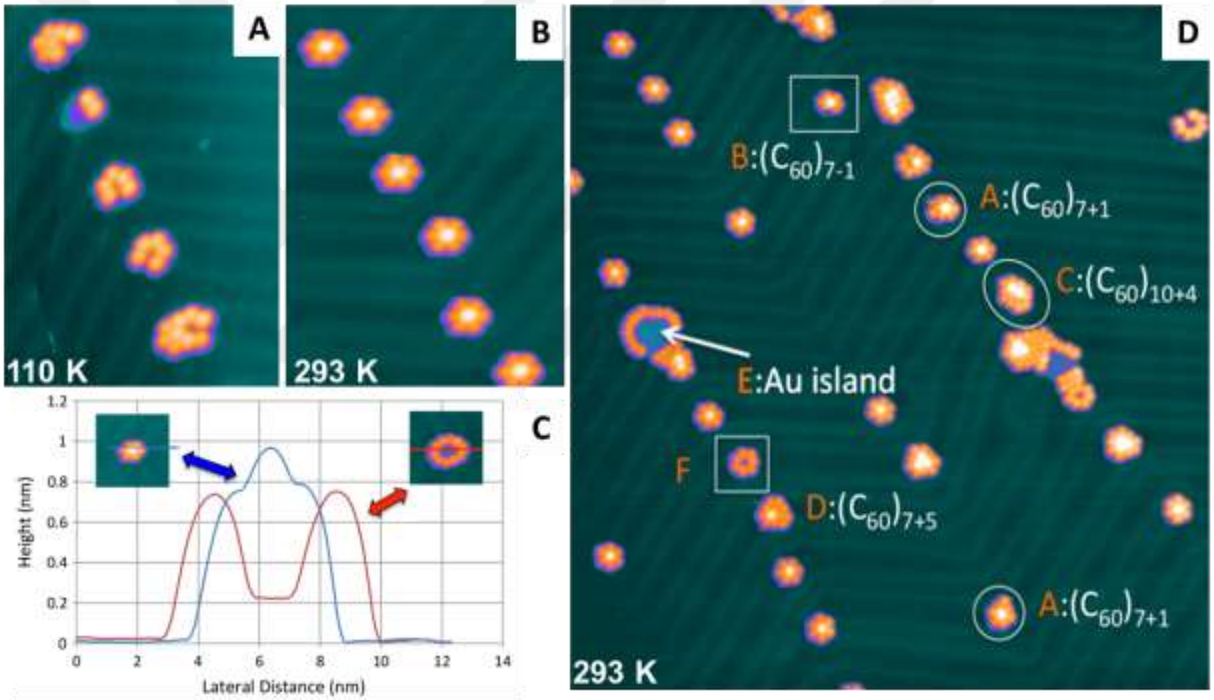

Figure 22: STM images (at -1.8 V, 0.03 nA) of magic number clusters produced on the Au(111) surface by cooperative self-assembly. A. After deposition of C_{60} molecules and Au atoms on the surface at 110 K. Both species prefer to sit on the elbow sites (mostly in FCC regions) with irregular shapes. B. The substrate temperature is brought gradually up to room temperature leading to more monodispersed $(C_{60})_7$-$(Au)_{19}$ clusters in the region shown. C. Height variations of two clusters as a function of lateral distance are indicated by the red and the blue lines, corresponding to $(C_{60})_7$-$(Au)_{19}$ and $(C_{60})_{12}$-$(Au)_n$ clusters, respectively. Orange balls are the C_{60} molecules around the Au islands. On top of the Au islands, C_{60} molecule/s (bright orange balls) are higher due to the atomic layer of Au island atoms. D. Irregular clusters are $(C_{60})_{7+1}$ (A), $(C_{60})_{7-1}$ (B), $(C_{60})_{10+4}$ (C), and $(C_{60})_{7+5}$ (D), Au island (E), a ring cluster with $(C_{60})_7$ (F) (All images are obtained from ref. [14]).

After deposition of C_{60} molecules and Au atoms on the surface at 110 K, the magic number C_{60}-Au clusters are formed by losing or capturing C_{60} molecule/s and Au atom/s while the substrate temperature is increased gradually to room temperature. The clusters consist of an optimal number of molecules packed around the Au island which are $(C_{60})_7$-$(Au)_{19}$, $(C_{60})_{10}$-$(Au)_{35}$, $(C_{60})_{12}$-$(Au)_{49}$, and $(C_{60})_{14}$-$(Au)_{63}$ and stable up to 400 K. For the clusters, there are two types of interactions in cluster components (C_{60} molecules and Au atoms). A C_{60} molecule on the top of the cluster interacts with three Au island atoms and six neighboring C_{60} molecules.

1.10 C_{60} Manipulations

1.10.1 Electron (or Hole) Induced Manipulation of C_{60}

An important electron induced manipulation (non-local) of C_{60} molecules on the Si(111)-7x7 surface at room temperature is mentioned in section 1.6.2 in Figure 15. The non-local reaction was observed by Nouchi *et al.*[29] by injection electrons and holes into an organized layer of C_{60} molecules on a Si(111)-7x7 surface. This manipulation causes a ring-shaped surface modification (polymerisation and depolymerisation) of the C_{60} close-packed layer on the Si(111)-7x7 surface at room temperature.

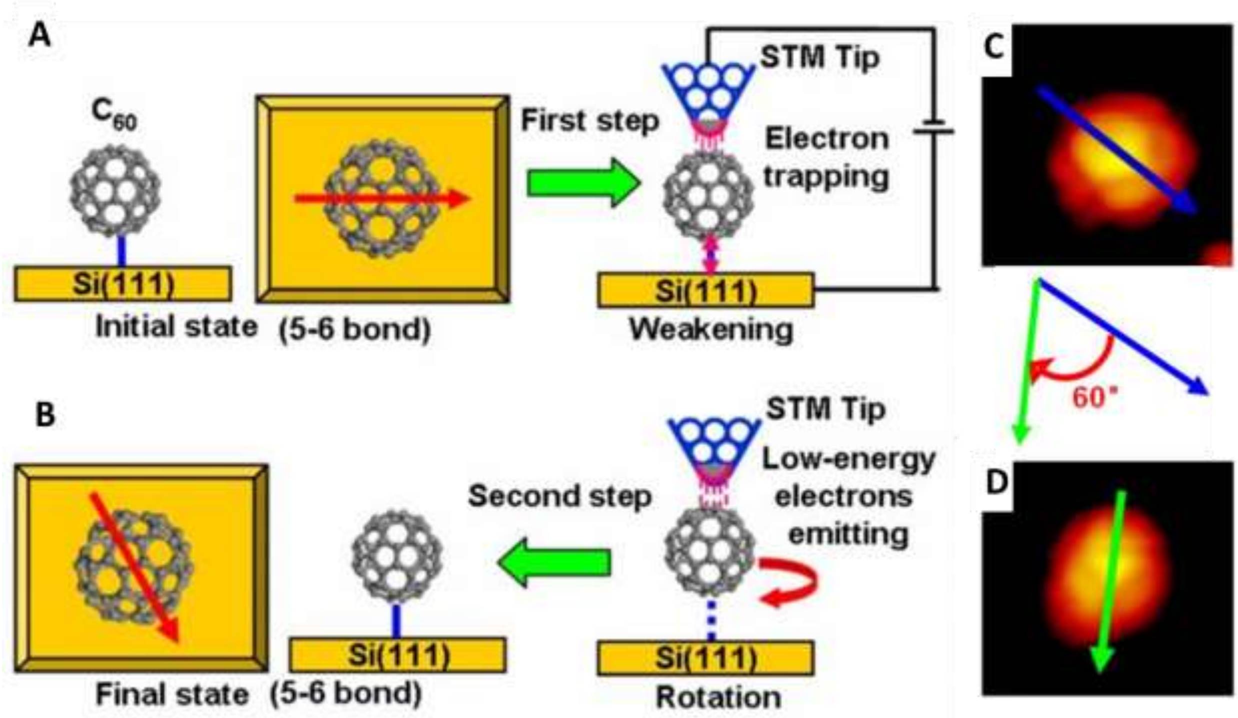

Figure 23: A model diagram for the rotation of a C_{60} molecule on the Si(111)-7x7 surface as a result of a bias voltage pulse at room temperature. A. First, determining the initial state (5-6 bond) of C_{60} molecule on the surface with a STM image and then weakening the bond between the molecule and the surface by electron excitation. B. Afterward, rotation of the molecule occurs by low energy electron bombardment. C and D. Before and after STM images illustrating C_{60} molecule rotation by 60° with respect to the $[10\bar{1}]$ surface direction (images modified from ref. [15]).

Another example is shown in Figure 23 for the rotation of the 5-6 bond of C_{60} molecules on the Si(111)-7x7 surface via bias voltage pulse at room temperature [15]. The rotation is made possible by first weakening the Si-C bond via injection electrons into the molecule and then rotate via low energy electron bombardment. In Figure 23, a model diagram is introduced for the rotation of C_{60} molecule. The weakening of the Si-C bond by electron excitation is presented in Figure 23A. This is followed in Figure 23B, by a rotation of the molecule, which occurs through low-energy electron bombardment. STM images showing the orientation of the C_{60} molecule before manipulation are shown Figure 23C and D, respectively. The 60° rotation is observed by applying a positive bias voltage of +7.0 V with respect to the $[10\bar{1}]$ surface direction. The threshold voltage required to produce a rotation was found to be +6.0 V. A total of 12 rotation angles were observed, thus 12 energy-equivalent states were found.

1.10.2 Mechanical Manipulation of C_{60}

The first mechanical manipulation of C_{60} was performed by Cuberes *et al.* on the Cu(111) step via a repulsive interaction between the C_{60} molecule and the tip at room temperature [21, 22]. They could build an abacus by pushing the molecules using the STM tip. Moreover, the pushing of the molecule was studied to explore the binding site and the polar angle using the STM images, STS measurements, DFT calculations [23] and analysis of vibrational modes [24]. Further, the rolling of C_{60} molecules was demonstrated on the Si(100)-2x1 reconstructed surface experimentally [25, 26] with an attractive force using the STM tip, and this mechanism is also studied theoretically [18, 27, 28].

A single C_{60} molecule manipulation mechanism on the In-modified Si(111)-$\sqrt{3}x\sqrt{3}$-Au surface (produced by depositing first Au then In atoms) has been studied in terms of bias voltage, tunnelling current, tip-sample distance and manipulation power [19]. It was observed that the manipulation was possible under a range of bias voltages (from -1.5 to +0.5 V) and tunnelling currents (from 0.02 to 100 nA). It was concluded that the manipulation was purely mechanical origin, the effect of electric field was ruled out by performing the manipulation at zero bias voltage. The thermal decomposition power threshold was found to be 1.0 to 21 μW [151, 152]. In this study, the average thermal decomposition power applied was 0.2 μW maximum. Therefore, the effect of the thermal decomposition was also eliminated.

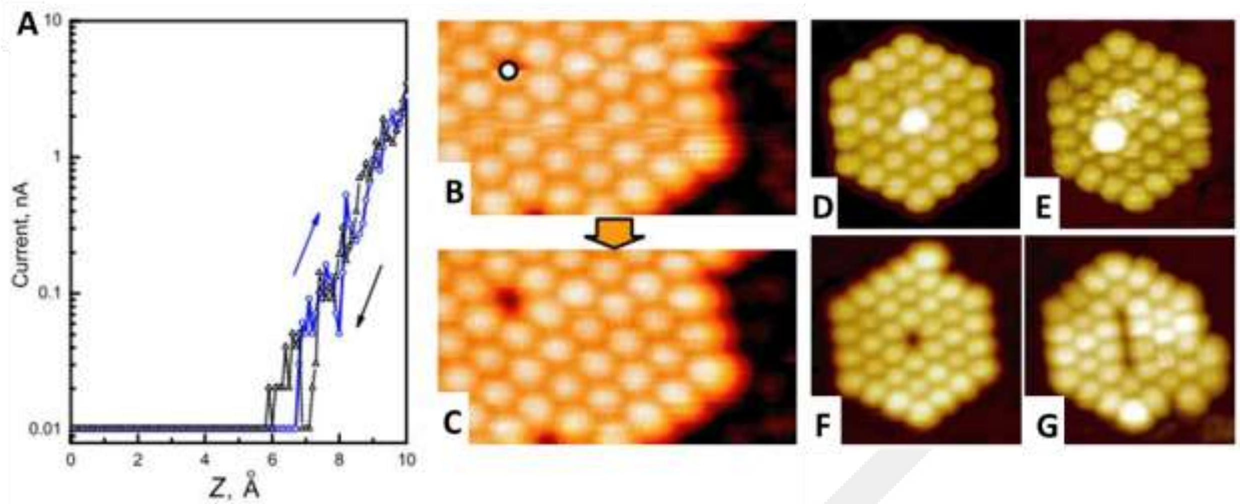

Figure 24: Typical I(Z) curve and STM images for C_{60} manipulation on the In-modified Si(111)-$\sqrt{3}x\sqrt{3}$-Au surface. A. I(Z) curve during manipulation at zero bias voltage, the manipulation has successfully occurred when the Z-displacement drops 0.4 nm. B and C. During and after manipulation images for a selected C_{60} molecule, indicated with the white spot, and a C_{60} vacancy in the next image. D. A hexagonal island which consists of 37 C_{60} molecules; the aim was to extract the bright molecule in the middle using the STM tip. E, F, and G. Sequence of images to extract three molecules which appeared at the side (all images are taken from ref. [19]).

In Figure 24, a typical I(Z) curve and STM images are presented for the C_{60} manipulation on the In-modified Si(111)-$\sqrt{3}x\sqrt{3}$-Au surface. The I(Z) curve, in Figure 24A, indicates a successful manipulation event with an acquisition time ~300 ms at zero bias voltage. The Z-displacement drops 0.4 nm and saturates with decreasing manipulation current. The STM images for during and after manipulation event are shown in Figure 24B and C, respectively. The manipulation was performed on a selected C_{60} molecule, which is indicated by the white spot, and a C_{60} vacancy in the next image is produced. Figure 24D, E, F, and G, show the hexagonal C_{60} islands that consist of 37 molecules. The aim was to extract a C_{60} molecule from the middle of the island using the STM tip. As seen in final image, G, three molecules were extracted and appeared at the side of the island.

When the STM tip approaches a selected C_{60} molecule, the molecule is pressed down by the tip and induces a stress on the molecule. This interaction between the tip and the molecule abruptly and releases the molecule from it's original position on the surface. This molecule either moves into a nearby vacancy (if there is one) or diffuses on the surface and decorates a step edge. Here, the average Z-displacement was found to be 4.7 ± 0.6 Å to extract a single C_{60} molecule. The idea of this study is used as a reference in Chapter 4 for the manipulation of hybrid $(C_{60})_m$-$(Au)_n$ clusters.

1.11 Diffusion and Nucleation

Surface diffusion has been the subject of considerable scientific interest for around a century. After the development of good vacuum systems, the study of surface diffusion and exploration of kinetic processes on surfaces became possible with high resolution field ion microscopy [153] and, subsequently, scanning tunneling microscopy [3]. In this section, I will describe the phenomenon of diffusion on surfaces including different diffusion modes and their mechanisms. Specifically, I will discuss the diffusion of molecules and fullerenes on the Au(111) surface.

1.11.1 Diffusion Mechanism

Surface diffusion can be defined as the motion of atoms, molecules and atomic/molecular clusters on solid surfaces. This motion usually occurs from one lattice site to the next nearest adsorption site on a surface by *jumping*. This movement depends on the nature of bonding between the adsorbent and the surface and it is further influenced by surface orientation and chemical potential gradients. The probability of a successful jump of an adsorbent on a surface depends on a thermodynamic factor and attempt frequency. The diffusivity rate of overcoming a potential barrier of a magnitude E_{diff}, which must be lower than the desorption energy, can be written as:

$$D = va^2 exp(\frac{-E_{diff}}{k_B T}).$$

Here a is the length between two neighboring adsorption sites, v is the attempt frequency of the system, k_B is the Boltzmann constant and T is temperature. va^2 can be written as a diffusion constant, D_0. The equation illustrates that the diffusion rate increases with increasing temperature. One important relationship in this formula is that between E_{diff} and $k_B T$ in the thermodynamic factor. When $E_{diff} < k_B T$, the particle or the adatom can be found at any point on the surface [154]. When $E_{\mathrm{diff}} \gg k_B T$, the diffusion rate is low allowing an accurate measurement of the diffusion coefficient D. From the measured values of D as a function of T, E_{diff} and D_0 can be determined from an Arrhenius plot of the rate constant versus the inverse temperature, $1/T$.

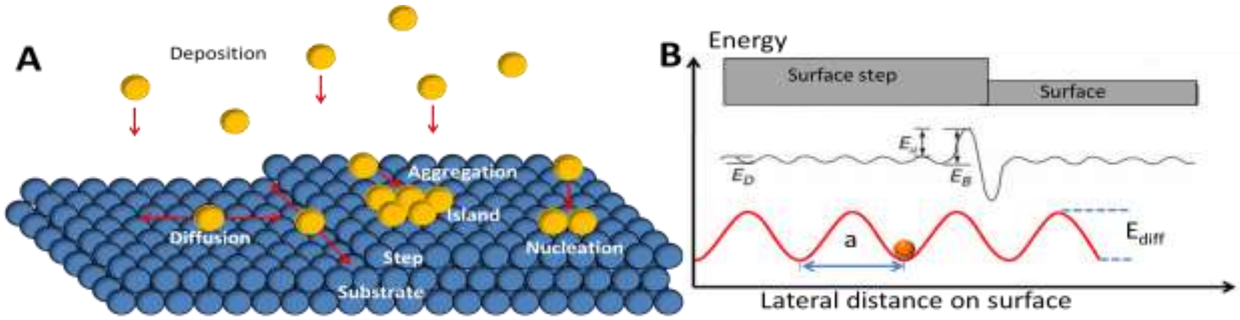

Figure 25: A. Schematic diagram of surface events after deposition. After atoms (yellow) land on the surface, diffusion, nucleation, and island growth are possible events depending on temperature and coverage. B. Energy diagram for 1D diffusion on a surface. The orange ball indicates an adsorbent which may diffuse on the surface from one adsorption site to another (at least by a distance of a) by overcoming the energy barrier E_{diff} (E_D in the inset schematic). The inset schematic shows the effect of step edges on interlayer surface transport, Ehrlich–Schwoebel barrier, E_a. The adsorbent can typically reflect from the top due to the barrier of E_B or bind to the edge from below.

Figure 25A shows surface events after deposition of atoms or molecules (yellow). When particles land on the surface, diffusion, nucleation, or island growth can be observed depending on the substrate temperature and the coverage. An energy diagram for 1D diffusion on a surface is illustrated in Figure 25B. The orange ball indicates an adsorbent which may diffuse on the surface from one adsorption site to another (at least by a distance of a) by overcoming the energy barrier E_{diff} (E_D in the inset schematic). The presence of step edges gives an extra contribution to the energy barrier on interlayer surface transport, Ehrlich–Schwoebel barrier, E_a [155], illustrated in the inset diagram. The adsorbent can typically reflect from the top due to the barrier of E_B or bind to the edge from below. Atomic/molecular clusters on the surface can diffuse via gliding, shearing, reptation and dislocation [156], depending on the size of the clusters and on surface directions. Moreover, there are different types of interactions which result in different bonding strength and length between adsorbent and surface. These typical interaction types and corresponding bond strength and length are presented in Table 2 with the nature of the interaction [157].

Table 2: Typical interaction energies, bonding length and nature of interaction for different interaction types **[157]**.

Interaction type	**Strength**	**Bonding length**	**Nature**
van-der-Waals	~0.1 eV	0.5…1 nm	Non-selective
H bonding	0.1…0.5 eV	0.20…0.35 nm	Selective, directed
Electrostatic	0.1…3 eV	Up to several nm	Non-selective
Dipole–dipole	0.1…0.5 eV	0.2…0.3 nm	Directed
Metal complexation	1…3 eV	0.2…0.3 nm	Selective
Substrate-mediated	0.1…1 eV	up to 7 nm	Oscillatory
Reconstruction mediated	1 eV	System dependent	Covalent

1.11.2 Nucleation

The classical nucleation theory has been studied, with continuous research contributions, for 90 years [158]. When individual particles arrive on a surface, they can from island by diffusion (random walk) and aggregation [159]. These islands, small or large, tend to form stable islands over time by the mechanism of Ostwald Ripening [160]. There are two characteristic approaches to nucleation: the kinetic and thermodynamic approach. The kinetics of nucleation is considered at the earlier stages in the time evolution of the system [161]. The number of particles increases very slowly during the transient nucleation phase (a time-lag), and then increases exponentially at the steady-state nucleation phase [158]. The free energy, ΔG, increases with increasing island size until this reach critical island size, N_c. Beyond this critical size, the free energy of the island decreases while the island sizes increase. [158, 162]. During this stage, the island growth is irregular due to random attachment of additional atoms/molecules. In such a system, the large island growth is a dominant process due to a high probability of attachment of particles.

The thermodynamics of nucleation is a temperature effect on growth in reaching a stable phase. The island size and nucleation energy barrier can be determined by the growth rate as a function of temperature [160]. The relationship between the surface and island chemical potential defines attachment/detachment and diffusion limited processes [133, 160, 163].

The activation energy of diffusion can also be determined by measuring the density of islands on the surface as a function of the substrate temperature. The density can be written as:

$$n_x = (v\frac{R}{D_0})^{1/3} exp(\frac{E_{diff}}{3k_B T}).$$

Here, R is the deposition rate (D_0, v and E_{diff} are as previously defined in section 1.11.1). The island density decreases with increasing substrate temperature, while island size increases. The activation energy for diffusion of atoms, molecules and clusters varies on different surfaces depending on coverage, substrate temperature and the nature of surface reconstruction [156]. Most relevant to the work reported in this thesis are the diffusion of Au atoms and C_{60} molecules and the formation of Au or C_{60} islands on the Au(111) surface.

There has been a number of studies of atomic diffusion on the Au(111) surface. The activation energy for diffusion of a single gold atom on the Au(111) surface is found to be 0.029 eV [164, 165]. This can be compared to the diffusion energies of non-gold atoms on the Au(111) surface as being higher for Ni: 0.078 eV, Cu: 0.089 eV, Pd: 0.111 eV, Ag: 0.075 eV, and Pt: 0.113 eV [156, 166]. Because of the unique surface structure of the Au(111) surface, it is hard to determine the diffusion mechanism. In Figure 26, an example of Al island density size and shape as a function of temperature on the Au(111) surface is presented via STM images (A-E). It can be seen from the STM images that the size of Al islands on the surface increased with increasing substrate temperature [167].

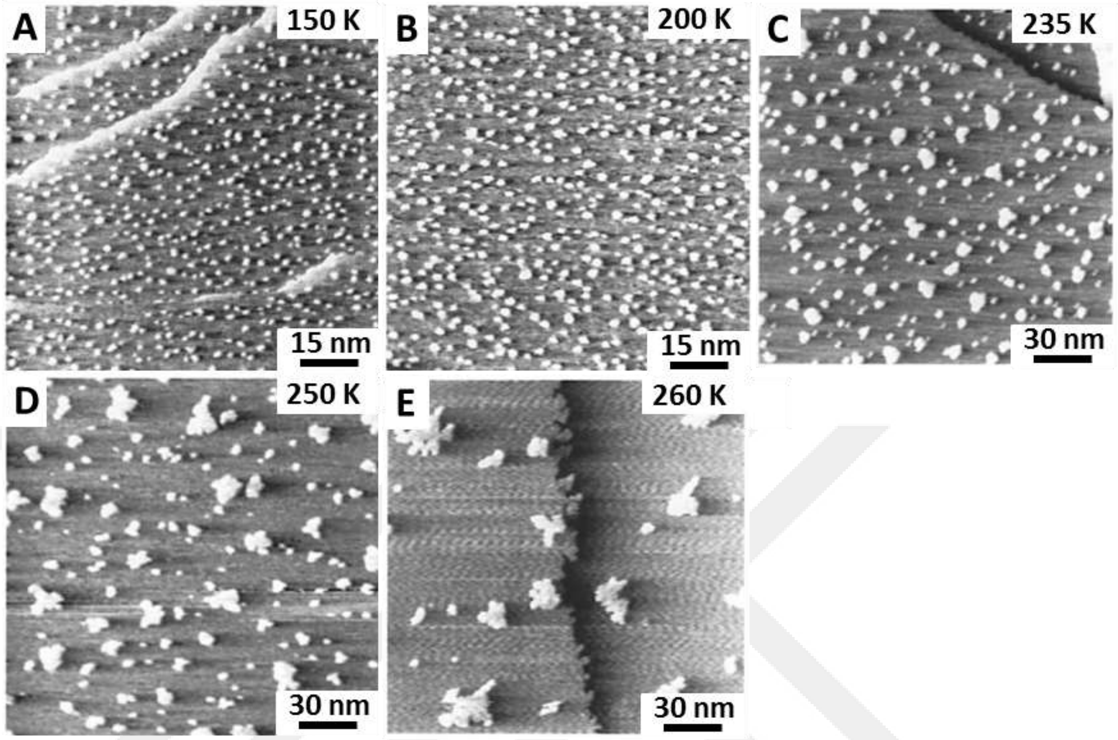

Figure 26: Image captions from ref. [167]. A – E showing Al island density, size, and shape as a function of temperature onto Au(111) with a coverage of 0.1ML. The island size increases with increasing the substrate temperature.

In comparison to atomic diffusion on surfaces, molecules and supramolecular self-assemblies exhibit a much more complex diffusion mechanism due to their increased number of degrees of freedom [168-170]. The diffusion of molecular assemblies can be observed as hopping, rotation and translation due to substrate temperature and coverage [156, 170]. Surface diffusion can be further influenced by the STM tip. The tip can cause diffusion by an electric field (benzene on the Au(111) [171, 172]), or weakening of the bond between molecule and surface via electron (or hole) injection (chlorobenzene on the Si(111)-7x7 surface [106]) or tip-induced diffusion (benzene on Au(111) [173]) under the STM tip.

Nucleation/growth of fullerenes on Au surfaces were studied by Altman *et al.* [174]. The growth at low substrate temperatures (< 200 K) was observed mostly on the FCC and HCP elbow sites, as well as at the step edge. But, at room temperature, the growth was mostly observed along Au steps. Nucleation of molecular C_{60} island on a uniform Au(111) surface is illustrated in Figure 27 [175]. Ball models of close-packed C_{60} islands with $2\sqrt{3}$x$2\sqrt{3}$ R30° (A) and 7×7 (B) structures are presented on the Au(111) surface. In the $2\sqrt{3}$x$2\sqrt{3}$ R30° structure, C_{60} molecules are at the atop position. In the 7x7 structure, there are two different sites available for C_{60} molecules: atop or bridge. Other structures of C_{60} islands are also possible but not presented due to the complexity of the surface.

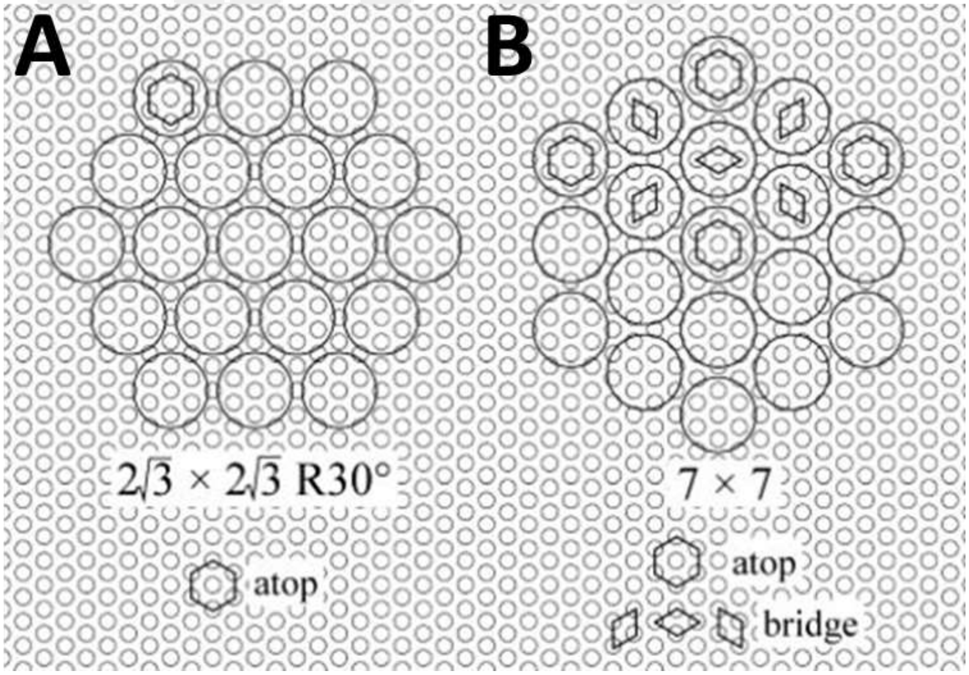

Figure 27: Ball model showing the $2\sqrt{3}x2\sqrt{3}$ R30° (A) and 7×7 (B) structures for close-packed C_{60} islands on the Au(111) surface. In the $2\sqrt{3}x2\sqrt{3}$ R30° structure, C_{60} molecules are at the atop positions. In the 7×7 structure, there are two different positions available for C_{60} molecules: atop or bridge. The C_{60}-C_{60} distances for a ideal $2\sqrt{3}x2\sqrt{3}$ R30° and 7×7 structures are found to be 9.98 and 10.08 Å, respectively [175].

C_{60} molecules on the Au(111) surface can freely diffuse on the surface or terminate at step edges [176]. Due to the stability of single-atomic vacancies of Au(111) and Ag(111) surfaces, it is difficult to reorder the close-packed C_{60} layer [176]. The diffusion energy of the C_{60} molecule is reported on the In-adsorbed Si(111))-√3×√3-Au surface by calculating the C_{60} island density as a function of increasing substrate temperature [177]. In Figure 28, STM images (A-D) show C_{60} island arrays formed by depositing 0.1 ML onto a Si(111)-√3×√3-(Au,In) surface held at various temperatures. An Arrhenius plot of C_{60} island number density is presented in Figure 28 F. Dashed blue and red lines show the plots for low temperature (110 – 140 K) and high-temperature (160 – 240 K) ranges, respectively. The sum of the two exponents is shown by the black line. One can clearly distinguish two regions which differ in gradient, and which indicate different energy regimes on the surface. The activation energies for C_{60} diffusion in these regimes are 33 ± 6 meV at 110 - 140 K and 128 ± 8 meV at 160 - 240 K [177].

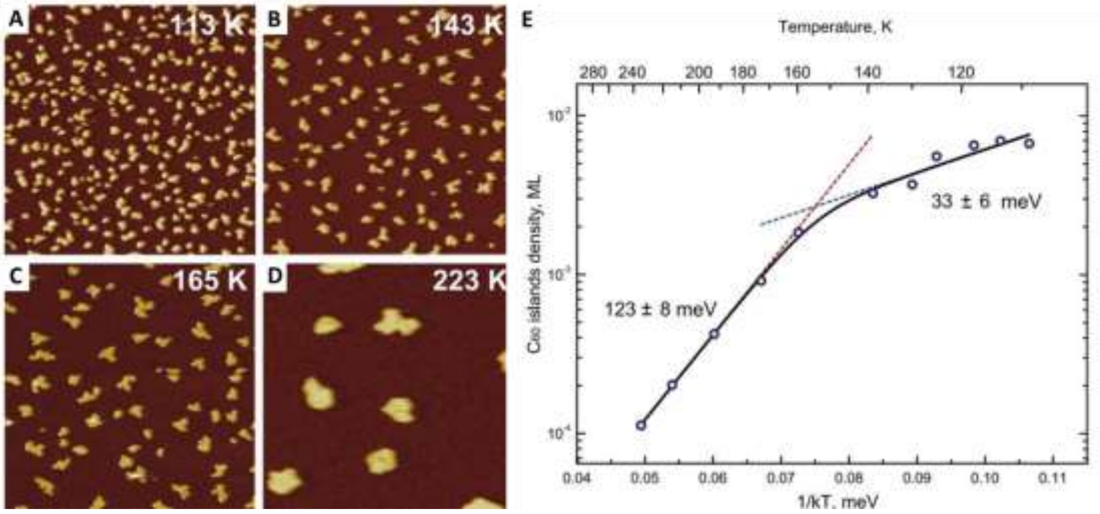

Figure 28: A-D. STM images showing C_{60} island arrays formed by depositing 0.1 ML onto an Si(111)-√3×√3-(Au,In) surface held at various temperatures. E. Arrhenius plot of C_{60} island number density. Dashed blue and red lines show the plot for the activation energies, 33 ± 6 meV and 123 ± 8 meV, at low temperature (110 – 140 K) and high-temperature (160 – 240 K) ranges, respectively; the sum of the two exponents is shown by the black line [177].

CHAPTER 2

EXPERIMENTAL METHODS

All experiments were carried out under UHV conditions to avoid impurities on the sample surfaces. Investigation of the hybrid C_{60}-Au clusters on the Au(111) surface was performed in a VT-STM and the local and non-local manipulation of chlorobenzene and oxygen molecules on the Si(111)-7x7 surface were performed in a RT-STM and the hybrid C_{60}-Au clusters on the Au(111) surface performed in a VT-STM. In this Chapter, the experimental research process and system details are discussed; the ultra-high vacuum (UHV) system along with essential processes such as pumping, venting, and baking. VT-STM and RT-STM general system properties, tip and sample preparations, and data analysis method will be discussed in this chapter.

2.1 UHV system

In order to study surface science in STM background gases ultra-high vacuum conditions are needed to eliminate surface contamination. The physics behind UHV conditions (i.e. a base pressure lower than 10^{-9} mbar) are based upon the gas density (ideal gas equation for rate of impingement on a surface $P\,V = nRT$), the mean-free-path of a gas molecule ($\lambda = \frac{k_B T}{\sqrt{2}\pi\epsilon^2\rho}$), and surface contamination (Hertz-Knudsen equation $R = \frac{P}{\sqrt{2\pi m k_B T}}$) [178]. From atmospheric pressure to UHV pressure at 300 K, the gas density decreases, the mean-free-path of a gas molecule increases, and the rate of surface contamination decreases by a factor of 10^{13} [179].

Best conditions are achieved by minimizing such factors, reducing background gases and reducing contaminations on the chamber walls and sample.

UHV chambers are made of materials such as glass, stainless steel, aluminum or titanium because of their low outgassing properties. To seal each connection, soft copper gaskets are widely used, which are compressed between two knife-edges that are machined into the port flanges. The alternative is to used rubber gaskets. Important considerations when dealing with UHV are pumping size, chamber conductance, and choice of low vapour pressure materials and elimination of contaminants.

Pumping and Pressure Measurement: Under typical operation conditions the UHV system needs to be pumped down to 10^{-10} mbar or lower in order to perform experiments. In this study, a several types of pumps and gauges used to reach and measure this desired pressure. Table 3 presents different type of pumps and gauges operating pressure [180].

Table 3: Different pumps and gauges corresponding operations pressures in this study.

Pump	Type	Operation Pressure (mbar)	Gauge
Rotary	Mechanical	atmosphere-10^{-3}	Pirani
Turbo Molecular	Mechanical	10^{-3}-10^{-9}	Penning
Ion	Getter	10^{-7}-10^{-12}	Ionisation
Titanium Sublimation (TSP)	Getter	10^{-7}-10^{-12}	Ionisation

Here, ion pumps work by applying a high electric potential (typically at 3-7 kV range) to electrodes to create ions in the vacuum. These ions ionize molecules which are then captured by the cathode. A TSP usually accompanies the ion pumps to reduce H_2, CO and O_2 gases in the system. The TSP usually runs at vacuum lower than 10^{-7} mbar by applying around 40 A direct current through a titanium wire. The sublimated Ti atoms chemically getter the reactive gas molecules in the system. Generally, the type of gauge is determined by the pressure range to be measured (which is dictated by the pump used) and sometimes by the gas being pumped, e.g. whether it is corrosive.

Venting: The venting process is required to load a sample or tip from the load-lock or to fix or change part of the vacuum system. The venting process is performed with pure N_2 gas produced from liquid nitrogen (L-N_2) or compressed N_2 gas, to reduce water vapour on the inside of the chamber walls.

Baking: The Omicron VT STM has an automated bakeout control system that controls the temperature (with an increment of 1 °C/min) to reach a maximum temperature (between 140 °C and 150 °C) after 6 hours. Baking time varies from 24 hours to 52 hours with the system protected by an interlock against excessive pressure or temperature during baking. Bakeout process for the home-built UHV RT-STM is controlled by in-house-written LabVIEW programs with monitoring temperatures at specific locations during baking. The baking process takes 48 hours to 72 hours by which time the pressure will reach 10^{-9} torr. An important point is the depolarization temperature of piezoelectric tubes on the STM head (~180 °C). The bakeout temperature (max 150 °C) is safe below the critical temperature for piezoelectric tubes. Once the entire system starts cooling down and the temperature reaches 100 ºC, the ion pumps and TPS need to be degased by turning on/off at different voltages (7 kV to 3 kV) and currents (25 A to 42 A), respectively.

We can decide whether or not the system require baking process by looking STM images after prepare the sample. In Figure 29, STM topographies are given for the clean p-type Si(111)-7x7 surface. The images take in 2 hours after flash and reconstruction the sample at 1200 °C and 960 °C, respectively. Figure 29A is a clean surface may acceptable for experiments after background (defects and impurities) subtractions. However, if the chamber is contaminated due to the impurities or high pressure in the system, more impurities will be placed on the sample surface before the start experiments (see Figure 29B). The evidence of impurities on the surface indicates that the system must be baked to obtain a clean surface as given in Figure 29C.

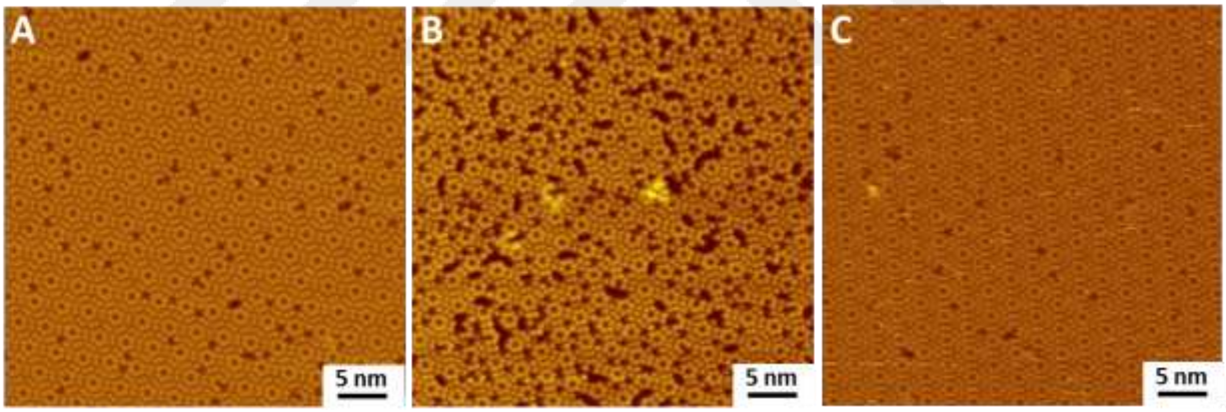

Figure 29: STM topographies 2 hours after flashing and reconstruction the surface at 1200 °C and 960 °C, respectively. A. Clean reconstructed Si(111) surface with an acceptable level of surface defects and impurities. B. More impurities present an surface. C. Successful bakeout process, a clean surface can be re-obtained. All images were taken at +1.0 V 500 pA and 40 nm x 40 nm area.

A residual gas analysis of systems was performed (using a Spectra Metrics RGA) and is presented in Figure 30. Mass spectra were taken for clean UHV (A), contamination (B), chlorobenzene (C) and oxygen gas (D).

Leak Detection**:** If the system pressure does not reach the UHV range, there might be a leak in the system. Before starting the leak detection, mass spectra lead to decide what kind of contamination occurred in the system (see Figure 30B). The most preferred method to detect a leak is by connecting separate unite a mass spectrometer to the system and with He gas detect possible leak spots. Because He gas has very small mass (4 amu), it will flow into the system and be detected by the mass spectrometer.

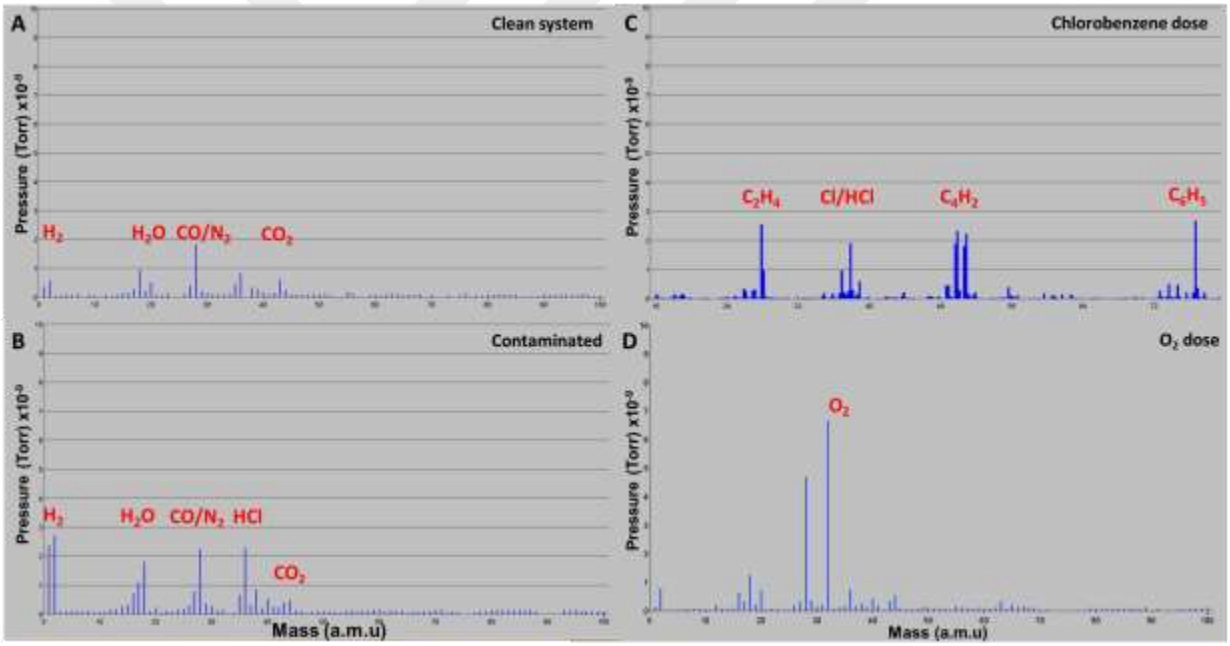

Figure 30: Mass spectra were taken for clean UHV (A), contamination (B), chlorobenzene (C) and oxygen gas (D).

2.2 Tip Preparation and High Temperature Annealing of W Tip

For the STM experiments, the tip is critical obtaining high-resolution images. The resolution depends upon the sharpness of the tip. To obtain a suitable tip for STM, there are two common methods: mechanical cutting and electrochemical etching. Mechanical cutting is typically done by cutting and simultaneously pulling up on a soft wire (mostly Au or Ir/Pt) [181, 182] with a sharp clipper, so that an angle is obtained forming a sharp tip. Electrochemical etching provides more control in obtaining a sharp tip when compared with mechanical cutting. In our experiments, we produced tips with the electrochemical etching method (for a schematic illustration of the etching layout see Figure 31) followed by in-vacuum heating and annealing to remove the residual oxide layer on the tungsten (W) tip [183-187]. W wire with a purity of 99.95% and a diameter a 0.25 mm was purchased from ADVENT Research Materials Ltd.. Before starting the etching process, the W wire was cleaned with isopropanol and acetone in an ultrasonic bath (each for 10 minutes) to remove organic contaminations. Moreover, the etching apparatus was kept clean and isolated from any vibration to avoid a nonuniform tip forming.

A 2 M NaOH solution is prepared and stored for no longer than 24 hours prior to use. A circular gold wire is mounted in to the solution beker and connected to the cathode on the etching unit. Here, the W wire serves as an anode (see Figure 31A). The overall electrochemical reaction between the anode and cathode is given by:

$$W(s) + 2OH^{-} + 2H_2O -> WO^{2-}{}_{4} + 3H_2(g).$$

Earlier works suggest that the aspect ratio of a tip should be less than 1 because a long tip (h/d>>1) causes more vibration (see Figure 31B). To obtain a good tip, two etching steps are performed. The first etch removes the mechanically cut edge which may cause splitting along the wire axis and multiple tips. The W wire is inserted into the solution 5 mm below the surface and the threshold current set to 1 mA, the etching voltage to 9 V, and differential sensitivity to 7 to control drop-off during tip etching [188]. The etching current is controlled and monitored via the power supply. When, the threshold current drops to 0.02 mA, then the power supply switches off automatically so that the tip is not etched further once drop-off occurs. Next, to obtain the actual tip, the tip is immersed 3 mm deeper into the solution and etched again [188]. A prepared tip is shown in Figure 31B. After the final process, any chemical or particles on the outer surface of the tip are removed by rinsing the tip with distilled water at least 10 times.

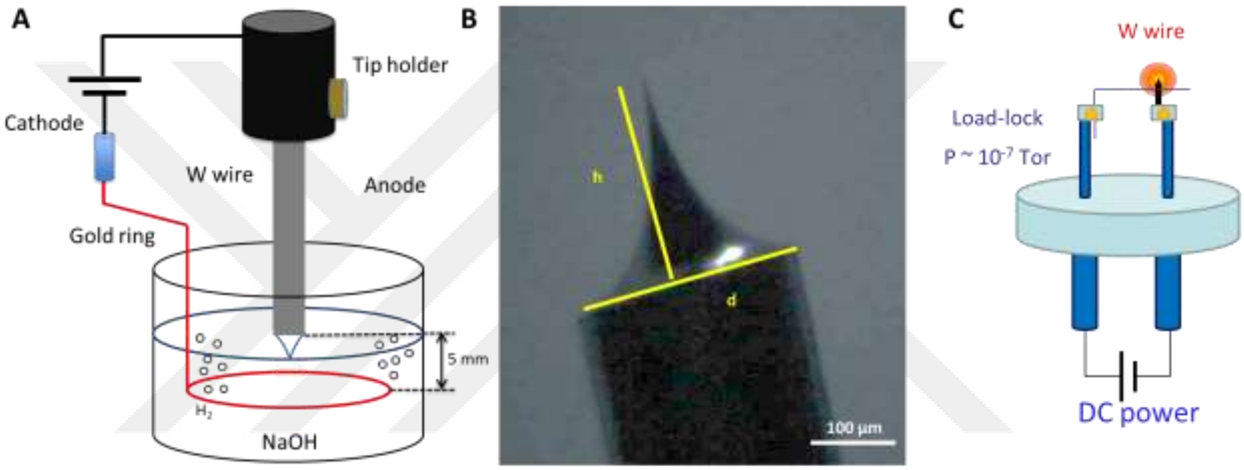

Figure 31. A schematic diagram of the tip etching system A. Here, the W wire and gold ring serve as the anode and cathode, respectively. B. An optical micrograph of an etched tip showing the aspect ratio h/d. C. Tip annealing stage in load-local with a ~10^{-7} torr base pressure.

Before installing the tip into the tip holder for the RT STM, tip heating-annealing is required to remove the oxide layer on the W tip. This layer sublimates at a high temperature, 1348 ºC [185]. After carefully mounting the tip into the tip annealing stage (Figure 31C), a DC power supply is connected to two metal electrodes to apply the current which passes directly though the tip shank. Nominal applied current is usually 3-5 A (until the tip turns a bright orange colour about 1000 °C) for 2 seconds in high vacuum followed by decreasing the current until it is a dark red colour for 10 minutes. After turning off the power supply, the tip reaches room temperature after 15 min. Alternatively, after tip preparation the tip may be inserted into the VT-STM and degased on the manipulator at 150 °C for 30 mins.

Once inserted into the STM, leaving the tip to scan at a high voltage for several minutes or increasing the voltage from ± 1 V to ± 5 V causes impurities to drop from the tip, giving improved resolution. Crashing the tip into the soft Au(111) surface may results in the formation of an Au nanotip at the end of the W tip apex. However, this process is not suitable for the hard Si(111) surface.

2.3 VT STM

In this thesis, all temperature-dependent studies concerning the production and manipulation of C_{60}-Au hybrid cluster on the Au(111) surface were performed in the VT STM (a block diagram for the VT STM is shown in Figure 32). This is because it is possible to follow changes on the surface as a function of substrate temperature. The substrate temperature is controlled by and cooling/heating control unit alows to study at helium temperature or up to 700 K.

A schematic view of the UHV VT STM is shown in Figure 32A. The system has two chambers: a fast-entry-lock (FEL) pumped with a Pfeiffer TS600 turbo pump and a rotary pump, and the main chamber which is pumped with a Varian Starcell ion pump, TSP, Leybold Turbovac 151 turbo pump and rotary pump. The sample/tip is loaded via the fast entry lock (FEL) and after 2 hours opens the valve between FEL and can be introduced in the main chamber after 2 h pump-down. The sample/tip is transferred via wobble stick to the manipulator for annealing or Ar^+ sputtering. Finally, it is placed in either sample/tip carousel or the STM stage. As seen in Figure 32, the main chamber has an ion gun, ion gauge, residual gas analyser (RGA), home-built effusion cell of C_{60} and a CreaTec high temperature effusion cell of Au.

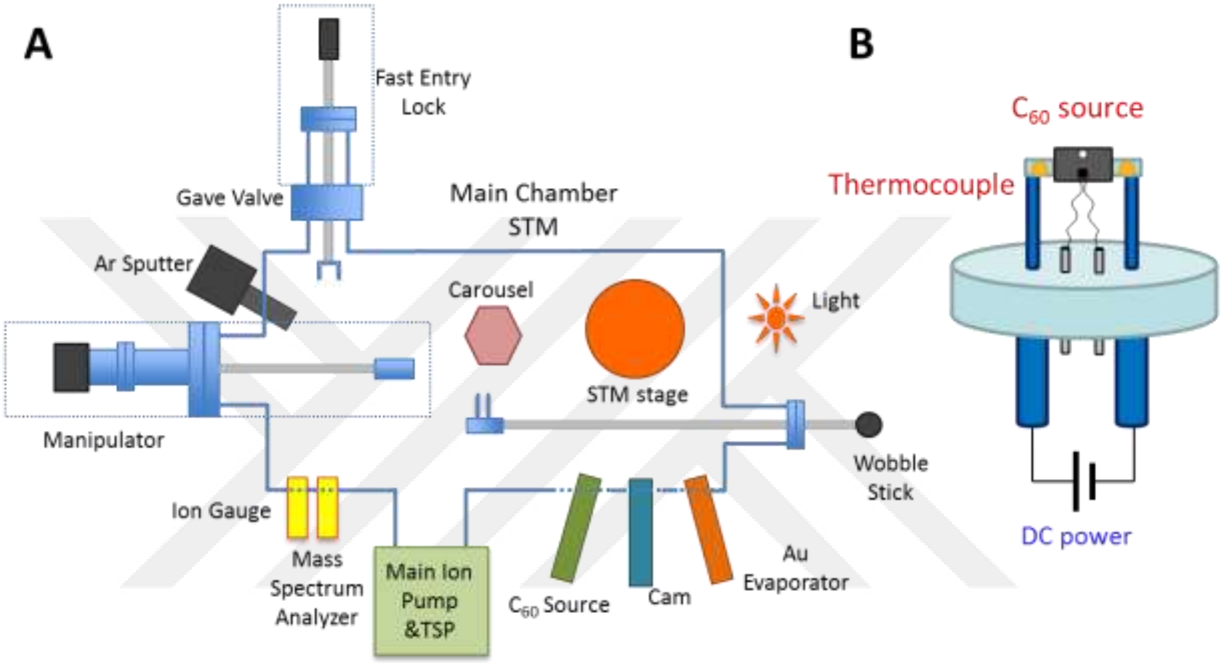

Figure 32. Schematic diagram for the UHV VT-STM (A) and home-built effusion cell for C_{60} (B).

In order to obtain high-resolution images, the vibration isolation system plays an important role. The STM system is located in an acoustic booth where vibration from the environment or the building is reduced. The vibration isolation system consists of three parts: a vibration isolation platform, a damping stage and a floating sample stage with four fixed springs. The STM stage can be locked in place with a push-and-pull motion (PPM) drive, during sample/tip loading, but is unlocked during scanning.

The Omicron VT STM can reach liquid nitrogen (~77 K) and helium level temperatures (~4 K) using a bath cryostat. This cryostat is connected to a copper braid which is mechanically connected to the top of the sample holder. While the sample cools, the tip can either remain at

RT or can be cooled somewhat by approaching it close to the surface (thus reducing thermal drift during scanning).

To cool down the sample, a valve that is connected to the cryogen storage dewar (L-N2 or He) is opened, and a rotary pump pumps the cryogen from the dewar to the bath cryostat. Here, a gas flow control block is used between the pump and cryostat to control the amount of flow. A temperature controller measures the temperature of the sample and in the bath cryostat and keeps the temperature either heating or cooling at a set value.

To heat the sample, direct heating or indirect resistive heating may be required depending on the sample. For indirect heating, a pyrolytic boron nitride (PBN) plate, which is directly behind the samole, which is heated and can be heated up to 750 K. During heating or cooling the sample, thermal drift may occur because of temperature differences between the sample and tip. To reduce this drift, scanning same area for an extended period is required until the temperature stabilises.

2.4 RT STM

The UHV 400 RHK model STM was purchased from RHK Technology. The UHV system can be separated into 4 main parts: the STM chamber (main chamber), the preparation chamber, the load-lock, and the gas line. The base pressure of the system is in the low 10-11 torr range. The microscope and preparation chambers are separated by a gate valve to avoid contamination of the microscope during sample preparation.

The main chamber contains a Varian Diode 300 Ion pump and TSP. In the preparation chamber, there are two pumps and an ion gauge: a Varian Diode 150 ion pump and a Pfeiffer TMU 250 pumping turbo pump used during the baking by opening V13. A quadrupole mass spectrometer can also be connected to this chamber to check the amount of PhCl in the vacuum. Tip and samples are transferred through the preparation chamber from the load-lock to the STM chamber. The load-lock is pumped by a Pfeiffer TPH 062 turbo pump and an Edwards RV 5 Dual-Mode rotary pump. The pressure here is monitored via a Penning gauge. Tip annealing/flashing to remove residual oxide is also performed in this chamber under low pressure (10^{-7} torr).

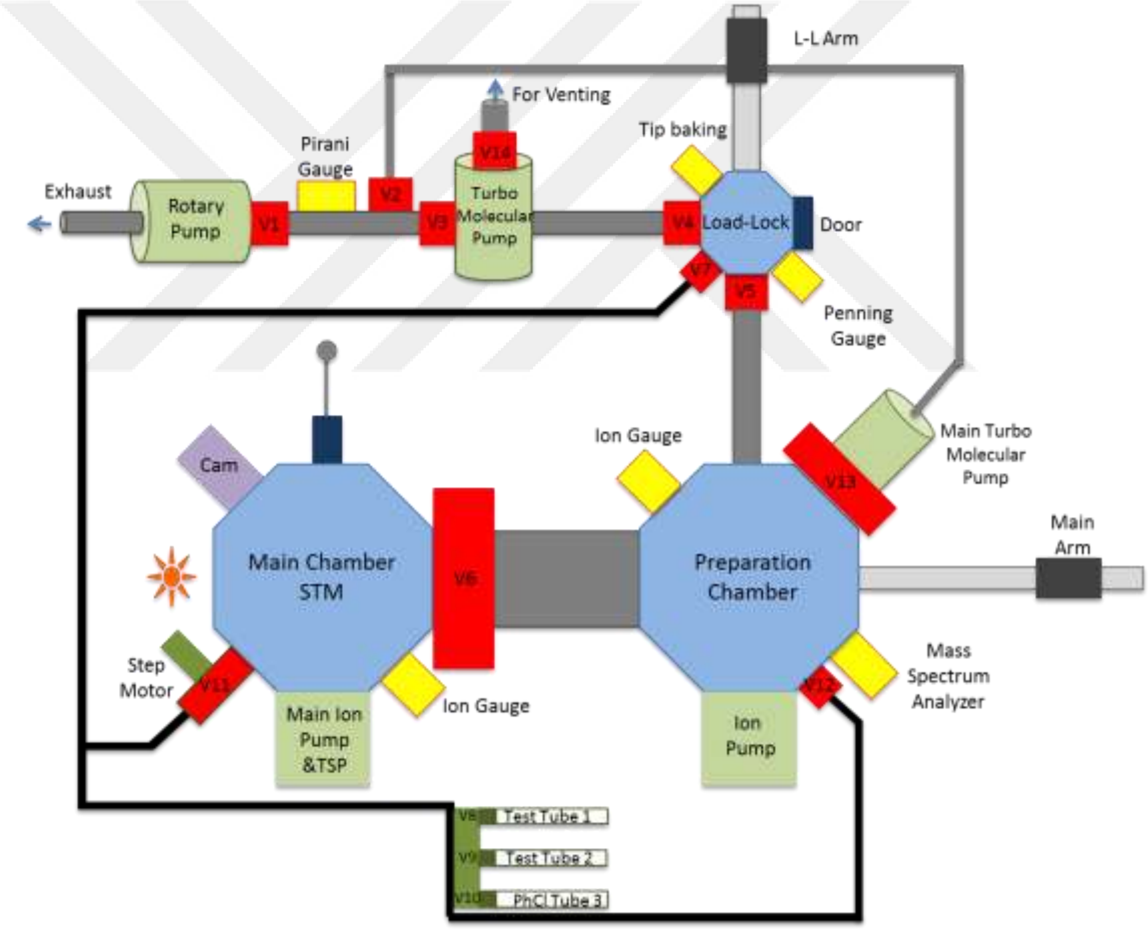

Figure 33. Shows a block diagram for UHV room temperature STM system

There are three gas lines connected to the three chambers for chlorobenzene and oxygen deposition. These gas lines are connected to leak valves for both the main chamber and the preparation chamber. A stepper motor which is attached to the leak valve of the main chamber is used precisely control gas introduction by computer using a LabVIEW program. The RT-STM system is in an acoustic booth and supported on a 10 ton vibration isolation platform. The STM itself is suspended in a single-stage spring system.

As seen in Figure 34, a *Beetle-type* [189] scan head has 4 piezo legs, three of them are separated by 120º and the other holds the tip for scanning in the middle. The bottom parts of the outer legs are made of sapphire balls which sit on the sample holder. When a voltage is applied, these piezo legs extend in x or y directions on the sample holder. The surface can scan a maximum area of 400 nm x 400 nm. RHK Technology provides a program (XPMPro 2.0.1.6) to control the tip, acquire data and analyse images.

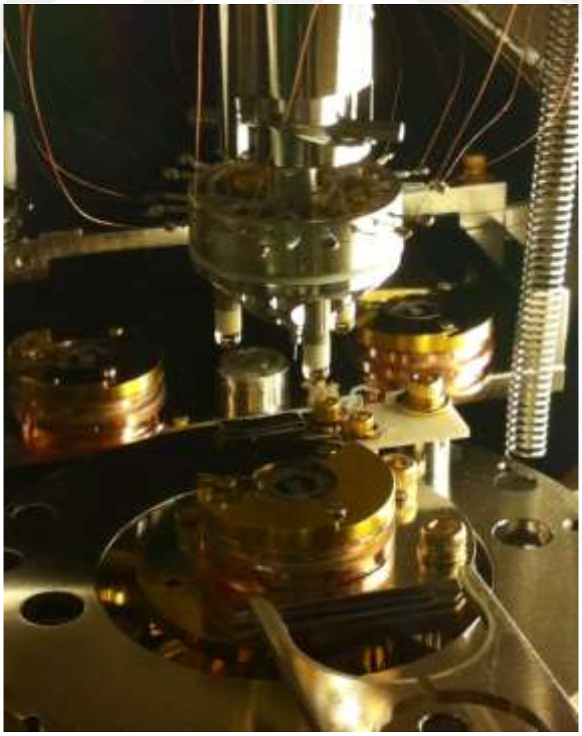

Figure 34. *Beetle-type* STM head, tip, piezo legs, and sample holder.

2.5 Sample Prepation

To obtain the Au(111) surface, Au is first deposited onto a HOPG substrate by thermal evaporation under high vacuum in an Edwards evaporator Auto 306 Turbo. This is followed by in-situ preparation of C_{60} molecules and Au atoms which are evaporated on the Au(111) surface using effusion cells in the UHV VT STM.

2.5.1 Au on HOPG

300 nm thick Au films on cleavead HOPG substrates (4 mm x 8 mm) were prepared by evaporation of 99.99% purity Au wire at 1 x 10^{-7} mbar in an Auto 306 Turbo Edwards thermal coater. The film thickness was monitored during deposition with a quartz crystal balance. The substrate was held at a temperature of 493 K during deposition to improve film quality [190]. After deposition, the sample is allowed to reach room temperature before being transferred to the UHV VT-STM system.

Further sample treatment is performed in the UHV system. The sample is first annealed by resistive heating at 1100 K for 90 mins in the sample manipulator (see Figure 32) to remove impuities and to obtain a flat surface (see Figure 35A). It is then sputtered with 1 keV Ar^{+} ions for 7 mins with a sputter current of 10-14 μA to remove impurities (see Figure 35B). This annealing-sputtering process is repeated until clean, large flat terraces (100 nm x 100 nm) are obtained in STM images of the surface, as seen in Figure 35C.

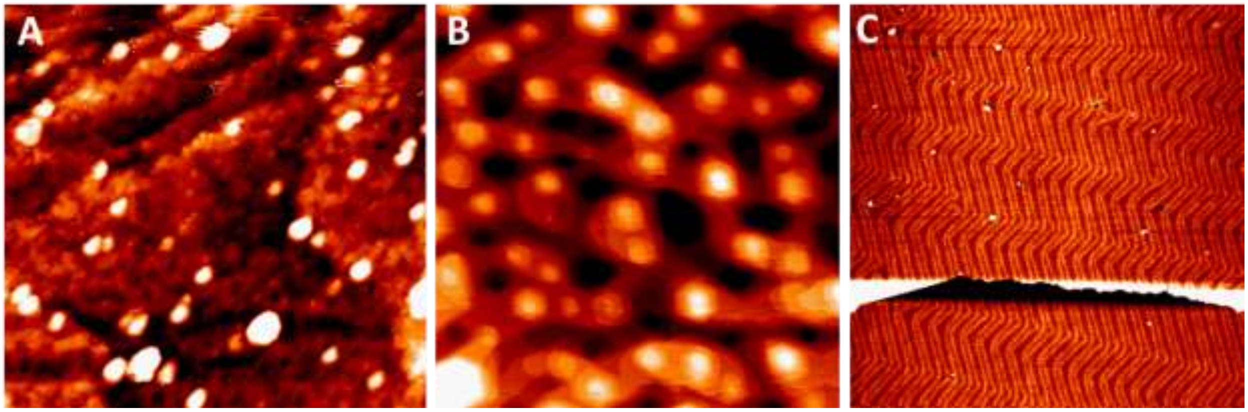

Figure 35: STM topographies for (A) the dirty Au surface (at -1.65 V, 47 pA, 44 x 42 nm^2), (B) after Ar^+ sputtering at 1 keV for 7 min (at -1.73 V, 47 pA, 105 x 105 nm^2), and (C) the clean Au(111) surface produced by annealing the sputtered surface for 2 h at 1000 K (-1.5 V, 47 pA, 182 x 186 nm^2).

2.5.2 Deposition of C_{60} Molecules and Au Atoms on the Au(111) Surface

To obtain $(C_{60})_m$-$(Au)_n$ clusters on the Au(111) surface, C_{60} molecules and Au atoms are deposited in-situ on the surface at different amounts and sequences. Au wire with 99.99 % purity placed in an alumina cirucible and evaporated at 1373 K from an effusion cell (purchased from CreaTec). The deposition is pricisely controlled using a shutter on the evaporator and measuring temperature with thermocouples. Here the Au deposition rate is 0.018 ML/min estimated direcly from STM images. For C_{60} deposition a home-built effusion cell is used with a tantalum foil crucible and K-type thermocouple to measure the foil temprerature (see Figure 32B). C_{60} moleucles are evaporated at 673 K at a base pressure of around 10^{-9} mbar and a deposition rate of 0.045 ± 0.003 ML/min which has been estimated direcly from STM images. Both evaporators were outgassed extensively prior to use. The surface is checked before and after every C_{60} or Au deposition by STM to ensure that C_{60} and/or Au have been successfully deposited.

2.6 Surface Prepration and Molecules Dosing

2.6.1 Si(111)-7x7 Surface Prepration

P-type (phosphorus doped) single crystal silicon wafers, which are (111) oriented, 100 mm diameter, 500-550 μm thickness, and 0.01-0.02 Ωcm resistivity (made by SILTRONIX), have been used for the local and non-local PhCl desportion experiments. A 2 mm x 9 mm wafer is cut using a diamond cutter and is placed onto the sample holder. Here the silicon wafer is placed on a ceramic washer and connected to the sample holder body with tantalum plates which allows a direct current to be applied throguh the sample for resistive heating. Before loading the sample into the load-lock, N_2 gas is used to blow off any particles or dust from the sample. After loading, the sample is degassed for 12 hours at 873 K by direct current heating to remove contamination from the surface. To obtain the Si(111)-7x7 reconstraction, the sample is flashed three times for 20 seconds each at 1473 K, followed by a final flash for 5 seconds at 1473 K and then annealed at 1233 K [89]. In order to calibrate these flashing and annealing temperatures to the applied current, the current power supply is incremented while the temperature is measured using an infrared pyrometer. Before starting the experiment, the sample was left for 3 hours to cool down to room temperature.

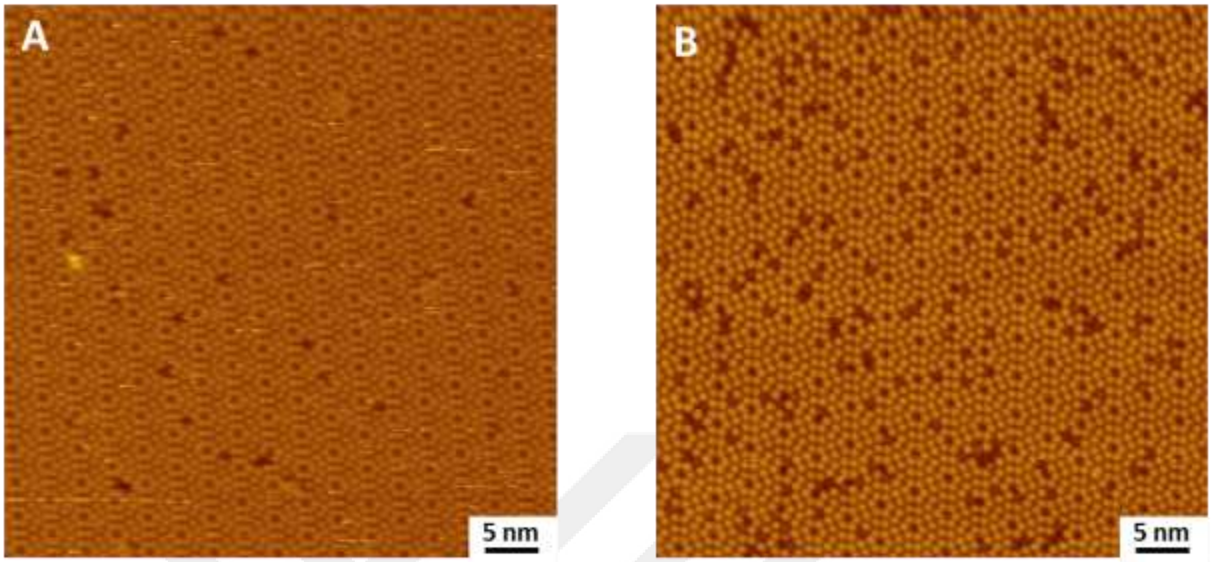

Figure 36. Clean Si(111)-7x7 surface images. A. A phosphorus doped (n-type) surface (500-550 μm thickness and 0.01-0.02 Ωcm resistivity) B. A boron doped (p-type) surface (380 μm thick and 1-30 Ωcm). Both images were taken in constant current mode at +1.0 V, 500 pA, over a 40 nm x 40 nm area.

Figure 36 shows a reconstructed Si(111)-7x7 of 40 nm x 40 nm in size. P-type silicon wafers have fewer surface defects than n-type wafers. Therefore, the statistical errors due to the surface defects are reduced and a p-type Si wafer was used for all experiments.

2.6.2 Molecule Dosing on the Si(111)-7x7 Surface at RT

For the local and non-local manipulation experiments chlorobenzene (PhCl) and oxygen molecules were dosed on the Si(111)-7x7 surface at RT. A laboratory bottle (1L) of oxygen gas was purchased from Argo International Ltd. with 99.6% purity (typical analysis of 0.4% is TCH (as CH_4) < 20 vppm and H_2O < 3 vppm). PhCl (Sigma-Aldrich) was diluted to 2% in 18.2 mL distilled water and 20 mL was decanted into a test tube with a DN16 conflat flange on one end. Both the PhCl tube and O_2 bottle were connected to the valves, V9 and V10, respectively (see Figure 33). The “freeze-pump-thaw” process must be conducted to pump some undesirable gases out and purify the PhCl gas in the tube. Cooling PhCl reduces the solubility of gas in the liquid, these gases separate out and are pumped away, PhCl luquid subsequent warming to room temperature results in purified.

To purifiy the PhCl in the tube, the load-lock first needs to be pumped. Then the valve V7 was opened and the gas line pumped to below 10^{-6} torr. The next process was to freeze the PhCl in the tube by submerging it in liquid N_2 and then thawing it in tap water. The thawing must be done carefully because the fast temperature change may break the tube. This freezing and thawing process was continued until no bubbles were observed in the tube (this may require 3-4 cycles). The purity of the PhCl gas can be tested via the mass spectrometer in the UHV system via filling the gas line with PhCl gas. Once this process was completed the PhCl was ready for dosing the sample surface.

The dosage of PhCl and O_2 were controlled and monitored using a LabVIEW program. The gas line is connected to the STM chamber with a leak valve that is controlled by a stepper motor. The LabVIEW program controls the amount of the molecules that are introduced in the chamber. Gas dosages are expressed in Langmuir (1 L=1 x 10^{-6} torr s) by multiplying the pressure (below 8 x10^{-8} torr) of gas by the time of exposure.

2.6.3 Analysis Methods and Programs

Image analysis was done by three separate purpose-written MATLAB programs. These address finding silicon atoms and PhCl molecules on an Si(111)-7x7 surface, locating the tip position on the surface, and the non-local desorption analysis. Si adatoms image as orange protrusions and PhCl molecules images as black depressions in STM images.

To find molecules on the surface, the program considers the image as a 2D matrix. The user can select a region and manually or automatically choose basis vectors over three corner holes in the raw image (see inlet Figure 37A). With the three selected corner hole sites, the program can identify Si atoms (bright colour) and PhCl molecules (dark colour) and count them (see Figure 37C). Moverover, defect areas on the surface or erroneously identified molecules could be selected and cut from the image. Misassigned adatoms and molecule sites could also be corrected.

After the molecules were mapped in the images taken before and after the experiments, the injection site (on a corner hole) could be found in the second program (black dots on Figure 37A and B). For non-local desorption analysis, ten experiments were performed for each measurements. The data were binned in 10 Å radius intervals. The error of distribution were calculated based on the binominal distrubution. By counting molecules (red circles) and silicon adatoms (yellow circles) in the images before and after injection (see Figure 37C and D) the probabilty of the desorption of PhCl can be calculated and the result saved into an output file.

After mapping molecules (i.e. counting PhCl molecules on the surface), the desorption probability $P(r) = N(r)/N_0(r)$ is calculated by comparing molecules before injection N_0(r) and molecules that have moved on the surface after injection N(r). In this process, there are roughly 1300 PhCl molecules and 3500 silicon atoms in a 51.2 nm x 51.2 nm image. When we compare the images taken within a 51.2 nm x 51.2 nm square, the matched maximum radius is about 250 Å. Therefore, the probability of non-local desorption is omitted after 250 Å for all data taken at different injection currents.

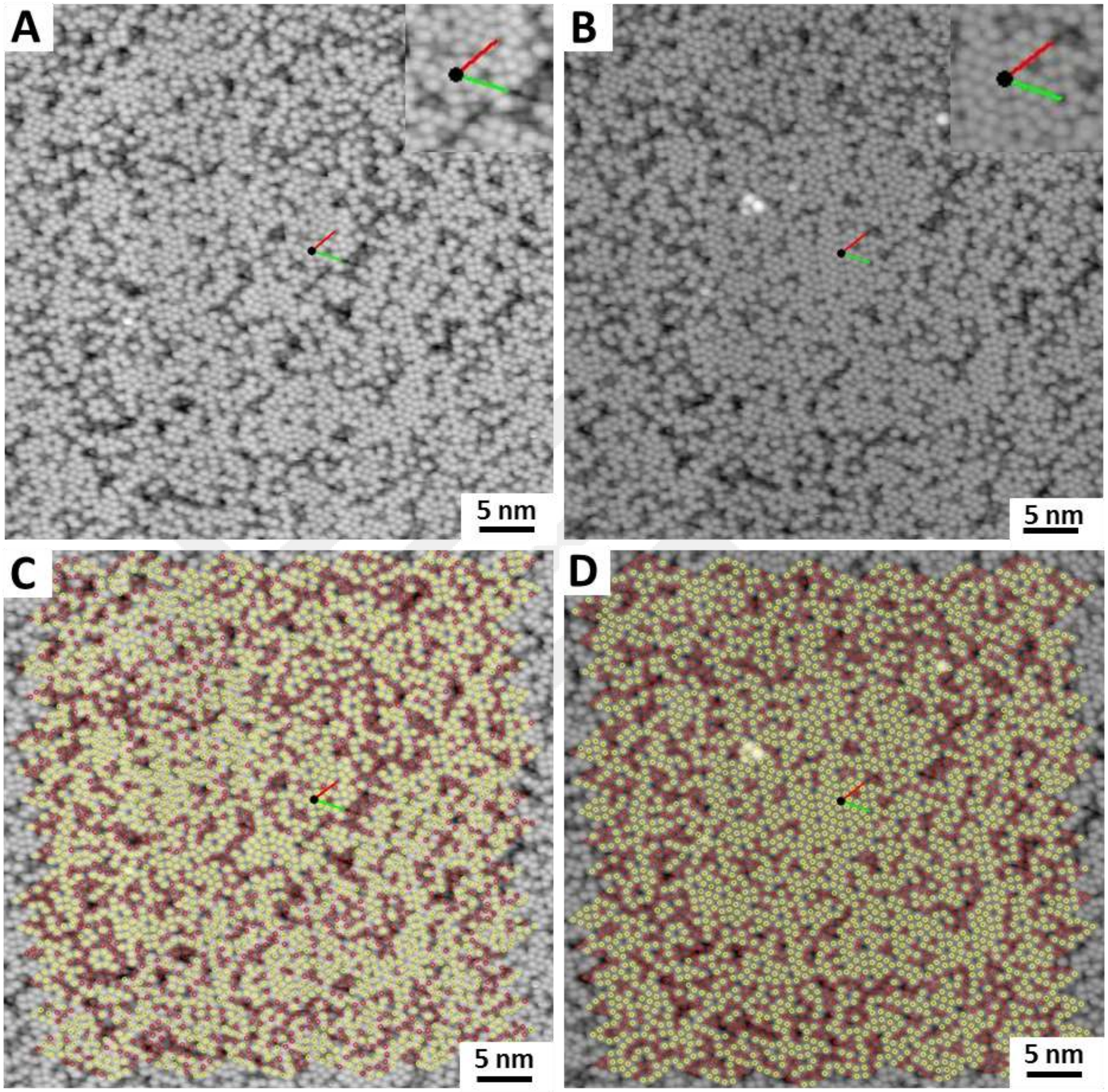

Figure 37. Non-local desorption experiment analysis programs. A. Before injection image with injection site (black dot) and inlet: unit vector (green and red line). B. After injection image with with injection site (black dot) and inlet: unit vector (green and red line). C and D. Counted molecules on the surface, red and yellow circles indicate PhCl molecules and the surface adatoms.

2.6.4 Desorption Probability Calculation

For the non-local desorption experiment, one of the important experimental errors may come from thermal desorption of PhCl molecules at room temperature during the experiment [35]. For thermal correction [191], 8 L of PhCl molecules were dosed on the Si(111)-7x7 surface and the STM images of the same area (51.2 nm x 51.2 nm) were recorded over a 1 h. This experiment was repeated three times for up to 35 minutes each time and thermal desorption could be observed after each scan. In order to account for the number of thermal desorption events, the time spent during each simulated desorption experiment was measured and matched against the comparable thermal desorption experiment. The number of the thermally desorbed molecules could be subtracted from the number of PhCl molecules before and after the injection at each annulus. Then the non-local desorption probability is calculated as described below.

Sloan *et al.* [39] investigated the non-local desorption probability formula per electron, taking into account background effects (i.e. thermal desorption, clean surface defects). The formulas used are presented below.

$$\frac{dN(r)}{dt} = -k_e N(r) a(r).$$

This equation is the change in the number of molecules (*N(r)*) over time at radius r from the injection site. Here *a(r)* is the number of injected electrons that impinge on a molecule per second and is given by;

$$a(r) = \left(\frac{sIL}{e2\pi r}\right) f(r).$$

Here, *f(r)* is the radial decay of the surface current, *L* is the cross section of a PhCl molecule (taken to be 5 Å), and *s* is the fraction of the current conductivity from the ratio of the surface to bulk (taken to be 1). Combining them and integrating, $k_e f(r)$ is given by;

$$k_e f(r) = -(e2\pi r ln[N(r)] - ln[N_0(r)])/stIL.$$

$N_0(r)$ is the number of molecules remaining on the surface after charge injection.

The defects, which are imaged as dark spots, will be counted by the atom-finding program. Most of the defects come from the doping (boron-phosphorus atoms) which comes out after the reconstruction process. This is why we need to subtract these dark spots generated by surface defects from the raw desorption data. For this reason, 4 clean surface images were taken by STM before the PhCl dosing, then the average dark spots on the clean Si(111)-7x7 surface can be counted. The number of the dark spots in the annulus *B(R)* (between *R* and *r*) is given by;

$$B(R) = \frac{number\ of\ dark\ spots}{number\ of\ adatom\ sites} \times \frac{outer\ area\ (R) - inner\ area\ (r)}{the\ area\ of\ the\ unit\ cell}$$

$$B(R) = \frac{number\ of\ dark\ spots}{number\ of\ adatom\ sites} \times \frac{\pi R^2 - \pi r^2}{A_{site}}$$

Here, *R* and *r* are the outer and inner radii, respectively. The ratio of dark spots to adatom sites is counted from the clean surface images and A_{site} is given by,

$$A_{site} = \frac{A_{unit\ cell}}{12\ (adatom)}.$$

Here, $A_{unit\ cell}$ is the area of the Si(111)-7x7 unit cell, and A_{site} is the area per silicon atom. The final process is subtracting *B(r)* from the number of molecules before and after injection using:

$$k_e f(r) = -e2\pi r ln[\frac{N(r)-B}{N_0(r)-B}]/stIL.$$

Finally, the probability of desorption of a PhCl molecule is obtained after subtraction of the thermal and clean surface defect populations. Figure 38 shows the plot of the non-local desorption probability for a 1 nA electron injection experiment (sample biased at +2.7 V and electron injection for 3.2 s). The raw data before subtraction and after thermal and clean surface subtraction is plotted as in the black and the red curves, respectively. The artificial increase of desorption after 150 Å is removed by the subtractions.

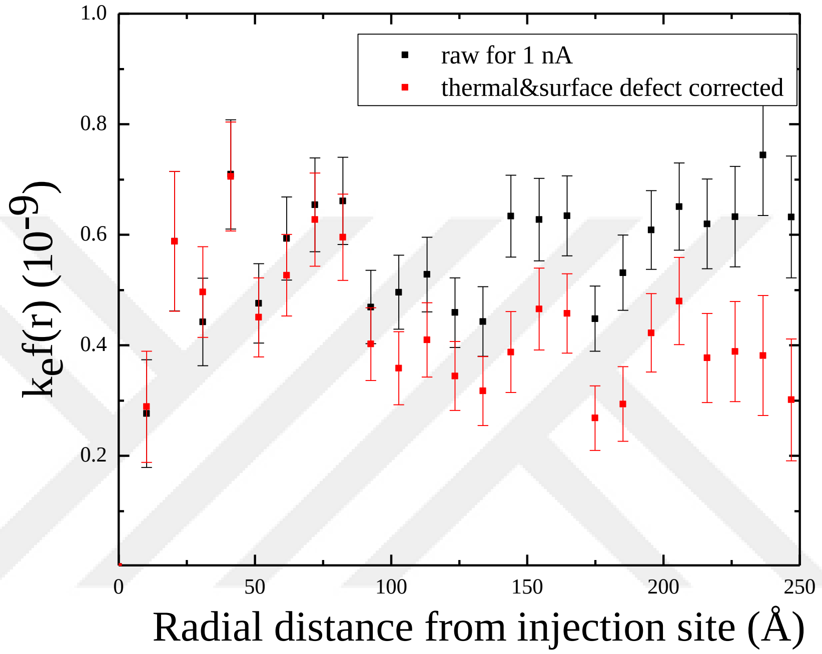

Figure 38: Non-local desorption probability analysis with raw data for the injection of electrons at 1 nA for 3.2 second with a sample bias of +2.7 V. The black points show raw data, and the red points show the data after correction for thermal desorption and surface defects.

CHAPTER 3

IMAGING HYBRID $(C_{60})_m$-$(Au)_n$ CLUSTERS ON an Au(111) SURFACE

In this chapter, the formation of hybrid clusters, as well as the rotation and transformation of clusters are presented in detail. First, the behavior of individual Au atoms and C_{60} molecules on an Au(111) surface at low temperature with a view to understanding the basic process of cluster formation and their spatial distribution on the FCC and HCP regions will be studied. The C_{60}/Au ratio is altered systematically by keeping the amount of deposited Au at a constant 0.036 ML and increasing the amount of C_{60} molecules. The idea was to find an optimized C_{60}/Au ratio for a particular sized cluster size, and hence improve the selectivity of the growth process.

3.1 Adsorption of C_{60} Molecules and Au Atoms on the Au(111) Surface

3.1.1 Adsorption of C_{60} Molecules on the Au(111) Surface at 110 K

C_{60} molecules have a relatively high mobility on the Au(111) surface at room temperature due to the weak interaction (van der Waals force) with the surface atoms, therefore, C_{60} molecules deposited at room temperature tend to diffuse long distances on the Au(111) surface and congregate at step edges. If deposited at low sample temperature (less than 200 K), C_{60} molecules can become trapped at the potential wells provided by the defects at elbow sites. However, once a second C_{60} molecule arrives due to continuous deposition of the C_{60}, the elbow site does not offer enough space to permanently hold the second C_{60}. Therefore, the second molecule tends to move away from the initial, single C_{60} molecule and finds another site, such as an empty elbow site, step edge or a big C_{60} island. In this study, the deposition of C_{60} molecules for all experiments is carried out at 110 K.

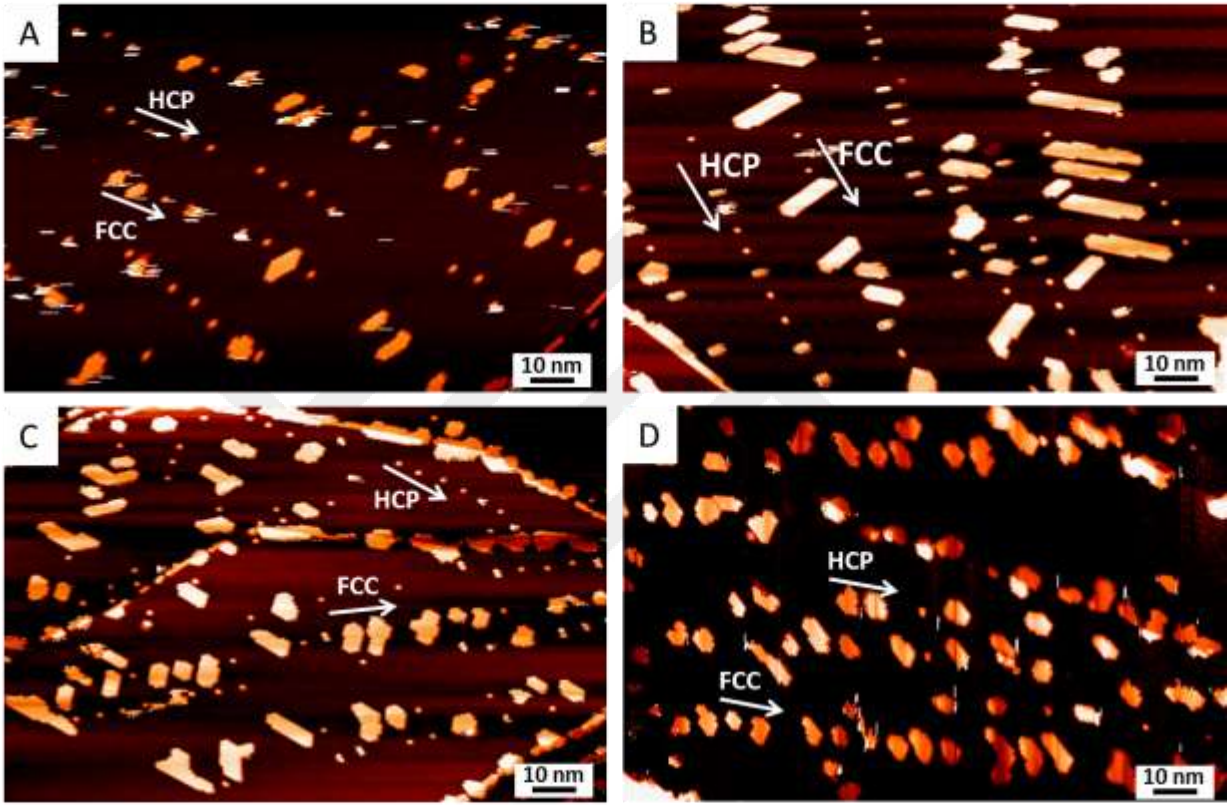

Figure 39: STM topographies are for different C_{60} molecule coverage on an Au(111) surface at 110 K, 0.036 ± 0.003, 0.072 ± 0.005, 0.108 ± 0.008, and 0.144 ± 0.010 ML, illustrated in images A, B, C, and D, respectively. Major FCC and HCP regions indicated with white arrows. The islands growth increases with increasing coverage on the FCC region, but the occupancy at the HCP region remained mostly single, or at most with only few C_{60} molecules, until the coverage reached 0.144 ML.

Figure 39 shows STM images, taken with different C_{60} coverages of the Au(111) surface using a tip bias of -1.97 V and a tunnelling current of 47 pA at 110 K. The coverages are 0.036 ± 0.003, 0.072 ± 0.005, 0.108 ± 0.008, and 0.144 ± 0.010 ML, in Figure 39A, B, C and D, respectively. The major FCC and HCP regions are indicated by the white arrows on the images.

During the deposition process, C_{60} molecules land randomly on the Au(111) surface. They have sufficient energy to diffuse along the surface until they are trapped at either an elbow site or step edges. The elbow site and the step edges have higher electron densities and are thus able to trap the molecules due to efficient charge transfer to the electronegative molecules and the subsequent formation of a chemical bond. As the surface coverage increases, growth on the FCC region increases much more quickly than on the HCP region. This is because the growth at the FCC region is more energetically favorable, having a higher surface potential energy and being wider than the HCP region [122]. Mostly, the C_{60} molecules either grow and become large islands or remain as isolated molecules at the elbow site. First, these large islands capture individual C_{60} molecules, diffusing on the surface with the strong attractive C_{60}-C_{60} force. On the other hand, because of an atomic defect at the elbow sites, the single C_{60} molecules prefer to sit as isolated moleculates at such a site. Therefore, most of the time, it is only a single C_{60} molecule which is immobilized at an elbow site. The growth was observed mostly on the pinched elbow sites for all coverages used.

In Figure 40A and B, the area selection of the STM images are presented for 0.036 ± 0.003 ML, 0.108 ± 0.008 ML C_{60} molecules coverage on the Au(111) at 110 K. The white arrows indicate the growth at the FCC and HCP elbow sites for both coverages. In Figure 40B, the formation of single and trimer C_{60} islands on the HCC elbow site are circled in red and yellow, respectively. At low coverage (e.g. 0.036 ML), both the FCC and HCP elbow sites prefer to capture a single C_{60} molecule. Additional C_{60} molecules are highly mobile around this single C_{60} island. This is because a single atomic defect on the surface can only capture single C_{60} molecules; therefore, a single C_{60} molecule is much more stable than a C_{60} dimer or trimer at an elbow site. Adding more C_{60} molecules to the surface leads to the molecules preferentially migrating into the FCC region, while the HCP elbow sites maintain only isolated molecule coverage. If the growth an the FCC elbow site is close to an HCP region, only a single C_{60} molecule is generally observed (the red circle) on the HCP elbow site. The fast growth on the FCC elbow site prevents the growth on the HCP elbow site due to the strong van der Waals interactions between C_{60} molecules. However, there is a possibility that the single C_{60} molecule can capture additional C_{60} molecules and from dimer or trimer islands (the yellow circle). However, if there is a nearby large island growth at an the FCC elbow site, the C_{60} molecule remains single. We observed that the close-packing directions of C_{60} islands, A, B, and C are found by using the surface $[11\bar{2}]$, $[01\bar{1}]$, and $[1\bar{1}0]$ directions.

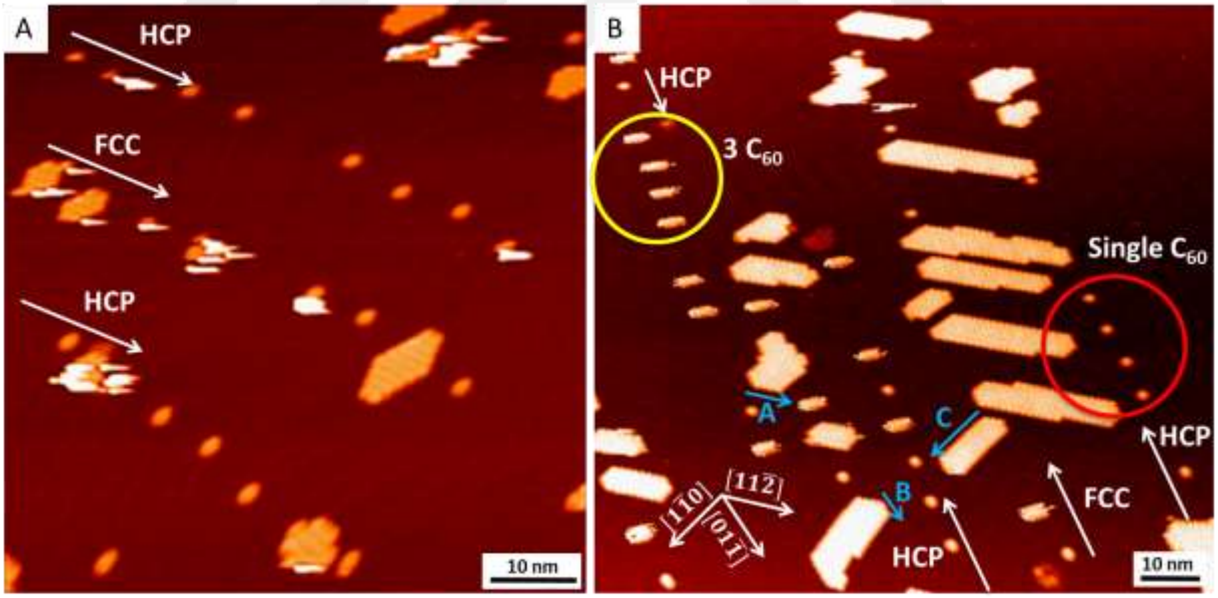

Figure 40: The area selection of the STM images from Figure 39, with 0.036 ± 0.003 ML and 0.108 ± 0.008 ML C_{60} molecule coverage on the Au(111) surface at 110 K, as illustrated in A and B, respectively. Single C_{60} and trimer islands are formed on the HCC elbow sites circled in red and yellow, respectively. The close-packed directions of the C_{60} islands, A, B, and C are found using the surface $[11\bar{2}]$, $[01\bar{1}]$, and $[1\bar{1}0]$ directions, respectively.

When C_{60} molecules land on the surface at 110 K, the molecules prefer to attach to large islands, rather than elbow sites or small C_{60} islands. This is because the strong interaction (van der Waals force) between the C_{60} molecules and the island occupying a large area on the Au(111) surface. Therefore, there is a tendency to favour attachment to, and hence the growth of, large islands rather than small islands. Deposition of C_{60} molecules at 30 K and 46 K results in different size and site distributions [146]. Because of the increased temperature of the surface, the C_{60} molecules are more mobile when they land on the surface. Thus, the molecules can diffuse longer distances and will tend only to become trapped at either step edges or big C_{60} islands.

3.1.2 Size Distribution of C_{60} Molecular Islands

In this section, a systematic study will be carried out on the growth of C_{60} islands on an Au(111) surface at 110 K. The adsorption of C_{60} molecules shows different behavior across the surface with as the potential energies and the surface depth of the FCC and HCP elbow sites. Therefore, the size distribution of the C_{60} island is studied as a function of surface coverage at 110 K. Figure 41 illustrates the normalised size distribution of C_{60} islands via counts of counting the number of C_{60} molecules in each island on each FCC elbow site. The molecules were counted as a function of increasing coverage, 0.036 ± 0.003, 0.072 ± 0.005, 0.108 ± 0.008, and 0.144 ± 0.010 ML, as panels A, B, C and D, respectively. More than 150 molecular islands were counted from several images and the frequency is normalised by dividing the number of C_{60} molecule each island to the total number of island in unit area.

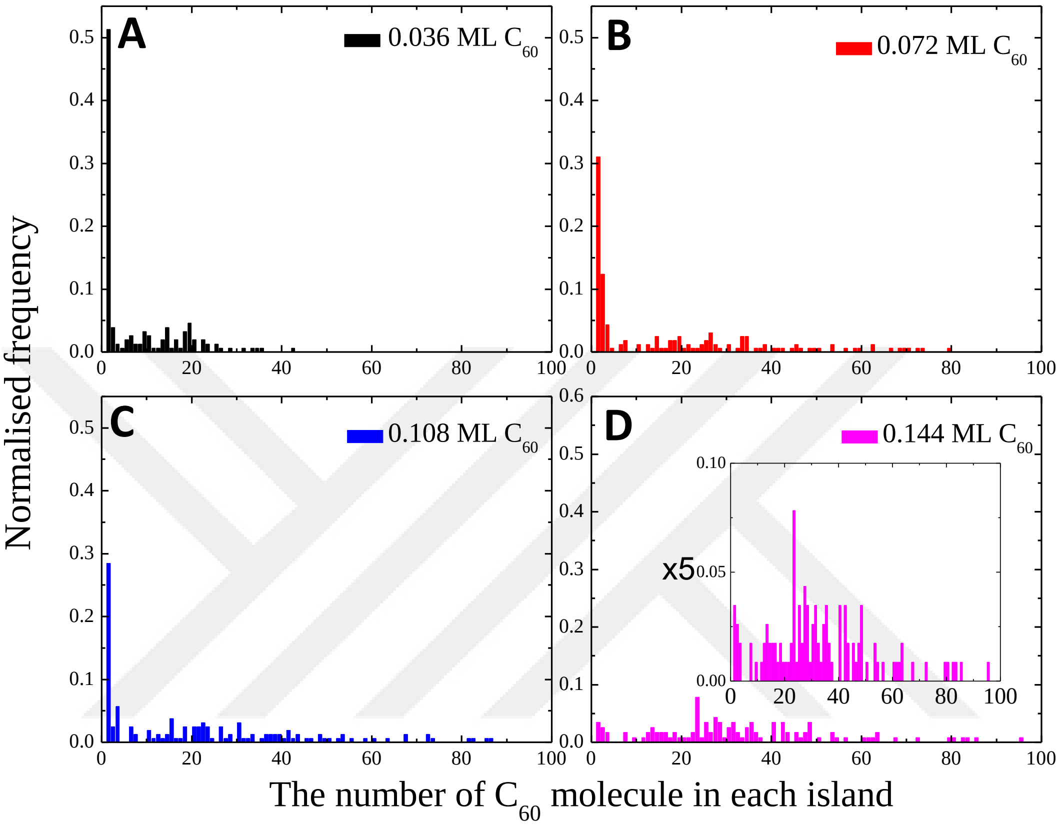

Figure 41: The normalised size distribution of C_{60} molecules at 110 K on FCC elbow sites for different coverages, 0.036 ± 0.003, 0.072 ± 0.005, 0.108 ± 0.008, and 0.144 ± 0.010 ML, for panels A, B, C and D, respectively. Increasing C_{60} coverage increases the extent of the size distribution and decreases the number of smaller C_{60} islands. An inlet-magnified distribution of 0.144 ML coverage is presented in D.

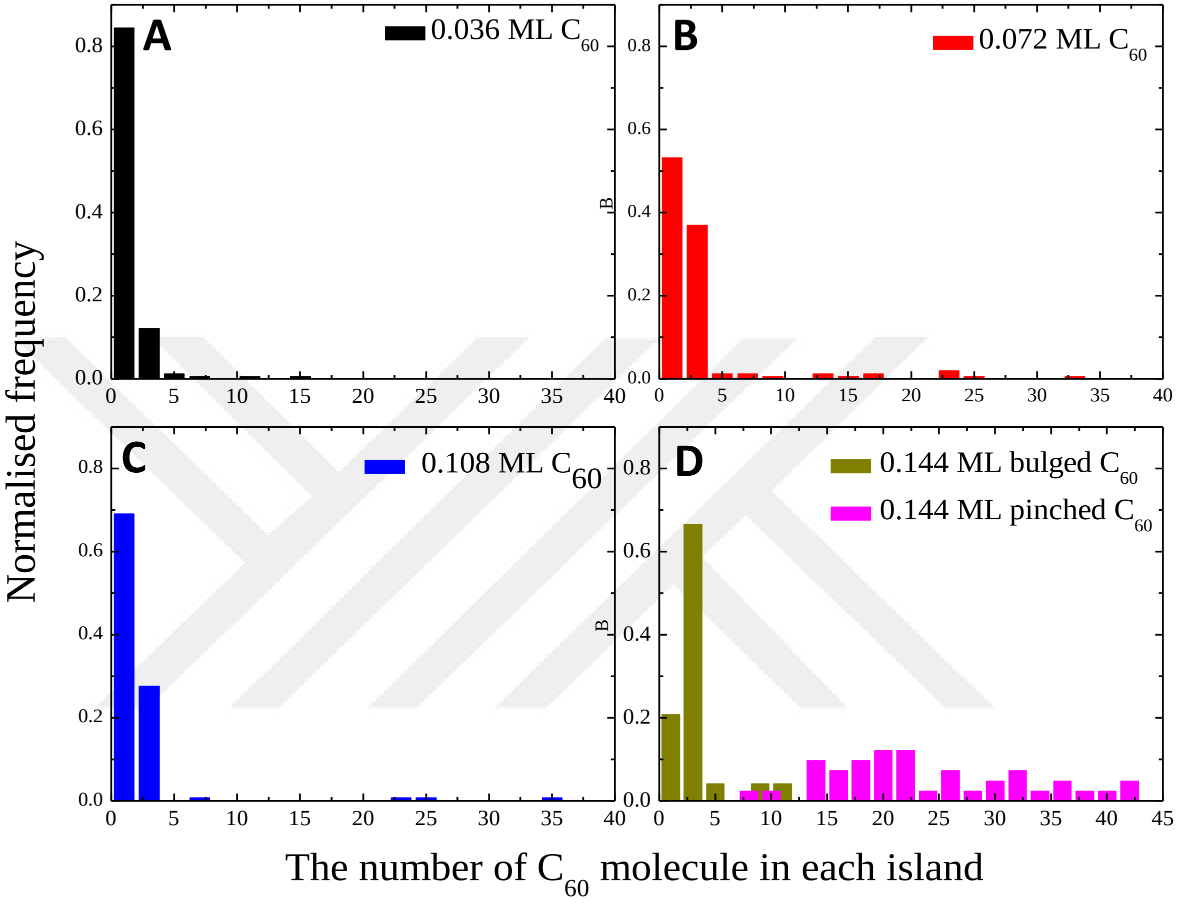

Figure 42: Panels A, B, C and D shows the normalised size distribution of C_{60} molecules at 110 K on the HCP elbow sites at different coverages of 0.036 ± 0.003, 0.072 ± 0.005, 0.108 ± 0.008, and 0.144 ± 0.010 ML, respectively. Increasing C_{60} coverage decrease the number of small C_{60} islands on the HCP elbow sites and increase the growth on the HCP bulged elbow site.

At 0.036 ML coverage, for the most part only single C_{60} molecules are observed, with a broad tail up to about 40 C_{60} molecule islands. It is found that approximately half of the islands on the surface are single C_{60} molecules on the FCC elbow sites for this lowest coverage. Increasing the amount of C_{60} molecules decreases the number of single C_{60} islands and increases the range of sizes seen in the distribution. As shown in Figure 43B, C, and D, increasing coverage increases island size and the extent of the size distribution, whilst simultaneously showing a reduced number of single C_{60} molecules. The percentage of single C_{60} islands for all coverages is presented in Figure 43. The percentage decreased from 0.51 ± 0.07% to 0.03 ± 0.02% as coverage was increased from 0.036 ± 0.003 ML to 0.144 ± 0.010 ML; at the same time, the number of C_{60} molecules forming the biggest islands was found to increase from 42 to 96.

The size distribution of C_{60} molecules (normalised as a function of surface area) on the HCP elbow site is presented in Figure 42A, B, C and D, showing the different coverages used of 0.036 ± 0.003, 0.072 ± 0.005, 0.108 ± 0.008, and 0.144 ± 0.010 ML, respectively. Increasing the C_{60} coverage decreases the amount of small C_{60} islands on the HCP elbow sites, and indeed the island that started to grow on the HCP bulged elbow site at 0.144 ± 0.010 ML coverage. The molecules in the HCP region preferentially remained single, only occasionally forming dimers or trimers. At lowest coverage, 0.84 ± 0.09% of the elbow sites are occupied with a single C_{60} molecule at the pinched elbow sites. Increasing coverage decreases the amount of single C_{60} molecules at the HCP elbow sites with the larges C_{60} islands being observed at 0.144 ± 0.010 ML coverage. Eventually, C_{60} growth starts at the HCP bulged and pinched sites, with the highest C_{60} coverages found on the surface.

Figure 43 illustrates the percentage of single C_{60} islands on the FCC and HCP elbow sites as a function of increasing C_{60} coverage. The percentage of single C_{60} islands on the FCC elbow site dramatically decreased with increasing coverage. The general trend of the percentages for the HCP elbow sites also decreased same trend.

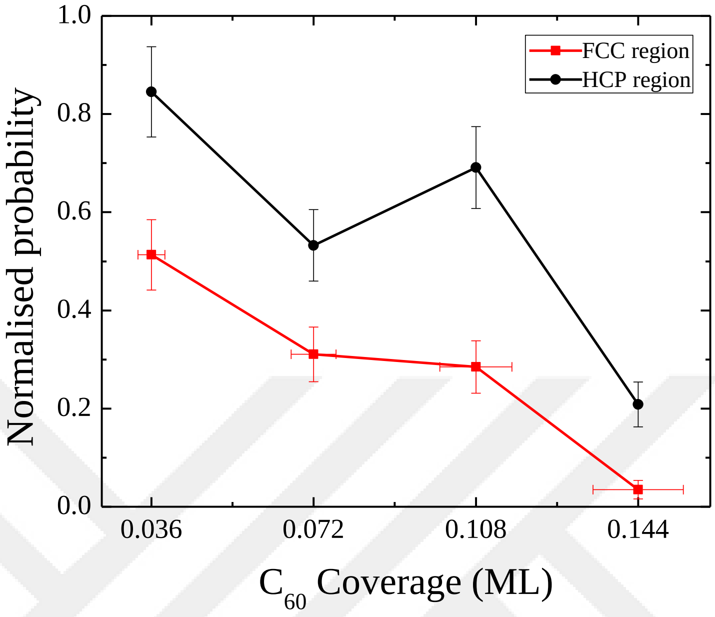

Figure 43: The normalised probability of single C_{60} islands on the FCC and HCP elbow sites as a function of C_{60} coverage. The probability of founding single C_{60} molecule on the surface decreases with increasing coverage.

3.1.3 Au Atoms on Au(111) Surface at 110 K

Au atoms on the Au(111) surface move to the step edges due to their high mobility at room temperature. At 110 K, the Au atoms preferentially stay at the FCC or HCP elbow sites. In this experiment, a coverage of 0.036 ± 0.006 ML of Au atoms was held constant whilst increasing the number of C_{60} islands on the surface to produce the hybrid cluster. In Figure 44, the STM topographies presented show a 0.036 ± 0.006 ML coverage of Au atoms on the Au(111) surface at 110 K. Figure 44A shows a 134 x 114 nm^2 area, which illustrates the Au atoms situated on the FCC and HCP elbow sites. The region in Figure 44B shows a 57 x 57 nm^2 area selected from that shown in Figure 44A and illustrates the FCC and HCP regions with surface directions. Au atoms are trapped by FCC and HCP elbow sites (excluding step edges).

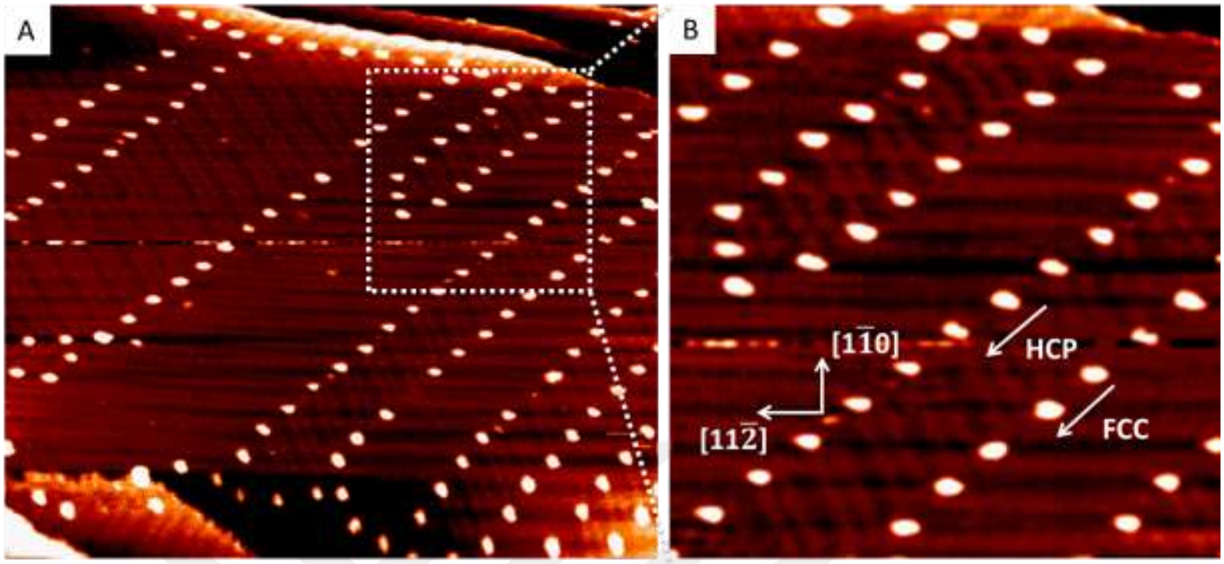

Figure 44: The STM topographies for a 0.036 ± 0.006 ML coverage of Au atoms on the Au(111) surface at 110 K. A. 134 x 114 nm^2 area showing Au atoms at FCC and HCP elbow sites. B. A selected 57 x 57 nm^2 area from panel A showing Au atoms at the FCC and HCP regions with surface directions.

3.1.4 Size Distribution of Au Atomic Islands

Most observed hybrid clusters contain two-dimensions islands of 19, 35, 49, and 63 Au atoms as suggested in ref. [14]. The Au coverage and deposition parameters remained constant for all experiments (0.036 ± 0.006 ML deposited on a Au(111) surface at an 110 K substrate temperature). The estimated areas of different sizes of Au islands, which are formed as hybrid clusters, are presented in Table 4. The estimated areas on the surface range from 1 to 4 nm^2 depending on the number of Au atoms.

After Au atoms are exposed to the Au(111) surface surface at 110 K, the area of the Au islands at the elbow sites are measured using the ImageJ image analysis program. The island sizes are binned in 0.4 nm^2 intervals, and the frequency is normalised by dividing the number of Au islands to the total number of island. The distribution fitted with Lorentzian multi-peaks. The blue line shows first four peaks at around 0.62, 1.40, 2.60, and 3.39 nm^2. The calculated Au island areas are in rough agreement with the measured areas of 2.60, and 3.39 nm^2.

Table 4: The number of Au atoms in most observed hybrid clusters and estimated areas on the surface.

Clusters	Au atoms	Au radius (nm)	Estimated Area (nm^2)
$(C_{60})_7$-$(Au)_{19}$	19	0.135	1.09
$(C_{60})_{10}$-$(Au)_{35}$	35	0.135	2.00
$(C_{60})_{12}$-$(Au)_{49}$	49	0.135	2.80
$(C_{60})_{14}$-$(Au)_{63}$	63	0.135	3.61

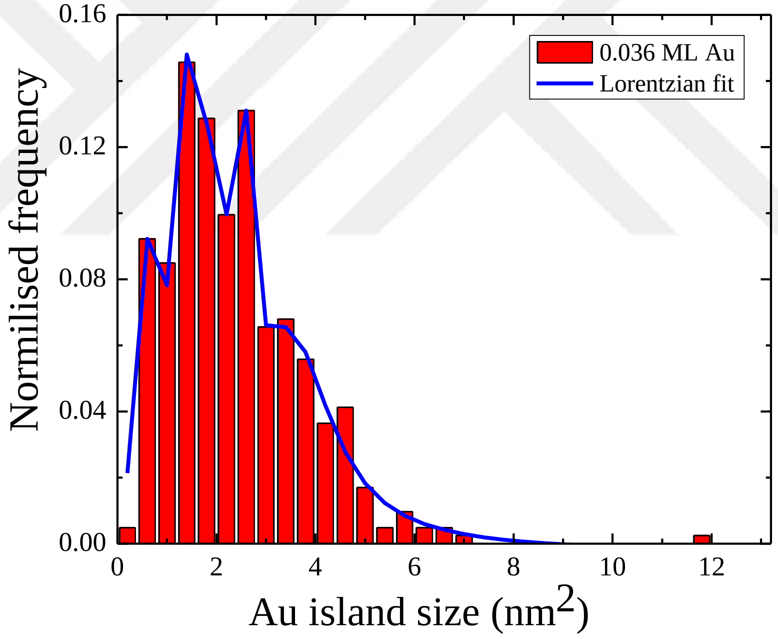

Figure 45: The normalised size distribution of Au atoms on the elbow sites at 110 K with a 0.4 nm^2 binning interval. The dark blue line is Lorentzian multi-peaks. The blue line shows first four peaks at around 0.62, 1.40, 2.60, and 3.39 nm^2.

3.2 Cluster Formation

This study focuses on understanding hybrid cluster formation in order to obtain further control over cluster formation. The ultimate aim is to produce one type of cluster across the entire surface. For this reason, after deposition, a single area was followed as the temperature the surface was raised from 110 K to 294 K to observe cluster formation as a function of elevated temperature. Figure 46 shows STM topographies of the observed area from 110 K, panels A and B, to 294 K, panels C and D. Deposition of the C_{60} molecules and then Au atoms at 110 K causes the formation of irregular clusters, whilst individual Au islands form at the empty elbow sites. The individual Au islands disappeared at around 160 K and clusters started to become compact at around 200 K. When the substrate temperature was brought to room temperature, only the hybrid clusters remained on the surface. In this section, unless stated otherwise, all images are taken with a -1.93 V tip bias and a 47 pA tunnelling current.

After C_{60} deposition, Au atoms were deposited on the surface and migrate under or around irregular C_{60} islands, or to empty elbow sites. In Figure 46 B and E, the blue rings show individual Au islands at the elbow site. The pink arrow shows Au atoms at the side of the C_{60} island in Figure 46B. The irregular clusters, circled in green in Figure 46C, are Au atoms located under C_{60} islands. Au atoms can diffuse on the surface at 110 K, but tend to stay on elbow sites whether covered with C_{60} islands or not. Once they reach a C_{60} island, the Au atoms either prefer to stay around the island or to diffuse under the C_{60} islands and sit directly on the elbow site. Au atoms under the C_{60} island results in increase the height of the C_{60} islands, which can be seen by an increase in brightness on the associated STM images (Figure 46C the green circle). To form a cluster, both C_{60} islands and Au atoms must combine. Additionally, individual Au atoms and C_{60} islands may diffuse to step edges as temperature increases (the blue and green circle in Figure 46 E and F, respectively).

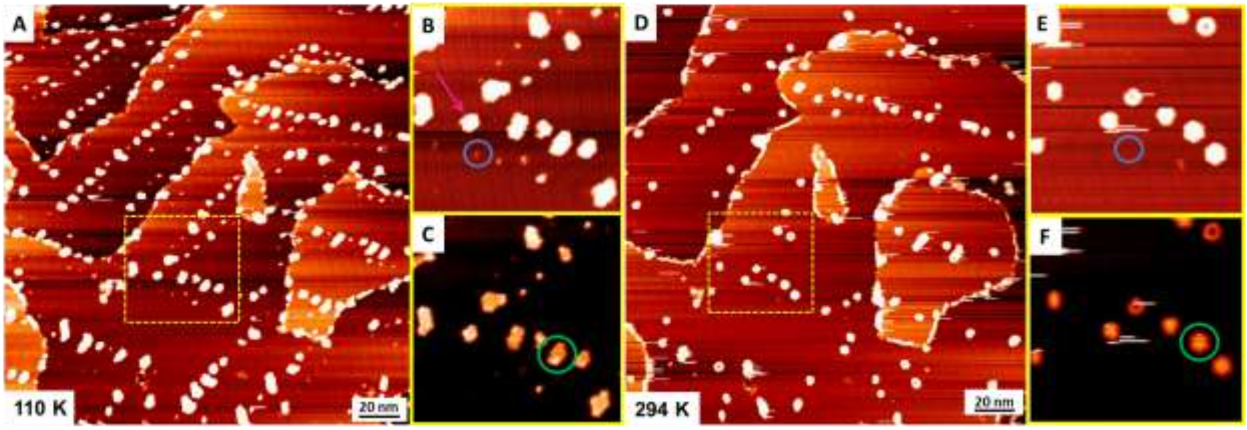

Figure 46: A surface area followed from 110 K, panels A, B and C, to 294 K, panels D, E and F. All images are recorded with a tip bias of -1.93 V and a tunnelling current of 47 pA. Evaporating first C_{60} molecules and then Au atoms at 110 K results in individual Au islands (blue circle) and formation of irregular clusters with Au atoms which have diffused under a C_{60} island (green circle). The pink arrow shows Au atoms at the side of the C_{60} island. Once the substrate temperature is brought to room temperature (D), the clusters become compact form. Here, the blue ring illustrates an removed Au island (E), whilst the green circle illustrates compact cluster (F).

The proof of cluster formation comes from the modified behavior of the Au atoms and C_{60} molecules; Figure 47 provides a good example of this. Two irregular clusters were followed from 110 K (Figure 47A) to 289 K (Figure 47K). The first is a large C_{60} island with a small Au island underneath it. The second is with a single C_{60} molecule and small number of Au atoms. Increasing the substrate temperature increases the thermal energy of C_{60} molecules, thus their mobility. The big island starts to lose its outer C_{60} molecules as the temperature increases. During the temperature increase, more Au atoms diffuse under the C_{60} island and the two C_{60} molecules become bright (Figure 47D); the height of the bright C_{60} molecules is same as one Au atomic step [14]. At all temperatures, the close-packed C_{60} island are directed parallel to the surface directions ($[11\bar{2}]$, $[01\bar{1}]$, and $[1\bar{1}0]$). On the other hand, the small cluster starts to capture additional C_{60} molecules and become an open cluster (Figure 47K). Due to the increased temperature, the mobility of the C_{60} molecules increases and they diffuse along the substrate surface. These C_{60} molecules may have come either from freely diffusing molecules, or from molecules that have escaped from a nearby large C_{60} island. Finally, close to room temperature, both clusters become hybrid clusters, $(C_{60})_{10}$-$(Au)_{35}$. It can be seen that the hybrid clusters may form due to either losing or capturing C_{60} molecules with increasing temperature.

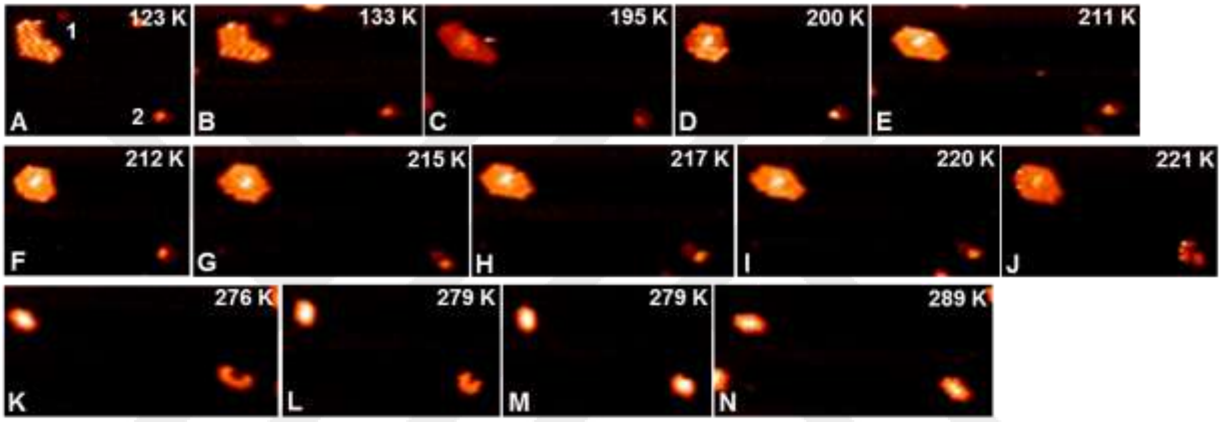

Figure 47: STM topographies to observe two examples of cluster formation with increasing substrate temperature from 123 K to 289 K. The big island (indicated as 1) formed a $(C_{60})_{10}$-$(Au)_{35}$ hybrid cluster by diffusion of Au atoms under the C_{60} island and the loss of outer C_{60} molecules. The small island (indicated as 2) with a single C_{60} and Au atoms formed a hybrid $(C_{60})_{10}$-$(Au)_{35}$ cluster by capturing mobile C_{60} molecules.

The STM topographies (250 x 250 nm^2) for a single area with time and temperature dependence are given in Figure 48A, B and C. The number of clusters on the surface is reduced as temperature is increased from 279 K to 294 K; this process continues whilst scanning same area for an hour at 294 K. The white and yellow circles indicate the clusters which have disappeared from the surface due to temperature and time, respectively. The small clusters, such as $(C_{60})_7$-$(Au)_{19}$ and $(C_{60})_{10}$-$(Au)_{35}$, are more prone to disappear. This is probably because it is easier to overcome interaction between C_{60} molecules when driven by temperature. Increasing temperature decreases the surface tension and increases the mobility of the molecules. Therefore, it was found that the cluster structure can break at 400 K [14].

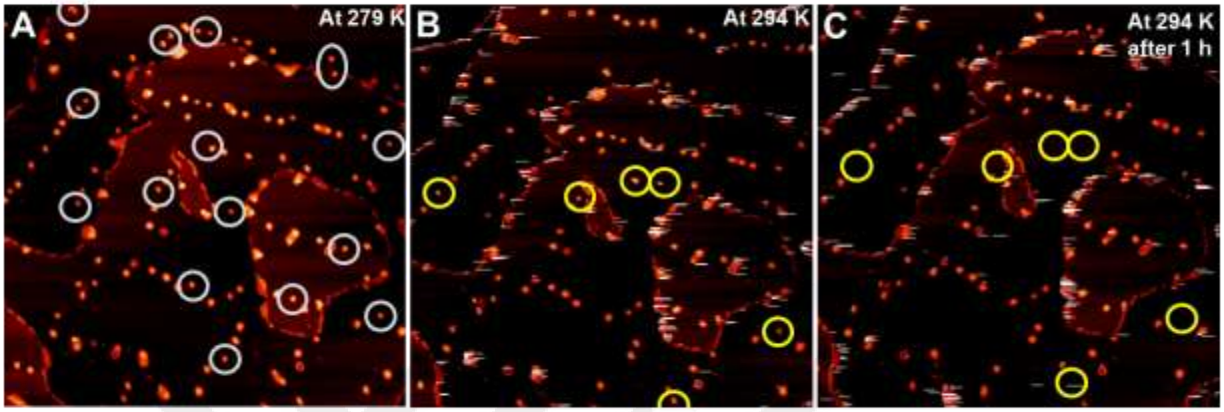

Figure 48: STM topographies (area of 250 x 250 nm^2 area) scanning the same area to show time and temperature dependence in panels A, B and C. Clusters on the surface disappeared with an increasing substrate temperature from 279 K to 294 K and were also found to disappear whilst scanning same area for about an hour, as indicated by the white and the yellow circles, respectively.

3.3 Hybrid Clusters at RT

At room temperature, the most commonly observed clusters were $(C_{60})_7$-$(Au)_{19}$, $(C_{60})_{10}$-$(Au)_{35}$, $(C_{60})_{12}$-$(Au)_{49}$, and $(C_{60})_{14}$-$(Au)_{63}$. In Figure 49A, the STM topography of a $(C_{60})_7$-$(Au)_{19}$ cluster is illustrated. This is the smallest stable cluster observed comprising of seven C_{60} molecules, six of which are located around the Au island with the remaining one located on top. The size and shape of the Au island formed by 19 Au atoms, is shown by yellow circles in Figure 49B. The structural model proposed shows optimal gold atom distances for the close-packed C_{60} island [14]. The C_{60} molecule is raised due to a single atomic layer of Au (the yellow spheres) which results in the topmost cluster showing a bright feature in the associated STM image. Here, the blue and purple atoms are the first and the second layers of the Au(111) surface, respectively. The green atoms are the first layer of the Au(111) surface atoms, which interact with the six C_{60} molecules around the cluster.

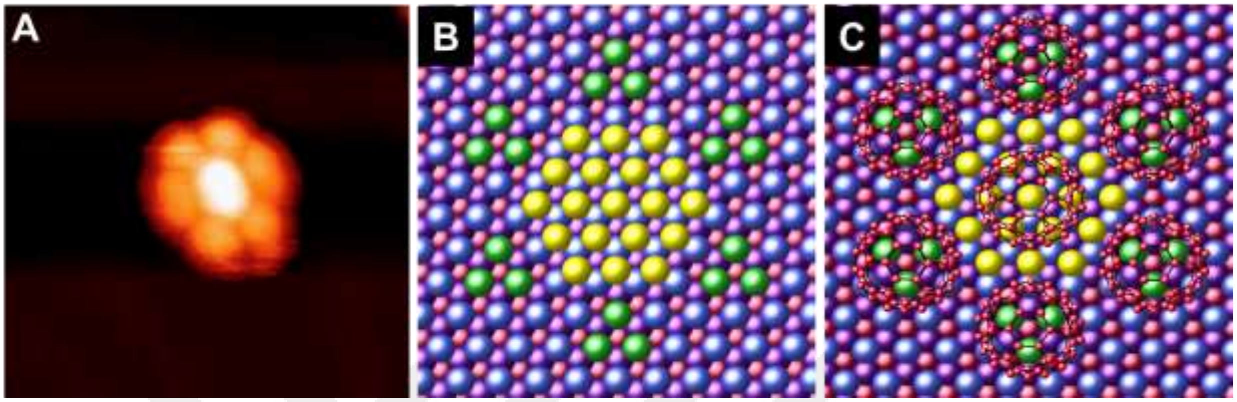

Figure 49: A. STM topography of $(C_{60})_7$-$(Au)_{19}$ cluster. B and C. The corresponding structural model proposes optimal Au atom distances for the close-packed C_{60} molecules. Here, the blue and purple atoms are the first and second layer of the Au(111) surface, respectively. Each three green (the first layer of the Au surface) atoms interacting with C_{60} molecules around the cluster. The 19 yellow atoms are an Au island surrounded by six C_{60} molecules with one further C_{60} molecule located on top. Therefore, the bright future appears in STM due to an atomic step height.

The $(C_{60})_{10}$-$(Au)_{35}$, $(C_{60})_{12}$-$(Au)_{49}$, and $(C_{60})_{14}$-$(Au)_{63}$ clusters are presented as atomistic models alongside the STM images in Figure 50A, B, and C, respectively. The size of the cluster increases with an increasing amount of Au atoms and C_{60} molecules. For the $(C_{60})_{10}$-$(Au)_{35}$ cluster, two C_{60} molecules sit on 35 Au atoms; for the $(C_{60})_{12}$-$(Au)_{49}$ cluster, three C_{60} molecules sit on 49 Au atoms; and, for the $(C_{60})_{14}$-$(Au)_{6}$ cluster, four C_{60} molecules sit on 63 Au atoms. The other C_{60} molecules are positioned around the edge of the Au island.

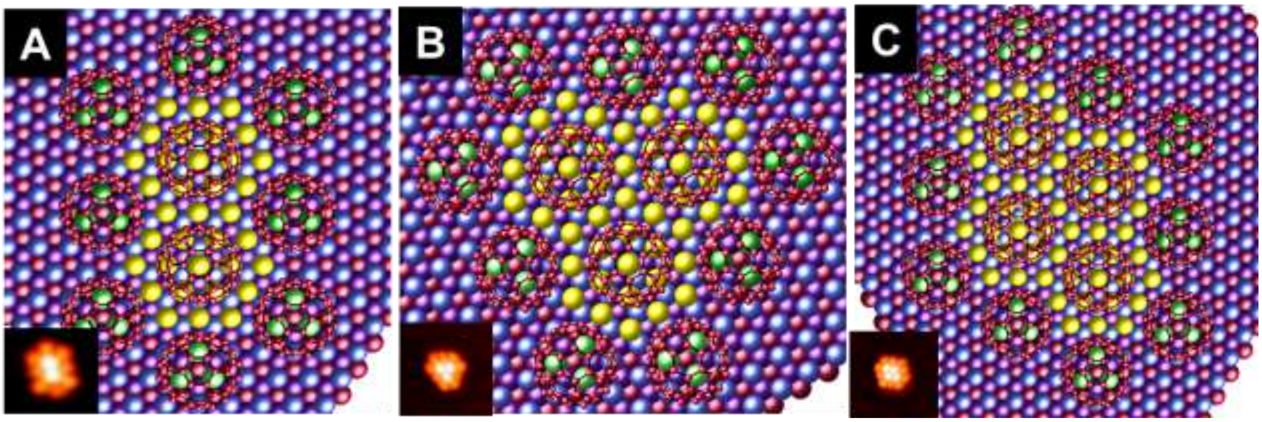

Figure 50: STM topographies and the associated structural models for the $(C_{60})_{10}$-$(Au)_{35}$, $(C_{60})_{12}$-$(Au)_{49}$, and $(C_{60})_{14}$-$(Au)_{63}$ clusters are shown in panels A, B, and C, respectively. The bright future arises from sitting two, three, and four C_{60} molecules on sitting on 35, 49, and 63 Au atom islands (the yellow spheres), respectively.

3.4 Diffusion and Rotation of Clusters on the Surface

As mentioned in cluster formation, section 3.2, some hybrid clusters may disappear with increasing temperature or over time at (constant) high temperature due to the increasing surface energy and thermal energy of the C_{60} molecules. Additionally, the independent rotation of clusters on the surface is also possible. We observed that only the $(C_{60})_{10}$-$(Au)_{35}$ cluster rotates on the surface elbow site (FCC region) and this rotation is shown in the associated STM images (Figure 51). We did not observe the rotation of the other hybrid clusters with the STM. In Figure 51, the rotation of $(C_{60})_{10}$-$(Au)_{35}$ clusters is observed by repeatedly scanning the same area for a period of time (~1 hour), during which time the temperature is also increased from 289 K to 294 K. For the $(C_{60})_{10}$-$(Au)_{35}$ cluster, three orientations are found by using the $[11\bar{2}]$ direction of the Au(111) surface as a reference: along the $[11\bar{2}]$ direction, and ± 60° from the $[11\bar{2}]$ direction (three-fold). Either the STM tip or the increasing thermal energy of the cluster may drive this rotation. Although an area is scanned at different time by retracting the tip and approaching it again, the rotation of the cluster is still observed. However, the effect of the tip on the rotation of the cluster is undeniable.

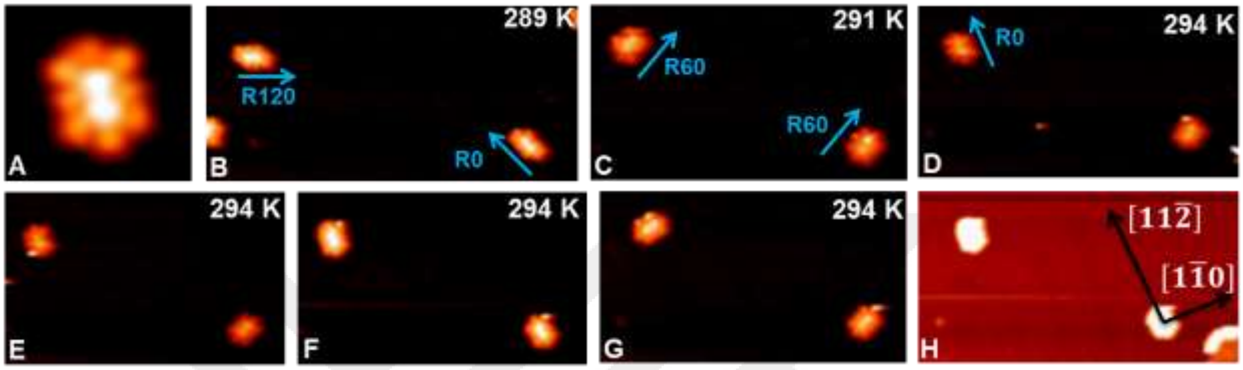

Figure 51: STM images showing the rotation of two $(C_{60})_{10}$-$(Au)_{35}$ clusters by increasing temperature and overscanning at room temperature. Three orientations are found by using the [11$\bar{2}$] direction of the Au(111) surface as a reference at R0 and ±R60.

Although, we observed that all clusters are formed at the elbow sites, the clusters may diffuse on the surface along the FCC region. This diffusion or, looked at another way, escape from the FCC elbow site, should be because of the increased surface energy and the increased thermal energy of the clusters at high temperature (close to room temperature). Figure 52A and B show the STM topographies for the diffusion and the rotation events at different contrasts (A1 and B1). About 95 ± 3% of the diffusion events were observed on ring clusters. A ring cluster probably diffused from the FCC elbow site to the FCC region as indicated by the blue arrow in Figure 52A. After retracting the tip, and subsequently returning it to the same area after 50 min, it was observed that the cluster had diffused back to an elbow site (shown with the yellow circle). During the STM tip absences, the cluster, indicated with the purple circle, also appears to have rotated on the surface when reimaged. Imaging to find same area is also an example of cluster rotation that is independent of the STM tip effect (or electric field effect).

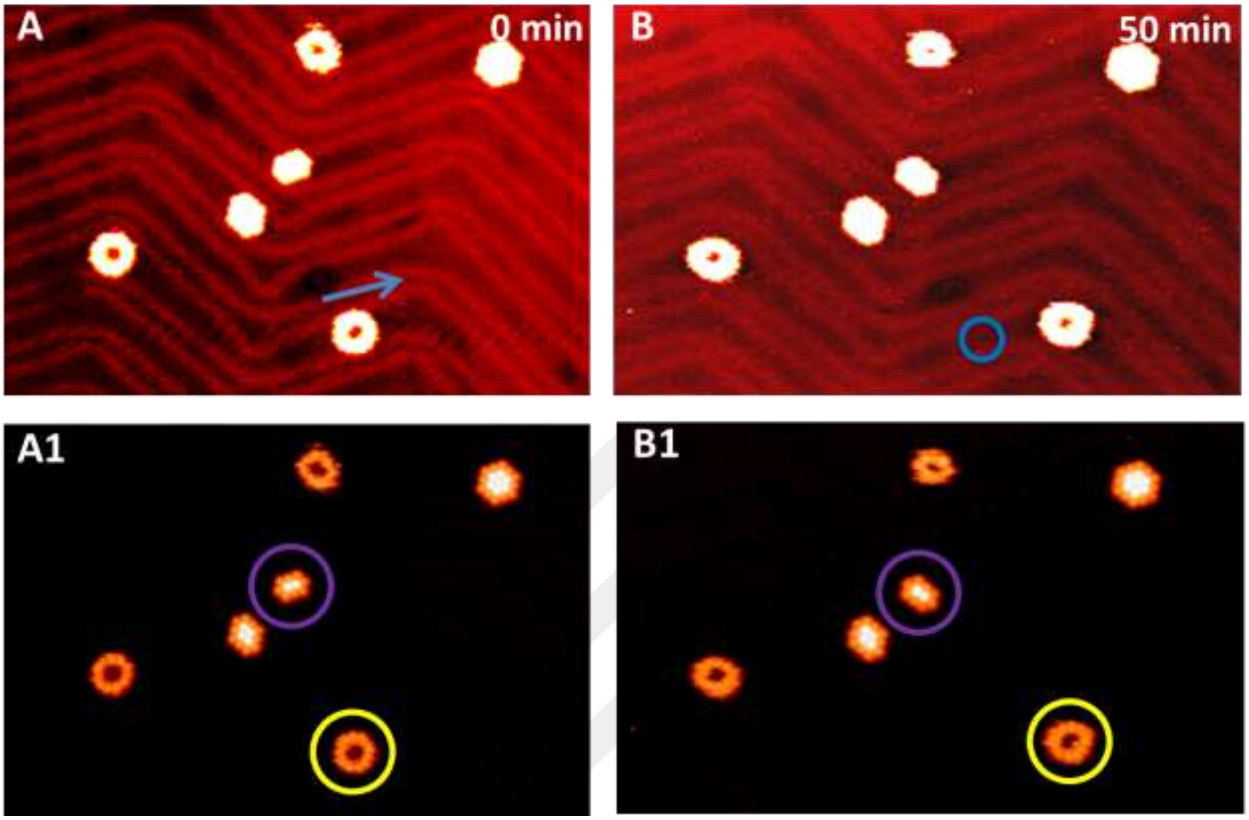

Figure 52: STM topographies at the different contrasts. A. A ring cluster, which probably diffused from the FCC elbow site to the FCC region. After 50 min., it had diffused back the original position (shown with the blue arrow and yellow circle). The cluster indicated with the purple circle had rotated on the surface after 50 min when scanning the same area (72 x 48 nm^2).

More diffusion of the ring clusters from the elbow sites to elsewhere on the FCC regions is shown with the yellow arrows and circles at different contrasts (85 x 41 nm^2) in Figure 53. Three clusters had already diffused from the elbow sites, as seen in Figure 53A. This diffusion was continued, and was observed again after 24 minutes. During this time, the tip was retracted and the same area is subsequently relocated for imaging (see Figure 53B). Moreover, the diffusion has been studied by scanning the same area over 5 hours at room temperature; however, all hybrid cluster remained on the elbow sites. As a conclusion, most of the ring clusters diffused easily over the surface with time, but the hybrid clusters remained in place.

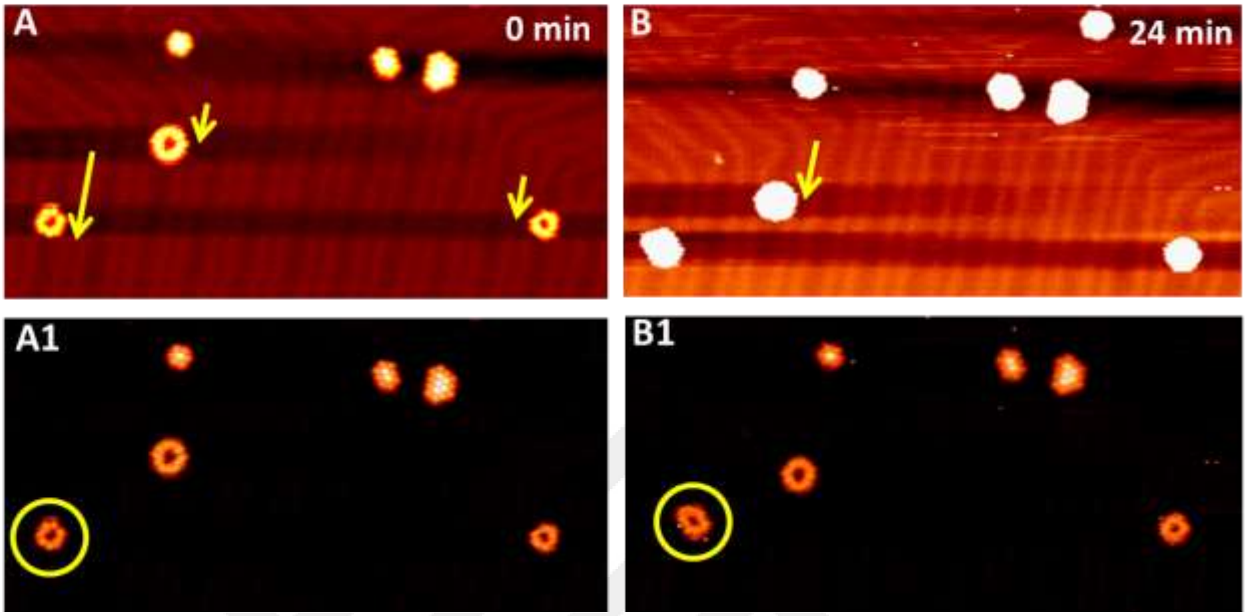

Figure 53: The diffusion of ring clusters is shown with the yellow arrows and circles at different contrasts (85 x 41 nm^2). A. Three clusters had already diffused from the elbow sites to the FCC regions. B. Continuous diffusion of the ring clusters observed after 24 minutes with the STM tip retracted and then relocating the same area.

3. 5 Cluster Distribution at Different C_{60} Coverages

To explore the effect of initial C_{60} deposition, we performed the experiment keeping the amount of Au constant and increasing the amount of C_{60} molecules on the surface. The idea was to control the growth process through the C_{60} molecule dose. All experiments were carried out using a 0.036 ± 0.006 ML dose of Au atoms and increasing the dose of C_{60} molecules from 0.036 ML to 0.144 ML. The reverse experiment, depositing Au atoms first at different coverages followed by a fixed C_{60} molecule dose, was performed by a colleague, Miss. Mahroo Rokni Fard [192]. In short, these two studies show that there was no observed effect due to deposition sequence, but increasing the number of Au atoms caused the formation of more ring-like clusters on the surface than hybrid clusters.

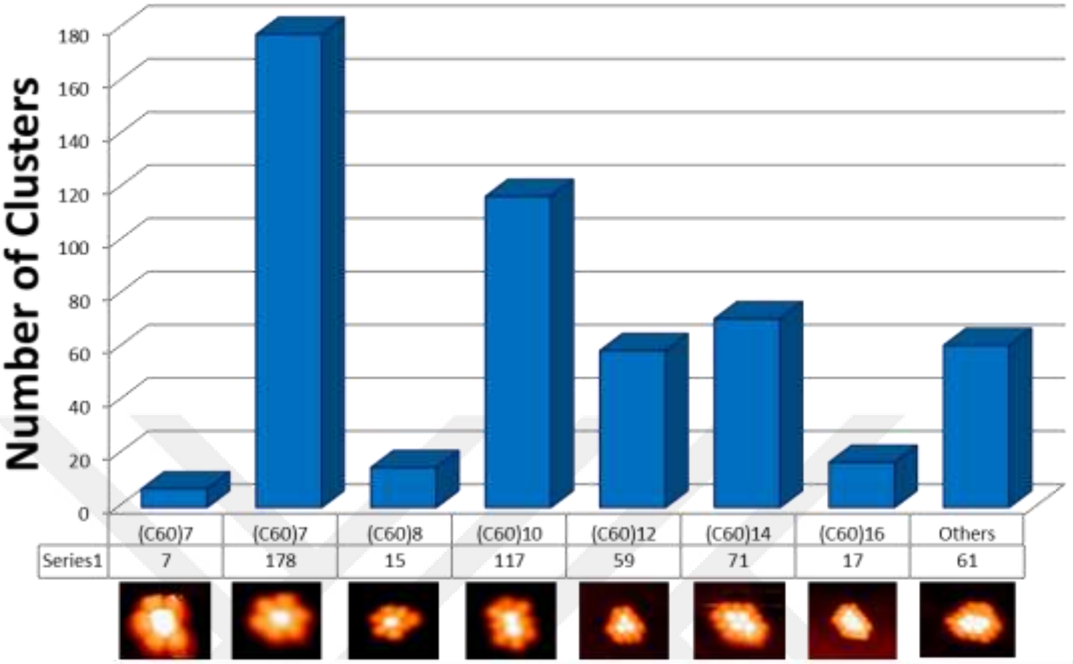

Figure 54: The clusters obtained dosing first 0.036 ML C_{60} molecule then 0.036 ML Au atoms at 110 K and size distribution for all type of clusters on the surface at RT (total 525 clusters counted). Major hybrid clusters are $(C_{60})_7$-$(Au)_{19}$, $(C_{60})_{10}$-$(Au)_{35}$, $(C_{60})_{12}$-$(Au)_{49}$, and $(C_{60})_{14}$-$(Au)_{63}$.

Figure 54 shows the size distribution of hybrid clusters obtained using a 0.036 ± 0.003 ML coverage of C_{60} molecules and a 0.036 ± 0.006 ML coverage of Au atoms at 110 K. The substrate temperature was brought to room temperature to obtain hybrid clusters. The dominant hybrid cluster fraction was found to be $(C_{60})_7$-$(Au)_{19}$, whilst other major hybrid clusters observed, had 10, 12, and 14 C_{60} molecules, as seen in Figure 54. For this rate, the big and combined clusters were also observed. For all coverages, the $(C_{60})_7$-$(Au)_{19}$ cluster is the most commonly observed hybrid cluster. This is because the initial amount of Au atoms deposited on the surface defines the cluster size distribution. On the other hand, the number of joined clusters increases with an increasing number of C_{60} molecules deposited.

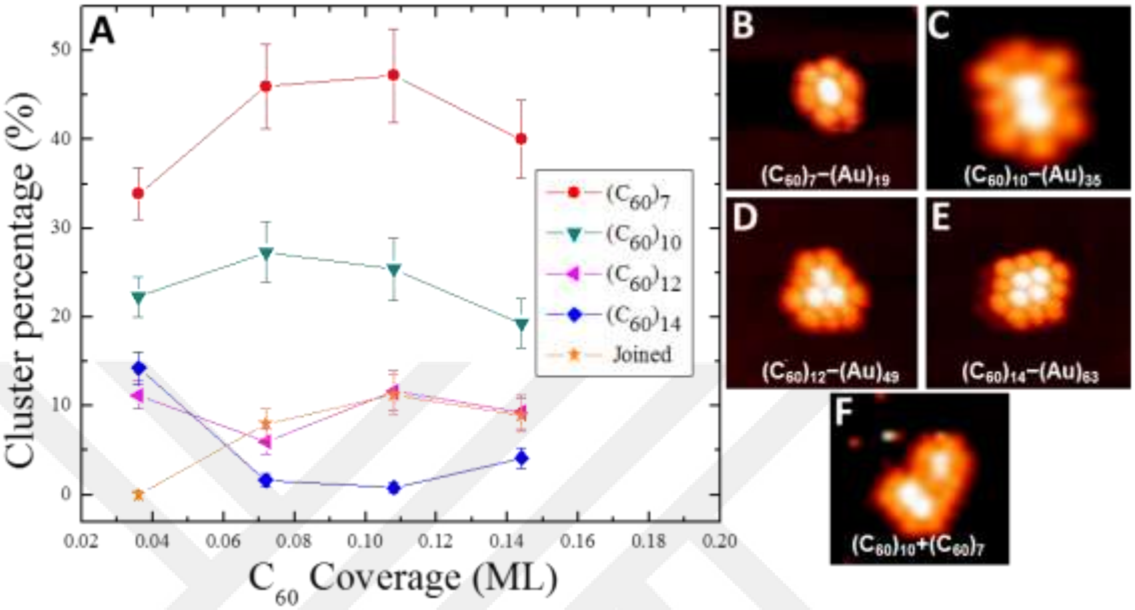

Figure 55: A. Cluster size distribution as a function of increasing C_{60} coverage. The percentage differences remained steady for $(C_{60})_7$-$(Au)_{19}$, $(C_{60})_{10}$-$(Au)_{35}$, $(C_{60})_{12}$-$(Au)_{49}$, and $(C_{60})_{14}$-$(Au)_{63}$ clusters. However, the number of joined clusters is increased. B, C, D, E, and F. Major types of clusters are the hybrid $(C_{60})_7$-$(Au)_{19}$, $(C_{60})_{10}$-$(Au)_{35}$, $(C_{60})_{12}$-$(Au)_{49}$, and $(C_{60})_{14}$-$(Au)_{63}$ clusters and joined clusters, respectively.

3.6 Adding C_{60} Molecules on the Surface at RT

The cluster transformation was explored by adding an additional 0.036 ± 0.003 ML coverage of C_{60} molecules to the existing clusters at room temperature. The diffusion length of C_{60} molecule on the Au(111) can be quite large at RT [193]. The extra molecules were added, whilst scanning the surface to see real-time cluster transformations. However, a cluster transformation was not observed with additional C_{60} molecules on the surface. This might have been because the tip was able to block the scanning area to the ingress of additional C_{60} molecules so, the experiment was continued with the tip retracted rather than actively scanning the area while the depositing C_{60} molecules were deposited. After C_{60} deposition, the tip was approached to the surface, and different areas were scanned to obtain statistically reliable results.

The cluster size distribution after adding more C_{60} molecules to the existing clusters at room temperature is shown in Figure 56A. The percentages of four major cluster fractions are given as a function of the initial coverage of C_{60} molecules. The numbers of clusters were counted before and after the C_{60} molecules are added. The associated before and after cluster percentage ratios are plotted in Figure 56B to emphasize the change in cluster percentage.

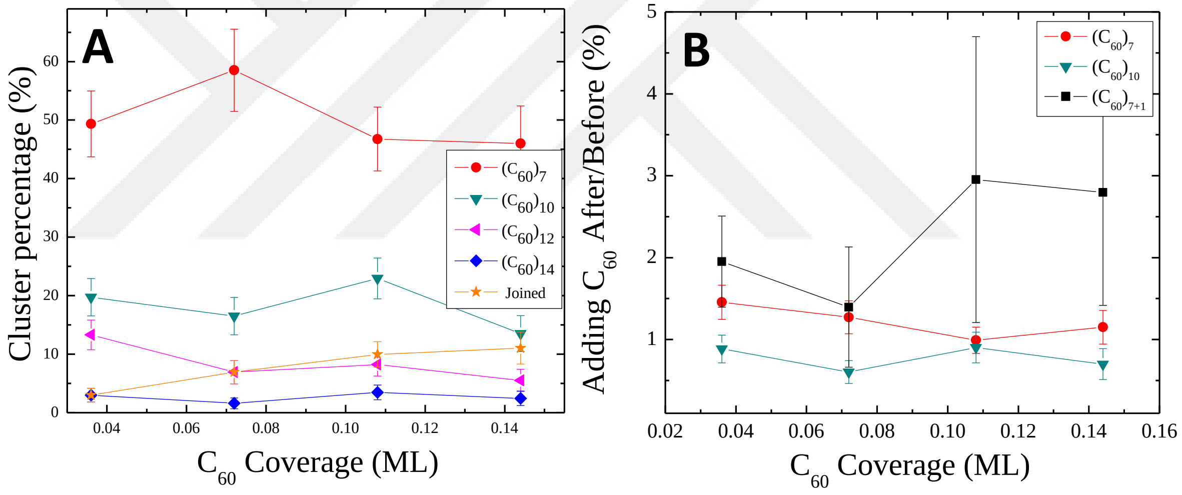

Figure 56: A. The percentages of $(C_{60})_7$-$(Au)_{19}$, $(C_{60})_{10}$-$(Au)_{35}$, $(C_{60})_{12}$-$(Au)_{49}$, and $(C_{60})_{14}$-$(Au)_{63}$ clusters and joined clusters after adding 0.036 ± 0.003 ML C_{60} on the existing clusters at room temperature. Four major cluster percentages are plotted as a function of the initial coverage of C_{60} molecules on the surface. B. The ratio of after/before comparisons of the cluster percentages for $(C_{60})_7$-$(Au)_{19}$, $(C_{60})_{10}$-$(Au)_{35}$, $(C_{60})_{7+1}$-$(Au)_{19}$.

As can be seen in Figure 56A, the percentages of the major cluster fractions remained constant with an increasing initial coverage of C_{60} molecules. However, the number of joined clusters increased. This was an expected result purely due to the additional C_{60} molecules. As more C_{60} molecules diffuse on the surface, they become captured by the larger clusters and transform into joined clusters or the combination of two nearby clusters with additional diffusing molecules. When we examine the ratio of clusters before and after the extra C_{60} dose for the $(C_{60})_7$-$(Au)_{19}$ cluster decreases from 1.5 ± 0.2 to 1.1 ± 0.2 and the $(C_{60})_{7+1}$-$(Au)_{19}$ clusters increases from 1.9 ± 0.55 to 2.8 ± 1.3. This means that additional C_{60} molecules prefer to attach to a cluster and remain attached, but that the $(C_{60})_7$-$(Au)_{19}$ clusters were not themselves transformed.

3.7 Adding Au Atoms to the Surface at RT

This final experiment was undertaken in order to understand the effect of additional Au atoms at room temperature on the hybrid cluster. Therefore, additional Au atoms, at 0.018 ± 0.003 ML, were added to the surface after standard hybrid cluster formation. We observed that at room temperature the additional Au atoms do not stay on the bare Au surface but diffuse to the step edges. It is predicted that Au atoms may preferentially join hybrid clusters and change the cluster forms. Several images were taken before and after each deposition to insure sufficient good quality images to allow for a statistically significant analysis. The STM tip was kept away from the surface to eliminate tip shadowing on the scan area. However, no differences were observed when comparing the before and after images. The tip was retracted before the Au dose was applied and found the original scan area located, after which several images were captured. This method showed unique transformations of the clusters.

The comparison of before and after images for the addition of Au atoms on the surface is shown in Figure 57A and B. The images were illustrated at different contrasts A1 and B1, respectively. The hybrid clusters were obtained by adding 0.036 ML ± 0.006 Au atoms and

0.108 ± 0.008 ML C_{60} molecules at 110 K; an additional 0.018 ML ± 0.003 of Au atoms was dosed on to the surface at room temperature.

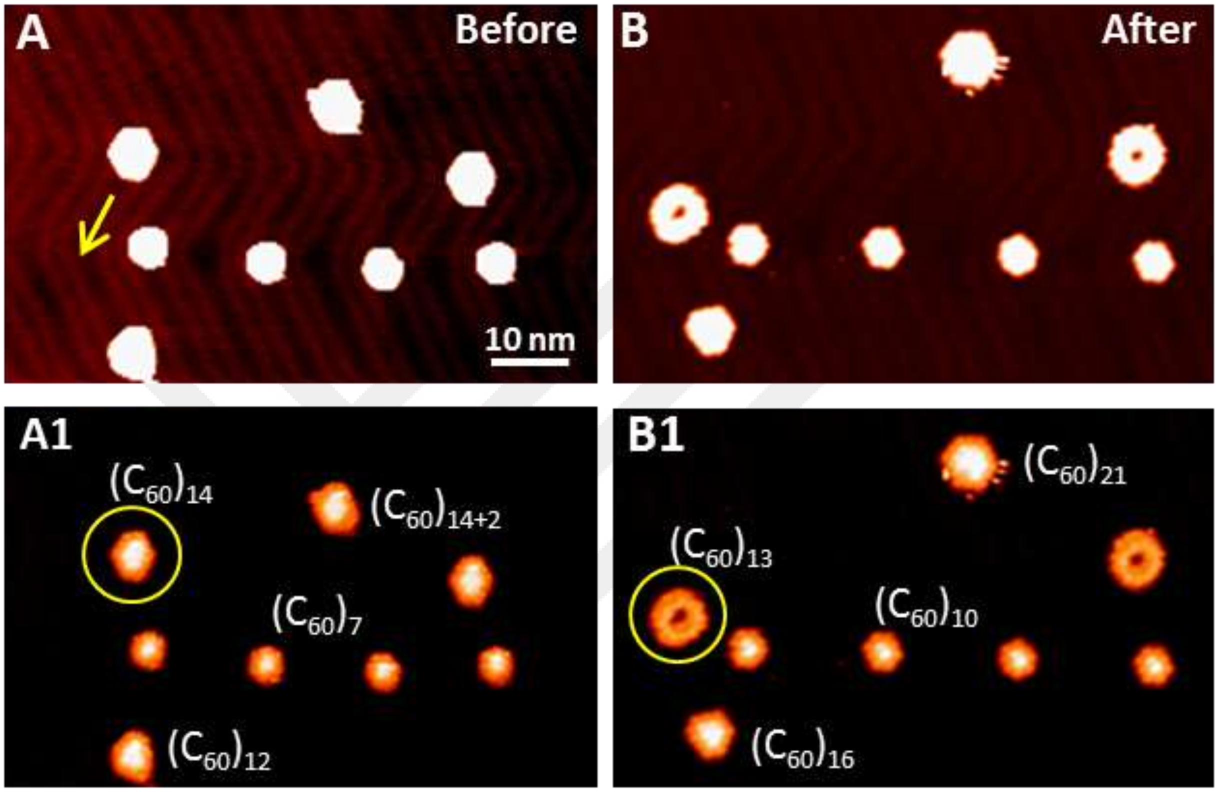

Figure 57: A and B. Before and after images at different contrasts A1 and B1, respectively. Additional Au atoms (0.018 ± 0.003 ML) prefer to join with the hybrid clusters and transform them by increasing their size. Here, C_{60} molecules, which are already on the surface, diffuse over long distances at room temperature and join the clusters simultaneously with the additional Au atoms. As can be seen images A1 and B1, the changes in the clusters sizes are indicated before and after.

Additional Au atoms prefer to join to the hybrid clusters and transform them to larger sized clusters, as well as migrating to the step edges. The C_{60} molecules can already diffuse large distances on the surface at room temperature. These molecules join to the clusters simultaneously with the additional Au atoms and induce the cluster's transformation. As can be seen in Figure 57A1 and B1, the change in the cluster size is indicated with the appropriate before and after images. From the results it is clear that there are high probabilities of capturing more C_{60} molecules with large clusters.

In Table 5, the percentage of hybrid clusters transformed by the additional Au atoms are reported. 70.3% of the $(C_{60})_7$-$(Au)_{19}$ clusters remained the same, whilst 18.5% were transformed to another hybrid cluster form, $(C_{60})_{10}$-$(Au)_{35}$. However, significant fractions of the $(C_{60})_7$-$(Au)_{19}$, $(C_{60})_{10}$-$(Au)_{35}$, $(C_{60})_{12}$-$(Au)_{49}$, and $(C_{60})_{14}$-$(Au)_{63}$ clusters transformed to a larger-sized cluster. The most common transformation was growth towards the next largest hybrid cluster by capturing two additional C_{60} molecules along with the appropriate number of Au atoms. It has been revealed that in order to transform clusters, Au atoms must be involved. Adding C_{60} molecules increases the size of joined clusters or C_{60} molecules around the cluster only, but does not cause cluster transformation.

Table 5: The percentage of transformed major clusters on the surface after adding Au atoms. The table information was obtained by counting 91 clusters.

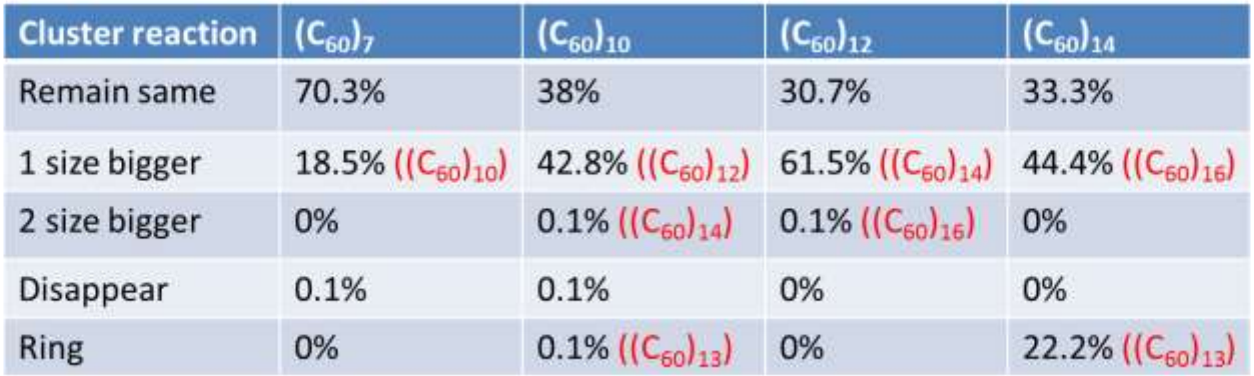

Cluster reaction	$(C_{60})_7$	$(C_{60})_{10}$	$(C_{60})_{12}$	$(C_{60})_{14}$
Remain same	70.3%	38%	30.7%	33.3%
1 size bigger	18.5% ($(C_{60})_{10}$)	42.8% ($(C_{60})_{12}$)	61.5% ($(C_{60})_{14}$)	44.4% ($(C_{60})_{16}$)
2 size bigger	0%	0.1% ($(C_{60})_{14}$)	0.1% ($(C_{60})_{16}$)	0%
Disappear	0.1%	0.1%	0%	0%
Ring	0%	0.1% ($(C_{60})_{13}$)	0%	22.2% ($(C_{60})_{13}$)

3.8 Bias Voltage Effect

The STM images in this study were taken at negative bias voltage as well as the manipulation of the hybrid cluster which will be presented in chapter 4. To explore the electric field effect on the size distribution of the hybrid clusters at room temperature, the surface was scanned using different bias voltages. The existing C_{60} molecules could migrate long distances on the surface due to their high mobility. These molecules may attach to clusters, but do not otherwise cause the transformation from one cluster to another (as indicated in section 3.6). The STM images recorded while scanning the surfaces at negative and positive bias voltages are presented in Figure 58 and Figure 59, respectively. The clusters remained unchanged whilst scanning at -1.93 V for one hour (see the before and after images in Figure 58A and B). However, as seen in Figure 58C and D, increasing the bias voltage to -2.46 V, and thus increasing the electric field, caused C_{60} molecules to migrate under the tip and attach to the clusters. It can be seen from the images that the hybrid clusters do not change due to the additional C_{60} molecules.

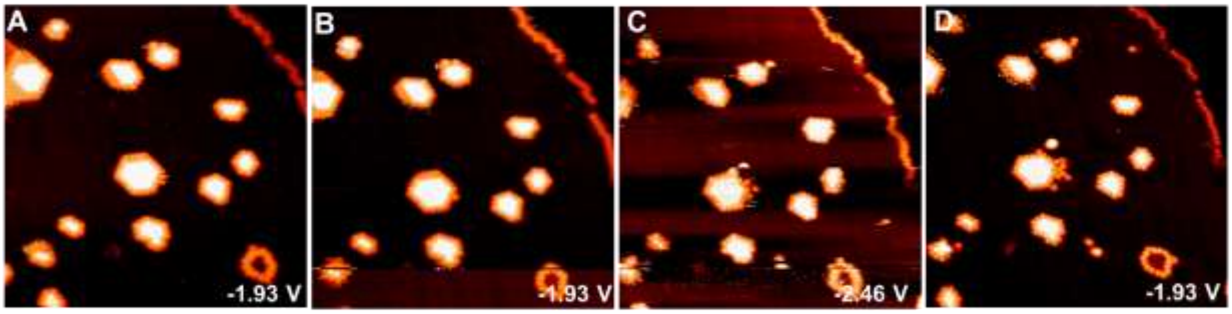

Figure 58: Negative bias voltage-dependent scanning. A and B. Before and after scans of the same area after 1 h at a -1.93 V bias voltage. There was no cluster transformation or no additional C_{60} molecules observed around the clusters. C. Scanning same area at -2.46 V resulted in additional C_{60} molecules around clusters, but again no cluster transformation was observed in D (All images areas 55 x 55 nm^2 and room temperature).

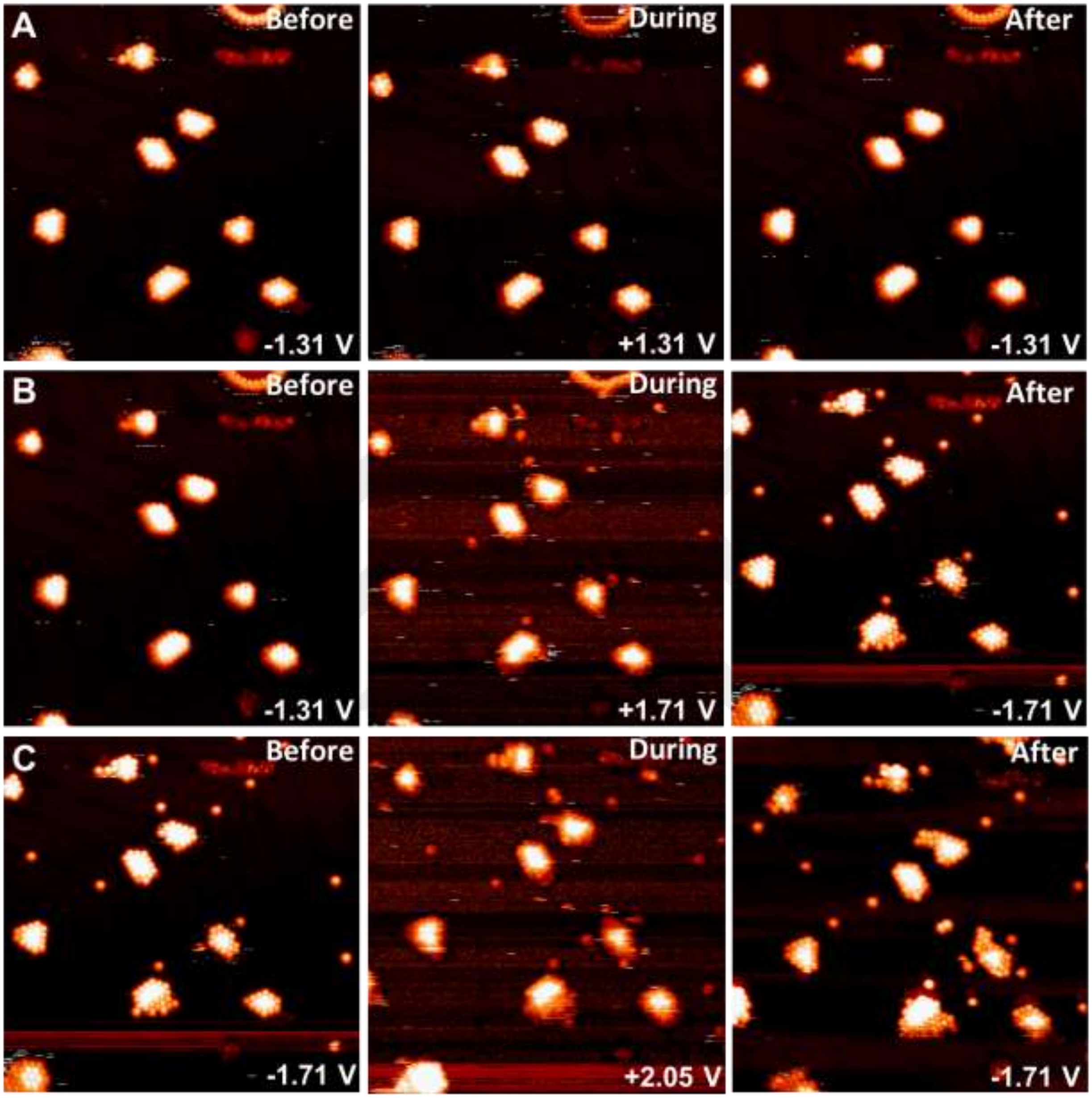

Figure 59: Before, during and after STM images. A. Scanning the area first at -1.31 V as a record and then scanning all areas at +1.31 V for after images for comparison. There is no transformation or additional C_{60} molecules around the clusters for +1.31 V. B. Scanning the area at +1.71 V resulted in additional C_{60} molecules around the clusters without transforming them. C. Scanning the area at +2.05 V lead to even more C_{60} molecules around the clusters. (All images are taken at 47 pA, 55 x 55 nm^2, at room temperature).

The surface was also scanned at positive bias voltages. It is known that STS shows two peaks at +0.8 V and +2.1 V and a further peak at -2.0 V (see Figure 21B). It can be seen that the positive bias voltage has a greater effect on the C_{60} molecules due to the filled state of the surface. The usage of three different positive bias voltages is presented in Figure 59 before, after and during the recording of the scan images. Scanning the surface at +1.31V did not affect on the clusters, and no additional molecules were observed (see Figure 59A). However, increasing the bias voltage to +1.71 V caused additional molecules to attach around the clusters (see Figure 59B). Moreover, at +2.05 V, further additional molecules migrated to positions around the clusters and elbow sites. Here, the additional molecules sat on the FCC regions. Typically, there is no stable single molecule on the surface due to the high mobility of the C_{60} molecules at room temperature. It is likely that applying a positive bias voltage (electrons tunnel from the tip to the surface) desorbed C_{60} molecules from the tip surface with some additional atoms (maybe Au or O). These molecules may sit on the elbow site due to the associated contamination.

3.9 Conclusions

In this chapter, the cluster formation studies started with C_{60} molecule and Au atom distributions on the Au(111) surface at 110 K, before investigating their formation up to room temperature. Four major hybrid clusters fractions were observed on the surface at room temperature, which were $(C_{60})_7$-$(Au)_{19}$, $(C_{60})_{10}$-$(Au)_{35}$, $(C_{60})_{12}$-$(Au)_{49}$, and $(C_{60})_{14}$-$(Au)_{63}$. The enhancement in the rate of C_{60} molecule coverage with constant Au atom coverage was studied. Increasing the amount of C_{60} molecules did not change the fractional percentages of the cluster distribution, but the amount of joined clusters increased. These clusters are mostly stable on the surface, however, for the $(C_{60})_{10}$-$(Au)_{35}$ cluster, three main rotation orientations, R0 and ±R60 were found by using the $[11\bar{2}]$ direction of the Au(111) surface as a fixed reference. In time, the ring clusters may diffuse from elbow sites along the FCC region of the surface.

Adding C_{60} molecules and Au atoms to the hybrid clusters at room temperature was also studied. Additional C_{60} molecules did not change the size distribution of the clusters due to the high mobility of these molecules. Surprisingly, added Au atoms joined with the hybrid clusters and increased the size of the cluster, typically increasing to the next major cluster fraction. This is because Au atoms combined with mobile C_{60} molecules on the surface, which then subsequently joined with clusters to transform them. Finally, these clusters were found to remain stable while scanning with a negative bias of up to -2.0 V. For positive bias voltages greater than +1.71 V, additional C_{60} molecules migrated to the clusters to the elbow sites.

CHAPTER 4

MANIPULATION HYBRID $(C_{60})_m$-$(Au)_n$ CLUSTERS on the Au(111) SURFACE

In this chapter, we study the manipulation of $(C_{60})_m-(Au)_n$ hybrid clusters on the Au(111) surface presented in Chapter 3. Here, we report the cascade manipulation of $(C_{60})_m-(Au)_n$ hybrid clusters by STM. We demonstrate that a $(C_{60})_m-(Au)_n$ clusters on the Au(111) surface can be tailor modified by downsizing them from one hybrid number cluster to another at room temperature. This manipulation is a pure mechanical interaction between the STM tip and a C_{60} molecule of the cluster. This highly efficient manipulation process does not need to remove atoms/molecules one-by-one using the STM tip and yet the final product is “error-free” due to the stability of the hybrid number cluster. C_{60} molecules are highly mobile at room temperature due to weak interactions forces between the molecule and the surface. Therefore, this experiment was also performed at 110 K to gain more thermal control over the C_{60} molecules and to determine the new state on the surface. With this in mind, directional manipulation has been achieved at 110 K.

4.1 Drift Velocity Over Time

Before starting to present the manipulation data, the STM tip drift during manipulation should be mentioned. STM manipulations are often disturbed by thermal drift or creep of the piezoelectric scanner. These drifts result in a moving scanning frame in a certain direction or angle. To avoid thermal drift, we scan the same area long enough (for our system, this time is about an hour) for the thermal extension of the tip and sample to become very small. Here, we are not trying to correct images for these drifts, as we manually correct the position of the scanning frame after each scan. Our aim is to ensure the STM tip is on the selected molecule during the manipulation event.

A schematic diagram is given for the calculation of drift velocities (v_x and v_y) in lateral directions in Figure 60A and B. First, the initial cluster coordinates are taken as (x_1, y_1) (see Figure 60A). Then, the final position of the cluster coordinates is taken as (x_2, y_2) with the two sets of coordinates obtained as consecutive images. The up lateral scanning direction is indicated with a blue arrow in each frame.

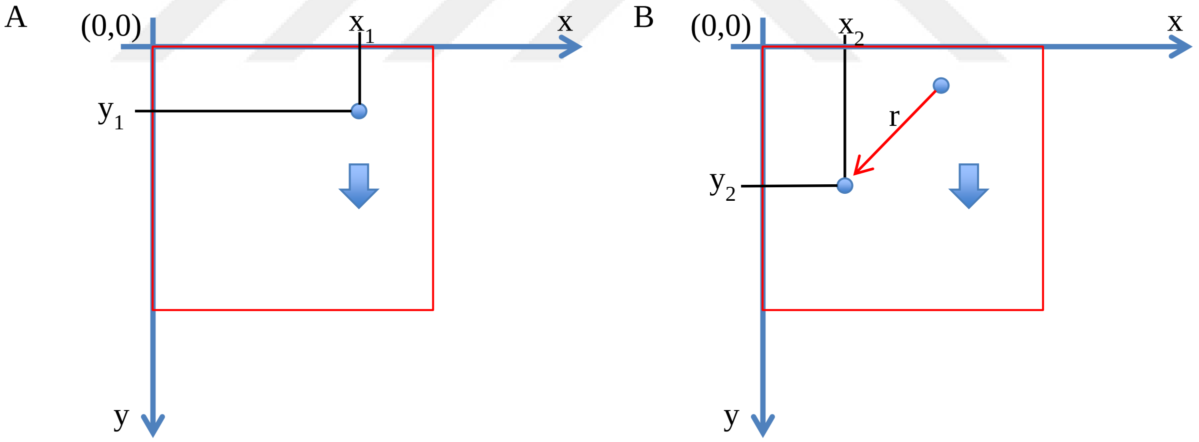

Figure 60: Schematic diagram to calculate lateral drift velocity with tracking a cluster at room temperature. A. Initial position of a cluster (x_1, y_1). B. The final position of the cluster in the consecutive image (x_2, y_2). The lateral scanning direction is indicated by the blue arrow in the frame.

Lateral drift velocity formulas, which are given by $v_x = \frac{x_2 - x_1}{\Delta t}$, $v_y = \frac{y_2 - y_1}{\Delta t}$, were generated from Ref. [194]. Using the schematics given in Figure 60, the v_x, v_y, and the resultant vector of lateral drift velocities, *r* is plotted as a function of scanning time in Figure 61A. Here, Δt is the time between two consecutive images.

Figure 61B, C, D, and E illustrate consecutive images taken at room temperature after 6, 30, 70, and 150 minutes, respectively. It can be seen that after the first scan the drift is extremely large as indicated by the green circle, at ~1.2 nm/min. Moreover, in first 50 minutes, the drift velocity is ~0.8 nm/min (indicated by the blue circle) then the velocity decreases dramatically to ~0.17 nm/min in 65 minutes. The acquisition time for all manipulation experiments is 12.8 ms.. The drift during manipulation is 19 pm, determined for immediately after the first scan where the drift is highest. The manipulation experiment can still be done successfully even with a 19 pm drift, as the STM tip will be still on the molecule. To reduce drift and to ensure the tip is indeed still on the molecule during manipulation, we scanned the same area for at least 45 minutes at room temperature. Thus, STM tip drift was eliminated accounting for thermal effects and piezo creeps. During the manipulation event, the image quality and the tip state did not change and, therefore, tip deformation could be neglected.

4.2 Manipulation of a Selected C_{60} Molecule in an Island

The aim of this chapter is to produce desired geometries and properties with C_{60} molecular nanostructures at both the nanoscale and at realistic temperatures for practical applications. Hence, the STM tip is a great tool with which to manipulate a selected C_{60} molecule on the different surfaces studied previously [15-22]. Before performing cluster manipulations, we investigated a single C_{60} manipulation on a C_{60} island on the Au(111) surface at room temperature to determine our various manipulation parameters.

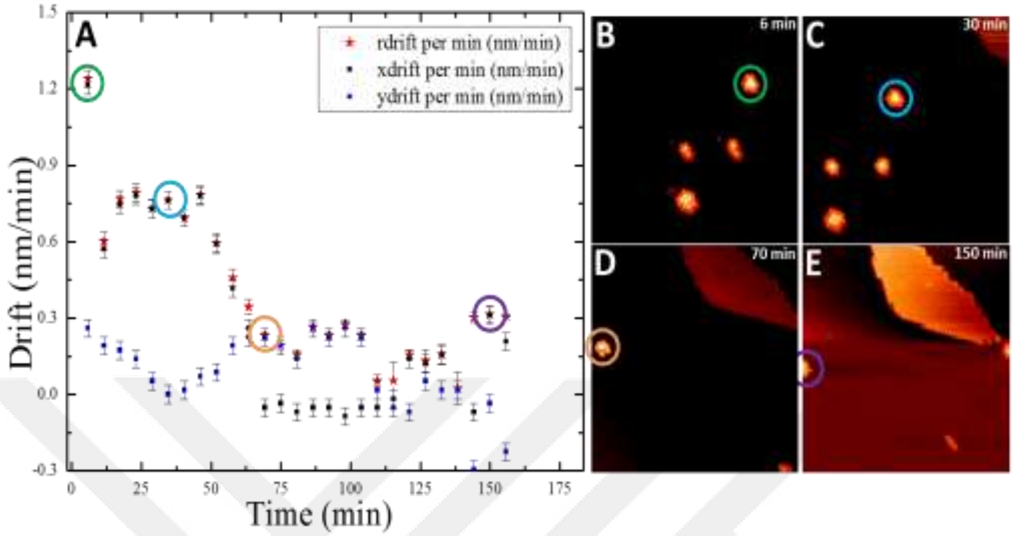

Figure 61:A. Analysis of lateral drift velocity at room temperature whilst tracking a cluster. B, C, D, E. In consecutively obtained images taken at a -1.97 V bias voltage and, 47 pA tunnelling current, with 150 nm/s scanning speed on a 50 x 50 nm^2 area after 6, 30, 70, 150 minutes, respectively. Green, blue, orange, and purple circles show the cluster on the images and the drift velocity analysis on the graph.

The experimental procedure was as follows, as can be seen in Figure 62A, B, C: first, a topographic scan of the Au(111) surface was taken to observe the C_{60} island under normal scanning conditions. Next, the STM tip was placed on a selected C_{60} molecule and the manipulation performed after the feedback loop was switched off for 12.8 ms acquisition time (Figure 62B). During this time, the tip-sample distance was decreased by up to 1.8 nm and the tunnelling current was recorded as a function of tip displacement. Finally, to see the manipulation event, the surface was scanned once more under normal scanning conditions (Figure 62C). A selected C_{60} molecule manipulation is possible at various bias voltages and tunnelling currents [19]. However, we determined the tip displacement parameter, Z, for a single C_{60} manipulation by moving the tip towards the surface by ~1.2 nm for gentle and precise manipulation experiments. All STM images reported in this chapter, unless otherwise indicated were taken at a -1.67 V bias voltage and 47 pA tunnelling current, using a 12.8 ms acquisition time.

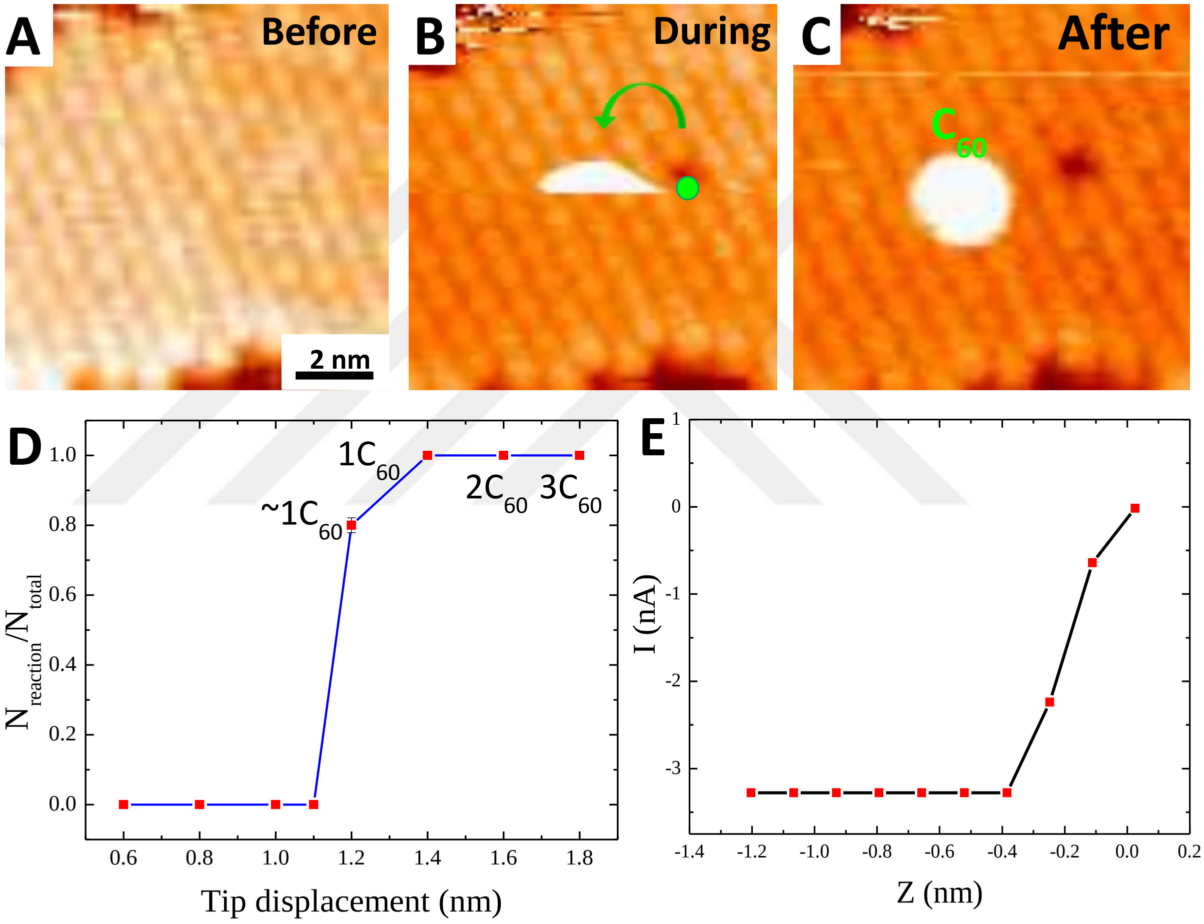

Figure 62. A, B, and C. Initial manipulation images showing before, during and after removing a single C_{60} molecule from a C_{60} island (at 0.072 ± 0.005 ML of C_{60} coverage) on the Au(111) surface at room temperature. The STM tip removes the C_{60} molecules highlighted by the green from the C_{60} island. After manipulation, the C_{60} molecule found on the island. D. The effectiveness of the manipulation a single C_{60} molecule from the island for different tip *Z*-displacements. Decreasing the tip-sample distance to 1.2-14 nm was found to be the optimal parameterisation for removing a single C_{60} molecule from the island with different tungsten tips. E. Manipulation current versus tip movement during a single C_{60} manipulation event. After 0.4 nm tip movement towards the island, the current saturates when the tip contacts a single C_{60} molecule.

Figure 62 illustrates the initial manipulation experiment to optimise the *Z* displacement. Removing a single C_{60} molecule from a C_{60} island with a coverage 0.072 ± 0.005 ML on the Au(111) surface is shown before, during and after manipulation in Figure 62A, B and C, respectively. The STM tip is placed on a selected C_{60} molecule on the C_{60} island, as indicated by the green circle in Figure 62B. After manipulation, the C_{60} molecule found on the island. Figure 62D illustrates the distribution of manipulation events for C_{60} molecule/s from the island for different tip-surface distances. Decreasing the tip-surface distance by 1.2 nm results in 80% successful manipulation. However, the optimal tip displacement for removing a single C_{60} molecule from the island (observed with different tungsten tips) is achieved at 1.3 nm. Figure 62E shows the recorded manipulation current as a function of tip displacement during the manipulation event. After a 0.4 nm tip Z-displacement towards the island, the tip contacts the C_{60} molecule and, consequently, the current saturates. Moreover, to explore the electric field effect on single C_{60} molecule extraction from the island, zero bias voltage manipulation was performed by using a macro program written in the Omicron Scala control program, which was coded as follows:

```
acq_time, 2000

delay, 200
feedback, 0
set_v, 0.0

delay, 50
loop_times, 10
delay, 50
measure
add_z, -0.13
loop_end
delay, 50
measure

reset_v
reset_z
```

```
delay, 100
reset_feedback
delay, 50
```

The feedback loop, first, switched off and sets the bias voltage to 0 V by the program for the manipulation experiment. Here, all timings and delays are given in units of microseconds. The *acq_time* (µs) is acquisition time for each loop, *set_v* (V) is the bias voltage for the manipulation event after feedback loop is off, *loop_times* is the number of measurement for the manipulation experiment, and *add_z* (nm) is the step size of the STM tip towards the surface. After the manipulation has been performed, all parameters are reset to scanning conditions.

The minimum Z-displacement for the manipulation of a single C_{60} molecule at zero bias voltage is found to be 1.2 nm. Thus, the manipulation ruled out electric field effect by using a zero bias voltage manipulation. The manipulation is also performed at negative bias voltage conditions. The threshold of the Z-displacement was found to be between 1.2 to 1.4 nm for a selected single C_{60} molecule for a given bias voltage and tunnelling current, (-1.67 V and 47 pA, respectively) without disturbing the island size and shape. By decreasing the tip-sample distance by a further 0.2 nm or 0.4 nm, two and three C_{60} molecules can be removed from the island. In this experiment, we used the 1.2 nm setting to produce a very gentle contact during manipulation.

The possible mechanism has been extensively studied in terms of bias voltage, manipulation current, tip-sample distance and manipulation power [19]. It has been concluded that the manipulation is not due to the thermal decomposition of C_{60}. It was observed that the manipulation is possible under a wide range of bias voltage and current values, and thus that the electric field and tunnelling current were not the reason. Moreover, the manipulation power is 5.4 ± 0.7 nW for our study, which is lower than the thermal decomposition threshold (1.0 to 21 μW) [151, 152]. Therefore, the manipulation event is purely mechanical in origin, where the tip apex interacts with the selected C_{60} molecule due to a repulsive force. The tip approaches a C_{60} molecule and makes contact, pressing on it until it is ejected from the island and moved somewhere onto the tip or the substrate surface, ending up on either the step edges or a neighbouring vacancy. The average of the tip displacement was found to be 0.44 ± 0.19 nm and the manipulation current as 3.27 ± 0.03 nA when the tip is in contact with the molecule. This displacement is quite similar to earlier findings [15, 19, 25].

4.3 Cascade Manipulation of Hybrid $(C_{60})_m$−$(Au)_n$ clusters at RT

We have reported the production of hybrid $(C_{60})_m$−$(Au)_n$ clusters in chapter 3, such as $(C_{60})_7$−$(Au)_{19}$, $(C_{60})_{10}$−$(Au)_{35}$, $(C_{60})_{12}$−$(Au)_{49}$, and $(C_{60})_{14}$−$(Au)_{63}$ at the elbow sites of an Au(111) surface. These $(C_{60})_m$−$(Au)_n$ clusters show a clear 'magic number' effect, in that only certain combinations of m and n are allowed [14] because of they maximise the interaction between close-packed Au islands with the surrounding C_{60} molecules.

In this section, we investigate an experiment at room temperature to obtain a transformation from one of the larger magic number clusters, $(C_{60})_{14}$−$(Au)_{63}$, to the smallest cluster, $(C_{60})_7$−$(Au)_{19}$, by removing a selected C_{60} molecule from its side. We also discuss the manipulation of a selected C_{60} molecule from the top of a cluster. During such manipulation, cluster rotation is also possible due to deformation by the tip. Performing the STM tip manipulation to produce nanostructures at room temperature rather than at low temperature is a great advantage in terms of realistic applications.

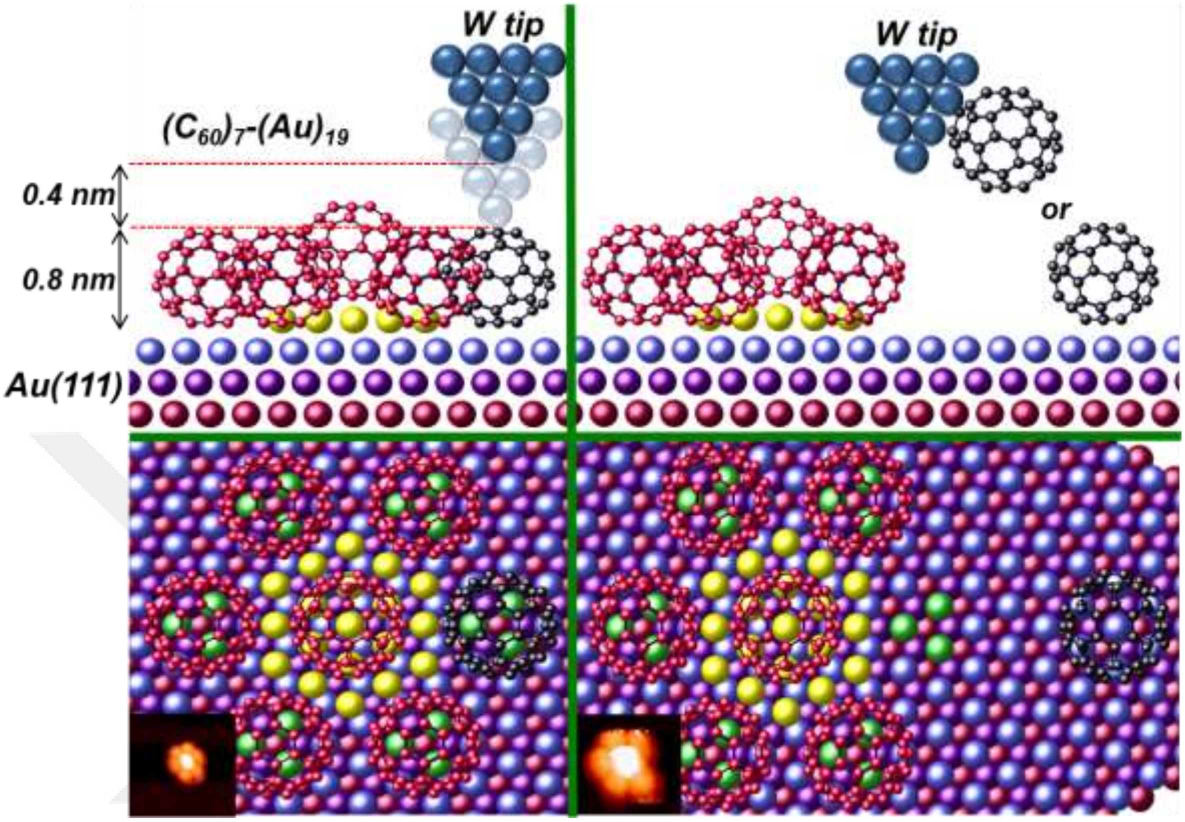

Figure 63: Schematic diagram of the manipulation of a $(C_{60})_7$–$(Au)_{19}$ cluster with STM images and atomic ball models. The atomic tip interacts with the selected molecule and squeezes it towards the surface and moves it elsewhere on the surface or the tip by breaking the weak interaction between the cluster components and the surface.

The schematic diagram in Figure 63 demonstrates the manipulation of a $(C_{60})_7$–$(Au)_{19}$ cluster via the STM tip. The atomic tip interacts with the selected molecule and squeezes it towards the surface; the molecule moves away due to breaking the interaction between the cluster components and the surface. After manipulation, the molecule either diffuses elsewhere on the surface or attaches to the tip. As can be seen in Figure 63, the interactions of C_{60} molecules on the side of the cluster involve three surface atoms (the green atoms), an Au island step edge (the yellow atoms), and three C_{60} neighbouring molecules (one on top and two at the sides). The interactions of the C_{60} molecule on the top of the Au island is with three Au island atoms and six C_{60} neighbouring molecules around the cluster. The interactions in the bigger clusters are as described above.

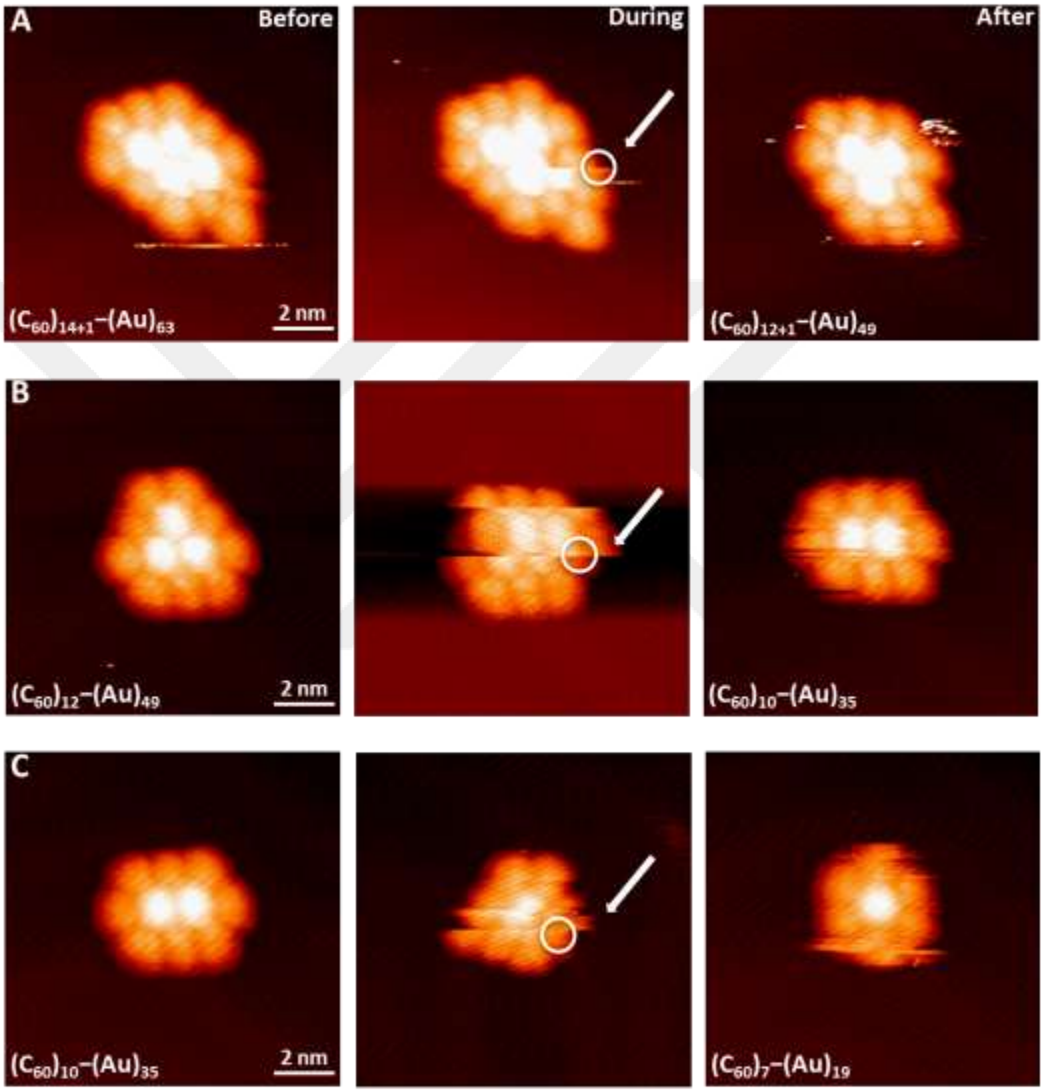

Figure 64. Cascade manipulation images showing before, during and after manipulation of the $(C_{60})_{14}-(Au)_{63}$, $(C_{60})_{12}-(Au)_{49}$ and $(C_{60})_{10}-(Au)_{35}$ clusters in panels A, B and C, respectively. The manipulation is performed at the site on clusters indicated with white circles by driving the tip toward the surface by 1.2 nm. After each manipulation, two C_{60} molecules and Au atoms were removed, a process that ultimately obtaining the smallest hybrid cluster, $(C_{60})_7-(Au)_{19}$.

A cascade manipulation process is illustrated with the before, during, and after STM images shown in Figure 64. A manipulation is performed to remove a single C_{60} molecule from the side of the $(C_{60})_{14}$–$(Au)_{63}$ cluster which is highlighted by the white circle and indicated with a white arrow. The manipulation of the molecule is made possible by driving the tip 1.2 nm nearer the surface. In Figure 64A, we start with a $(C_{60})_{14+1}$–$(Au)_{63}$ cluster, which consists of four C_{60} molecules sitting on top of an Au_{63} island and 10 C_{60} molecules around the island. Here, an additional C_{60} molecule (+1) is attached to the side but, in the next step, this molecule is removed. Figure 64B illustrates how the $(C_{60})_{12}$–$(Au)_{49}$ cluster can be further modified to $(C_{60})_{10}$–$(Au)_{35}$ and $(C_{60})_{7}$–$(Au)_{19}$, which is the smallest stable cluster (see Figure 64C).

We achieved the manipulation of a $(C_{60})_{14}$–$(Au)_{63}$ cluster to a $(C_{60})_{7}$–$(Au)_{19}$ cluster. The STM tip is actually driven towards a selected molecule by 1.2 nm by temporarily disrupting the close-packed cluster. The atoms and molecules are able to re-group, forming the $(C_{60})_{12}$–$(Au)_{49}$ cluster, which is a magic number cluster that is "one size smaller" than $(C_{60})_{14}$–$(Au)_{63}$. Immediately upon removal of the C_{60} molecule, the cluster's transforms over a very short timeframe. During this interval, the cluster close-packed structure is disturbed and forced to transform to another stable structure. Hence, two C_{60} molecules and 14-16 Au atoms are removed simultaneously from the initial $(C_{60})_{14}$–$(Au)_{63}$ cluster. As studied in chapter 3 and reported in ref. [14], there is no another transition hybrid cluster between $(C_{60})_{14}$–$(Au)_{63}$ and $(C_{60})_{12}$–$(Au)_{49}$. We can show that the $(C_{60})_{10}$–$(Au)_{35}$ cluster can be modified further to $(C_{60})_{7}$–$(Au)_{19}$, which is the smallest and most observed cluster. Here, C_{60} molecules and Au atoms that have been removed either move elsewhere on the surface due to their high mobility at room temperature, or to somewhere on the tip. This transformation occurs very short timescale (immediately after manipulation), so cannot be imaged by STM. The tip may also disturb the cluster by removing a few Au atoms from the Au island. This may increase the distance between the C_{60} molecules and the step edge of the island, and hence the cluster transforms to a "one size smaller" stable cluster. Certainly, these molecules and atoms do not move to the tip apex, because the tip state did not change during or after the manipulation.

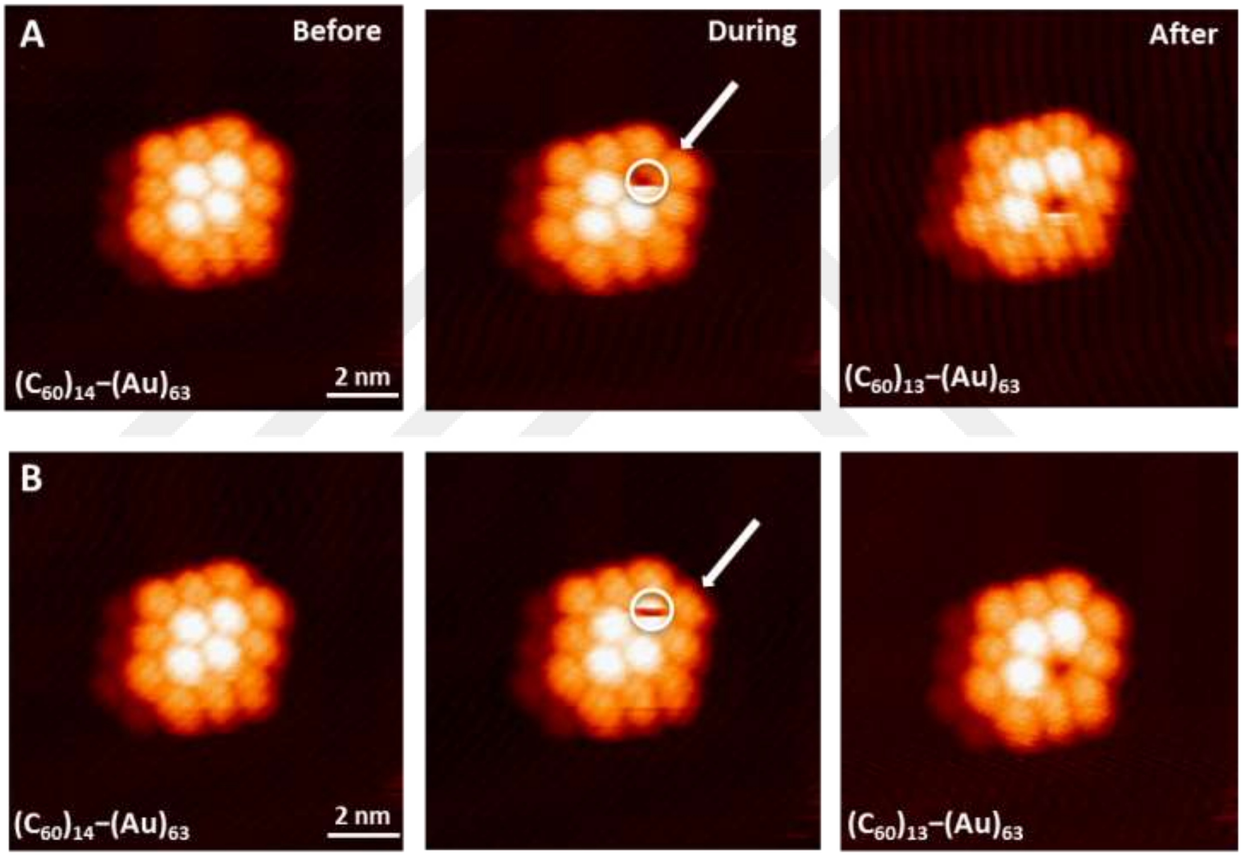

Figure 65. A and B. Before, during, and after images of the manipulation of a single C_{60} molecule on the top of a $(C_{60})_{14}$–$(Au)_{63}$ cluster. The manipulation of the selected single C_{60} molecule on the top is possible by a 1.2 nm Z- displacement towards the surface. However, because of the mobility of single C_{60} molecules at room temperature and the tip effect, the C_{60} molecule on the top of this cluster hops from one empty site to another.

Figure 65 demonstrates the removal of a selected C_{60} molecule from the top of a $(C_{60})_{14}$–$(Au)_{63}$ cluster with before, during and after images. Figure 65A shows a successful manipulation (the white circle) for a selected C_{60} molecule. However, it can be seen that on the after image, the C_{60} molecule on the top moves to the empty site. Figure 65B is another example showing the repositioning of a C_{60} molecule from the top of the cluster after attempting to remove the selected C_{60} molecule. Nevertheless, this attempt was also unsuccessful and another C_{60} molecule filled the position.

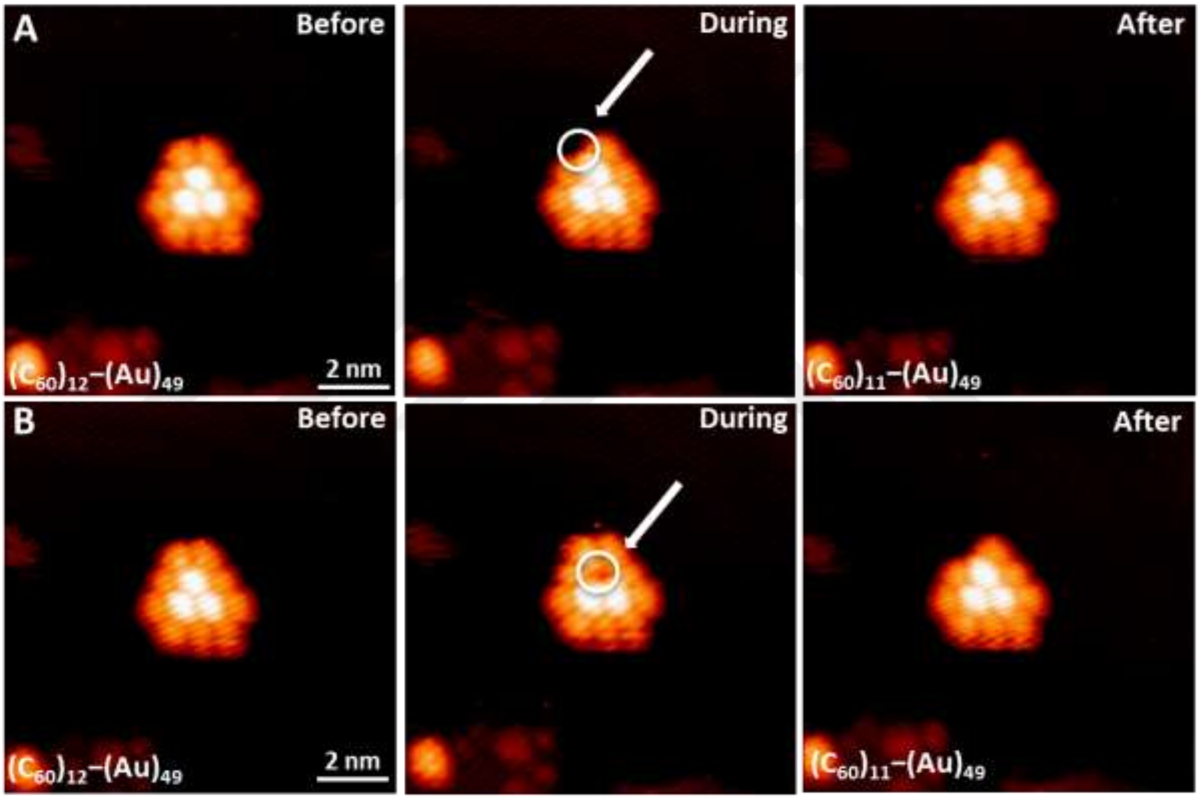

Figure 66. Before, during, and after images for a single C_{60} molecule manipulation on the side and top of the $(C_{60})_{12}$–$(Au)_{49}$ cluster are shown in panels A and B. A. Manipulation of a single C_{60} molecule from the side of the cluster without deforming the cluster. B. Manipulation of a single C_{60} molecule from the side of the cluster.

A first C_{60} manipulation is possible on the top. However, because of the high mobility of the C_{60} molecule and the tip effect, the C_{60} molecule moves to another empty site on the top of the structure. Therefore, it was not possible to manipulate a second C_{60} molecule away from the top of the cluster. Once the binding stability of the top four C_{60} molecules has been broken, they move on the Au island towards the empty sites via an attractive tip-induced force [18, 25].

During the cascade manipulation process, there is a small possibility that the cluster shape can remain unchanged. Figure 66 shows the manipulation of a single C_{60} molecule from the tops and sides of $(C_{60})_{12}$–$(Au)_{49}$ clusters with before, during and after images. In Figure 66A, a selected C_{60} molecule from the side of the cluster is removed successfully and whilst the cluster framework remains the same, it is transformed to the $(C_{60})_{11}$–$(Au)_{49}$ cluster. In Figure 66B, a selected C_{60} molecule from the top of the cluster is removed successfully; however, a C_{60} molecule from the side of the cluster jumps onto the top of the cluster. We consider the number of Au atoms in the island did not change due to the unchanged cluster framework.

Removing a C_{60} molecule from the side and top of the cluster is possible at room temperature. As mentioned earlier, the molecules interact only weakly with the Au(111) surface so, therefore, C_{60} molecules have a high mobility and can thus travel large distances across the surface. As seen in Figure 66B, the after image, one of the C_{60} molecules has jumped to top of the cluster to fill the empty site. We assume that the C_{60}-C_{60} interaction on the top of the cluster is stronger than the side, because a C_{60} molecule on the side of the cluster can interact with two neighboring and one on the top C_{60} molecules, an additional Au surface and an Au island step. However, a C_{60} situated on the top of the cluster interacts with two neighbouring clusters on the top, four sides of the cluster and an Au island. From this, it is probable that the summed interactions for a C_{60} molecule situated on the top of the cluster are larger than those for one situated on the side, and therefore the C_{60} jumps from the side to the top of the cluster.

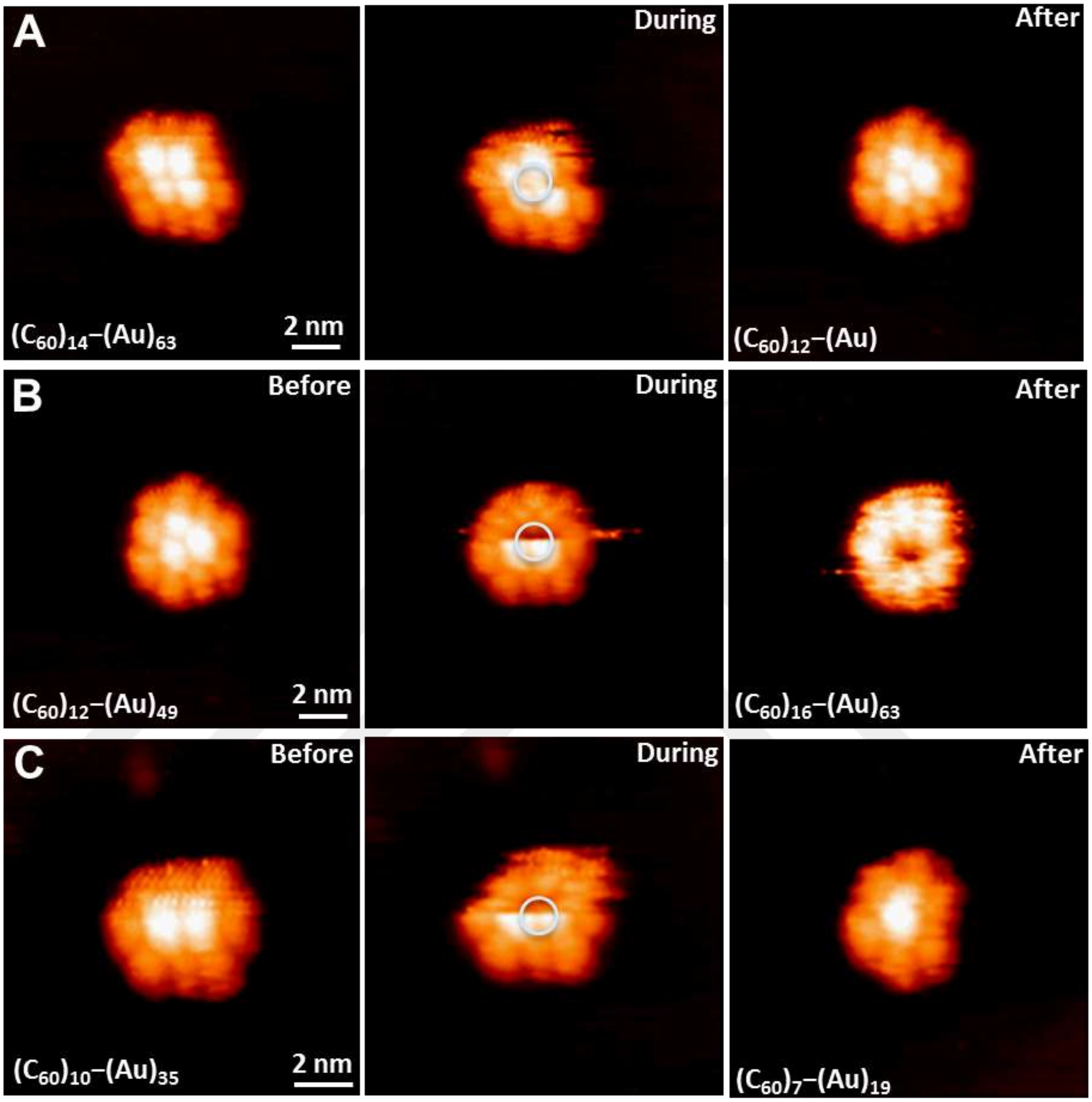

Figure 67: Pushing down at the centre of the bright molecules with an STM tip, as applied to different clusters: $(C_{60})_{14}$–$(Au)_{63}$, $(C_{60})_{12}$–$(Au)_{49}$, and $(C_{60})_{10}$–$(Au)_{35}$, shown in panels A, B, and C, respectively. Driving the tip at the centre of clusters with Z=1.3 nm, transforms the clusters to either a one (magic number) size smaller cluster, or a ring cluster.

Pushing down on the bright molecules on the top of the cluster with an STM tip, Z=1.3 nm, allows for the transformation of the cluster to either one (magic number) size smaller or to a ring cluster (see Figure 67). The STM tip is placed on the middle of the $(C_{60})_{14}$–$(Au)_{63}$,

$(C_{60})_{12}$–$(Au)_{49}$ and $(C_{60})_{10}$–$(Au)_{35}$ clusters, as indicated by the white circle in Figure 67A, B and C. After manipulation, the $(C_{60})_{14}$–$(Au)_{63}$, and $(C_{60})_{10}$–$(Au)_{35}$ clusters are transformed to the next smallest stable cluster, $(C_{60})_{12}$–$(Au)_{49}$ and $(C_{60})_{7}$–$(Au)_{19}$, respectively. On the other hand, the $(C_{60})_{12}$–$(Au)_{49}$ cluster is transformed to a ring cluster.

Different Z-displacements (1.5, 1.4, 1.3 and 1.2 nm) were used for the manipulation of the middle of the clusters. The best displacement was found to be 1.3 nm; the displacements of 1.5 and 1.4 nm destroyed the clusters.

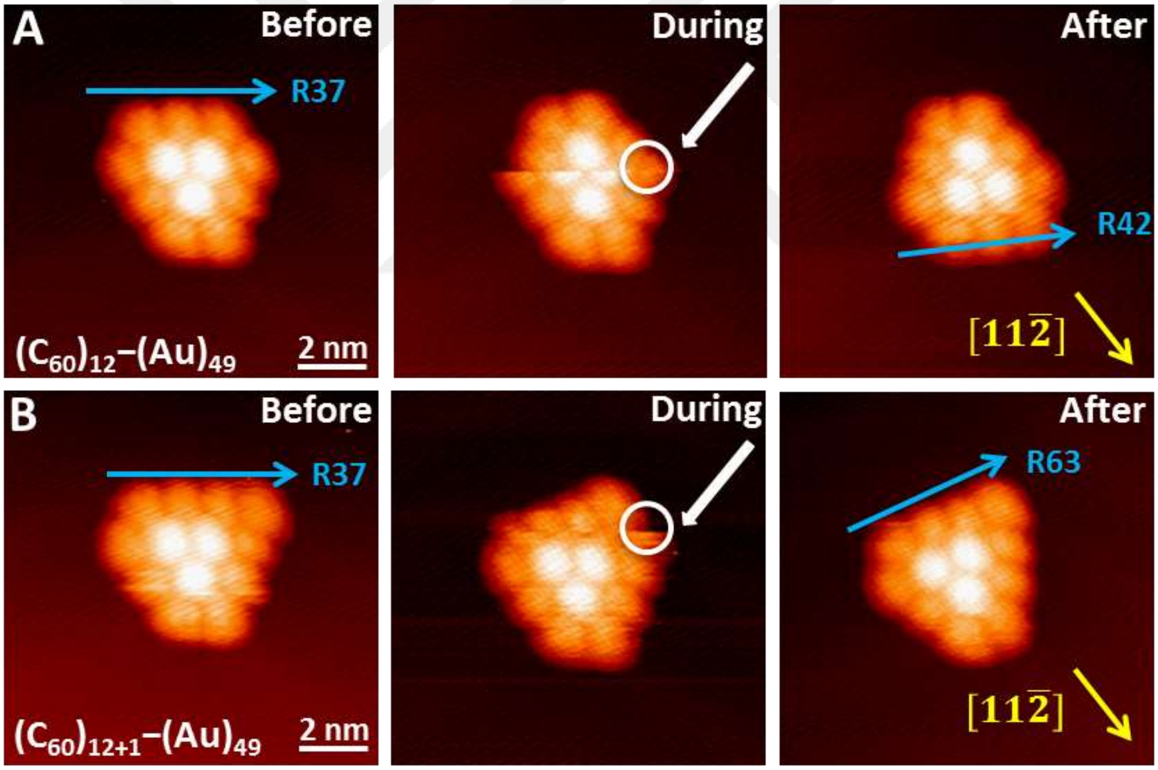

Figure 68. STM images showing, before, during, and after images for the clusters disturbed by STM and causing a rotation with the STM tip. A. The $(C_{60})_{12}$–$(Au)_{49}$ cluster rotates 180° from initial R37 to R42. B. The $(C_{60})_{12+1}$–$(Au)_{49}$ cluster rotates from initial R37 to R63. The close packing directions of the clusters are found by using the $[11\bar{2}]$ direction of the Au(111) surface as a reference.

The manipulation of a selected C_{60} molecule (indicated by the white circle) belonging to the $(C_{60})_{12}$−$(Au)_{49}$ cluster caused a rotation, which is illustrated by before, during, and after images in Figure 68A. The manipulation caused a rotation (upside down) R47 without destroying the shape of the cluster. Figure 68B is another example of a rotation by the $(C_{60})_{12+1}$−$(Au)_{49}$ cluster, from R37 to R63. Here, the close packing directions of the clusters are found by using the $[11\bar{2}]$ direction of the Au(111) surface as a reference.

During the manipulation, the STM tip modifies the orientation of the cluster on the Au(111) surface. The manipulation of the clusters is successful about 80% of the time at room temperature. When manipulation is not successful, the clusters will at rotate on the surface due to the tip. Once a C_{60} molecule is removed from the cluster, the molecule may return to the cluster due to the high mobility of the C_{60} molecule at room temperature. This may, in itself, result in a rotation of the cluster on the surface.

The atomic configuration of the tip is not well known. We consider two possibilities for the tip apex. First, annealing the tip up to 473 K does not remove the oxide layer that forms during the electrochemical etching process. The adsorption of C_{60} molecules study on the WO_2/W(111) surface at room temperature [195] also demonstrates that the weak molecule-surface interaction causes diffusion of the molecules on the WO_2/W(111) surface due to the low barrier to diffusion. Therefore, if the molecule moves the tip state, it can diffuse across a long distance instead of a localised attachment to the tip apex. Second, the tip apex is very likely to be terminated by crashing the tip to the surface and picking up Au surface atoms due to the high voltage pulses used. This is because molecules not attached to the tip apex probably diffuse either onto the surface or elsewhere on the tip.

In the contact regime, short-range forces, van der Waals forces and electrostatic forces can be valid. The electrostatic force increases with increasing bias voltage (independent of polarity). We observed that manipulation is also successful at zero-bias voltage. Thus, the effect of bias voltage can be easily excluded. The short-range and van der Waals forces depend on the tip/sample separation; as separation decreases, the forces increase. In the contact regime, the molecule is mechanically pushed away from the STM tip due to the repulsive forces between the tip apex and the C_{60} molecule.

4.4 Conclusion for Manipulation at RT

In conclusion, with the STM tip, the manipulation of a selected C_{60} molecule is possible for C_{60} islands or for the hybrid clusters. In this section, we determined the best manipulation parameters at room temperature. The manipulation of a $(C_{60})_{14}$–$(Au)_{63}$ cluster to another small size cluster in the appropriate magic number sequence is possible by disturbing the clusters packing. Here, we showed that there is no transition form of cluster between the hybrid clusters. Removing a C_{60} molecule also results in the removal of the Au atoms attached to it (or maybe attached to the tip). Removing these Au atoms leads to a shift of the Au island underneath the C_{60} layers and, therefore, the cascade manipulation from the $(C_{60})_{14}$–$(Au)_{63}$ cluster to $(C_{60})_7$–$(Au)_{19}$ cluster is successful at room temperature. A selected C_{60} from the top of the cluster can be successfully removed; however, removing a second C_{60} is ‘prohibited’ because of tip effects and the switching of C_{60} molecules from one empty site to another on the top of the cluster. If we consider the two different configurations for a cluster, the bright and the framing C_{60} molecules, then a C_{60} on *top* of the Au island is more stable than those arranged *around* the island. This is most probably due to a stronger total van der Waals interaction between the C_{60} molecules on the top of the island than those at its edges. During manipulation, the STM tip may alter the orientation of a cluster on the Au(111) surface. This is because the high mobility of C_{60} molecules at room temperature and the consequently, relatively high possibility of a C_{60} molecule coming back to the cluster after any attempt to remove a selected C_{60} molecule. Pushing down on the top bright molecules on the clusters caused a cluster transformation, either to one magic number size smaller or to a ring cluster. When such a transformation was not observed after manipulation, there was the likelihood that a rotation of the cluster had occurred on the surface (at room temperature). In this manner, hybrid clusters are stable on the Au(111) surface at room temperature even when removing a selected C_{60} molecule via the STM tip. Such a manipulation is also successful with a zero bias voltage, thus it can be seen that the manipulation is independent of the electric field. It was found that the manipulation of the hybrid clusters is possible via the mechanical interaction between the tip and C_{60} molecule.

4.5 Manipulation of Hybrid $(C_{60})_m$−$(Au)_n$ Clusters at 110 K

Because of the high mobility of C_{60} molecules on the Au(111) surface at room temperature, we decided to perform manipulation experiments at low temperature (110 K). One of the main reasons behind this thinking was that, if we were to perform the manipulation experiment at low temperature, we might be able to take away *all* C_{60} molecules from the upper terrace of the cluster, because the thermal motion of the molecules is effectively frozen (or, at least, significantly reduced). This would allow for the creation of a hollow cluster. One might consider, however, the possible consequences of the removal of the top bright molecules: would the shape of the cluster remnant change, or would it lose its regular shape? If you then contact the tip on a different cluster to pick up C_{60} molecules and move the tip over the hollow cluster, can one (re)fill the hollow?

Next, if we remove one molecule from the edge of the cluster, where does the molecule move to? Simply, the removed molecule may attach to the tip, or might displace sideways on the cluster. In subsequent scan, we might find this molecule at the side of the cluster or, indeed, if this molecule had a small number of Au atoms around it, this molecule might have a different appearance from a normal isolated C_{60} molecule.

Finally, for the $(C_{60})_{12}$-$(Au)_{43}$ cluster, if the tip is pushed down at the centre of the three bright molecules, can we perhaps squeeze all three molecules down the atomic terrace? Therefore, after the production of hybrid clusters, the sample will be cooled to 110 K and we will perform our manipulation experiments. First, we determined the optimal manipulation Z displacement, which is determined from the same statistic approach as discussed in section 4.2. Hence, the Z displacement chosen for our experiments was 1.2 nm for the majority of manipulations. In this section, unless otherwise indicated, all images are recorded at a -1.744 V bias voltage and 47 pA tunnelling current, and manipulations are performed with tip displacement of 1.2 nm at 110 K.

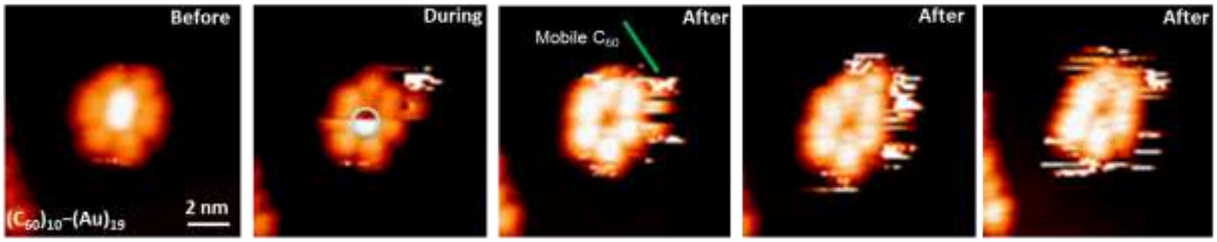

Figure 69: Manipulation of the molecules on the top of the $(C_{60})_7$-$(Au)_{19}$ cluster, as performed at 110 K (are shown is 10 x 10 nm^2). A C_{60} molecule on the top was removed (indicated by the white circle on the during image) and observed at the side of the cluster in subsequent scans (indicated by the green arrow).

We performed the manipulation on the smallest cluster, $(C_{60})_7$-$(Au)_{19}$, at 110 K, attempting to remove a C_{60} molecule from the top of the cluster, as shown in Figure 69. It can be seen that the molecule was successfully removed from the top (indicated by the white circle on the during image). A hollow cluster was generated and the removed molecule was observed at the side of the cluster in subsequent scans (indicated by the green arrow on the first after image).

It is obvious that the removed C_{60} molecule preferred to stay around the cluster. This is because the mobility of the molecules is decreased by the reduction in temperature to 110 K. Certainly, this temperature is not enough to freeze the molecule on the surface, so we observed mobile single C_{60} molecule even around the cluster, after only a few subsequent scans. It is hard to know whether the number of Au atoms in the cluster remained the same or not as shown in Figure 69. Therefore, the manipulation experiment performed for the top three molecules of the $(C_{60})_{12}$-$(Au)_{49}$ cluster is shown in Figure 70. The three C_{60} molecules were systematically removed from the top of the cluster. These molecules were subsequently observed at the side of the cluster in scans performed after the manipulation. The selected molecules are indicated by the white circles on the during images.

Figure 70: Manipulation of the C_{60} molecules on the top of the $(C_{60})_{12}$-$(Au)_{49}$ cluster was performed at 110 K (15 x 15 nm^2). The three C_{60} molecules (indicated by the white circles on the during images) were systematically removed from the top. These molecules were later observed at the side of the cluster.

Removing C_{60} molecules from the top of the cluster was successfully achieved without removing any Au atoms and destroying the Au island orientation. The first C_{60} molecule removed was observed around the cluster, and was quite mobile. This movement of the single C_{60} molecule around the cluster is probably due to the tip field effect or temperature. The energetic barrier to escape from around the cluster to moving elsewhere on the surface is larger at 110 K. However, once we remove the second and third molecule at the side, these three molecules became stable. This is probably because the first molecule (mobile) interacts with additional two C_{60} molecules and results in to stopping the mobility of the molecule. If it can overcome the effect of the additional C_{60} molecule, it may leave this orbit and move elsewhere on the surface.

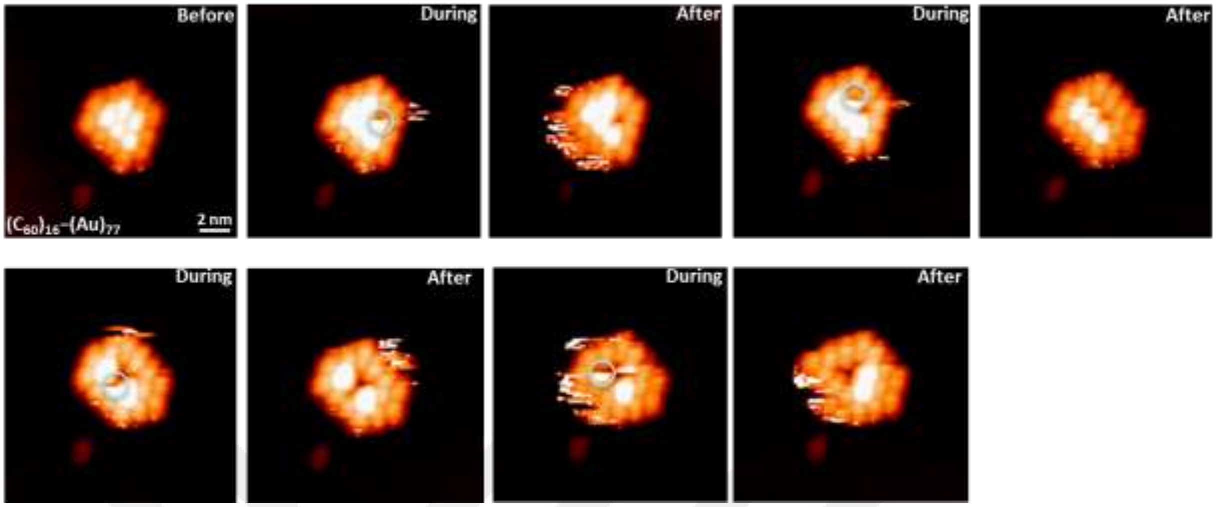

Figure 71: Manipulation of the molecules on the top of the $(C_{60})_{16}$-$(Au)_{77}$ cluster, as performed at 110 K (15 x 15 nm^2). The STM images show the successful manipulation of three molecules on the top of the cluster. However, after removing the third molecule, the next molecule starts to jump to the empty sites on the top while the removed molecules can be observed around the cluster.

The results of the manipulation of the selected molecules on the top of the $(C_{60})_{16}$-$(Au)_{77}$ cluster are presented in Figure 71. The first three molecules were removed without destroying the cluster framework, as can be seen in consecutive STM images. After removing the three molecules, the next molecule starts to jump to the empty sites on the top, while the removed molecules remain around the cluster. Performing the manipulation to the molecules on the top of the $(C_{60})_{16}$-$(Au)_{77}$ cluster indicates that removing three C_{60} molecules resulted in empty sites on the top of the cluster. In the following manipulations, the molecules preferred to jump to the empty sites on the top, rather than jump to the side, of the cluster.

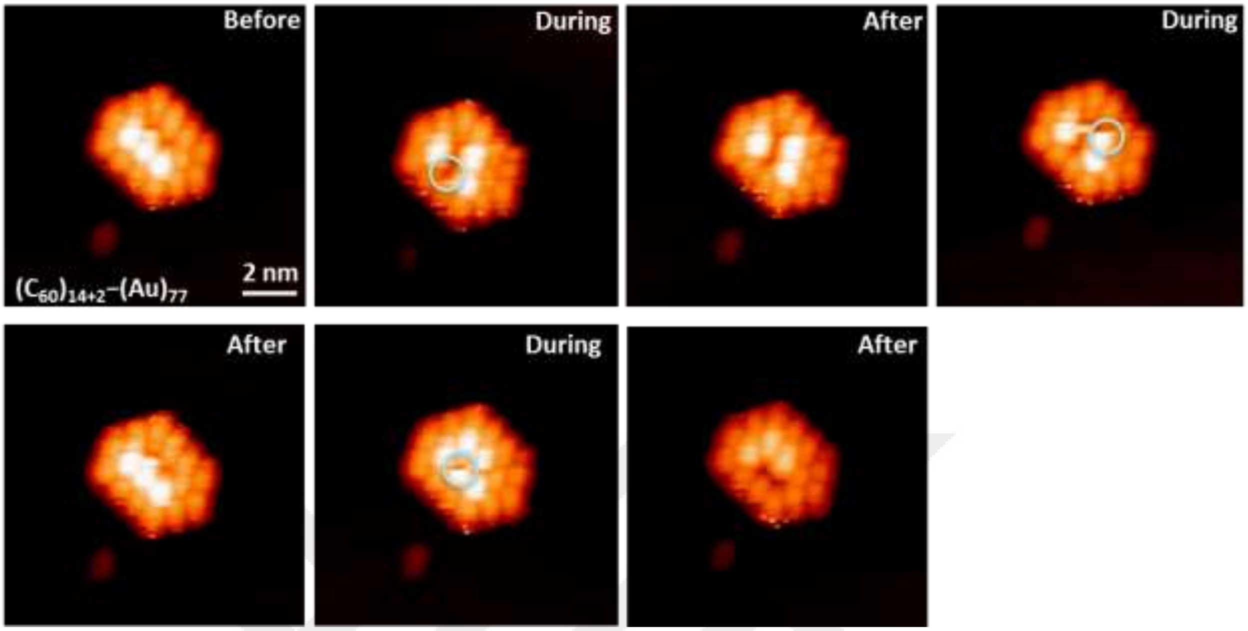

Figure 72: Manipulation of the $(C_{60})_{14+2}$-$(Au)_{77}$ cluster, as performed at 110 K (15 x 15 nm^2) to remove the molecules on the top of the cluster, which already has vacancies. As seen in consecutive before, during and after images, the manipulation was performed on the bright molecules one by one. However, the molecule moved to existing vacancies.

In Figure 72, the manipulation of the $(C_{60})_{14+2}$-$(Au)_{77}$ cluster is continued at 110 K to remove three top molecules when the cluster already had vacancies. As seen in the associated consecutive images, the molecules jumped to existing vacancies on the top of the cluster. Removing a molecule from the top where several vacancies are already present is clearly not possible.

4.6 Directional Manipulation of Hybrid $(C_{60})_m$−$(Au)_n$ Clusters at 110 K

Using with the considerable advantages offered by low temperature, the manipulation can be performed with increased control. After manipulation of the clusters at room temperature, the C_{60} molecules and Au atoms move instantly from the clusters and transform into another small, stable cluster. However, at 110 K, the C_{60} molecules prefer to stay at elbow sites around the clusters, as well as Au atoms. Therefore, we achieved a removal of C_{60} molecules without the associated room temperature removal of Au atoms. With this advantage, we investigated a directional manipulation. A schematic diagram for the directional manipulation on a C_{60} molecule is illustrated in Figure 73. The green line indicates what is considered to be the imaginary centre line of the molecule, the red cross indicates the selected manipulation point, and the yellow arrows indicate the direction of motion of the molecule after the manipulation attempt. If the manipulation was performed at the bottom of the line, the molecule moves in the ‘ up’ direction (see Figure 73A). If the manipulation is performed to the left, the molecule moves to the right (see Figure 73B).

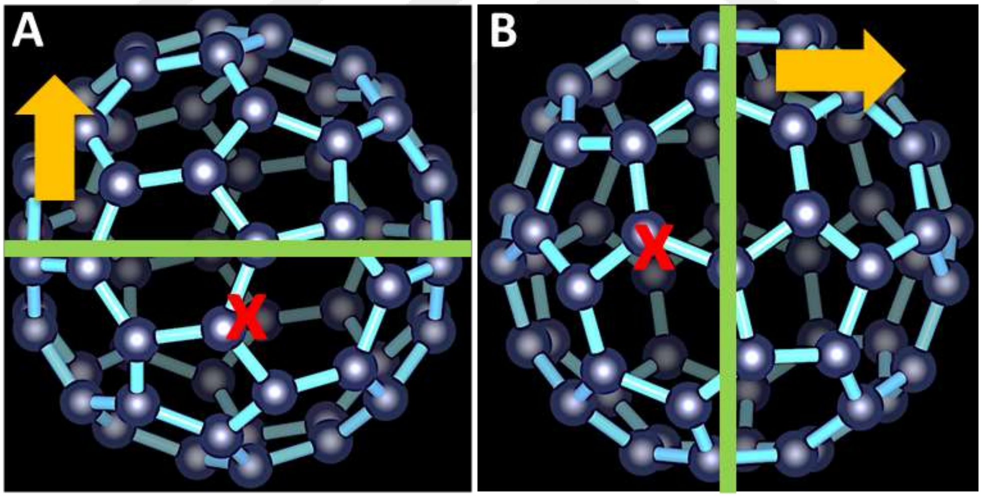

Figure 73: Schematic diagram for the directional manipulation experiment. A. If the manipulation is performed at the bottom, the molecule moves towards the ‘up’ direction around the cluster. B. If the manipulation is performed to the left, the molecule moves to the right. Here, the green line is considered the nominal imaginary centre line of the molecule, the red cross indicates the selected manipulation point, and the yellow arrow indicates the direction of motion of the molecule.

The directional manipulation of a selected C_{60} molecule on the $(C_{60})_{16}$-$(Au)_{77}$ cluster was performed with a tip displacement of 1.3 nm (indicated by the white circles) in Figure 74. As seen in these consecutive images, the molecule at the side is removed to a location near to the cluster. In the next manipulation process, the additional molecule at the side is kicked back to original position and the hybrid cluster is reformed. This is because the cluster does not lose Au atoms during manipulation, thus maintains the shape of the Au island.

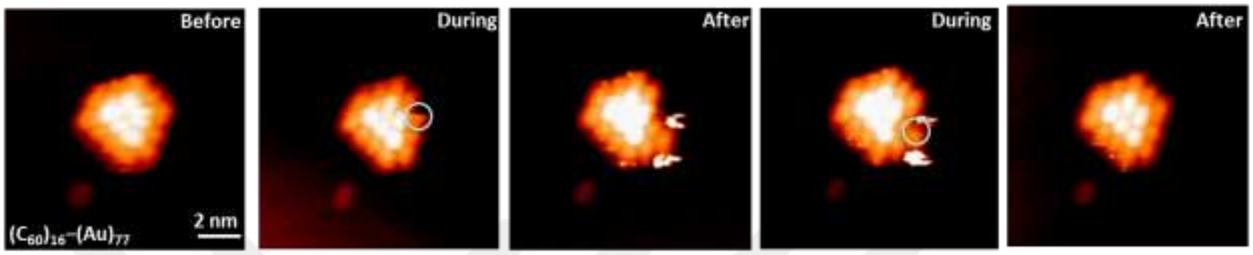

Figure 74: Manipulation of the $(C_{60})_{16}$-$(Au)_{77}$ cluster, as performed at 110 K (15 x 15 nm^2) to remove a molecule from the side (indicated by the white circles). As seen in consecutive before, during and after images, the molecules are removed from the side to nearby the cluster. In the next manipulation process, the additional molecule at the side is kicked back to its original position, reforming the original hybrid cluster.

With the directional manipulation, the removed C_{60} molecule can return to its original position. This arises from the fact that the manipulation can be performed without the lost of Au atoms from the Au island of the cluster. We decided to try the directional manipulation by removing a few C_{60} molecules, which we anticipated might then kick back to empty sites to obtain a hybrid cluster. This idea was tested on the $(C_{60})_{12}$-$(Au)_{49}$ cluster.

In Figure 74, the manipulation of a selected C_{60} molecule on the $(C_{60})_{12}$-$(Au)_{49}$ cluster was performed (indicated by white circles). Three molecules were removed from the side of the cluster, one by one to lie nearby the cluster. In the next manipulation process, the additional molecules on the side had kicked back to their original positions, thus reforming the original hybrid $(C_{60})_{12}$-$(Au)_{49}$ cluster. First, the cluster is intentionally disturbed towards another irregular cluster, as seen in Figure 75. The removed molecules stayed around the cluster. Then, using the directional manipulation idea, the molecules were manipulated back to their original positions.

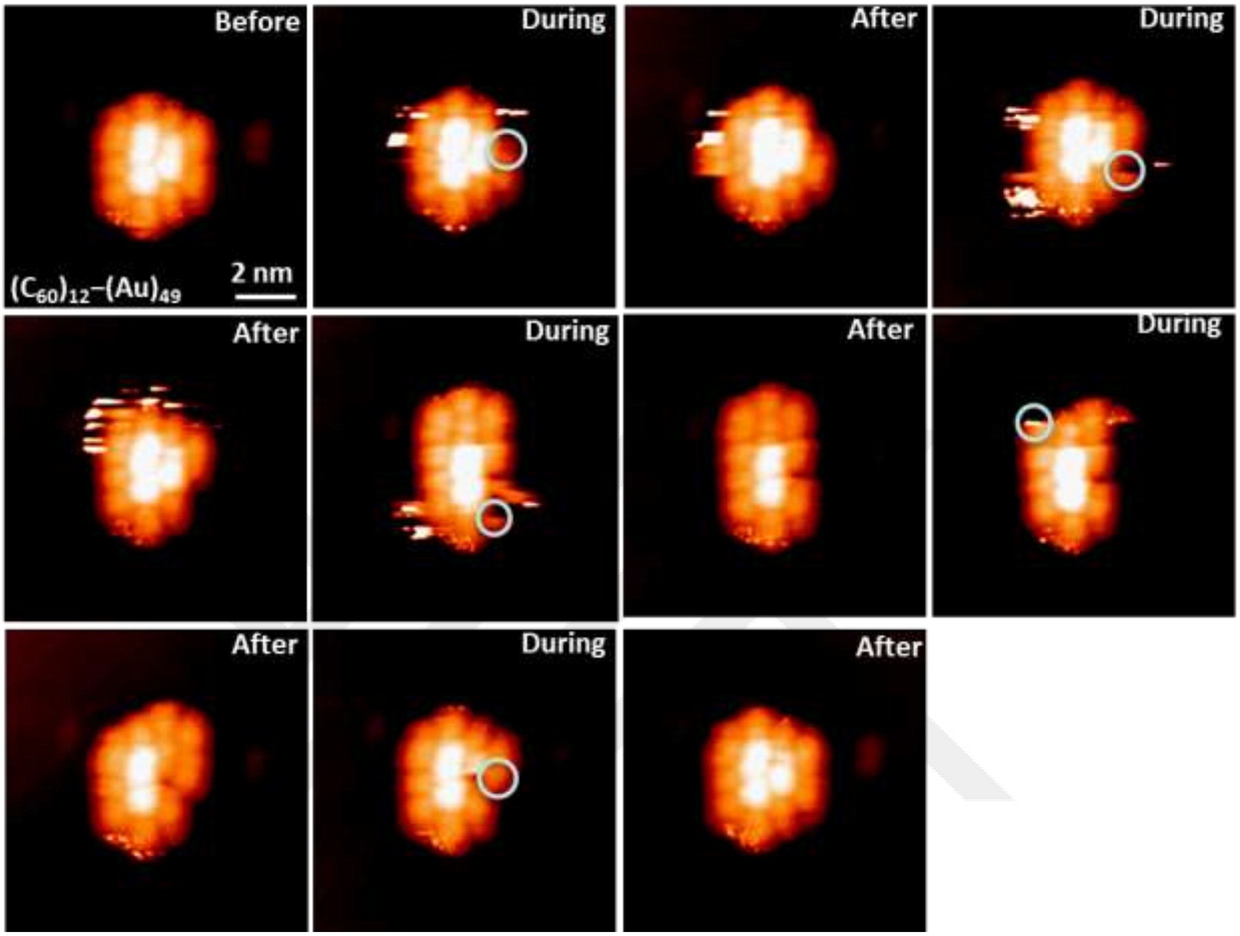

Figure 75: Manipulation of the $(C_{60})_{12}$-$(Au)_{49}$ cluster, as performed at 110 K (12 x 12 nm^2) to remove a molecule from the side (indicated by white circles). STM images before, during and after show the three molecules removed from the side of the cluster, one by one, to lie around the cluster. In the next manipulation process, the additional molecules on the side kicked back to their original positions to obtain the hybrid $(C_{60})_{12}$-$(Au)_{49}$ cluster.

4.7 Conclusion for Manipulation at 110 K

Cluster manipulation at 110 K contributed to the answers to the questions reised in section 4.2. Removing all the C_{60} molecules from the top for small clusters (i.e. less than 12 C_{60} molecules) can be achieved *without* destroying the cluster frame or removing Au atoms form the Au island. However, removing a molecule from the top for big clusters is not possible when there are more than a few vacancies on the top of the cluster. Even at 110 K, the molecules are still sufficiently mobile that they can jump to the empty sites on the top of the Au island. After manipulation, C_{60} molecules prefer to stay on the surface around the cluster. It is clear that the molecules did not attach to the tip. A single molecule around the cluster is highly mobile until an additional molecule is kicked to the side. It can be seen that even a surface temperature of 110 K is not enough to freeze molecules on the surface or the top of the Au island. The molecules still have sufficient mobility to move around fairly freely. One other important achievement is the directional manipulation. The molecule can be manipulated in such a way as to be moved a certain direction via the STM tip. Hence, we can reform the cluster without changing the Au island orientation.

CHAPTER 5

COMPARATIVE STUDY of MANIPULATION of CHLOROBENZENE and OXYGEN MOLECULES on the Si(111)-7x7 SURFACE

The surfaces of semiconductors play in important role in microelectronic and photonic device technologies. The scanning tunnelling microscope is a powerful tool to determine not only the surface structure but also to manipulate individual atoms and molecules adsorbed on these surfaces [5]. The main purpose of this chapter is to compare (suppression of) *non-local manipulation* of two different molecules (chlorobenzene (PhCl) and oxygen) on the Si(111)-7x7 surface at room temperature. The suppression effect was discussed in terms of injection current-dependent measurement of PhCl molecules and the effect of electric field across the surface. Non-local manipulation of oxygen has not been studied before. The chapter also covers the details of the *local* manipulation of chlorobenzene molecules on the Si(111)-7x7 surface at room temperature. Further, the local manipulation of bright and dark sites of oxygen molecules was performed to determine the manipulation threshold voltage.

5.1 Local and Non-local Desorption of Chlorobenzene Molecules

5.1.1 Local Desorption of Chlorobenzene Molecules

In this section, local manipulation of PhCl molecules was studied by electronic excitation of the bond between the adsorbate and the surface atoms. Initial adsorption of chemisorbed and physisorbed chlorobenzene molecules on the Si(111)-7x7 surface has been extensively studied

[32, 91-93, 110, 196]. In this preliminary study, we focused on local STM manipulation by measuring the excitation time for manipulation of chemisorbed PhCl molecules on the Si(111)-7x7 surface as a function of applied bias voltage. The excitation time is the time for desorption of a PhCl molecule to occur as a results of the electron current. During the manipulation, the STM tip was kept over the molecule in constant current mode (100 pA), then a sample bias voltage was applied for 2 seconds.

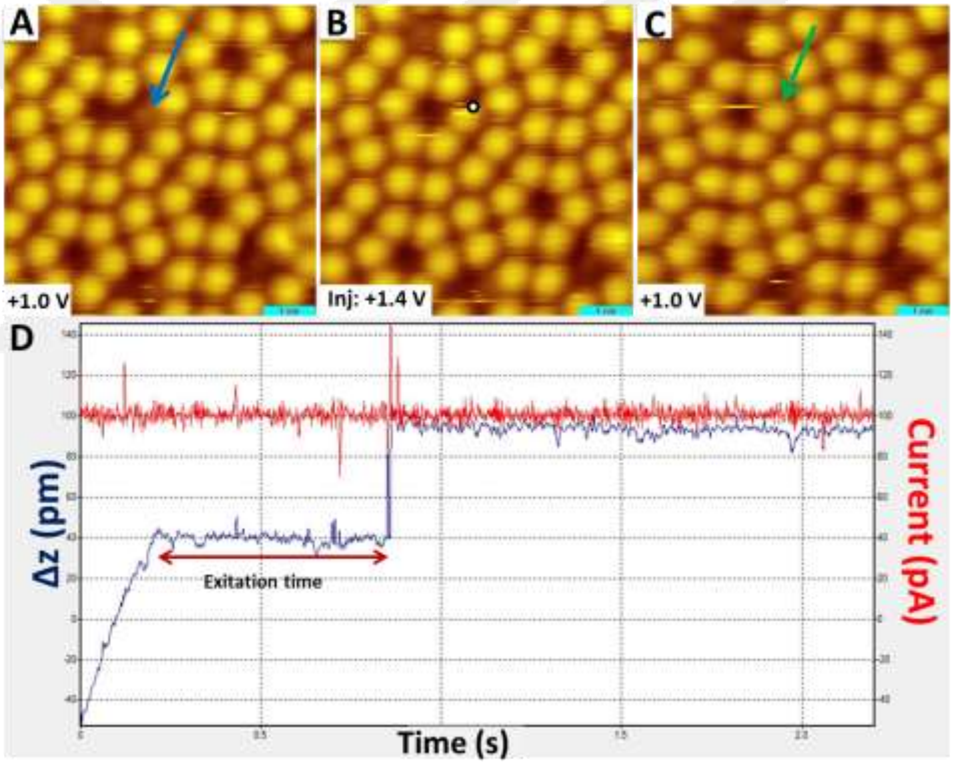

Figure 76: Local manipulation of PhCl molecules on the Si(111)-7x7 surface performed at fixed tunnelling current at room temperature. A, B, C. STM topographies show before, during and after manipulation images, respectively. The manipulation was performed with a bias voltage of +1.4 V and tunnelling current of 100 pA for 2 s while feedback loop is switched on and scanning conditions were +1.0 V and 100 pA for all images. The blue arrow indicates the site of PhCl molecule (bonding with an adatom and a rest-atom), the black circle indicates the manipulation site, and the green arrow indicates the clear Si surface site after manipulation. D. The tip displacement and tunnelling current recorded during manipulation as a function of the injection time.

A dose of 0.4 ± 0.06 L of PhCl molecules was dosed on the Si(111)-7x7 surface at room temperature to obtain one molecule per unit cell. A local manipulation experiment is shown in Figure 76. In this experiment, a single PhCl molecule is removed from the Si(111)-7x7 surface by electron injection at fixed tunnelling current at RT. Figure 76A, B, C are STM topographies taken respectively before, during and after the manipulation. Here, the manipulation was performed at +1.4 V and 100 pA for 2 s and scanning conditions were +1.0 V and 100 pA. A 2 second injection was repeated up to 5 times (total 10 s), so that the drift of the STM tip was reduced during electron injection. The blue arrow indicates the site of the PhCl molecule (dark adatom site) bonding to an adatom and a rest-atom. The red dot indicates the manipulation site, and the green arrow indicates the clear Si surface after the manipulation. The tip displacement and fixed tunnelling current are recorded during manipulation as a function of the injection time (see Figure 76D).

The feedback loop remains engaged with a constant tunnelling current during electron injection into the PhCl molecule. Thus the tip movement as a function of time confirms the successful desorption of the molecule, by pulling away from the surface (since the molecule suppresses the conductance), as seen in Figure 76D. At constant tunnelling current, the tip displaces ~55 pm during the manipulation event. The meaning of this tip displacement is that the molecule is desorbed from the surface after the excitation time of 0.65 s via electron injection. This injection leads to breaking of the bond between the adatom and rest-atom of silicon and the carbon atoms of the PhCl molecule. This desorption results in the appearance of a normally bright adatom spot at the site corresponding to an increased tunnelling current, thus the STM tip displaces.

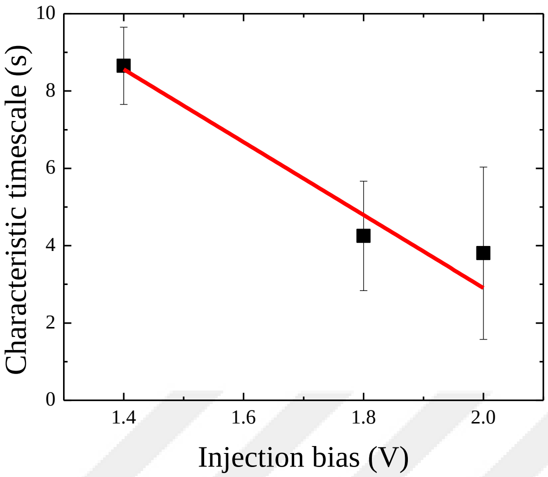

Figure 77: The characteristic timescale of desorption of the PhCl molecule as a function of injection bias voltage. The desorption threshold is found to be +1.4 V and the desorption time decreases linearly with increasing injection bias voltage.

Figure 77 illustrates the characteristic timescale of the PhCl molecule as a function of injection bias voltage. All injections were induced into the molecule at fixed tunnelling current of 100 pA for 2 s pulse as demonstrated in Figure 77. The injection voltage was increased from +1.0 V to +2.0 V. The timescale decreases linearly with increasing injection bias voltage. This linear trend is similar with the timescale of desorption of toluene molecule on the Si(111)-7x7 surface [109]. The desorption threshold is found to be +1.4 V (no desorption observed below this point). This point reveals the position of lowest unoccupied molecular orbital (LUMO) for electron induced desorption [109]. The non-local desorption activated at +2.1 V for the PhCl molecule on the Si(111)-7x7 surface at room temperature [66]. The local desorption threshold, +1.4 V, is lower than non-local desorption, +2.1 V.

5.1.2 Non-local Desorption of Chlorobenzene Molecules

To explore the effect of the tip-sample distance in non-local desorption of the PhCl molecule on the Si(111)-7x7 surface, the non-local injection current was increased from 0.2 nA to 8 nA at constant injection voltage of +2.7 V while keeping the number of injected electrons constant. The idea is to decrease the tip-sample distance up to 1 Å to explore the effect of the tip proximity and especially the electric field on desorption in a range of 40 Å from the tip which is called the "suppression" region.

The clean surface was prepared at RT as mentioned in Section 2.6. First, a Si(111)-7x7 surface with chemisorbed PhCl was scanned (51 x 51 nm^2 area) at +1.0 V bias, 100 pA tunnelling current, as shown in the STM image of Figure 78A. Then, a corner hole was chosen in the middle of the image (indicated with a red dot). Electrons were injected into the selected corner hole with a bias of +2.7 V (chosen above non-local desorption threshold of +2.1 V) while keeping the number of electrons constant. Here, Charge (C) = Current (A) x Time (s), therefore, the charge dose is constant at about $4.0 \pm 0.1 \times 10^{10}$ e^- per injection experiment. The XPMPro 2.0.1.6 software allows us to apply drift correction, which is used to minimize unwanted tip x and y displacement due to piezo creep and thermal expansion/contraction during the injection. Finally, after the charge injection step, the area is scanned again to compare before and after images and thus count the number of desorbed molecules. It is apparent from the image shown in Figure 78B that there is a central area (diameter of 40 Å) where the PhCl molecules are removed from the surface. The size of this area increases with increasing bias voltage or with an increasing number of electrons injected into the surface.

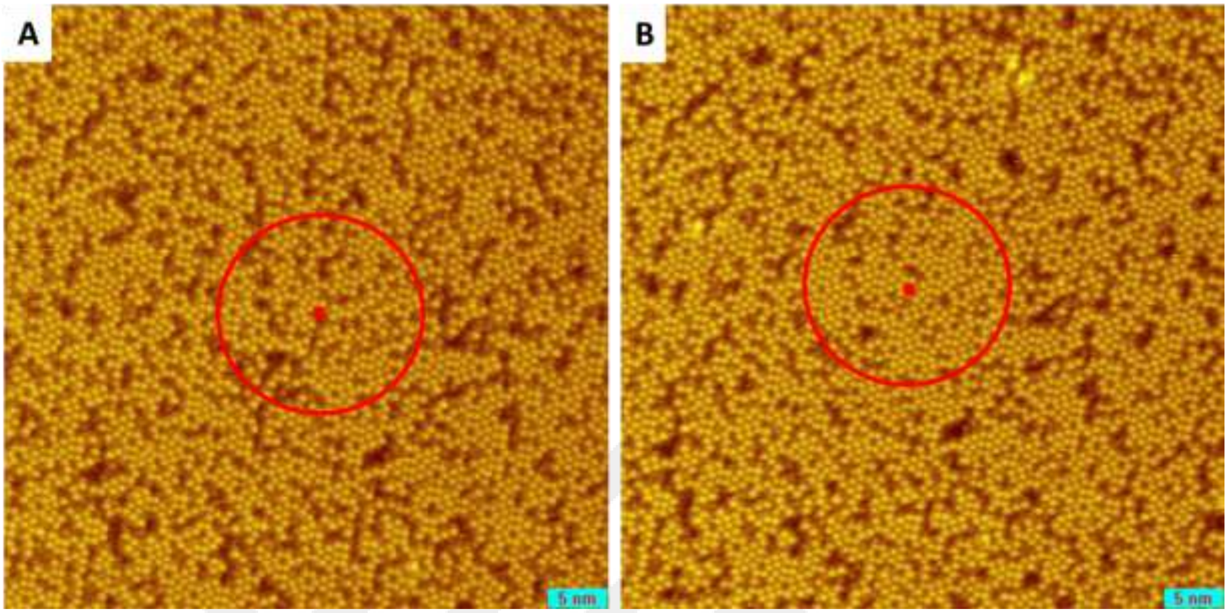

Figure 78. STM images before (A) and after (B) for non-local desorption. The red dot and circle indicate the injection point and the main affected area. The images cover a 51.2 x 51.2 nm^2 area and the passive imaging parameters are +1 V, 100 pA. The injection is performed at +2.7 V, 0.5 nA, for 14 s.

Sloan *et al.* [39] employed a formula for the non-local desorption probability per electron when counting the number of PhCl molecules in ‘before’ and ‘after’ images (for more details see section 2.6.3 “Analysis Method”). Additionally, background effects, i.e. thermal desorption and clean surface defects were carefully subtracted from the raw data. The formula used in ref. [39] is given by

$$k_e f(r) = -e2\pi r ln[\frac{N(r)-B}{N_0(r)-B}]/stIL.$$

Here, $k_e f(r)$ is the non-local desorption probability as a function of radial distance from the injection site. $N(r)$ and $N_0(r)$ are the number of molecules on the surface before and after charge injection for t seconds. s is the fraction of the current (I) which propagated across the surface (taken to be 1), $f(r)$ is the radial decay function of the surface current, L is the in-plane linear cross section of a PhCl molecule (taken to be 5 Å). Finally, B contains the number of surface defects of p-type (phosphorus doped) silicon and the number of dark sites which occurs in time after reconstructing. The detailed formula derivations are explained in section 2.6.4.

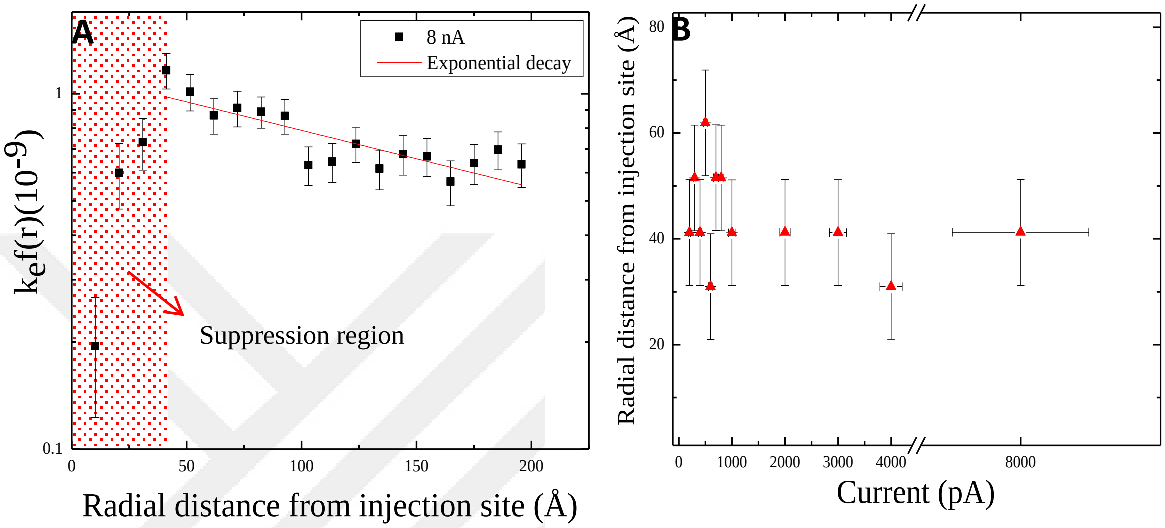

Figure 79. A. Non-local desorption probability as a function of radial distance from the injection site for 8 nA injection (+2.7 V, 8 nA for 0.8 s). Shaded area shows the suppression region for this specific experiment. B. The length-scale of the suppression region as a function of tunnelling currents ranging from 0.2 nA to 8 nA.

The first results presented by Sloan *et al.* [39] concerned the probability of the non-local desorption as a function of injection current (from 50 pA to 300 pA). They did not report the region up to ~40 Å from the tip injection site. One example of our new non-local desorption probability data (after 3-point smoothing) is illustrated as a function of radial distance from the injection site in Figure 79A. Here the electrons were injected at a bias voltage of +2.7 V with tunnelling current of 8 nA for 0.8 s and normal scanning parameters before and after injection were +1.0 V, 100 pA. In our case, the probability first increases, up to around 40 Å, and then exponentially decays. The shaded area in Figure 79A shows the suppression region for this specific experiment (at +2.7 V and 8 nA for 0.8 s). The radius of the "suppression region" as a function of different injected currents (from 0.2 nA to 8 nA) is presented in Figure 79B. We observe that the radius of the suppression region (~40 Å) does not change when the tip-sample distance is decreased by increasing the tunnelling current from 0.2 nA to 8 nA. This results will be discussed in section 5.4.1.

5.2 Oxygen Molecules on the Si(111)-7x7 Surface

The oxidation process of the clean Si(111)-7x7 surface has been studied for increasing oxygen exposures at room temperature in UHV (base pressure 1 x 10^{-10} torr). The clean surface was imaged before oxygen exposure of the surface in all cases. In Figure 80A, B, C, and D, the STM images correspond to the clean surface and oxygen exposures of 0.3 ± 0.05 L, 0.4 ± 0.06 L and 25 ± 3.7 L, respectively. The results of the oxidation process can be seen in the images for 0.3 ± 0.05 and 0.4 ± 0.06 L as an increasing number of black sites on the surface, Figure 80D corresponds to a few MLs of coverage (25 L). All the images were taken at a surface bias voltage of +1.0 V and tunnelling current of 100 pA over a 40 x 40 nm^2 area. The oxidation process was explored to determine a reasonable coverage for the local and non-local manipulation experiments. The coverages of 0.3 ± 0.05 and 0.4 ± 0.06 L were used for local and non-local manipulation, respectıvely.

A coverage of 0.3 ± 0.05L oxygen dosed on the Si(111)-7x7 surface at RT is again seen in Figure 81 but now at two different voltages, +1.0 V and +2.0 V. Increasing voltage causes the appearance of multiple bright sites of oxygen across the whole image, both bright and dark sites can be seen in Figure 81B at a bias voltage of +2.0 V. The dark sites on the surface can be seen at both +1.0 V and +2.0 V bias voltages.

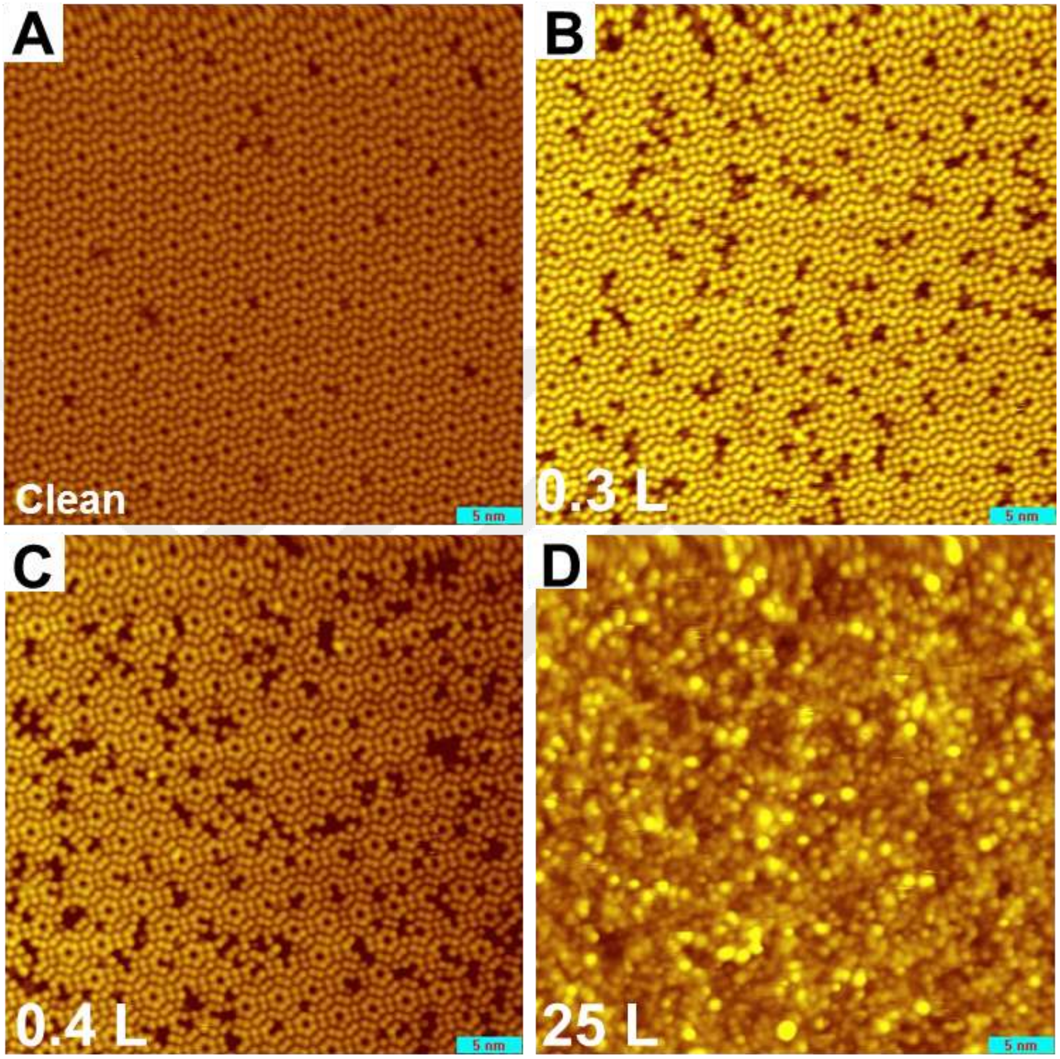

Figure 80: Oxidation of the clean Si(111)-7x7 surface (A) at different oxygen exposures, 0.3 ± 0.05 L (B), 0.4 ± 0.06 L (C) and 25 ± 3.6 L (D), respectively. All images recorded at +1.0 V bias voltage, 100 pA tunnelling current over a 40 x 40 nm^2 area.

When the exposure to oxygen is less than 0.1 L (low coverage), bright sites are prominent on the surface and mostly on faulted sites [197]. Increasing the amount of oxygen increases the proportion of dark sites on the Si(111)-7x7 surface. The additional oxygen molecules seem to join the bright site and this results in the formation of dark sites. The initial oxidation process with the bright and dark site structures is presented schematically in Figure 82.

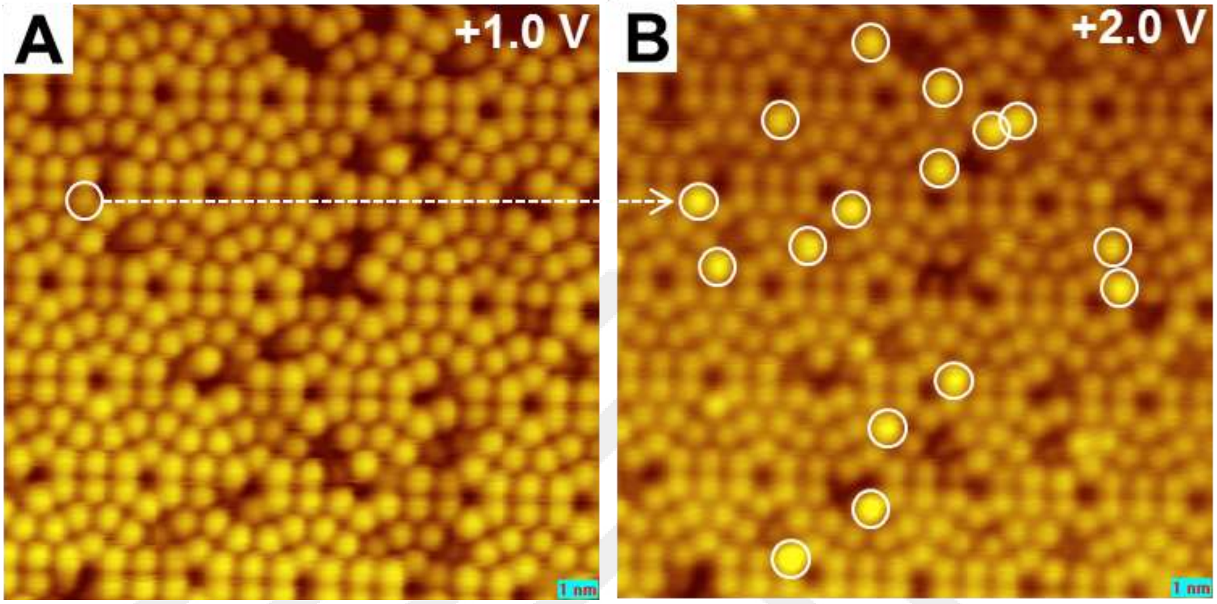

Figure 81: A and B. STM images at different bias voltages, +1.0 V and +2.0 V for 0.3 ± 0.05 L oxygen dosage on the Si(111)-7x7 surface at RT. Increasing voltage causes the appearance of bright sites which are indicated with white circles and both the bright and dark oxygen configurations are observed at +2.0 V.

A ball model of the oxygen adsorption on the Si(111)-7x7 surface is presented in Figure 82. The model is produced from references [35, 198, 199]. The top orange atoms indicate the silicon adatoms with their dangling bonds, the lower three orange balls are the silicon rest-atoms and the blue atoms are oxygen atoms. The initial oxidation of the clean surface by an oxygen molecule is given in Figure 82A. Oxygen atoms are believed to ‘back bond’ between rest-atom and adatom and appear bright under positive sample bias (>+1.5 V) of the STM image. Continuing oxidation of the surface results in an increasing number of dark sites due to bonding of additional oxygen atom which transform the bright sites into dark sites (see Figure 82B).

Oxygen saturates on top dangling bond, thus lower density of state which results in dark site [34, 198, 200].

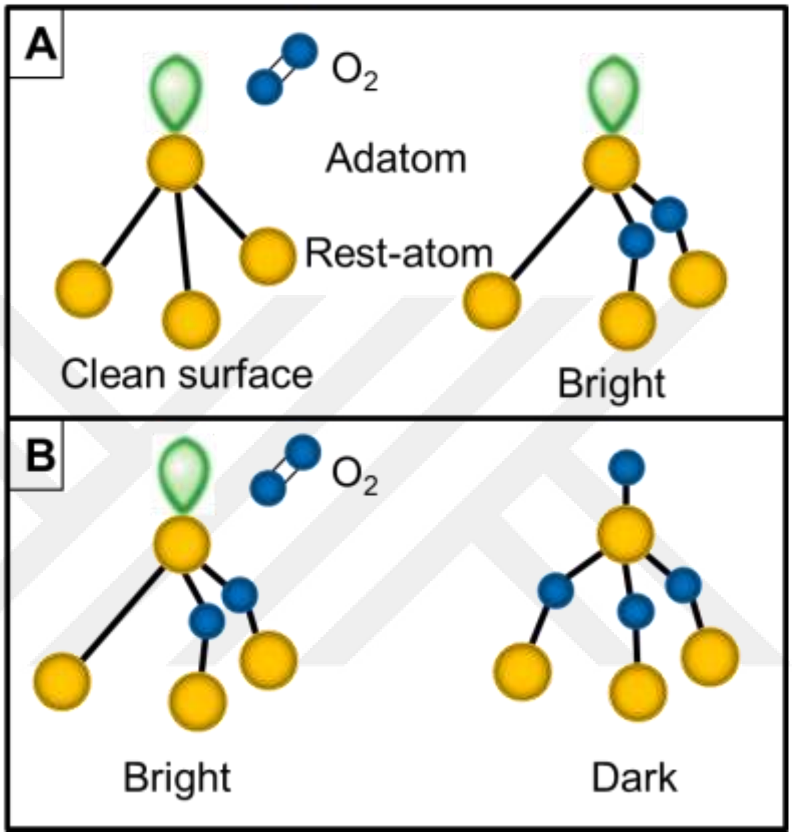

Figure 82: A ball model of oxygen adsorption on the Si(111)-7x7 surface at 300 K [35]. The top orange atoms indicate the silicon adatoms with their dangling bonds, the lower three orange balls are the silicon rest-atoms and the blue atoms are oxygen atoms. A. The initial oxidation of the clean surface by an oxygen molecule which is believed to back bond between rest-atom and an adatom and appears bright on the STM image. B. Continuing oxidation process which transform bright sites into dark sites.

In one unit cell there are 12 dangling bonds associated with the adatoms, 6 from rest-atoms and one from the corner hole. Oxygen molecules are dissociatively adsorbed by the surface adatoms and rest-atoms. The involvement of the bonding configuration of oxygen with the silicon adatoms manifests in the STM images, however the bonding with the rest-atoms is hard to show due to the limited capacity of STM of an Si(111)-7x7 surface to observe rest atoms.

Table 6: The number of bright and dark sites due to oxygen on the Si(111)-7x7 surface at RT in a 56 x56 nm^2 area . Four different positions are presented in the unit cell of the Si(111)-7x7 surface at an STM image bias of -1.5 V. Corner and center positions for faulted half (FH) and unfaulted half (UH) are indicated with the red and blue arrows, respectively.

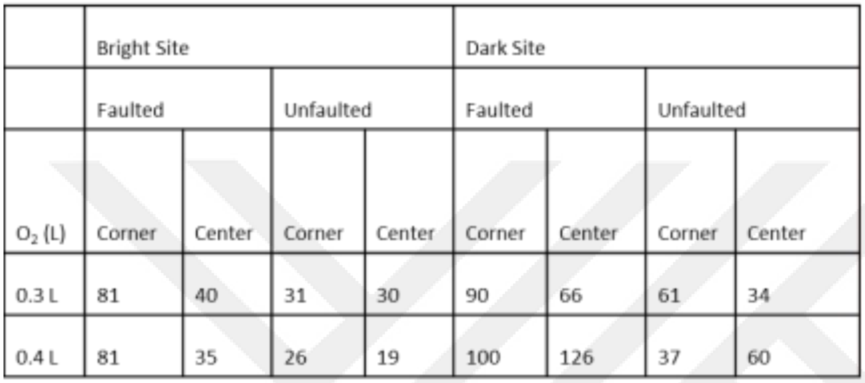

	Bright Site				Dark Site			
	Faulted		Unfaulted		Faulted		Unfaulted	
O_2 (L)	Corner	Center	Corner	Center	Corner	Center	Corner	Center
0.3 L	81	40	31	30	90	66	61	34
0.4 L	81	35	26	19	100	126	37	60

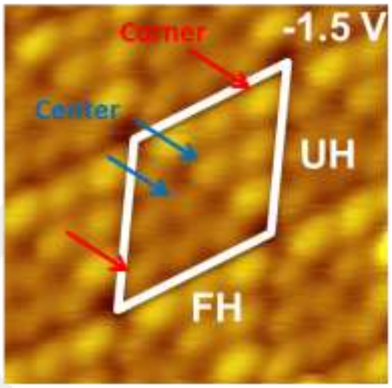

The number of bright and dark sites due to oxygen adsorption at the Si(111)-7x7 surface is counted at RT over a 56 x 56 nm^2 area and presented in Table 6. Four different positions are determined for a unit cell of the Si(111)-7x7 surface in the STM image at a bias of -1.5 V. Corner and center positions for the faulted half (FH) and unfaulted half (UH) are indicated on the image with the red and blue arrows, respectively. The surface defects have been subtracted from the number of dark sites. When increasing the oxygen dosage, the number of dark sites increased on both faulted and unfaulted halves. In contrast, the number of bright sites remained constant for faulted corner sites but decreased for other sites. This is because less number of dangling bonds at the corner hole site.

5.3 Local and Non-local Manipulation of Oxygen Molecules

5.3.1 Local Manipulation of Oxygen

Local manipulation experiments were performed on the bright and dark sites of oxygen on the Si(111)-7x7 surface at room temperature. The chemisorbed oxygen atoms were subject to electron injection from the STM tip to see whether oxygen atoms desorbed, dissociated or transformed their bonding configurations. Three examples of such local site manipulations for dark and bright sites are presented in Figure 83 and Figure 84, which show before and after STM images (bias voltage of +1.5 V, tunnelling current of 100 pA, 6 x 6 nm^2). All manipulations were performed on the labelled site (white points) with a tunnelling current of 6 nA for 50 ms while the feedback loop was switched on and a given bias voltage labeled. Figure 83 shows before (A) and after (B) STM images for a successful dark site manipulation at a bias voltage of +9.1 V. The dark site is displaced to a neighboring adatom site due to electron injection, which is indicated with a white arrow. Another dark site manipulation is presented in Figure 83C and D for a bias voltage of +9.8 V, here the site is transformed to a bright site. Removal of a dark site at a bias voltage of +5.0 V is illustrated in Figure 83E and F.

Electron injection into a bright site at +7.7 V, Figure 84A and B, causes a new dark site to be created on a neighboring adatom while the bright site still remains. Figure 84C and D show the bright site manipulation at +8.5 V. The site is transformed to a dark site. The last example for a successful bright site manipulation at +8.5 V is presented in Figure 84E and F, here the site is removed and new dark sites are created near the injection site.

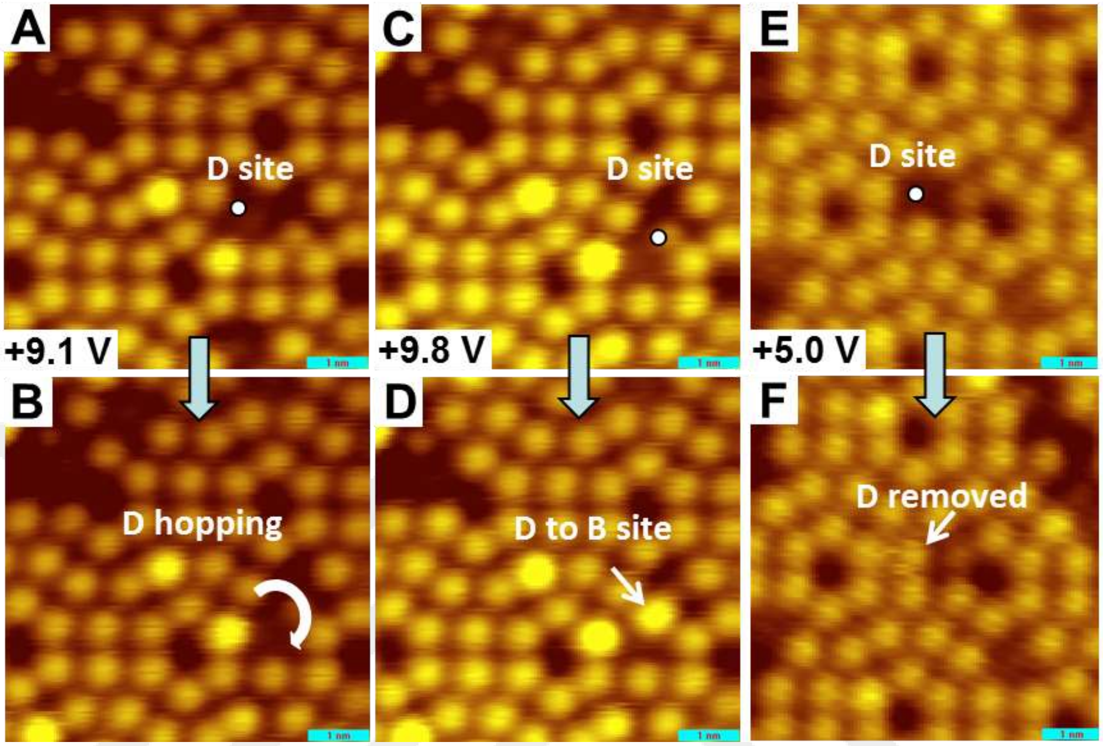

Figure 83: Before and after STM images are taken at a bias voltage of +1.5 V and tunnelling current of 100 pA, 6 x 6 nm^2 for the dark site manipulation. All manipulations are performed on a selected point (white circles) with a tunnelling current of 6 nA for 50 ms and the bias voltages labelled. A and B. A dark site manipulation at +9.1 V shows the dark site displaced to a neighboring adatom. C and D. A dark site manipulation at +9.8 V shows the site transformed to a bright site. E and F. A dark site removed at +5.0 V.

In summary, electron injection leads to three possible manipulation outcomes for each of the bright and dark sites. First, for the dark site: 1) the dark site moves to a neighboring adatom; 2) the dark site is transformed to a bright site; 3) the dark site is removed. Secondly, for the bright site (reproduced with statistic): 1) the bright site remains and a neighboring adatom is transformed into a dark site (46.1 ± 8.1%); 2) the bright site disappears and a dark site appears on a neighboring adatom (30.8 ± 7.5%); 3) the bright site is transformed to a dark site (23.1 ± 7.0%). The percentages given were found over 15 manipulation events.

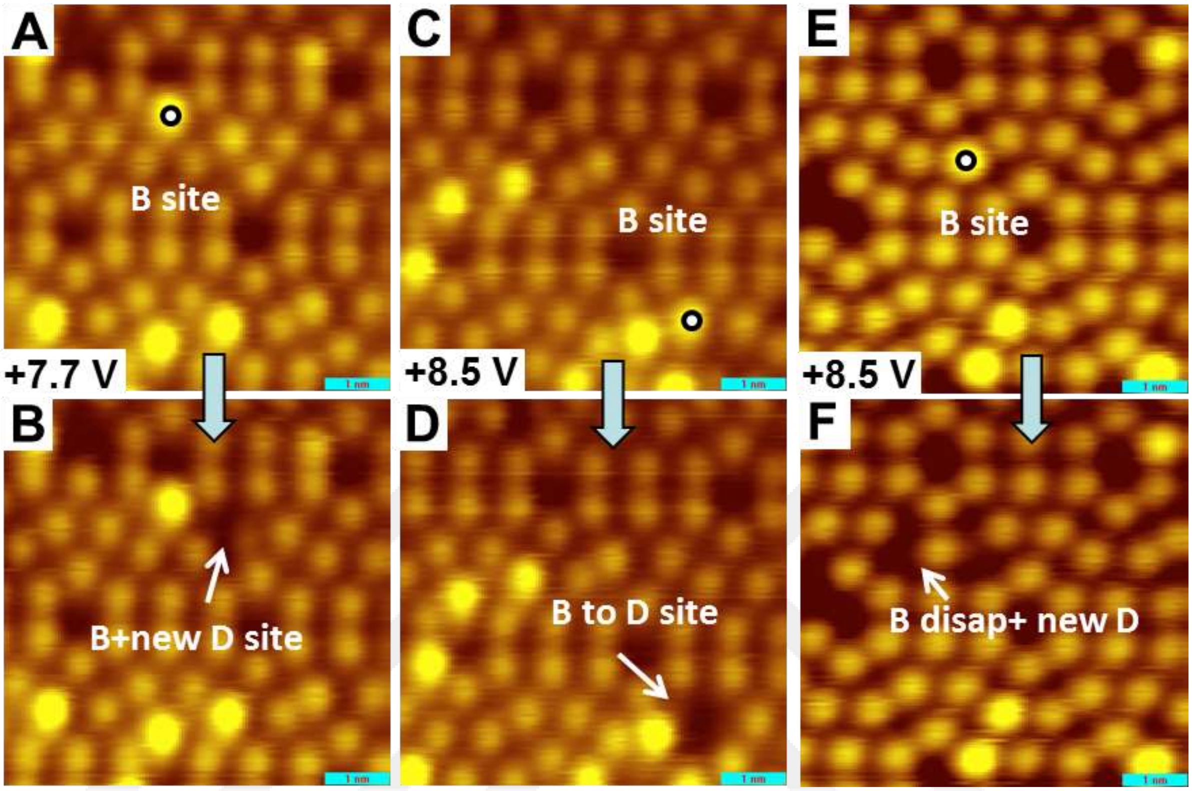

Figure 84: Before and after STM images are taken at a bias voltage of +1.5 V and tunnelling current of 100 pA, 6 x 6 nm^2 for the bright site manipulation. All manipulations are performed on a selected point (white circles) with a tunnelling current of 6 nA for 50 ms and the bias voltages labelled. A and B. A bright site manipulation at +7.7 V and the site remain and a new dark site appeared on an adatom. C and D. A bright site manipulation at +8.5 V shows the site transformed to a dark site. E and F. A bright site manipulation at +8.5 V shows the site removed and new dark sites created.

The threshold voltage for local manipulation of bright site plotted in Figure 85. The threshold voltage for the manipulation of the sites is found +3.8 V, which is quite a match with earlier finding [35]. Removing a dark site indicates that a single oxygen atom is removed from the top of a silicon adatom which is not backbonded with oxygen. In contrast, the transformation of the dark site to a bright site indicates that a single oxygen atom is removed from the top of a silicon adatom which has three oxygen backbonds [35]. However, the final structure of O/Si cannot be concluded with confidence because, although this is only one type B site more than one D site configuration is possible.

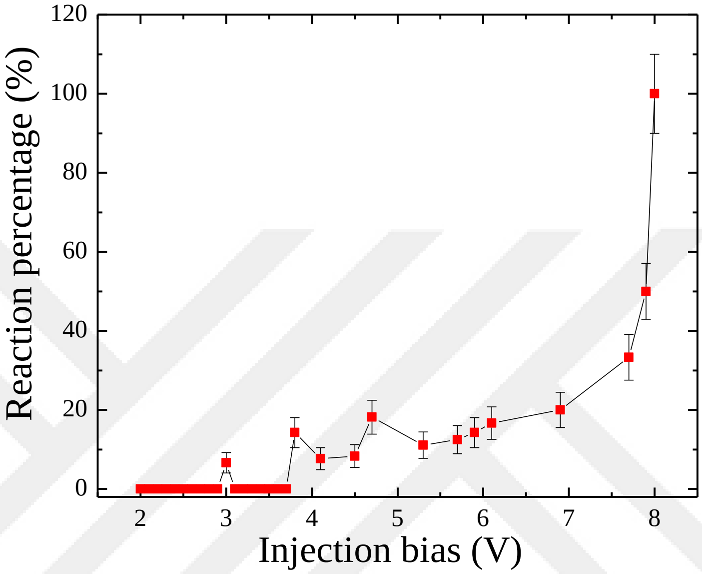

Figure 85: Reaction probability of local manipulation of bright site as a function of injection bias. All injection performed at tunnelling current of 6 nA for 50 ms.

5.3.2 Non-local Manipulation of Oxygen Molecules

Oxygen molecules on the Si(111)-7x7 surface were manipulated non-locally via injection of electrons at a corner hole. In Figure 86A, B and C, before, during and after STM images (15 x 15 nm^2) are presented for the non-local manipulation of oxygen on the Si(111)-7x7 surface at room temperature. Electrons were injected at the corner hole marked with black circles in each case for 8 s at +4.0 V bias voltage and 100 pA tunnelling current. The bias voltage was chosen above the threshold voltage for manipulation which was found in section 5.3.1. Transformation of dark sites associated with adsorbed oxygen is observed in a range of 90 Å. The blue arrows show the transformations in which the dark sites are removed and adatoms appeared. The red arrows indicate the transformations from dark sites to bright sites (i.e extra bright adatom sites).

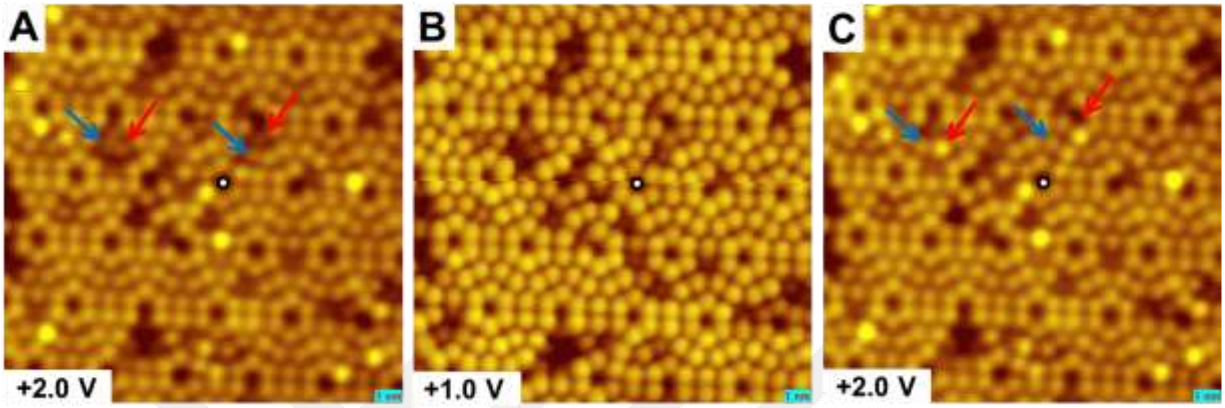

Figure 86:A, B and C. Before, during and after STM images (15 x 15 nm^2) for non-local manipulation of oxygen on the Si(111)-7x7 surface at RT. Electrons injected for 8 s at +4 V bias voltage and 100 pA tunnelling current at a corner hole which is indicated with black circles. Transformations are observed only at the dark sites. The blue arrows show the transformations which the dark sites removed and adatoms appeared. The red arrows indicated the transformation from the dark site to the bright site.

The non-local manipulation of dark sites is illustrated in Figure 87A. The data induced desorption, transformation (to bright site), and diffusion, which are all possible as also for local manipulation. The reaction probability was increased as a function of injection bias (at a tunnelling current of 100 pA for 2 s). The threshold voltage of +4.0 V for non-local reaction was identified for the surface state. The non-local reaction probability plotted in Figure 87B as a function of radial distance from the injection site (at an injection bias of +4 V and tunnelling current of 100 pA for 8 s). We clearly observe that the manipulation probability first increases in a range of 50 Å then decrease. The reaction beyond 90 Å vanishes for the chosen injection parameters. There is no transformation observed for bright sites, which are quite stable for the chosen injection parameters.

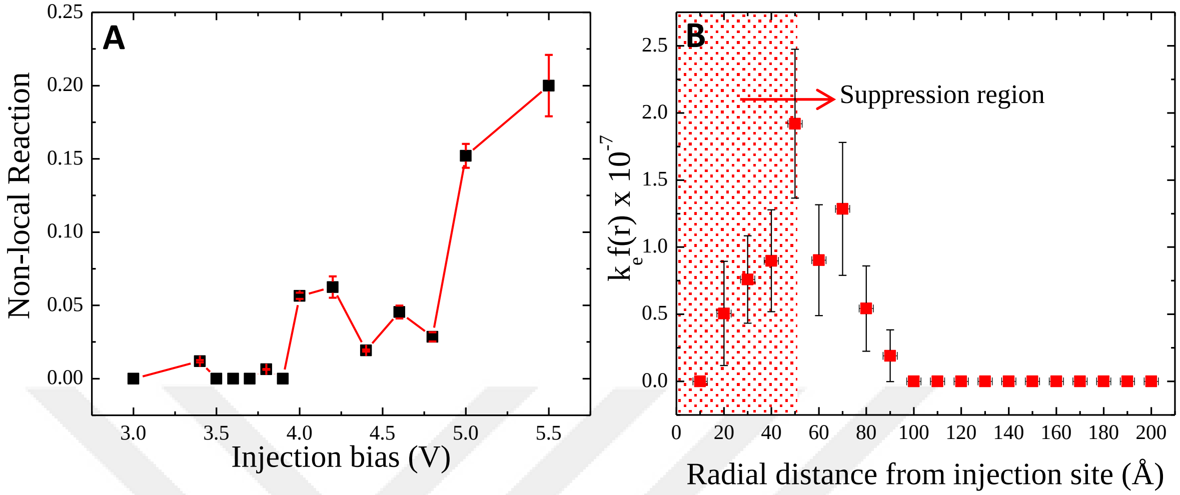

Figure 87: A. Non-local reaction of dark sites increasing as function of injection bias and threshold voltage is found to be +4.0 V (injection at 100 pA for 2 s). B. Non-local reaction probability of dark sites as function of radial distance from injection site (injection bias of +4 V at tunnelling current of 100 pA for 8 s). Shaded area shows the suppression region for this experiment.

Table 7 presents the possible transformation events after non-local electron injection at a corner hole. There is no transformation observed for 165 bright sites over 12 non-local manipulation experiments. Only dark sites are manipulated in the range of 90 Å. The possible dark site transformations are found 1) dark site removal, 2) dark site transformation from into a bright site, 3) dark site moves to next adatom. These possible transformations are the same as those observed for local manipulation experiments, as well as in the study of local manipulation of dark sites performed by Mayne *et al*. [35].

Table 7: The reaction of dark sites by non-local (in this work) and local [35] electron injection showing the number of events and calculated percentages.

	Non-local (In this work)		**Local (Mayne *et al*. [35])**	
Transformation on Dark Site	Event	Percentage	Event	Percentage
D removed	41	(69.4 ± 6.0) %	9	56.2%
D transformed into B	15	(25.4 ± 5.7) %	5	31.3%
D moved to next adatom	3	(5.1 ± 2.9) %	2	12.5%

5.4 Discussion

5.4.1 Discussion of Desorption of Chlorobenzene Molecules

The threshold voltage for PhCl molecules desorption is determined as +1.4 V, which indicates LUMO, in local electron-induced manipulation of the molecule at a positive bias voltage. As found by Sukulsermuk *et al.* [106], the desorption is induced by a single electron. The desorption probability increases with increasing bias voltage. This effect is also observed for toluene molecules on the Si(111)-7x7 surface [109] of previous PhCl as a function of bias voltage [201], and our data.

We observed the suppression region which is about 40 Å for all electron injections up to 8 nA tunnelling current. This region is independent of the tip-sample separation, thus tunnelling current. In order to explore the region in terms of dopant effect, previous studies by Sloan *et al.* reported the voltage-dependent (for both positive and negative polarity at 100 pA) desorption yield of PhCl on p-type and n-type Si (111)-7x7 surfaces [39, 65]. The conclusion was that the desorption yield is enhanced with increasing bias voltage, is not dependent on the dopant, and that the threshold voltage is different for the positive (+2.1 V) and the negative (-1.1 V) bias voltages [65]. Moreover, further experiments were done with increasing current (from 50 pA to 300 pA at a constant voltage of +2.7 V) where the suppression behaviour of PhCl molecule observed in below 40 Å on the n-type silicon surface [39]. In this work, p-type silicon wafer used for non-local desorption experiments and the same suppression behaviour observed. Therefore, we ruled out the dopant effect on the suppression behaviour.

5.4.2 Discussion of Manipulation of Oxygen Atoms

A total of six types of transformations were observed via local electron injection on the bright and dark sites of oxygen for 50 ms at 6 nA tunnelling current over a wide range of bias voltage from +3.8 V to +10.0 V. Comparison of these statistic with earlier findings in ref. [35] shows that the bright sites are more stable in our experiments. This may be because of the increased oxygen coverage from 0.05 ML to 0.4 ML, which results in saturated dark and bright sites. However, the atomic structure of the transformed oxygen configurations on the Si(111)-7x7 surface after manipulation is unknown. The non-local injection at a corner hole with a bias voltage of +4.0 V, tunnelling current of 100 pA and duration 8 s, results in only dark site reaction in the range of 90 Å. Most importantly, there is also a suppression region observed on the scale of 50 Å. This region is quite comparable as mentioned in section 5.4.1. Observing this region for different nature molecules may also questioned a ring formation of C_{60} molecule in a range of 60 Å [29] on the Si(111)-7x7 surface both bias voltage polarities.

The diffusion length of hot-electrons is calculated to be ~10 nm for non-local desorption of chlorobenzene molecules on the Si(111)-7x7 surface at room temperature, as given by Lock *et al.* [201]. This length matches quite with the oxygen reaction length. Therefore, injected electrons may correspond to a manipulation of dark sites far away from the injection point. However, there is no decay observed beyond the suppression region 50 Å. There is no transformation observed for bright sites due to non-local injection. This may be because either the bright sites are much more stable at room temperature than the dark sites or the number of electrons is not sufficient to cause a transformation. It is known that the bright site may diffuse due to increased substrate temperature to 620 K [35].

5.4.3 Discussion of Suppression Region

We will now discuss possible causes for the suppression region observed in the non-local desorption experiments, specifically, electric field, hot electron transport, a result of the physical presence of the tip suppression of desorption.

***Electric Field Simulation*:** In this section, we explore the effect of the electric field on the surface as a function of tip-sample separation. The separation can be decreased with increasing tunnelling current, thus the current dependent data will be simulated. A considerable amount of literature has been published on the tip-sample bias dependence of the induced electric field. These studies report that at high sample bias voltages (>+3.0 V) the field has a significant effect on the tunnelling barrier [202]. On the other hand, a low bias voltage (<+3.0 V) generates a field that is rather weak and ineffective [5, 50, 202]. Considering “the effect of an electric field an atomic manipulation” under the STM tip, one possible mechanism was proposed by Tsong [68]. Regardless of the bias voltage polarity, adsorbates on the surface migrate to the region under the tip due to the inhomogeneous electric field. In our case (electron injection at a constant bias voltage of +2.7 V), increasing the tunnelling current results in a tip displacement towards the surface. However, for our experiments, it is difficult to prove that new molecules migrate under the tip due to electric field. All PhCl molecules appear as dark site on the Si(111)-7x7 surface in the STM images and the dark site cannot be distinguished either diffused or existing molecule.

The electric field between the tip and surface is inversely proportional to the distance from the tip apex to the surface. Performing manipulation at low bias voltage means the electric field is weak [37]. However, at higher voltages the electric field may induce many effects on the surface [203-205]. In the case of a 10 Å tip height and 10 nm radius tip, the field beneath the tip apex is 1 V/m and decreases by approximately 80% at 50 Å radius [69]. To investigate whether the electric field plays a role in the short-range suppression of non-local manipulation of PhCl on Si(111)-7x7 surface we performed Finite Element Method Magnetics (FEMM) method simulations.

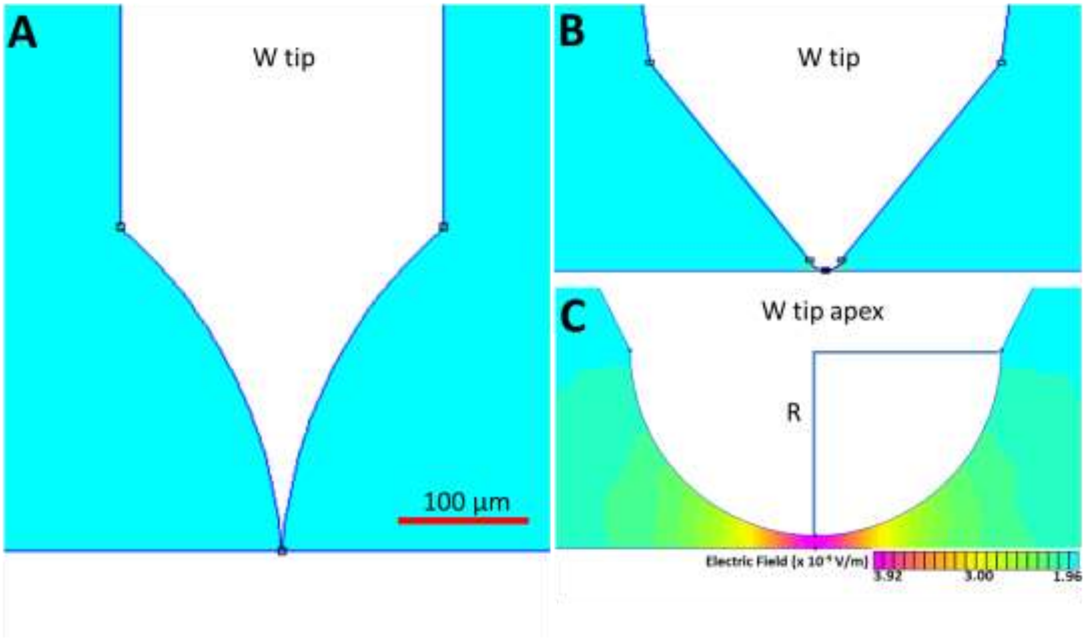

Figure 88:FEMM simulation at 7 Å tip-surface separation. A. Magnified W tip. B. Zoom of tip apex. C. Tip apex with radius shown. Colour map of the simulated electric field, from turquoise (1.96 x 10^{-9} V/m) to purple (3.92 x 10^{-9} V/m), shows strong electric field under tip apex.

The metallic tip is simulated in FEMM based on a real tip length, radius, and shape, as seen in Figure 88. In the simulation, the semiconductor surface is modelled as silicon with relative permittivity, ε = 12, and the realistically size metallic tip as tungsten ε =1 [206]. For the simulation meshes are created with 638655 nodes. The tip-sample system is modelled with different radii of 5, 10 and 20 nm, different fixed bias voltages (from +1.7 V to +3.3 V) and several tip-sample distances (from 7 Å to 6 Å). The initial tip height is estimated as 7 Å from ref. [33] while increased because of the tunnelling current, from 0.2 nA to 8 nA, the tip-sample distance is decreased by about 1 Å. The colour map of the simulated electric field shows field strength and ranging from 1.96 x 10^{-9} V/m (turquoise) to 3.92 x 10^{-9} V/m (purple). Figure 88C shows a strong electric field under the tip apex which decays rapidly away from the point of minimum separation.

The simulation results along the surface under the tip apex are presented in Figure 89. The field strength is plotted in Figure 89A as a function of voltage from +1.7 V to +3.3 V and for different tip radii of 5, 10, and 20 nm (black, red and blue, respectively). Figure 89B shows the effect of tip radius at a set voltage of +2.7 V. The tip radii are again 5, 10, and 20 nm (black, red and blue, respectively). The change of the field strength along the surface is plotted in Figure 89C with increasing bias voltages from +1.7 to +3.3 V for 10 nm tip radius. Figure 89D shows the decreasing tip-sample distance from 7 Å to 6 Å for a +2.7 V biased tip with 10 nm radius simulating an increase in the tunnelling current from 0.2 nA to 8 nA.

Looking at Figure 89A, we see a linear dependence of maximum field strength upon sample bias. This is true for all tip radii, with only a small variation in the field strength seen under the tip as radius varies. However, the radius of the tip has a strong effect on the lateral decay of the field across the surface. As can be seen in Figure 89B, the field for a 20 nm tip is high across a significantly larger area of the sample. Also the maximum electric field is 3.48 x 10^{-9} V/m and 3.60 x 10^{-9} V/m for 5 nm and 20 nm tip radii. The maximum field slightly increases with increasing the tip radius.

Figure 89C and D show that the tip bias and tip-sample separations have a pronounced effect on the maximum field strength. In Figure 89C, the maximum field strength grows from 2.35 x 10^{-9} V/m to 4.60 x 10^{-9} V/m with a change in the bias from +1.7 V to +3.3 V. In Figure 89D, we see that the variation in the tip-sample separation (which corresponds to changing the current set point in the manipulation experiments) also alters the maximum field strength though to a limited degree. The electric field increases only 15% when decreasing the tip-sample separation from 7 Å to 6 Å.

Our colleagues at the University of Bath have been working on bias-dependent non-local desorption. They have also observed the suppression region for different aromatic molecules on the Si(111)-7x7 surface. The size of the region increases linearly with increasing bias voltage at constant tunnelling current [201]. Thus one possible origin of the suppression behaviour might be the electric field, since it is obvious that increasing the bias voltage increases the electric field on the surface. However, there is a serious problem with this idea that a study of non-local desorption at step edges up to 5 monatomic steps high on the Si(111)-7x7 surface clearly shows that the suppression region on the upper or lower terraces has the same size on both side of the step [40]. Therefore, the electric field effect model is not a likely explanation for the suppression region.

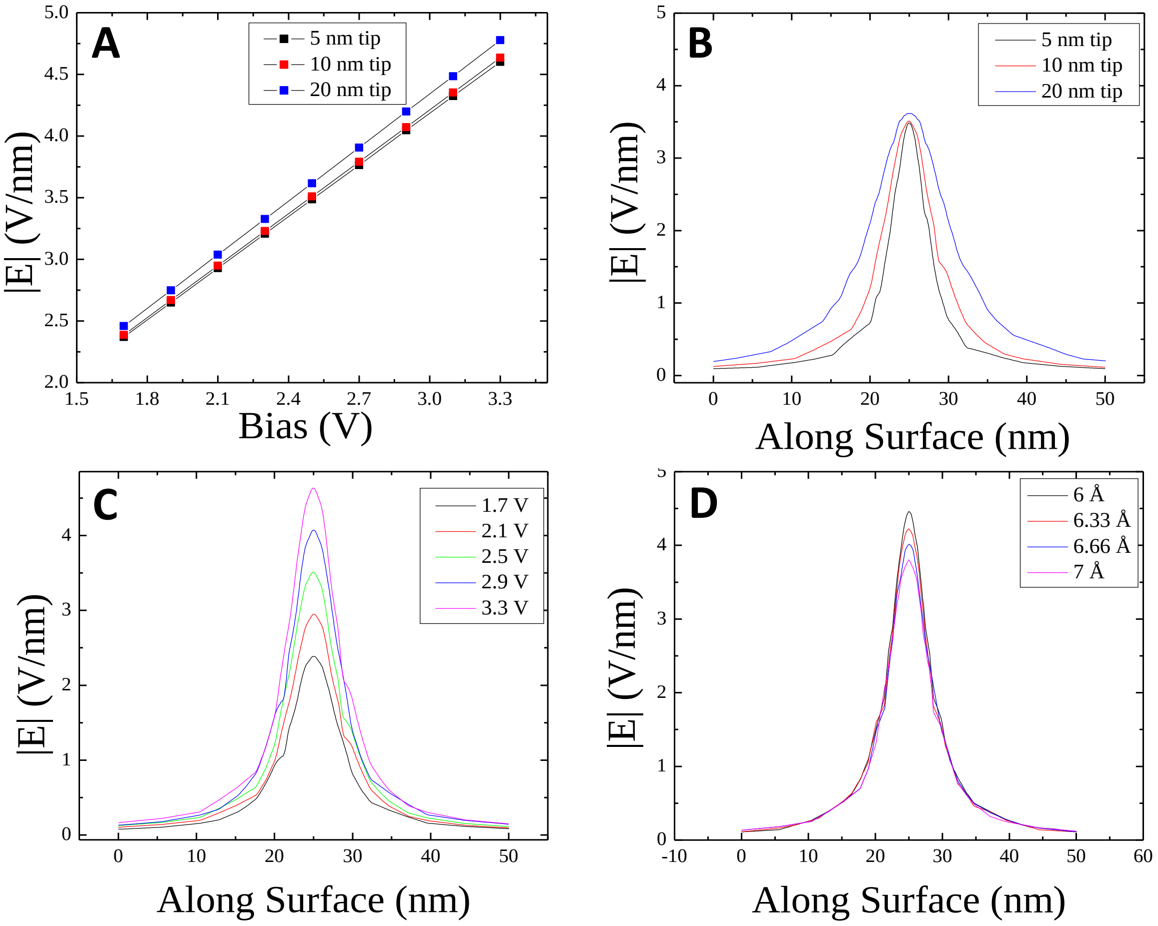

Figure 89: FEMM simulation of tip-surface electric field. A. The electric field across the surface simulated for voltages from +1.7 V to +3.3 V and for different tip radii 5, 10, and 20 nm (black, red and blue, respectively). B. The electric field simulated at +2.7 V for three tip radii 5, 10, and 20 nm (black, red and blue, respectively). C. The lateral of the field is simulated for a 10 nm tip radius at different bias voltages. D. The lateral profile of the field increase with decreasing tip-sample distance (from 7 Å to 6 Å) for a +2.7 V biased tip with 10 nm radius

Tip Induced Re-Adsorption: Numerous studies have found that typical electrochemically etched tungsten (W) tips radii have less than 100 nm [183, 186, 207]. The suppression region may be related to the tip size or tip proximity effect. One interpretation could be tip proximity effect. When the tip apex is close enough to the surface during injection, physisorbed state of Si and W tip will interpenetrate. Once injected electrons interact with the PhCl, molecules may either desorb from surface or move to chemisorbed tip state or the interpenetrated tip-surface physisorbed state. The molecule is then prevented from desorbing by the presence of the tip and prefers to move back to the surface chemisorbed state because of the lower energy barrier to the surface. Therefore, a suppression region may occur beneath the STM tip and then exponentially decreases away from the tip. However, it is obvious that the tip does not have spherical or uniform shape. Moreover, this region is also observed on silicon atomic steps (up to 5) [40] and independent of temperature [109].

5.5 Conclusions

The main purpose of this chapter has been to study the initial adsorption states as a basis for *local* and especially *non-local* manipulation studies of oxygen and chlorobenzene on the Si(111)-7x7 surface at RT. In local manipulation, the molecules are manipulated via electron injection by placing the STM tip right above the molecule. In non-local manipulation, the molecules are manipulated far from the tip by electronic propagate across the surface. First, the desorption of chemisorbed chlorobenzene molecules was induced from +1.4 V by local charge injection on the molecule. This threshold indicated LUMO for PhCl molecule on the Si(111)-7x7 surface. Increasing the bias voltage decreases the characteristic desorption time of the molecule from the surface. In non-local manipulation, a suppression regime of 40 Å radius was observed, that was not reported by Sloan *et al*. [39]. We studied the effect of increasing tunnelling current from 0.2 nA to 8 nA (thus decreasing tip-sample separation) on the suppression regime which is independent of tip-sample separation.

For oxygen, both the observed bright and dark sites correlate to different oxygen bonding configurations in a unit cell of the Si(111)-7x7 surface [35]. It is found that the number of bright sites decreases with increasing oxygen dosage from 0.3 L to 0.4 L. The local manipulation of the bright and dark sites of oxygen molecules was performed over a wide range of bias voltage for an electron injection of 50 ms.. The threshold voltage is found to be +3.8 V which refers LUMO for local manipulation. Displacement, transformation and desorption of oxygen molecules were all observed due to electron injection at the oxygen sites and the same channels observed in the non-local experiment. Moreover, in the non-local studies only the manipulation of the dark sites was possible in the range up to 90 Å, beyond this point there no reaction was observed. There is also no transformation observed on the bright sites due to non-local injection.

We find a suppression region of 50 Å for non-local manipulation of adsorbed oxygen. This region is quite comparable with our findings for chlorobenzene, as well as other studies, toluene, benzene [201], and C_{60} molecules [29] on the Si(111)-7x7 surface. It was found that the region seems to be quite universal in the STM experiments. This region is also independent of the tip-sample separation for chlorobenzene molecules. The best currently available mechanism, proposed by the University of Bath group, is coherent inflation of the electron wave packet, which inhibits desorption on the scale of the suppression region. Beyond this point diffusive transport gives rise to efficient manipulation. In another words, the electrons propagate out quite far from the injection site before they undergo the first scattering event [208], and this defines the suppression region.

CHAPTER 6

CONCLUSIONS AND OUTLOOK

6.1 Conclusions

In this thesis, I have presented a detailed study of hybrid clusters formed from Au atoms and C_{60} molecules assembled on the Au(111) surface and local and non-local manipulation of oxygen and chlorobenzene molecules on the Si(111)-7x7 surface. In chapter 3, the production and transformation of these clusters studied in terms of C_{60} coverage, while keeping the amount of Au coverage constant. In chapter 4, mechanical manipulation by the STM tip was performed on the hybrid clusters at RT and a "*cascade manipulation*" was achieved. Similarly, this manipulation was continued at 110 K with more control and "*directional manipulation*" was achieved. In chapter 5, local and non-local manipulation of oxygen and chlorobenzene molecules on the S(111)-7x7 surface at RT was performed at RT using electron induced manipulation technique.

The first part of this work, we studied the formation of hybrid clusters with imaging the surface while increase the substrate temperature from 110 K to room temperature. This allowed us to demonstrate the clusters only exist when C_{60} molecules and Au atoms simultaneously on the elbow site. Surprisingly, the clusters were transformed to a size bigger cluster due to additional Au atoms introduced on the surface at RT. These Au atoms forced to the clusters captured additional mobile C_{60} molecules (already diffuse on the surface at RT) to maintain optimal distance and maximal interaction between C_{60} molecules and Au island [14]. The size distributions of the major hybrid clusters were defined by the initial and additional amount of Au atoms.

In chapter 4, a successful *cascade* and *directional* manipulation were investigated via mechanical manipulation by removing a selected C_{60} molecule within either C_{60} islands or hybrid clusters. First, the $(C_{60})_{14}$–$(Au)_{63}$ cluster was manipulated to another small size cluster by removing a selected C_{60} molecule from the side of the clusters packing. Removing the molecule from the $(C_{60})_{14}$–$(Au)_{63}$ cluster caused a transform to $(C_{60})_{12}$–$(Au)_{49}$ cluster due to additional simultaneous separation of C_{60} molecule and Au atoms from the cluster. These additional separations led to a shift and rearrangement of the C_{60} molecules and Au atoms in the island of the cluster. Further, the $(C_{60})_{12}$–$(Au)_{49}$ cluster successfully transformed to $(C_{60})_{7}$–$(Au)_{19}$ cluster at RT. This manipulation was purely mechanical origin between the STM tip and the molecule ruling out the effect of electric field via performing the manipulation at zero bias voltage and the tip effect [19]. Manipulation of hybrid clusters at 110 K provided more control on C_{60} molecules. All C_{60} molecules (up to 3 C_{60}) on the upper terrace of the clusters were removed without destroying the cluster frame and Au island. These molecules were preferred to stay on the surface around the cluster rather than attaching to the tip or diffusing somewhere on the surface. We observed that 110 K was not enough to freeze the C_{60} molecules on the top of the cluster. Therefore, the molecules on the top jumped on an existence vacancies in presence of the tip. The C_{60} molecule around the cluster was manipulated to a certain directions. Thus, a *directional* manipulation was achieved by which a C_{60} molecule around the cluster moved back the original position to obtain the original form of the cluster.

In chapter 5, the study of local electron injection on chemisorbed chlorobenzene molecules on the Si(111)-7x7 surface at RT showed that the excitation time was decreased by increasing bias voltage. Non-local desorption of chlorobenzene molecules were also studied as a function of tunnelling current from 0.2 nA and 8 nA to explore the suppression region at ~40 Å. the region was independent of the change of the tunnelling current (thus decreasing tip-sample separation). Exploring possible reasons such as electric field (by FEMM), the macroscale tip structure and the dopant (n or p-type) did not explain the suppression region.

Following, the initial adsorption states and *local* and *non-local* manipulation of oxygen and chlorobenzene molecules studied on the Si(111)-7x7 surface at RT. Bright and dark sites of oxygen were appeared under STM image due to different bonding configuration between silicon adatoms and rest-atoms. The local manipulation on these sites caused a displacement, transformation and desorption of oxygen molecules [35]. The manipulation threshold voltage such a wide range of bias voltage from +2.0 V to +10.0 V corresponded to +3.8 V for an electron injection of 50 ms. The non-local manipulation results in a suppression region in a range of 50 Å nm via electron injection in a corner hole at +4.0 V. Surprisingly, no transformation observed on the bright sites. It was found that the region seems to be quite universal in the STM experiments. A private communication with our colleague Miss. Rusimova from The University of Bath, the possible reason can be interpreted as a coherent inflation of an electron wave packet which no desorption happens in the suppression region. Another word, the electrons explode quite far before they undergo the first scattering event [208].

6.2 Outlook

Controlling number of Au atoms and C_{60} molecules on the elbow site of the Au(111) surface was a great challenge to produce just one type of hybrid cluster. We achieved to covered the surface about 50% with $(C_{60})_7$-$(Au)_{19}$ clusters by varying the initial amount of C_{60} molecules.

Instead of finding the right amount of C_{60} molecules and Au atom dosages, elevating the substrate temperature up to 400 K may lead to reduce the size of the cluster vie loosing C_{60} molecules and Au atoms. Thus we can also study the diffusion of hybrid clusters on the surface. An STS measurement will be a useful technique to determine the electronic structure of the cluster components (the top or side of the clusters) as well as theoretical calculation. Perhaps, a local and non-local electron (or hole) induced manipulation can be performed to manipulate the cluster via controlling charge transfer between C_{60} molecule and Au atoms. We experienced that performing manipulation at 110 K was not enough to stop the mobility of the C_{60} molecules. Therefore, with helium temperature, we may be able to take away all molecules from the upper terrace and thus create a hollow on the cluster. Then we could fill the hollow by contacting the tip on a different cluster to pick up C_{60} molecule/s, and move the tip back to the hollow cluster. Moreover, instead of C_{60} molecules and Au islands, C_{70} molecules and other metals (such as Ni, Ag, Cu, Pt, Pd, etc.) can be possible candidates for the hybrid cluster formation.

Local and non-local manipulation of oxygen molecules resulted in diffusion, desorption or transformation of the bright and dark site features. The atomic-level structures are still unknown after manipulation event. DFT calculations could calculate the energy levels of the HOMO and LUMO for the possible structures at room temperature. One other important question is the suppression region under the STM tip. The Si(111)-7x7 surface could be replaced with other surfaces such as Ge(a few ML) or silicene on the Si(111) [209, 210] or Si(100) with different reconstructed surface structures. Then the suggested “inflation” mechanism [208] could be examined on these different surfaces and a test with simulation in femtosecond electron inflation scattering event.

References

[1] M. Knoll, Ruska, E. , Das Elektronenmikroskop (Electron Microscopy) Z. Phys., (1932) 78318–78339.

[2] P.B. Hirsch, A. Howie, R.B. Nicholson, D.W. Pashley, M.J. Whelan, Electron Microscopy of Thin Crystals, (1966) 20014.

[3] G. Binnig, H. Rohrer, C. Gerber, E. Weibel, Surface Studies by Scanning Tunneling Microscopy, Physical Review Letters, 49 (1982) 57-61.

[4] D.M. Eigler, Positioning Single Atoms with a Scanning Tunnelling Microscope, Nature, 344 (1990) 524.

[5] S.W. Hla, K.H. Rieder, STM Control of Chemical Reaction: Single-Molecule Synthesis, Annual Review of Physical Chemistry, 54 (2003) 307-330.

[6] L. Gross, F. Mohn, N. Moll, B. Schuler, A. Criado, E. Guitián, D. Peña, A. Gourdon, G. Meyer, Bond-Order Discrimination by Atomic Force Microscopy, Science, 337 (2012) 1326-1329.

[7] L. Gross, N. Moll, F. Mohn, A. Curioni, G. Meyer, F. Hanke, M. Persson, High-Resolution Molecular Orbital Imaging Using a p-Wave STM Tip, Physical Review Letters, 107 (2011) 086101.

[8] L. Gross, F. Mohn, N. Moll, P. Liljeroth, G. Meyer, The Chemical Structure of a Molecule Resolved by Atomic Force Microscopy, Science, 325 (2009) 1110-1114.

[9] C.J. Chen, Introduction to Scanning Tunneling Microscopy, Oxford University Press., New York, 2007.

[10] I.R. McNab, J.C. Polanyi, Patterned Atomic Reaction at Surfaces, Chemical Reviews, 106 (2006) 4321-4354.

[11] C. Joachim, J.K. Gimzewski, A. Aviram, Electronics Using Hybrid-molecular and Mono-molecular Devices, Nature, 408 (2000) 541-548.

[12] L. Sánchez, R. Otero, J.M. Gallego, R. Miranda, N. Martín, Ordering Fullerenes at the Nanometer Scale on Solid Surfaces, Chemical Reviews, 109 (2009) 2081-2091.

[13] F. Besenbacher, J.V. Lauritsen, T.R. Linderoth, E. Lægsgaard, R.T. Vang, S. Wendt, Atomic-scale Surface Science Phenomena Studied by Scanning Tunneling Microscopy, Surface Science, 603 (2009) 1315-1327.

[14] Y.-C. Xie, L. Tang, Q. Guo, Cooperative Assembly of Magic Number C_{60}-Au Complexes, Physical Review Letters, 111 (2013) 186101.

[15] L. Liu, S. Liu, X. Chen, C. Li, J. Ling, X. Liu, Y. Cai, L. Wang, Switching Molecular Orientation of Individual Fullerene at Room Temperature, Scientific Reports, 3 (2013) 3062.

[16] D.V. Gruznev, A.V. Matetskiy, L.V. Bondarenko, O.A. Utas, A.V. Zotov, A.A. Saranin, J.P. Chou, C.M. Wei, M.Y. Lai, Y.L. Wang, Stepwise Self-assembly of C_{60} Mediated by Atomic Scale Moiré Magnifiers, Nature Communication, 4 (2013) 1679.

[17] W. Chen, H. Zhang, H. Huang, L. Chen, A.T.S. Wee, Orientationally Ordered C_{60} on p-Sexiphenyl Nanostripes on Ag(111), ACS Nano, 2 (2008) 693-698.

[18] N. Martsinovich, L. Kantorovich, Theoretical Modelling of Tip Effects in the Pushing Manipulation of C_{60} on the Si(001) Surface, Nanotechnology, 19 (2008) 235702.

[19] A.O. Dmitry, G.K. Vasily, V.U. Tatiana, V.Z. Andrey, A.S. Alexander, The Manipulation of C_{60} in Molecular Arrays with an STM Tip in Regimes Below the Decomposition Threshold, Nanotechnology, 24 (2013) 055302.

[20] P.H. Beton, A.W. Dunn, P. Moriarty, Manipulation of C_{60} Molecules on a Si surface, Applied Physics Letters, 67 (1995) 1075-1077.

[21] M.T. Cuberes, R.R. Schlittler, J.K. Gimzewski, Room Temperature Repositioning of Individual C_{60} Molecules at Cu Steps: Operation of a Molecular Counting Device, Applied Physics Letters, 69 (1996) 3016-3018.

[22] H. Tang, M.T. Cuberes, C. Joachim, J.K. Gimzewski, Fundamental Considerations in the Manipulation of a Single C_{60} Molecule on a Surface with an STM, Surface Science, 386 (1997) 115-123.

[23] J.A. Larsson, S.D. Elliott, J.C. Greer, J. Repp, G. Meyer, R. Allenspach, Orientation of Individual C_{60} Molecules Adsorbed on Cu(111): Low-temperature Scanning Tunneling Microscopy and Density Functional Calculations, Physical Review B, 77 (2008) 115434.

[24] A. Stróżecka, J. Mysliveček, B. Voigtländer, Scanning Tunneling Spectroscopy and Manipulation of C_{60} on Cu(111), Appl Phys A, 87 (2007) 475-478.

[25] D.L. Keeling, M.J. Humphry, P. Moriarty, P.H. Beton, Attractive Mode Manipulation of Covalently Bound Molecules, Chemical Physics Letters, 366 (2002) 300-304.

[26] P. Moriarty, Y.R. Ma, M.D. Upward, P.H. Beton, Translation, Rotation and Removal of C_{60} on Si(100)-2×1 Using Anisotropic Molecular Manipulation, Surface Science, 407 (1998) 27-35.

[27] N. Martsinovich, L. Kantorovich, Modelling the Manipulation of C_{60} on the Si(001) Surface Performed with NC-AFM, Nanotechnology, 20 (2009) 135706.

[28] N. Martsinovich, L. Kantorovich, Pulling the C_{60} Molecule on a Si(001) Surface with an STM Tip: A Theoretical Study, Physical Review B, 77 (2008) 115429.

[29] R. Nouchi, K. Masunari, T. Ohta, Y. Kubozono, Y. Iwasa, Ring of C_{60} Polymers Formed by Electron or Hole Injection from a Scanning Tunneling Microscope Tip, Physical Review Letters, 97 (2006) 196101.

[30] S.W. Hla, Scanning Tunneling Microscopy Single Atom/Molecule Manipulation and its Application to Nanoscience and Technology, Journal of Vacuum Science & Technology B, 23 (2005) 1351-1360.

[31] G. Dujardin, E. Boer-Duchemin, E. Le Moal, A.J. Mayne, D. Riedel, DIET at the Nanoscale, Surface Science, 643 (2016) 13-17.

[32] D. Lock, S. Sakulsermsuk, R.E. Palmer, P.A. Sloan, Mapping the Site-specific Potential Energy Landscape for Chemisorbed and Physisorbed Aromatic Molecules on the Si(1 1 1)-7 × 7 Surface by Time-lapse STM, Journal of Physics: Condensed Matter, 27 (2015) 054003.

[33] L. Soukiassian, A.J. Mayne, M. Carbone, G. Dujardin, Atomic Wire Fabrication by STM Induced Hydrogen Desorption, Surface Science, 528 (2003) 121-126.

[34] G. Comtet, L. Hellner, G. Dujardin, K. Bobrov, Adsorption of O_2 on Si(111)-7x7 at 300 and 30 K Studied by Ion Photodesorption and Electron Photoemission, Physical Review B, 65 (2001) 035315.

[35] A.J. Mayne, F. Rose, G. Comtet, L. Hellner, G. Dujardin, Variable Temperature STM Studies of the Adsorption of Oxygen on the Si(111)-7×7 Surface, Surface Science, 528 (2003) 132-137.

[36] I.S. Hwang, R.L. Lo, T.T. Tsong, Mechanisms and Energetics of Site Hopping and Chemical Reactions of O_2 Molecules at Si(111)-7×7 Surfaces, Surface Science, 399 (1998) 173-189.

[37] S. Sakulsermsuk, P.A. Sloan, W. Theis, R.E. Palmer, Calibrating Thermal and Scanning Tunnelling Microscope Induced Desorption and Diffusion for the Chemisorbed Chlorobenzene/Si(111)7×7 System, Journal of Physics: Condensed Matter, 22 (2010) 084002.

[38] C. Shen, M. Buck, Nanoscale Patterning of a Self-assembled Monolayer by Modification of the Molecule–substrate Bond, Beilstein Journal of Nanotechnology, 5 (2014) 258-267.

[39] P.A. Sloan, S. Sakulsermsuk, R.E. Palmer, Nonlocal Desorption of Chlorobenzene Molecules from the Si(111)-(7×7) Surface by Charge Injection from the Tip of a Scanning Tunneling Microscope: Remote Control of Atomic Manipulation, Physical Review Letters, 105 (2010) 048301.

[40] T.L. Pan, P.A. Sloan, R.E. Palmer, Non-Local Atomic Manipulation on Semiconductor Surfaces in the STM: The Case of Chlorobenzene on Si(111)-7×7, The Chemical Record, 14 (2014) 841-847.

[41] T.L. Pan, P.A. Sloan, R.E. Palmer, Concerted Thermal-Plus-Electronic Nonlocal Desorption of Chlorobenzene from Si(111)-7 × 7 in the STM, The Journal of Physical Chemistry Letters, 5 (2014) 3551-3554.

[42] R. Young, J. Ward, F. Scire, Observation of Metal-Vacuum-Metal Tunneling, Field Emission, and the Transition Region, Physical Review Letters, 27 (1971) 922-924.

[43] J.A. Stroscio, R.M. Feenstra, A.P. Fein, Electronic Structure of the Si(111)2x1 Surface by Scanning-Tunneling Microscopy, Physical Review Letters, 57 (1986) 2579-2582.

[44] CRC Handbook of Chemistry and Physics, 96th ed., CRC, 2015-2016.

[45] C. Joachim, M.A. Ratner, Molecular Electronics: Some Views on Transport Junctions and Beyond, PNAS, 102 (2005) 8801-8808.

[46] I.V. Pobelov, C. Li, T. Wandlowski, Electrochemical Scanning Tunneling Microscopy, in: B. Bhushan (Ed.) Encyclopedia of Nanotechnology, Springer Netherlands, Dordrecht, 2012, pp. 688-702.

[47] D.A.B.B.D. Huey, Scanning Probe Microscopy and Spectroscopy: Theory, Techniques, and Applications, 2nd ed., Wiley-VCH, New York, 2001.

[48] S.W. Hla, K.F. Braun, K.H. Rieder, Single-Atom Manipulation Mechanisms During a Quantum Corral Construction, Physical Review B, 67 (2003) 201402.

[49] H.C. Manoharan, C.P. Lutz, D.M. Eigler, Quantum Mirages Formed by Coherent Projection of Electronic Structure, Nature, 403 (2000) 512-515.

[50] K.F. Braun, S.W. Hla, N. Pertaya, H.W. Soe, C.F.J. Flipse, K.H. Rieder, Force, Current and Field Effects in Single Atom Manipulation, AIP Conference Proceedings, 696 (2003) 109-116.

[51] L. Gross, F. Moresco, M. Alemani, H. Tang, A. Gourdon, C. Joachim, K.-H. Rieder, Lander on Cu(211) – Selective Adsorption and Surface Restructuring by a Molecular wire, Chemical Physics Letters, 371 (2003) 750-756.

[52] F. Moresco, G. Meyer, K.-H. Rieder, H. Tang, A. Gourdon, C. Joachim, Recording Intramolecular Mechanics during the Manipulation of a Large Molecule, Physical Review Letters, 87 (2001) 088302.

[53] F. Moresco, G. Meyer, K.-H. Rieder, H. Tang, A. Gourdon, C. Joachim, Conformational Changes of Single Molecules Induced by Scanning Tunneling Microscopy Manipulation: A Route to Molecular Switching, Physical Review Letters, 86 (2001) 672-675.

[54] G. Meyer, S. Zöphel, K.-H. Rieder, Scanning Tunneling Microscopy Manipulation of Native Substrate Atoms: A New Way to Obtain Registry Information on Foreign Adsorbates, Physical Review Letters, 77 (1996) 2113-2116.

[55] L. Bartels, G. Meyer, K.H. Rieder, Basic Steps of Lateral Manipulation of Single Atoms and Diatomic Clusters with a Scanning Tunneling Microscope Tip, Physical Review Letters, 79 (1997) 697-700.

[56] A. Kühnle, G. Meyer, S.W. Hla, K.H. Rieder, Understanding Atom Movement During Lateral Manipulation with the STM Tip Using a Simple Simulation Method, Surface Science, 499 (2002) 15-23.

[57] J.A. Stroscio, R.J. Celotta, Controlling the Dynamics of a Single Atom in Lateral Atom Manipulation, Science, 306 (2004) 242-247.

[58] I.S. Tilinin, M.A. Van Hove, M. Salmeron, Tip–surface Transfer of Adatoms in AFM/STM: Effect of Quantum Oscillations, Applied Surface Science, 130–132 (1998) 676-681.

[59] I.-W. Lyo, P. Avouris, Field-Induced Nanometer- to Atomic-Scale Manipulation of Silicon Surfaces with the STM, Science, 253 (1991) 173-176.

[60] L. Bartels, G. Meyer, K.H. Rieder, D. Velic, E. Knoesel, A. Hotzel, M. Wolf, G. Ertl, Dynamics of Electron-Induced Manipulation of Individual CO Molecules on Cu(111), Physical Review Letters, 80 (1998) 2004-2007.

[61] S.P. Jarvis, Resolving Intra- and Inter-Molecular Structure with Non-Contact Atomic Force Microscopy, International Journal of Molecular Sciences, 16 (2015) 19936-19959.

[62] G. Kichin, C. Weiss, C. Wagner, F.S. Tautz, R. Temirov, Single Molecule and Single Atom Sensors for Atomic Resolution Imaging of Chemically Complex Surfaces, Journal of the American Chemical Society, 133 (2011) 16847-16851.

[63] G. Dujardin, A. Mayne, O. Robert, F. Rose, C. Joachim, H. Tang, Vertical Manipulation of Individual Atoms by a Direct STM Tip-Surface Contact on Ge(111), Physical Review Letters, 80 (1998) 3085-3088.

[64] G. Dujardin, R.E. Walkup, P. Avouris, Dissociation of Individual Molecules with Electrons from the Tip of a Scanning Tunneling Microscope, Science, 255 (1992) 1232-1235.

[65] P.A. Sloan, R.E. Palmer, Manipulation of Polyatomic Molecules with the Scanning Tunnelling Microscope at Room Temperature: Chlorobenzene Adsorption and Desorption from Si(111)-(7 × 7), Journal of Physics: Condensed Matter, 18 (2006) 1873.

[66] P.A. Sloan, M.F.G. Hedouin, R.E. Palmer, M. Persson, Mechanisms of Molecular Manipulation with the Scanning Tunneling Microscope at Room Temperature: Chlorobenzene/Si(111)-(7×7), Physical Review Letters, 91 (2003) 118301.

[67] T. Komeda, Y. Kim, M. Kawai, B.N.J. Persson, H. Ueba, Lateral Hopping of Molecules Induced by Excitation of Internal Vibration Mode, Science, 295 (2002) 2055-2058.

[68] T.T. Tsong, Effects of an Electric Field in Atomic Manipulations, Physical Review B, 44 (1991) 13703-13710.

[69] L.J. Whitman, J.A. Stroscio, R.A. Dragoset, R.J. Celotta, Manipulation of Adsorbed Atoms and Creation of New Structures on Room-Temperature Surfaces with a Scanning Tunneling Microscope, Science, 251 (1991) 1206-1210.

[70] M.A. Rezaei, B.C. Stipe, W. Ho, Atomically Resolved Adsorption and Scanning Tunneling Microscope Induced Desorption on a Semiconductor: NO on Si(111)-(7×7), The Journal of Chemical Physics, 110 (1999) 4891-4896.

[71] P.A. Redhead, Interaction of Slow Electrons with Chemisorbed Oxygen, Canadian Journal of Physics, 42 (1964) 886-905.

[72] A. Yu, S. Li, G. Czap, W. Ho, Single-Molecule Rotational and Vibrational Spectroscopy and Microscopy with the Scanning Tunneling Microscope, The Journal of Physical Chemistry C, 119 (2015) 14737-14741.

[73] A. Wykrota, M. Bazarnik, R. Czajka, K. Morgenstern, A Molecular Switch Based on the Manipulation of 1,3-dichlorobenzene on Ge(001) Between Two Adsorption Sites by Inelastic Tunneling Electrons, Physical Chemistry Chemical Physics, 17 (2015) 28830-28836.

[74] K. Motobayashi, Y. Kim, M. Ohara, H. Ueba, M. Kawai, The Role of Thermal Excitation in the Tunneling-Electron-Induced Reaction: Dissociation of Dimethyl Disulfide on Cu(111), Surface Science, 643 (2016) 18-22.

[75] E. Inami, I. Hamada, K. Ueda, M. Abe, S. Morita, Y. Sugimoto, Room-Temperature-Concerted Switch Made of a Binary Atom Cluster, Nature Communication, 6 (2015).

[76] K.-H. Ernst, S. Baumann, C.P. Lutz, J. Seibel, L. Zoppi, A.J. Heinrich, Pasteur's Experiment Performed at the Nanoscale: Manual Separation of Chiral Molecules, One by One, Nano Letters, 15 (2015) 5388-5392.

[77] V. Schendel, B. Borca, I. Pentegov, T. Michnowicz, U. Kraft, H. Klauk, P. Wahl, U. Schlickum, K. Kern, Remotely Controlled Isomer Selective Molecular Switching, Nano Letters, 16 (2016) 93-97.

[78] T. Niu, Electric-Field-Induced Molecular Switch of Single Dipolar Phthalocyanine on Cu(111): A Scanning Tunneling Microscopy Study, The Journal of Physical Chemistry C, 119 (2015) 19802-19807.

[79] X.-S. Zhou, Y.-M. Wei, L. Liu, Z.-B. Chen, J. Tang, B.-W. Mao, Extending the Capability of STM Break Junction for Conductance Measurement of Atomic-Size Nanowires: An Electrochemical Strategy, Journal of the American Chemical Society, 130 (2008) 13228-13230.

[80] L. Lafferentz, F. Ample, H. Yu, S. Hecht, C. Joachim, L. Grill, Conductance of a Single Conjugated Polymer as a Continuous Function of Its Length, Science, 323 (2009) 1193-1197.

[81] T. Kumagai, F. Hanke, S. Gawinkowski, J. Sharp, K. Kotsis, J. Waluk, M. Persson, L. Grill, Controlling Intramolecular Hydrogen Transfer in a Porphycene Molecule with Single Atoms or Molecules Located Nearby, Nat. Chem., 6 (2014) 41-46.

[82] J.N. Ladenthin, L. Grill, S. Gawinkowski, S. Liu, J. Waluk, T. Kumagai, Hot Carrier-Induced Tautomerization within a Single Porphycene Molecule on Cu(111), ACS Nano, 9 (2015) 7287-7295.

[83] E.G. McRae, R.A. Malic, Low Energy Electron Diffraction Beam Profiles and Phase Transition at Si(111)-7 X 7 Surface, Surface Science, 161 (1985) 25-32.

[84] S.Y. Tong, H. Huang, C.M. Wei, W.E. Packard, F.K. Men, G. Glander, M.B. Webb, Low Energy Electron Diffraction Analysis of the Si(111)-7×7 Structure, Journal of Vacuum Science & Technology A, 6 (1988) 615-624.

[85] R.S. Becker, J.A. Golovchenko, E.G. McRae, B.S. Swartzentruber, Tunneling Images of Atomic Steps on the Si(111)-7x7 Surface, Physical Review Letters, 55 (1985) 2028-2031.

[86] F.J. Himpsel, Structural Model for Si(111)-(7x7), Physical Review B, 27 (1983) 7782-7785.

[87] J. Kim, M.-L. Yeh, F.S. Khan, J.W. Wilkins, Surface Phonons of the Si(111)-7x7 Reconstructed Surface, Physical Review B, 52 (1995) 14709-14718.

[88] I.K. Robinson, W.K. Waskiewicz, P.H. Fuoss, L.J. Norton, Observation of Strain in the Si(111)-7x7 Surface, Physical Review B, 37 (1988) 4325-4328.

[89] K. Takayanagi, Y. Tanishiro, M. Takahashi, S. Takahashi, Structural Analysis of Si(111)-7x7 by UHV Transmission Electron Diffraction and Microscopy, Journal of Vacuum Science & Technology A: Vacuum, Surfaces, and Films, 3 (1985) 1502-1506.

[90] J.W.P. Hsu, C.C. Bahr, A.V. Felde, S.W. Downey, G.S. Higashi, M.J. Cardillo, Si(111)(7 x 7) Dangling Bond Contribution to Surface Recombination, Journal of Vacuum Science & Technology A 10 (1992) 985-989.

[91] Y. Cao, J.F. Deng, G.Q. Xu, Stereo-selective Binding of Chlorobenzene on Si(111)-7x7, The Journal of Chemical Physics, 112 (2000) 4759-4767.

[92] Z.-H. Li, Y.-C. Li, W.-N. Wang, Y. Cao, K.-N. Fan, A Density Functional Theory Study on the Adsorption of Chlorobenzene on the Si(111)-7×7 Surface, The Journal of Physical Chemistry B, 108 (2004) 14049-14055.

[93] M. Utecht, T. Pan, T. Klamroth, R.E. Palmer, Quantum Chemical Cluster Models for Chemi- and Physisorption of Chlorobenzene on Si(111)-7×7, The Journal of Physical Chemistry A, 118 (2014) 6699-6704.

[94] C. Silvestre, M. Shayegan, Observation of a Metastable Precursor for Adsorption of Oxygen on Si(111) and the Activation Energy for Chemisorption, Physical Review B, 37 (1988) 10432-10435.

[95] U. Höfer, P. Morgen, W. Wurth, E. Umbach, Initial Stages of Oxygen Adsorption on Si(111). II. The Molecular Precursor, Physical Review B, 40 (1989) 1130-1145.

[96] K. Kato, T. Uda, K. Terakura, Backbond Oxidation of the Si(001) Surface: Narrow Channel of Barrierless Oxidation, Physical Review Letters, 80 (1998) 2000-2003.

[97] T. Hoshino, Y. Nishioka, Molecular Adsorption and Dissociative Reaction of Oxygen on the Si(111)7x7 Surface, Physical Review B, 61 (2000) 4705-4713.

[98] F. Matsui, H.W. Yeom, K. Amemiya, K. Tono, T. Ohta, Reinterpretation of the Molecular O_2 Chemisorbate in the Initial Oxidation of the Si(111)-7x7 Surface, Physical Review Letters, 85 (2000) 630-633.

[99] K. Sakamoto, S. Doi, Y. Ushimi, K. Ohno, H.W. Yeom, T. Ohta, S. Suto, W. Uchida, Adsorption Process of Metastable Molecular Oxygen on a Si(111)-7x7 Surface, Physical Review B, 60 (1999) R8465-R8468.

[100] H. Ibach, H.D. Bruchmann, H. Wagner, Vibrational Study of the Initial Stages of the Oxidation of Si(111) and Si(100) Surfaces, Appl Phys A, 29 (1982) 113-124.

[101] K. Edamoto, Y. Kubota, H. Kobayashi, M. Onchi, M. Nishijima, Oxidation of the Si(111) (7×7) surface: Electron energy loss spectroscopy, low-energy electron diffraction, and Auger electron spectroscopy studies, The Journal of Chemical Physics, 83 (1985) 428-436.

[102] B.N.J. Persson, P. Avouris, Local Bond Breaking via STM-Induced Excitations: the Role of Temperature, Surface Science, 390 (1997) 45-54.

[103] T.C. Shen, C. Wang, G.C. Abeln, J.R. Tucker, J.W. Lyding, P. Avouris, R.E. Walkup, Atomic-Scale Desorption Through Electronic and Vibrational Excitation Mechanisms, Science, 268 (1995) 1590-1592.

[104] B.C. Stipe, M.A. Rezaei, W. Ho, S. Gao, M. Persson, B.I. Lundqvist, Single-Molecule Dissociation by Tunneling Electrons, Physical Review Letters, 78 (1997) 4410-4413.

[105] D. Riedel, M.-L. Bocquet, H. Lesnard, M. Lastapis, N. Lorente, P. Sonnet, G. Dujardin, Selective Scanning Tunnelling Microscope Electron-Induced Reactions of Single Biphenyl Molecules on a Si(100) Surface, Journal of the American Chemical Society, 131 (2009) 7344-7352.

[106] S. Sakulsermsuk, P.A. Sloan, R.E. Palmer, A New Mechanism of Atomic Manipulation: Bond-Selective Molecular Dissociation via Thermally Activated Electron Attachment, ACS Nano, 4 (2010) 7344-7348.

[107] T.L. Pan, S. Sakulsermsuk, P.A. Sloan, R.E. Palmer, Site- and Energy-Selective Intramolecular Manipulation of Polychlorinated Biphenyl (PCB) Molecules, Journal of the American Chemical Society, 133 (2011) 11834-11836.

[108] P. Maksymovych, D.B. Dougherty, X.Y. Zhu, J.T. Yates, Nonlocal Dissociative Chemistry of Adsorbed Molecules Induced by Localized Electron Injection into Metal Surfaces, Physical Review Letters, 99 (2007) 016101.

[109] D. Lock, K.R. Rusimova, T.L. Pan, R.E. Palmer, P.A. Sloan, Atomically Resolved Real-space Imaging of Hot Electron Dynamics, Nature Communication, 6 (2015).

[110] R.E.P. T.L. Pan, Activation Energy of Chlorobenzene Molecule on the Si(111)-7x7 Surface, in, 2013.

[111] B. Guan, H. Siampour, Z. Fan, S. Wang, X.Y. Kong, A. Mesli, J. Zhang, Y. Dan, Nanoscale Nitrogen Doping in Silicon by Self-Assembled Monolayers, Scientific Reports, 5 (2015) 12641.

[112] M.-H. Bae, Z. Li, Z. Aksamija, P.N. Martin, F. Xiong, Z.-Y. Ong, I. Knezevic, E. Pop, Ballistic to Diffusive Crossover of Heat Flow in Graphene Ribbons, Nature Communication, 4 (2013) 1734.

[113] D.D. Chambliss, K.E. Johnson, R.J. Wilson, S. Chiang, Surface Structure and Metal Epitaxy: STM Studies of Ultrathin Metal Films on Au(111) and Cu(100), Journal of Magnetism and Magnetic Materials, 121 (1993) 1-9.

[114] J.A. Stroscio, D.T. Pierce, R.A. Dragoset, P.N. First, Microscopic Aspects of the Initial Growth of Metastable fcc iron on Au(111), Journal of Vacuum Science & Technology A, 10 (1992) 1981-1985.

[115] S. Helveg, J.V. Lauritsen, E. Lægsgaard, I. Stensgaard, J.K. Nørskov, B.S. Clausen, H. Topsøe, F. Besenbacher, Atomic-Scale Structure of Single-Layer MoS2 Nanoclusters, Physical Review Letters, 84 (2000) 951-954.

[116] T. Yokoyama, S. Yokoyama, T. Kamikado, Y. Okuno, S. Mashiko, Selective Assembly on a Surface of Supramolecular Aggregates with Controlled Size and Shape, Nature, 413 (2001) 619-621.

[117] M. Böhringer, K. Morgenstern, W.-D. Schneider, M. Wühn, C. Wöll, R. Berndt, Self-assembly of 1-nitronaphthalene on Au(111), Surface Science, 444 (2000) 199-210.

[118] Y. Wang, X. Ge, G. Schull, R. Berndt, C. Bornholdt, F. Koehler, R. Herges, Azo Supramolecules on Au(111) with Controlled Size and Shape, Journal of the American Chemical Society, 130 (2008) 4218-4219.

[119] C. Wöll, S. Chiang, R.J. Wilson, P.H. Lippel, Determination of Atom Positions at Stacking-fault Dislocations on Au(111) by Scanning Tunneling Microscopy, in: H. Neddermeyer (Ed.) Scanning Tunneling Microscopy, Springer Netherlands, 1993, pp. 114-117.

[120] S. Narasimhan, D. Vanderbilt, Elastic Stress Domains and the Herringbone Reconstruction on Au(111), Physical Review Letters, 69 (1992) 1564-1567.

[121] Z.-X. Xie, Z.-F. Huang, X. Xu, Influence of Reconstruction on the Structure of Self-assembled Normal-alkane Monolayers on Au(111) Surfaces, Physical Chemistry Chemical Physics, 4 (2002) 1486-1489.

[122] L. Bürgi, H. Brune, K. Kern, Imaging of Electron Potential Landscapes on Au(111), Physical Review Letters, 89 (2002) 176801.

[123] M.A. Van Hove, R.J. Koestner, P.C. Stair, J.P. Bibérian, L.L. Kesmodel, I. BartoŠ, G.A. Somorjai, The surface Reconstructions of the (100) Crystal Faces of Iridium, Platinum and Gold: I. Experimental Observations and Possible Structural Models, Surface Science, 103 (1981) 189-217.

[124] P. Maksymovych, D.C. Sorescu, D. Dougherty, J.T. Yates, Surface Bonding and Dynamical Behavior of the CH3SH Molecule on Au(111), The Journal of Physical Chemistry B, 109 (2005) 22463-22468.

[125] F. Reinert, G. Nicolay Influence of the Herringbone Reconstruction on the Surface Electronic Structure of Au(111), Appl Phys A, 78 (2004) 817-821.

[126] Z.W. Wang, O. Toikkanen, F. Yin, Z.Y. Li, B.M. Quinn, R.E. Palmer, Counting the Atoms in Supported, Monolayer-Protected Gold Clusters, Journal of the American Chemical Society, 132 (2010) 2854-2855.

[127] W.G. Cullen, P.N. First, Island Shapes and Intermixing for Submonolayer Nickel on Au(111), Surface Science, 420 (1999) 53-64.

[128] D.S. He, Y. Han, J. Fennell, S.L. Horswell, Z.Y. Li, Growth and stability of Pt on Au nanorods, Applied Physics Letters, 101 (2012) 113102.

[129] C.F. Sanz-Navarro, R. Smith, D.J. Kenny, S. Pratontep, R.E. Palmer, Scaling Behavior of the Penetration Depth of Energetic Silver Clusters in Graphite, Physical Review B, 65 (2002) 165420.

[130] F. Yin, Z.W. Wang, R.E. Palmer, Ageing of Mass-selected Cu/Au and Au/Cu core/shell Clusters Probed with Atomic Resolution, Journal of Experimental Nanoscience, 7 (2012) 703-710.

[131] Y. Li, Z.W. Wang, C.-Y. Chiu, L. Ruan, W. Yang, Y. Yang, R.E. Palmer, Y. Huang, Synthesis of Bimetallic Pt-Pd core-shell Nanocrystals and their High Electrocatalytic Activity Modulated by Pd Shell Thickness, Nanoscale, 4 (2012) 845-851.

[132] B.V. Reddy, S.N. Khanna, Self-Stimulated NO Reduction and CO Oxidation by Iron Oxide Clusters, Physical Review Letters, 93 (2004) 068301.

[133] M. Giesen, C. Steimer, H. Ibach, What does one Learn from Equilibrium Shapes of Two-dimensional Islands on Surfaces?, Surface Science, 471 (2001) 80-100.

[134] A. Moghaddasi, M. Zahedi, P. Watson, Theoretical Study of Site Dependency on Charge Transfer at Au(111) Nanoclusters, The Journal of Physical Chemistry C, 116 (2012) 5014-5018.

[135] D.D. Chambliss, R.J. Wilson, S. Chiang, Nucleation of Ordered Ni Island Arrays on Au(111) by Surface-Lattice Dislocations, Physical Review Letters, 66 (1991) 1721-1724.

[136] J.W.A. Sachtler, G.A. Somorjai, Influence of Ensemble Size on CO Chemisorption and Catalytic n-hexane Conversion by Au-Pt(111) Bimetallic Single-Crystal Surfaces, Journal of Catalysis, 81 (1983) 77-94.

[137] L.A. Kibler, M. Kleinert, R. Randler, D.M. Kolb, Initial Stages of Pd Deposition on Au(hkl) Part I: Pd on Au(111), Surface Science, 443 (1999) 19-30.

[138] H.W. Kroto, J.R. Heath, S.C. O'Brien, R.F. Curl, R.E. Smalley, C_{60}: Buckminsterfullerene, Nature, 318 (1985) 162-163.

[139] R.D. Johnson, G. Meijer, D.S. Bethune, C_{60} has Icosahedral Symmetry, Journal of the American Chemical Society, 112 (1990) 8983-8984.

[140] C.S. Yannoni, R.D. Johnson, G. Meijer, D.S. Bethune, J.R. Salem, Carbon-13 NMR study of the C_{60} Cluster in the Solid State: Molecular Motion and Carbon Chemical Shift Anisotropy, The Journal of Physical Chemistry, 95 (1991) 9-10.

[141] K. Hedberg, L. Hedberg, D.S. Bethune, C.A. Brown, H.C. Dorn, R.D. Johnson, M. De Vries, Bond Lengths in Free Molecules of Buckminsterfullerene, C_{60}, from Gas-Phase Electron Diffraction, Science, 254 (1991) 410-412.

[142] G.D. M. S. Dresselhaus, P. C. Eklund, Science of Fullerenes and Carbon Nanotubes: Their Properties and Application, 1995.

[143] M. Paßens, R. Waser, S. Karthäuser, Enhanced Fullerene–Au(111) Coupling in (2√3×2√3)R30° Superstructures with Intermolecular Interactions, Beilstein Journal of Nanotechnology, 6 (2015) 1421-1431.

[144] L.-L. Wang, H.-P. Cheng, Rotation, Translation, Charge Transfer, and Electronic Structure of C_{60} on Cu(111) Surface, Physical Review B, 69 (2004) 045404.

[145] D. Fujita, T. Yakabe, H. Nejoh, T. Sato, M. Iwatsuki, Scanning Tunneling Microscopy Study on the Initial Adsorption Behavior of C_{60} Molecules on a Reconstructed Au(111)-(23 × √3) Surface at Various Temperatures, Surface Science, 366 (1996) 93-98.

[146] X. Zhang, L. Tang, Q. Guo, Low-Temperature Growth of C_{60} Monolayers on Au(111): Island Orientation Control with Site-Selective Nucleation, The Journal of Physical Chemistry C, 114 (2010) 6433-6439.

[147] L. Tang, X. Zhang, Q. Guo, Y.-N. Wu, L.-L. Wang, H.-P. Cheng, Two Bonding Configurations for Individually Adsorbed C_{60} Molecules on Au(111), Physical Review B, 82 (2010) 125414.

[148] G. Gensterblum, J.J. Pireaux, P.A. Thiry, R. Caudano, J.P. Vigneron, P. Lambin, A.A. Lucas, W. Krätschmer, High-resolution Electron-energy-loss Spectroscopy of Thin Films of C_{60} on Si(100), Physical Review Letters, 67 (1991) 2171-2174.

[149] J.L. Wragg, J.E. Chamberlain, H.W. White, W. Kratschmer, D.R. Huffman, Scanning Tunnelling Microscopy of Solid $C(_{60})/C(_{70})$, Nature, 348 (1990) 623.

[150] G. Schull, R. Berndt, Orientationally Ordered (7x7) Superstructure of C_{60} on Au(111), Physical Review Letters, 99 (2007) 226105.

[151] G. Schulze, K.J. Franke, A. Gagliardi, G. Romano, C.S. Lin, A.L. Rosa, T.A. Niehaus, T. Frauenheim, A. Di Carlo, A. Pecchia, J.I. Pascual, Resonant Electron Heating and Molecular Phonon Cooling in Single C_{60} Junctions, Physical Review Letters, 100 (2008) 136801.

[152] S. Gunnar, J.F. Katharina, P. Jose Ignacio, Resonant Heating and Substrate-mediated Cooling of a Single C_{60} Molecule in a Tunnel Junction, New Journal of Physics, 10 (2008) 065005.

[153] E.W. Müller, K. Bahadur, Field Ionization of Gases at a Metal Surface and the Resolution of the Field Ion Microscope, Physical Review, 102 (1956) 624-631.

[154] K. Oura, Lifshits, V.G., Saranin, A., Zotov, A.V., Katayama, M. , Surface Science An Introduction, Springer Berlin Heidelberg, 2003.

[155] O. Pierre-Louis, M.R. D'Orsogna, T.L. Einstein, Edge Diffusion During Growth: The Kink Ehrlich-Schwoebel Effect and Resulting Instabilities, Physical Review Letters, 82 (1999) 3661-3664.

[156] G.E. Grazyna Antczak, Surface Diffusion Metals, Metal Atoms, and Clusters, Cambridge University Press, Cambridge, 2010.

[157] A. Kühnle, Self-assembly of Organic Molecules at Metal Surfaces, Current Opinion in Colloid & Interface Science, 14 (2009) 157-168.

[158] E. Clouet, Modeling of nucleation processes, arXiv preprint arXiv:1001.4131, (2010).

[159] T.A. Witten, L.M. Sander, Diffusion-Limited Aggregation, a Kinetic Critical Phenomenon, Physical Review Letters, 47 (1981) 1400-1403.

[160] V.G. Dubrovskii, Nucleation theory and growth of nanostructures, Springer, 2014.

[161] J.W. Schmelzer, G. Röpke, V.B. Priezzhev, Nucleation theory and applications, Wiley Online Library, 2005.

[162] H. Reiss, The kinetics of phase transitions in binary systems, The Journal of Chemical Physics, 18 (1950) 840-848.

[163] M. Giesen, Step and island dynamics at solid/vacuum and solid/liquid interfaces, Progress in Surface Science, 68 (2001) 1-154.

[164] Y. Li, A.E. DePristo, Predicted Growth Mode for Metal Homoepitaxy on the fcc (111) Surface, Surface Science, 351 (1996) 189-199.

[165] G. Boisvert, L.J. Lewis, M.J. Puska, R.M. Nieminen, Energetics of Diffusion on the (100) and (111) Surfaces of Ag, Au, and Ir From First Principles, Physical Review B, 52 (1995) 9078-9085.

[166] S.Y. Kim, I.-H. Lee, S. Jun, Transition-pathway Models of Atomic Diffusion on fcc Metal Surfaces. I. Flat Surfaces, Physical Review B, 76 (2007) 245407.

[167] B. Fischer, H. Brune, J.V. Barth, A. Fricke, K. Kern, Nucleation Kinetics on Inhomogeneous Substrates: Al/Au(111), Physical Review Letters, 82 (1999) 1732-1735.

[168] R. Mahaffy, R. Bhatia, B.J. Garrison, Diffusion of a Butanethiolate Molecule on a Au{111} Surface, The Journal of Physical Chemistry B, 101 (1997) 771-773.

[169] E. Mateo-Martí, C. Rogero, C. Gonzalez, J.M. Sobrado, P.L. de Andrés, J.A. Martin-Gago, Interplay between Fast Diffusion and Molecular Interaction in the Formation of Self-Assembled Nanostructures of S-Cysteine on Au(111), Langmuir, 26 (2010) 4113-4118.

[170] F. Buchner, J. Xiao, E. Zillner, M. Chen, M. Röckert, S. Ditze, M. Stark, H.-P. Steinrück, J.M. Gottfried, H. Marbach, Diffusion, Rotation, and Surface Chemical Bond of Individual 2H-Tetraphenylporphyrin Molecules on Cu(111), The Journal of Physical Chemistry C, 115 (2011) 24172-24177.

[171] S.-C. Yan, N. Xie, H.-Q. Gong, Q. Sun, Y. Guo, X.-Y. Shan, X.-H. Lu, Mapping the Diffusion Potential of a Reconstructed Au(111) Surface at Nanometer Scale with 2D Molecular Gas, Chinese Physics Letters, 29 (2012) 046803.

[172] K. Jooyoung, U. Hironaga, Y. Kazuhiro, K. Heejoon, N. Kazuhiro, I. Mitsuteru, Local Atomic Diffusion on Au(111) Surface Induced by Au Tip, Japanese Journal of Applied Physics, 42 (2003) 3616.

[173] P. Han, B.A. Mantooth, E.C.H. Sykes, Z.J. Donhauser, P.S. Weiss, Benzene on Au{111} at 4 K: Monolayer Growth and Tip-Induced Molecular Cascades, Journal of the American Chemical Society, 126 (2004) 10787-10793.

[174] E.I. Altman, R.J. Colton, Nucleation, Growth, and Structure of Fullerene Films on Au(111), Surface Science, 279 (1992) 49-67.

[175] S. Guo, D.P. Fogarty, P.M. Nagel, S.A. Kandel, Thermal Diffusion of C_{60} Molecules and Clusters on Au(111), The Journal of Physical Chemistry B, 108 (2004) 14074-14081.

[176] E.I. Altman, R.J. Colton, The Interaction of C_{60} with Noble Metal Surfaces, Surface Science, 295 (1993) 13-33.

[177] A.V. Matetskiy, L.V. Bondarenko, D.V. Gruznev, A.V. Zotov, A.A. Saranin, J.P. Chou, C.R. Hsing, C.M. Wei, Y.L. Wang, Peculiar Diffusion of C_{60} on In-adsorbed Si(111)$\sqrt{3} \times \sqrt{3}$-Au Surface, Surface Science, 616 (2013) 44-50.

[178] R. Hołyst, M. Litniewski, Evaporation into Vacuum: Mass Flux from Momentum Flux and the Hertz–Knudsen Relation Revisited, The Journal of Chemical Physics, 130 (2009) 074707.

[179] R.A. Nevshupa, L.S. Sinev, Model of Pressure Variation in a Vacuum System for Volatile Liquid Evacuation, Technical Physics, 50 1255-1258.

[180] Instrumentation Reference Book, Butterworth Heinemann, Agilend Technologies, 2003.

[181] B. Ren, G. Picardi, B. Pettinger, Preparation of Gold Tips Suitable for Tip-enhanced Raman Spectroscopy and Light Emission by Electrochemical Etching, Review of Scientific Instruments, 75 (2004) 837-841.

[182] B.L. Rogers, J.G. Shapter, W.M. Skinner, K. Gascoigne, A Method for Production of Cheap, Reliable Pt–Ir Tips, Review of Scientific Instruments, 71 (2000) 1702-1705.

[183] I. Ekvall, E. Wahlström, D. Claesson, H. Olin, E. Olsson, Preparation and Characterization of Electrochemically Etched W tips for STM, Measurement Science and Technology, 10 (1999) 11.

[184] P. Kim, J.H. Kim, M.S. Jeong, K. Do-Kyeong, J. Lee, S. Jeong, Efficient Electrochemical Etching Method to Fabricate Sharp Metallic tips for Scanning Probe Microscopes, Review of Scientific Instruments, 77 (2006) 103705-103706.

[185] A.-S. Lucier, H. Mortensen, Y. Sun, P. Grütter, Determination of the Atomic Structure of Scanning Probe Microscopy Tungsten tips by Field Ion Microscopy, Physical Review B, 72 (2005) 235420.

[186] A.I. Oliva, A.R. G, J.L. Pena, E. Anguiano, M. Aguilar, Electrochemical Preparation of Tungsten Tips for a Scanning Tunneling Microscope, Review of Scientific Instruments, 67 (1996) 1917-1921.

[187] A.K. Kar, S. Gangopadhyay, B.K. Mathur, S. Gangopadhyay, A Reverse Electrochemical Floating-layer Technique of SPM tip Preparation, Measurement Science and Technology, 11 (2000) 1426.

[188] Y. Khan, H. Al-Falih, Y. Zhang, T.K. Ng, B.S. Ooi, Two-step Controllable Electrochemical Etching of Tungsten Scanning Probe Microscopy Tips, Review of Scientific Instruments, 83 (2012) 063708.

[189] B. Gasser, A. Menck, H. Brune, K. Kern, Design of a ‘‘beetle-type’’ Atomic Force Microscope Using the Beam Deflection Technique, Review of Scientific Instruments, 67 (1996) 1925-1929.

[190] E.M. Mkawi, K. Ibrahim, M.K.M. Ali, K.M.A. Saron, M.A. Farrukh, N.K. Allam, Influence of Substrate Temperature on the Properties of Electrodeposited Kesterite Cu_2ZnSnS_4 (CZTS) Thin Films for Photovoltaic Applications, Journal of Materials Science: Materials in Electronics, 26 (2014) 222-228.

[191] S. Sakulsermsuk, Moleculer Manipulation with the Scaning Tunnelling Microscope, in: School of Physics and Astronomy, University of Birmingham, Birmingham, 2010.

[192] M.R. Fard, Unpublished Work: Cluster Distribution with Increasing Amount of Au Atoms, in.

[193] G.M. Francis, L. Kuipers, J.R.A. Cleaver, R.E. Palmer, Diffusion Controlled Growth of Metallic Nanoclusters at Selected Surface Sites, Journal of Applied Physics, 79 (1996) 2942-2947.

[194] P. Rahe, R. Bechstein, A. Kühnle, Vertical and Lateral Drift Corrections of Scanning Probe Microscopy Images, Journal of Vacuum Science & Technology B, 28 (2010) C4E31-C34E38.

[195] S.A. Krasnikov, S.I. Bozhko, K. Radican, O. Lübben, B.E. Murphy, S.-R. Vadapoo, H.-C. Wu, M. Abid, V.N. Semenov, I.V. Shvets, Self-assembly and Ordering of C_{60} on the WO_2/W(110) Surface, Nano Research, 4 (2010) 194-203.

[196] R.E. Palmer, P.A. Sloan, Manipulation of Polyatomic Molecules with the Scanning Tunnelling Microscope at Room Temperature: Chlorobenzene Adsorption and Desorption from Si(111)-(7x7), Journal of Physics: Condensed Matter, 18 (2006) 1873-1885.

[197] R. Martel, P. Avouris, I.W. Lyo, Molecularly Adsorbed Oxygen Species on Si(111)-(7×7): STM-Induced Dissociative Attachment Studies, Science, 272 (1996) 385-388.

[198] S.-H. Lee, M.-H. Kang, Identification of the Initial-Stage Oxidation Products on Si(111)-(7x7), Physical Review Letters, 82 (1999) 968-971.

[199] Y. Ono, M. Tabe, H. Kageshima, Scanning-Tunneling-Microscopy Observation of Thermal Oxide Growth on Si(111)7x7 Surfaces, Physical Review B, 48 (1993) 14291-14300.

[200] S.-H. Lee, M.-H. Kang, Origin of O 1s Core-Level Shifts on Oxygen Adsorbed Si(111)-(7x7), Physical Review Letters, 84 (2000) 1724-1727.

[201] D. Lock, Scanning Tunneling Microscopy Studied of Nonlocal Atomic Manipulation and Molecular Kinetics on the Si(111)-7x7 Surface, in: Department of Physics, University of Bath, University of Bath, 2015, pp. 210.

[202] K. Stokbro, U. Quaade, F. Grey, Electric Field Effects in Scanning Tunneling Microscope Imaging, Appl Phys A, 66 (1998) S907-S910.

[203] M. Alemani, M.V. Peters, S. Hecht, K.-H. Rieder, F. Moresco, L. Grill, Electric Field-Induced Isomerization of Azobenzene by STM, Journal of the American Chemical Society, 128 (2006) 14446-14447.

[204] A.J. Mayne, G. Dujardin, G. Comtet, D. Riedel, Electronic Control of Single-Molecule Dynamics, Chemical Reviews, 106 (2006) 4355-4378.

[205] H.C. Akpati, P. Nordlander, L. Lou, P. Avouris, A Density-functional Study of the Effects of an External Electric Field on Admolecule–surface Systems, Surface Science, 401 (1998) 47-55.

[206] D. Meeker, FEMM 4.2 Magnetics, Electrostatics, Heat Flow, and Current Flow, in.

[207] A.D. Muller, F. Muller, M. Hietschold, F. Demming, J. Jersch, K. Dickmann, Characterization of Electrochemically Etched Tungsten Tips for Scanning Tunneling Microscopy, Review of Scientific Instruments, 70 (1999) 3970-3972.

[208] K. R. Rusimova, N. Bannister, P. Harrison, D. Lock, S. Crampin, R. E. Palmer, a.P.A. Sloan, Unpublished Work: Initiating and Imaging the Coherent Dynamics of a 2D Charge Carrier in Real Space, in.

[209] W. Beyer, J. Stuke, Influence of Evaporation Parameters on Electrical Properties of Amorphous Germanium and Silicon, Physica Status Solidi (a), 30 (1975) 511-520.

[210] P. De Padova, C. Quaresima, C. Ottaviani, P.M. Sheverdyaeva, P. Moras, C. Carbone, D. Topwal, B. Olivieri, A. Kara, H. Oughaddou, B. Aufray, G. Le Lay, Evidence of Graphene-like Electronic Signature in Silicene Nanoribbons, Applied Physics Letters, 96 (2010) 261905-261905-261903.